An analysis of the principium in Meister Eckhart's metaphysics of creation according to the Latin works

Visitkul, Viput

Awarding institution:
King's College London

Novel method for high throughput FRET screening with microfluidics

Thesis submitted to King's College London, University of London
in part fulfilment for
the degree of Doctor of Philosophy

Viput Visitkul

Supervisors:
Doctor Simon M. Ameer-Beg
Doctor Klaus Suhling

Randall Division of Cell and Molecular Biophysics,
Richard Dimbleby Department of Cancer Research,
Guy's Campus,
King's College London

Abstract

Functional imaging can provide a level of quantification that is not possible in what might be termed traditional high-content screening. This is due to the fact that the current state-of-the-art high-content screening systems take the approach of scaling-up single cell assays, and are therefore based on essentially pictorial measures as assay indicators. Such phenotypic analyses have become extremely sophisticated, advancing screening enormously, but this approach can still be somewhat subjective. Recent advances in high-content screening with functional read-outs such as FRET (by FLIM or anisotropy imaging) have enabled screening of compound libraries of inhibitors and siRNA against a known protein interaction readout but this is still relatively slow in comparison to true high throughput methodologies. In order to further increase the predictive and statistical power of functional FRET assays, we have developed a compact lifetime-based flow cytometer, utilising a commercial microfluidic chip, to screen large non-adherent cell population. Fluorescent signals from cells are detected using time correlated single photon counting (TCSPC) in the burst integrated fluorescence lifetime (BIFL) mode and used to determine the fluorescence lifetime of each cell. Initially, the system was tested using 2 μm and 10 μm highly fluorescent beads to determine optical throughput and detection efficiency. The system was validated with a number of cell lines transiently transfected with FRET standards, consisting of eGFP and mRFP1 fluorescent proteins linked by 7, 19, and 32 amino acid chains. Analysis software was developed to process detected signals in BIFL mode and chronologically save the transient burst data for each cell in a multi-dimensional image file. Furthermore, the system was validated using an EGFR phosphorylation assay in MCF7 cells to ascertain the sensitivity of the system for protein-protein interaction screening with a transfected protein and a labelled antibody.

Colophon

This thesis was typeset using the LaTeX typesetting system originally developed by Leslie Lamport, based on TeX created by Donald Knuth. The document and bibliography were written and compiled with latex editor, "Texmaker" and "BibTex" respectively. The layout template was obtained from the latex support of Imperial College London. I (Viput Visitkul) sincerely thank the authors and contributors for their helpful contributions.

E-mail: viput.dv@gmail.com

Dedicating this thesis to my parents, Xanxai and Sibhasamond Visitkul, and my late family members, brother Var and both grandmothers, who now all gracefully rest in peace.

Acknowledgements

I would like to generously thank my supervisor Simon for his guidance and support, EPSRC for funding the project, Angus Bain and John Girkin for the invaluable feedbacks and their detailed efforts in examining the thesis, and Keith Brennan for the extra hardship support and understanding. Finally, I hold unreserved praise for Dan Soon on his generosity, empathy and tolerances.

Elena thank you for everything, hopefully we can publish something soon. Barrett – words have eluded me when I think of you, but I do miss you and congratulation again on your engagement.

I have already sorely miss the beautiful Maughan library. It feels extremely privileged to have had access to such magnificent facility during my time in London...

Contents

List of Figures

List of Tables

Chapter 1

Introduction

The control of cellular function and intracellular signalling is clearly complex and highly regulated. Hence, identifications and characterisations of these functional units or establishments of any first-order connectivity would require a top-down research methodology to gain access to cellular contents and their associated information all the way down to the lowest hierarchical level in molecular assemblies. Proteins provide the building blocks for these multicomponent molecular units, or pathways from which higher cellular functions emerge [6]. These units consist of either assemblies of physically interacting proteins or myriads of dispersed biochemical activities connected by rapidly diffusing second messengers, metabolic intermediates, ions or other proteins [6].

A typical way to access proteomic information is to use immunocytochemistry to label any functional proteins of interest with compatible biosensors. The sensor normally consists of a genetically fluorescent protein and an antibody linker, which targets small and specific binding sites on cell surfaces. Therefore it does not excessively disturb the endogenous cellular functions, and subsequently, the global biochemical connectivity [7–16]. Fluorescence immunocytochemistry and variety of contemporary fluorescence imaging techniques, notably time-resolved measurements, have facilitated the means of observing biochemical processes in living cells under quiescent or stimulated conditions [7–16]. The affinity of functional proteins in binding to their permanent or transiently generated conjugated sites in cells, thus allows tracking of any biochemical activities with fluorescence

imaging with a very high resolution (for example a far-field system, which is operating on blue light excitation with 0.5 NA objective can achieve a resolution of 0.5 microns).

Although the resolution of standard time-resolved fluorescence imaging is limited to the diffraction limit ($\sim \lambda/2$) of conventional optical microscopy, the novelty in the lifetime readout which replaces the intensity measurement, can provide a very high dynamic range of output which is sensitive to the local environments of fluorescence origins. This "digitisation" of data, in essense, provides a clear image contrast that would have otherwise been hampered by different types of aberrations of Far-field microscopy. The adaptation of Frster resonance energy transfer (FRET) [17] in time-resolved fluorescence imaging is thus, pragmatic. FRET signals are specifically sensitive to intra- and intermolecular distances , which are comparable to a typical eukaryotic cell size. This makes the resolution of this functional readout comparable to those of the super-resolution techniques [17], which can effectively delineate the cellular contents and spatio-temporal activities of the highly stoichiometric protein-protein chemistries in each organelle [18].

The use of FRET in high throughput drug screening assays has seen some recent limited development into laboratory-scale instruments [5, 19–21]. Temporal domain FRET measurements in Time-Correlated Single Photon Counting (TCSPC) are often utilised in the context. TCSPC has the potential to detect single emission events, has high dynamic range [22] and can be implemented into low on-sample powers which are destructive to cells. The analytical throughputs of these systems, however, are limited to the speed of the automation mechanisms and the time requirement for the detection of sufficient photons per resolved pixel to achieve meaningful lifetime measures [5,20]. Users must therefore make a compromise between the number of cells analyzed and resolved, and the time taken to perform the assay. Scaling assays still further, to the high-throughput arena, where hundreds of thousands of compounds may be screened against an interacting target protein pair, the multi-well plate format becomes unmanageable. Reducing readouts from the assay, as in flow cytometry, to a per cell basis, in suspension, allows us to significantly simplify the optical system and reduce the

automation requirement to a simple flow system.

Conventional benchtop flow cytometers are excessively large, expensive, and lack the robust methodology of FRET quantification (which is traditionally based on intensity read-out [23–28]), and parallel sample streams and interrogation points, to turn them into high-content screening systems. Microfluidics or the micro-total-analysis system (μTAS) is now emerging as an ideal cell handling platform for the instrumentation downscaling of flow-base devices, for both cost, assay flexibility and size implications. Any cells/molecules of interest are analysed at significantly reduced volumes of reagent and samples, at high speed and high throughput (subject to the sample volume) [29, 30]. The micro- or nano-scale transporting channels with diameters comparable to those of biological cells are ideal for the improvement in signal-to-noise ratio (SNR) when resolving single particles [30]. The focal volume of a laser microscope can be in the order of 100 fl. Fluorescence intensity and lifetime fluctuations can thus be linked to diffusion, and conformational changes with TCSPC to good effect. The fluctuations of the fluorescence behaviour are the basis of the typical single molecule spectroscopy techniques, like fluorescence correlation spectroscopy (FCS) [31–33], fluorescence intensity distribution analysis (FIDA) [34–38], and burst-integrated fluorescence lifetime (BIFL) techniques [39–41], in the microfluidic platform. The important question now is if one of these techniques can be used to monitor protein-protein interactions of cells in suspension at a high volume with the resolution comparable to FLIM on adherent cells. The prospect of measuring the stimulated/basal function of live cells with immunocytochemistry and drug treatment has far reaching application in the pharmaceutical industry.

Although the fluorescence lifetime-imaging, has been performed in microfluidics [42], there has been very little exploitation of the technique for the high throughput screening. This thesis will examine the applicability of screening protein interactions in non-adherent cell lines in a continuous flow, using microfluidics. We will discuss the development of a custom- built flow cytometric fluorescence lifetime spectrometer utilizing time-correlated single-photon counting detection at a single detection channel, which was used to acquire fluorescence lifetime data

for individual cells in suspension.

1.1 Fluorescence

Fluorescence is a radiative emission from electronically excited singlet states of fluorescent molecules. The excitation can be induced by absorption of photons of sufficient energy, typically from a laser. Fluorescence can be characterised by its emission wavelength, spatial origin, intensity, relative polarisation (orientation) from the excitation light, and the fluorescence lifetime of the parent fluorescent molecules.

1.1.1 Fluorescence Excitation and Emission

The excitation states of fluorophores are simplified and summarised by a Jablonski diagram (Figure 1.1). When a fluorescent molecule absorbs a photon from a radiative excitation, the transfer of energy (from the photon to molecule) can promote an electron to a higher electronic energy state in an order of a femtosecond. This is extremely fast compared to the periods of most molecular vibrations at room temperature (10^{-10} to 10^{-12} s). According to the conservation of momentum, the disturbance on the electron momentum will cause a minimal change to the nucleus velocity, due to a large difference in masses between the atomic components (Born-Oppenheimer Approximation [43]). Frank-Condon Principle simplifies the situation further by assuming the electronic transition is likely to occur without a change in the nuclei position. Hence, after an electron promotion, the excited molecule would immediately find itself in a non-equilibrium and unstable state. If an electron promotion happens to exceed the first electronic state ($>S_1$), then the excess energy will be internally converted into the vibrational energy of the molecular entity. A typical lifetime of an excited electron, S_1, is in the order of 10^{-10} to 10^{-7} s, and so there would be time for several of thousands of energetic electronic vibrations, which results in some heat exchange with the surrounding media (thermalisation), as well as molecular collisional en-

ergy loss (if in aqueous). The reductions in excited energy consequently result in vibrational relaxation of the excited electron to the lowest level of the 1st singlet state (in a typical time scale of 10^{-13} to 10^{-11} s). The remnant energy of the electron at the lowest vibrational energy of S_1 then decays back to the ground state S_0 radiatively through fluorescence emission or non-radiatively due to further thermalisation.

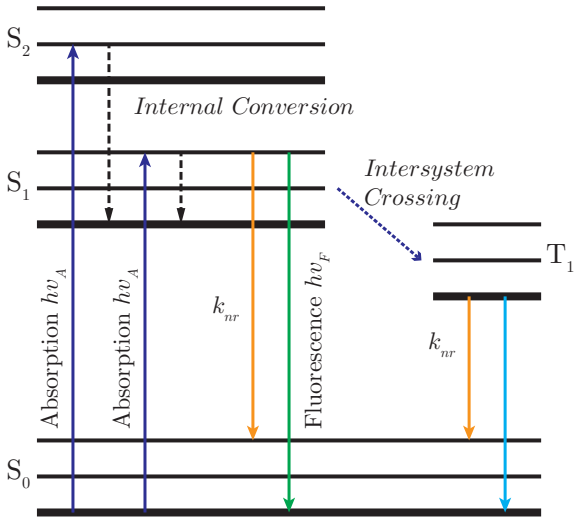

Figure 1.1: Simplified Jablonski Diagram demonstrating the ground and first few excited energy singlet states of molecular electrons S_0, S_1 and S_2 respectively. The mode of the oscillations for each state is denoted as 0,1 and 2 - where 0 is the vibrational level in the thermal equilibrium for each state. The diagram also include the spin degeneracy (Triplet) state T_1 which molecular electrons can undergo a spin change, resulting in a quantum mechanically forbidden T_1-S_0 radiative transition (phosphorescence emission hv_p).

The average amount of time that molecules remain excited prior to the de-excitation to S_0 is known as the fluorescence lifetime; where every fluorescent molecule has its own characteristic value. A number of energy interactions can occur within fluorescence lifetime, such as, molecular collisions with the surrounding solvent molecules, electronic spin conversions (intersystem crossing) and transfer of energy to neighbouring molecules (see section 1.4). These energy-loss processes in practice can be grouped together as Stokes shift [44], which weakens the energy of the radiative decay from the original absorption and in turn increases

the wavelength of the radiation due to the Planck Relation ($E = h\frac{c}{\lambda}$); where h is Plancks constant, and c the speed of light λ in vacuum). More importantly, the Stokes shift will reduce the characteristic lifetimes of excited fluorophores. Hence when an excited electron gains an extra energy (for instance during the molecular collisions), its lifetime and fluorescence emission can be extended and blue-shifted, respectively (anti-Stokes shift).

The intersystem crossing is the least frequently occurred process of the Stokes shift, as the spin conversion from the excited singlet state to the triplet state T_1 is forbidden by the selection rules of quantum mechanics. In this case, the excited orbital electrons would have the same spins as the ones in the ground state. The excited electron in the triplet state will eventually decay to S_0 due to a further competition between the radiative (phosphorescence) and non-radiative processes. The typical lifetime in T_1 can be relatively long; somewhere between a micro- to millisecond timescale. The excited energy is considerably consumed by the process and the radiative wavelength is very red shifted Fluorescence lifetime is, hence, a very highly sensitised and informative probe of the instantaneous condition of the molecules, due to its extremely short interaction time window.

1.1.2 Useful Fluorescence Parameters

In addition to the fluorescence lifetime, another important characteristics of a fluorophore is the quantum yield (Q); the ratio of photon emission to photon absorption. Q is given as:

$$Q = \frac{\Gamma}{\Gamma + \kappa_{nr}} \tag{1.1}$$

Here Γ is the radiative decay rate and κ_{nr} is the total non-radiative decay rate due to Stokes Loss. Q indicates how efficient the dye is in terms of light conversion. If κ_{nr} is extremely small ($\ll \Gamma$), Q would approach unity. For example enhanced green fluorescent protein (eGFP) has a quantum yield of 0.60 [10].

1.1.3 Fluorescence Decay Profile

Since the fluorescence is proportional to the population of electrons in the S_1 state (in a simple system), it can be shown (see Equation 1.2 that for an ensemble of molecules, the fluorescence emission will decay exponentially with respect to time due to the radiative and non-radiative competition, as previously mentioned in subsection 1.1.1 and subsection 1.1.2:

$$\begin{aligned} N_{ex}(t) &= N_{ex}(t=0)\exp\left(-(k_{rad}+k_{ic}+k_{isc}+...)\right)t) \\ &= N_{ex}(t=0)\exp\left(-k_{total}t\right) \end{aligned} \tag{1.2}$$

Here $N_{ex}(t)$ is the number of excited electrons with respect to time t, $N_{ex}(t=0)$ is the initial number of excited electrons immediately from a radiative stimulation, k_{rad} is the radiative decay rate, k_{ic} is the internal conversion rate, k_{isc} is the intersystem crossing rate, i represents a fluorescence specie, and k_{total} is the total decay rate.

The intensity of fluorescence emission is directly proportional to the number excited electrons of a single fluorescent specie, where:

$$I(t) \propto k_{rad}N_{ex}(t) \tag{1.3}$$

When there is a multiple number of fluorescent specie, the overall intensity with respect to time would become:

$$I_\lambda(t) \propto \sum_i q_{i\lambda}\, k^i_{rad}\, \exp(-k^i_{total}t)N^i_{ex}(t=0) \tag{1.4}$$

Here $I_\lambda(t)$ is the overall fluorescence intensity from every emitted wavelength, $q_{i\lambda}$ is a factor of the emission of species i contribution to the signal at the detection wavelength.

Due to the closed loop process between the excitation and emission system, the fluorescence lifetime, τ, is thus inversely proportional to the total decay rate (γ).

$$\tau = \frac{1}{\gamma} = \frac{1}{\Gamma + \kappa_{nr}} \tag{1.5}$$

It is useful to note that the radiative decay rates of any stimulated molecules are pseudo-random; as τ is merely an average time of excited electrons spent in the excited state.

1.2 Fluorescence Lifetime Imaging and Spectroscopy

In the fields of analytical biochemistry and interaction network modelling, light microscopy is still widely used in observing the localisations of key signalling proteins, despite the enormous advancements brought about by electron and scanning probe microscopy [45]. The most general form of light spectroscopy lies within the steady-state measurements (SSM) of fluorescence, which can be achieved through the conventional wide-field microscopy. The type of microscope is relatively cheap and easy to implement, and can serve as a quick tool to monitor the presence of fluorescence from biosensors or background environment.

A single fluorescence emission normally takes place within nano-seconds, and so most fluorescent molecules under a continuous wave (CW) excitation can achieve steady-state fluorescence expressions almost instantaneously. CW excitation and pulsed fluorescence time-resolved signals are sensitive to the photo physical pathways in the Jablonski diagram to different degrees, for example, a CW operation could quickly lead to saturation of fluorescence and trapping of triplet excited electrons, which can bias the decay dynamics. The fluorescence intensity readout from SSMs is thus a time-averaged intensity weighted by the fluorescence lifetime of the fluorochrome under observation.

In detection terms, the spatial origin of the far field steady-state fluorescence signals can be difficult to determined even if the detection system was set up in an epi-configuration [43, 46]. This is due to the Abbes diffraction limit [47] imposed by the optical system and the interference from the out-of-focus light in a non-

confocal setup. In molecular terms, the time-average information is insufficient in providing some dynamic information, such as the stoichiometry of specific near field molecular interactions during the excited lifetime.

Therefore there is a true merit in the time-resolved microscopy, which is linked to the FRET ability in determining molecular distances between specific sites in a variety of proteins or the global structural change of protein complexes occurring on the FRET operating range (which is usually in the nanometre scale - see section 1.4). which could not be resolved by the traditional far-field microscopy.

1.3 Time-resolved Spectroscopy

Time-resolved measurements are usually carried out through a unique 3D image acquisition, known as fluorescence lifetime imaging microscopy (FLIM). The image structure comprises of a square intensity image (front plane), and a time axis along in the third dimension. The imaging is computed on a pixel-by-pixel basis, whereby the functional parameter encompassing fluorescence lifetime information is stored along the time axis and integrated intensity of each fluorescence is displayed on the front plane. FLIM can be implemented on either the frequency or the frequency Fourier transformation counterpart, temporal domains.

1.3.1 Frequency domain FLIM (FD-FLIM)

FD-FLIM operates by modulating a light source (when using a CW excitation) and the gain of a detector to calculate the fluorescence lifetime from a range of demodulation and phase shift of the fluorescence [22, 43, 46].

As the modulation time and fluorescence lifetime are finite, there could be some delay between the excitation and emission, depending on the speed of angular modulation frequency ($\omega = 2\pi f$). The delay is expressed as the phase shift between the two waveforms shown in Figure 1.2. At low frequency, the fidelity of the

signal conversion from a modulated carrier (demodulation) (m_ω) would be high ($m_\omega \to 1$ as $\omega \to 0$). This is because the sample would have enough time for an efficient de-excitation of the excited population, with a relatively minimal phase delay (which is limited to the rates of vibrational relaxation and internal conversion). However, as increases, the time available for the de-excitation would proportionally diminish and consequently result in a weaker intensity emission (Figure 1.2). To put this into perspective, for any fluorescent molecules with lifetime around 10 ns, the corresponding lifetime calculation would typically be derived from a demodulation of fluorescence emission from a laser/detector frequency modulation between 2 to 200MHz [22, 46].

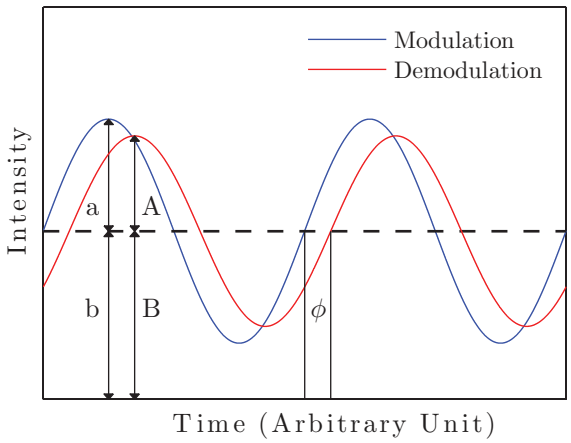

Figure 1.2: The excitation/emission scheme of FD-FLIM, where the blue and red lines represent modulated light source and converted signal respectively. Here ϕ is the phase delay between the two signals. A and a represents the amplitude and background signal level of a converted emission signal, respectively. B and b represents the amplitude and background signal level of a modulated light source, respectively. Demodulation is calculated by $m_\omega = \frac{(B/A)}{(b/a)}$

In theory, the phase and demodulation of a single exponential decay are conformed to the following expressions [43, 46].

$$\phi_\omega = \tan^{-1}(\omega\tau) \quad (1.6)$$

$$m_\omega = (1+\omega^2\tau^2)^{-0.5} \quad (1.7)$$

Here ϕ_ω is the phase delay between a modulated light source and a converted signal, respectively, ω is the modulated frequency and τ is the lifetime of a sample in question. Therefore, any parametric values at a given modulation frequency can be used to calculate the lifetime of the sample. There can be some unwanted fluorescent species or impurities in the sample and so it would generally be safer to screen samples over the entire corresponding range of modulation and then use a non-linear least square fitting to derive any fluorescence lifetime component(s) in each pixel. For a single exponential or multi-exponential decay, a sweep in the modulation frequency range would typically seen as a phase angle delay varying from 0 to a maximum of 90° [46].

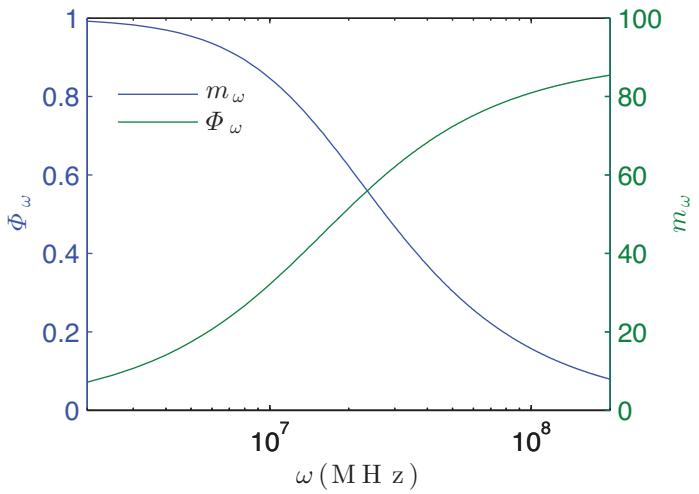

Figure 1.3: The relationships of demodulation and phase delay with modulation frequency

FD-FLIM is generally fast. One of the FD-FLIM techniques known as wide-field time-gated FLIM [22, 46] takes snapshots of the fluorescence emission at various intervals (at the nanosecond scale) after the excitation using high-speed gated

image intensified cameras [22, 46]. Every pixel is collected in parallel and requires no de-convolution with the instrument response. Although the technique can resolve a lifetime difference between fluorescence species by as much as 80 ps [22], its dynamic range is strictly limited to the modulation range on the excitation source [22]. A 100 Hz FLIM frame rate has been reported [48], but any further increase in the recording rate could cause the detection to be susceptible to a noticeable degradation in the resolution (loss of brightness and crosstalks between consecutive frames) due to the finite refresh time of the phosphor screen on the intensified CCD camera. In summary, FD-FLIM would require a long exposure of powerful excitation to record the frequency response of the samples which can quickly lead to photo-bleaching. A 100 Hz frame rate corresponds to a temporal resolution of 10 ms this will also be insufficient to record a flow sequence, which is travelling at a speed (see chapter 3 for further details). Most importantly, the technique requires the samples to be stationary during the modulation [46], which make it unsuitable for this research project [46].

1.3.2 Temporal domain FLIM (TD-FLIM)

TD-FLIM is usually performed with a scanning confocal microscopy, which includes a laser whose pulsewidth is significantly shorter than the fluorescence lifetime of the species under investigation, a high gain detector, a pair of scanning mirrors and a fast single photon counting electronic module.

When a pulsed laser continuously excites fluorescent samples with photon emission rates below 0.01% of the laser repetition [49], the time-dependent fluorescence decay profiles will be continuously recorded by the photon counting module with high fidelity. These real-time decay profiles can appear in steady states for the duration of the excitation when observing in an oscilloscope output, provided there are no dynamic energy interactions during the excited state of molecules.

Modern TD-FLIM mostly utilises the time-correlated single photon counting (TCSPC) to serially record photons on a one-by-one basis from sample emissions, owing to the accuracy at the single photon resolution and the high dynamic range

of the intensity measurement (typically up to 0.8 MHz for a 80 MHz pulse laser).

As the excitation/detection is localised to a single-point measurement, a set of scanning mirrors is required to scan the beam across a domain of interest to build up photon distributions along the time axis of each pixel on the front plane of a FILM image (see subsection 2.3.6 in chapter 2 for further details). Due to the linearity of the TCSPC measurement, an image can be repeatedly scanned to globally accumulate the signals to address the Poissonian nature of the data, without having to take an account of excitation intensity fluctuations or photobleaching. The main advantage and disadvantage of a scanning FLIM microscope lie within the reduction of photobleaching and damages induced by the excitation laser, and the time consumption in building up a sufficient photon count per pixel to enable an accurate determination of fluorescence lifetime respectively (see Lifetime fitting in section 2.5 in chapter 2 for further details).

1.4 Förster (Fluorescence) Resonance Energy Transfer FRET

One of the most important and utilisable aspects of Stokes shift in life sciences, is, the transfer of energy from the excited molecules to the unexcited neighbours, which is formally known as FRET.

In the molecular scale, the concept of FRET can be viewed as a long-range resonant energy coupling between the excited and intrinsic oscillation dipoles of the interacting donor and acceptor molecules respectively - long range in the sense that that the electronic wavefunctions of the donor and acceptor do not interact with one and another, and the interaction distances between the two are long compared to the individual dimensions over which the excitations and de-excitations in the acceptor and donor take place. FRET is thus a highly sensitised tool for studying co-localisations and/or structural change of macromolecules of comparable sizes such as distributions or conformations of proteins/ligands in the cell

domain [46].

The key parameters in determining the strength of the energy transfer between interacting dipoles are the extent of energy overlap between the donor emission and acceptor absorption spectra, the quantum yield of the donor, the relative orientations between the donor and acceptor dipoles (κ^2) and most importantly the distance (r) between the dipoles. The rate of the energy transfer is defined as:

$$k_\tau = \frac{1}{\tau_D}\left(\frac{{R_0}^6}{\tau}\right) \tag{1.8}$$

Here k_τ is the rate of the energy transfer, τ_D is the donor fluorescence lifetime without the presence of acceptors, and R_0 is the critical Förster distance at which the efficiency of the transfer falls to 50%.

Equation 1.8 strongly depicts that the rate of energy transfer is dependent on the distance between donors and acceptors, which is inversely proportional to the sixth power of r. The transfer is a direct energy exchange (no radiative emission and reabsorption), and so the excited electrons of a donor specie would be prematurely de-excited from the vibrational relaxation and internal conversion rates, resulting in shorter lifetimes compared to their characteristic values.

A common way to express the strength of the interaction would be to calculate the efficiency of the transfer (E), which is defined as a ratio of the transfer rate to the decay rate of the donor.

$$E = \frac{k_\tau}{\tau_D^{-1} + k_\tau} \tag{1.9}$$

Re-arranging Equation 1.8 and Equation 1.9, FRET efficiency can also be expressed in terms of R_0 as:

$$E = \frac{R_0^6}{R_0^6 + r^6} \tag{1.10}$$

Equation 1.10 is convenient, as it gives an intuitive insight on the relationship

between r and R_0 (see Figure 1.4). The figure suggests that as long as r is comparable to or less than R_0, an energy transfer between the neighbouring pair can be confidently assumed ($\geq 50\%$ efficient). While FRET interaction is strong when $r < R_0$, the efficiency would contrarily vanish to less than 2% if r becomes twice the distance of R_0.

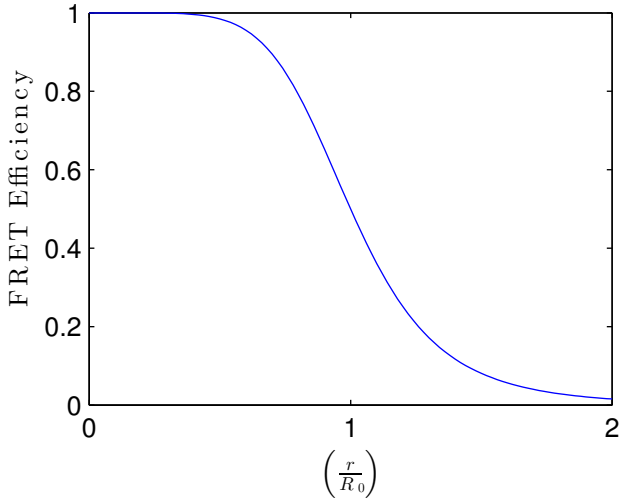

Figure 1.4: FRET efficiency as function of r with respect to the Förster distance

Experimentally, FRET efficiency can be calculated by the comparing the quenched lifetime of any interacted donors (τ_{DA}) (positive) with the intrinsic lifetime of the donor (τ_D) (control).

$$E = 1 - \frac{\tau_{DA}}{\tau_D} \tag{1.11}$$

The typical value of R_0 normally varies between 2 to 6 nm, and can be predicted by accounting for its parametric dependencies with the following general expression [43, 46]:

$$R_0(in\ nanometer) = 0.0211(\kappa^2 n^{-4} Q_D J(\lambda)) \tag{1.12}$$

Where $J(\lambda)$ is the degree of spectral overlap between the donor emission and the acceptor absorption in $(\text{nm})^4$, κ^2 is the orientation factor between interacting

dipoles and n is the refractive index of the medium.

Provided most of the key parameters are satisfied to guarantee FRET interactions, the efficacy of FRET in providing accurate distances would have some limitations due to the randomness relative orientations between dipoles.

The spatial relationship between interacting dipoles can be mathematically described with the spherical coordinate system from a 3D vector diagram as: (see Figure 1.5 for reference)

$$\kappa^2 = (\cos\theta_T - 3\,cos\theta_D\,cos\theta_A)^2 \tag{1.13}$$

Which has an equivalent expression of:

$$\kappa^2 = (\sin\theta_D\,\sin\theta_A\,cos\phi - 2\,cos\theta_D\,cos\theta_A)^2 \tag{1.14}$$

Both expressions are valid under the assumption that dipoles are immobilised over the duration of energy transfers. Here θ_T is the angle between the donor and acceptor transition moments, θ_D and θ_A the angles between these, respectively, and the separation vector; ϕ is the angle between the projections of the transition moments on a plane perpendicular to the line through the centres (see Figure 1.5).

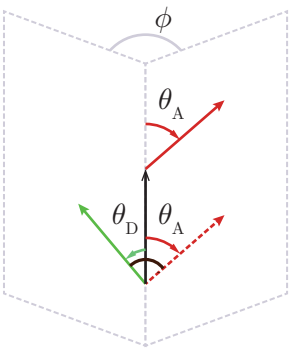

Figure 1.5: Spatial relationship between donor and acceptor

As long as θ_T is fixed, κ^2 can vary to any values between 0 and 4; where 0, 1, and 4 correspond to some distinctive relative orientations of interacting pairs, such as

perpendicular, parallel, and collinearly parallel, respectively.

When the molecules are free to rotate at a rate that is much faster than the de-excitation rate of the donor (isotropic dynamic averaging), the average value of $\kappa^2 = \frac{2}{3}$. Therefore the actual value of r could in theory have a maximum overall uncertainty of 35% (see Equation 1.15):

$$\begin{aligned} r &= (1.5\,\kappa^2)^{1/6}\, r_{2/3} \\ &= (0\ to\ 1.35)\ r_{2/3} \end{aligned} \tag{1.15}$$

The most cautious approach in determining this uncertainty would be to derive the upper and lower bounds of κ^2 from an anisotropy measurement of the donor and the acceptor [reference]. This would in turn give the lower and upper experimental limits on an expected range of r [43, 46]. However a variation of κ^2 generally does not result in major errors in the calculated distance and is rarely taken into the account of FRET efficiency error [43, 46].

1.5 Flow Cytometry

Flow cytometry is an effective technology for quantitative multi-parameter measurement of cell fluorescence characteristics in flow, and plays an important part in todays immunology, drug screening and other cell biology applications. It combines both spectroscopy and light scatter detection to sequentially screen individual cells at approximately 10^4 cells per second, on the basis of their emission wavelengths and the amount of forward and side scatterings which is proportional to the cellular morphological structures such as the cell size and its granularity (all in steady-state measurements). Commercial systems often include additional automated cell sorting option, commonly known as fluorescent-activate cell sorter, FACS, at extra costs. The cells for interrogation are hydro-dynamically focused to a narrowly wide laminar stream comparable to the cell width, by bio-chemically inert sheath fluid of the system for a more efficient and uniform excitation.

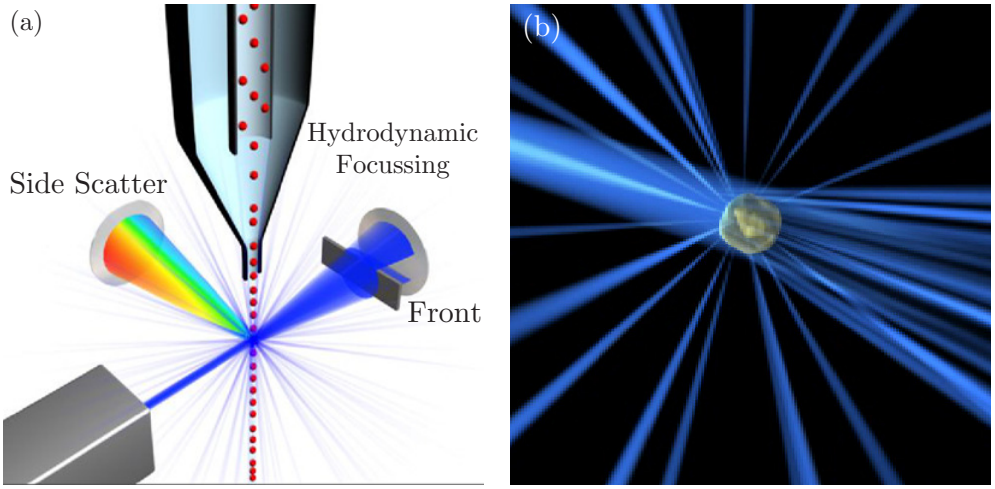

Figure 1.6: (a) A simplified diagram of flow cytometer (b) Illustration of light scatter in the forward and side directions (`http://probes.invitrogen.com/resources/education/tutorials/4Intro_Flow/player.html`)

Unquestionably, flow cytometry is an attractive platform for high throughput analysis of biochemistry. Some of the early protocols of FRET screening with conventional flow cytometers, formally known as flow cytometric fluorescence energy transfer (FCET), were mostly performed with a dual excitation laser [23,27,28,50]. The similar protocol with a single laser excitation was less popular, as the tandem of biosensors or the excitation laser line has to be carefully chosen to avoid a co-excitation of donor and acceptor molecules [26]. The methodology generally aimed to separately collect unquenched donor intensity, non-enhanced acceptor intensity, and enhanced (or sensitised) acceptor emission to calculate FRET efficiency on a cell-by-cell basis. A sole detection of donor-quenching cannot be used to determine FRET efficiency on the cell-by-cell basis, due to uncertainties imposed by a combination of auto-fluorescence and the general variability of fluorescence expression from labeled proteins, especially of a cell population with low FRET efficiency [50]. Otherwise, the data would be sufficient to estimate a mean FRET efficiency from a single cell culture.

Auto-fluorescence always remains as the biggest threat to the efficacy of FCET protocols [50], or microscopical cell experiments in general. While sodium tetrahy-

dridoborate or sodium borohydride has been used successfully to reduce the autofluorescence of immunochemically stained cells in suspension to a degree [51], further subjective efforts on auto-fluorescence correction are still actively pursued. A particular FCET protocol utilised red-shifted fluorophores, cyanines-3 [1] (cy-3) and cyanines-5 [2] (cy-5), as a FRET bio-sensor [28] to correct for auto-fluorescence on a cell-by-cell basis. This was derived from the observation that auto-fluorescence from the red spectra are lower in comparison to those from the green and blue. The sensor sufficiently conforms to the optical requirement of a commercial dual-laser benchtop cytometer (488 nm and 635 nm) (FACSCalibur flow cytometer (Becton Dickinson, San Jose, CA)), with 4 fluorescence detector channels. In the excitation terms, the 488 nm and 635 nm lasers can preferentially excite cy-3 and cy-5 respectively with no spectral overlaps. In the emission terms, auto-fluorescence (530 nm) induced by the 488 nm laser, is distinctively different from those of cy-3 (565 nm) induced by the same laser and cy-5 (667 nm) induced by the 635 nm laser. The emission spectral lines of cy-3 and cy-5 are also well separated, allowing relatively clean detections of auto-fluorescence, unquenched donor, non-enhanced acceptor, and sensitised acceptor intensities, to be collected for FRET efficiency calculation with corrected background signal per cell. However the prospect of the dual-laser excitation was not available in all commercial flow cytometers, and the number of available biosensors would be strictly limited to the excitation bands in-use.

1.6 Time-Resolved Flow Cytometry

The need for time resolved measurement in flow cytometry remains essential, as the intensity readouts data from FRET positive populations would be insufficient to resolve the stoichiometry of ligand induced associations of membrane proteins between the intrinsic and stimulated states. Any subtle to large changes to the concentration of protein-protein activities in non-adherent cells can only be resolved by the temporal resolution of fluorescence decays. The time-resolved

[1] Cy-3: peak excitation wavelength = 550 nm; peak emission wavelength = 565 nm
[2] Cy-5: peak excitation wavelength = 650 nm; peak emission wavelength = 667 nm

measurement in the frequency domain would be incompatible to flow cytometeric applications, due to the continuous movements of samples. As mentioned in section 1.3, TCSPC can measure fluorescence decays up to single photon accuracy. It is in our aim to develop a compact time-resolved flow cytometer with a microfluidic integration, which is modular and easily configurable in terms of spectroscopy and flow speed required for sufficient photon collection (see subsection 2.3.1 in chapter 2 for details of the system). TCSPC would also allow any background signals or any presences of auto-fluorescence to be directly measured, for an accurate correction of signals. Time-resolved in flow applications are currently exist in just a few reports [42, 52–55].

1.7 Miniaturisation of Flow Cytometry with Microfluidic Chips

Developments of microfluidics have gained significant attention over recent years, especially from flow cytometric applications, as it can handle a small numbers of cells (100 to 100,000) in the starting population efficiently, with minimal loss [29,30,42,52,56–60]. The simplicity in cell handling and small sample preparation time allow rapid measurements of precious or vulnerable samples soon after any cell treatment. The microfluidic platform is an ideal interface for the project, as the typical flow rates associated with a fluidic (approximately 100 microns wide in diameter) would complement the time needed for an efficient photon collection by TCSPC for each sample (see chapter 3 and chapter 4 for further details).

Chapter 2

Instrumentation: Materials and Methods

The majority of the work presented in the thesis was undertaken using a custom-built automated microscope system, which incorporates single point laser scanning and wide-field imaging. The microscope system, microfluidics subsystem, data analysis methodologies and sample preparation are summarised below. Details pertaining to specific experiments are described in chapter 4 to chapter 6.

2.1 Development of fluorescence lifetime flow-cytometer

As discussed in the preceding Chapter, flow cytometry in microfluidics is well established for low speed cell cytometry. Until recently, very little work has been undertaken to investigate the use of fluorescence lifetime imaging and spectroscopy in microfluidics. Here the development of a microfluidic flow microscopy system for cell spectroscopy using the time-correlated single-photon counting fluorescence lifetime detection methodology is described.

2.1.1 Prototype System

Initially, a prototype stand-alone flow cytometer system was developed as shown in Figure 2.1 and Figure 2.2, which was mainly used for a flow characterisation with green fluorescence beads and preliminary cell investigation with eGFP-mRFP (see chapter 4 for experimental details).

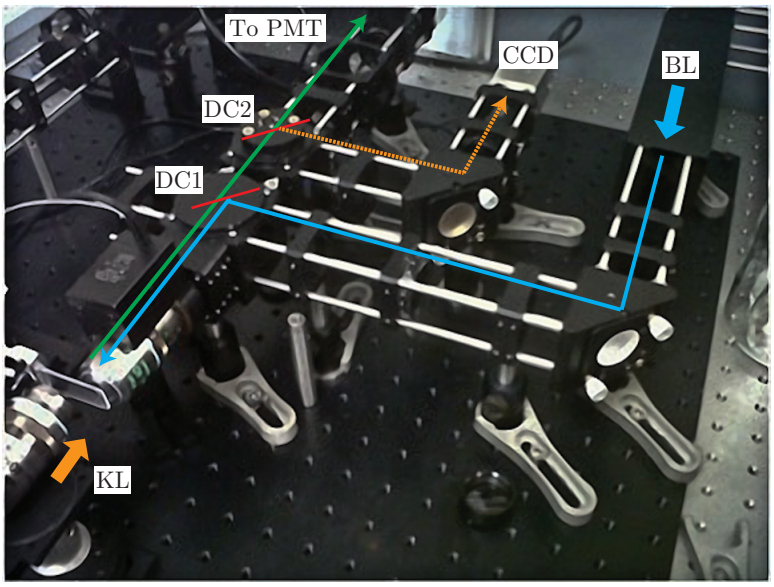

Figure 2.1: Overview of the prototype system. Where BL is the blue excitation laser, DC1 and DC2 are GFP dichroic mirrors, CCD is the CCD camera and KL is the Köhler illumination. See Figure 2.2 for the full apparatus details.

Time-resolved detection was performed using a single-photon non-scanning confocal microscope with single photon excitation and TCSPC detection. The excitation source was a 475 nm, 45 – 60 picosecond diode laser (BDL-475, Becker & Hickl GmbH, Berlin, Germany) with a repetition rate adjustable between 20, 40 and 80 MHz, together with a continuous wave (unpulsed) operating mode. The 80 MHz repetition rate was predominantly employed in this work. The beam was spectrally filtered by narrow-pass filter, 470 ± 10 nm (Z470/10x, Chroma Technology Corp, Rockingham, VT, USA) to clean up any amplified spontaneous emission from the diode laser that might persist following spatial filtering but unmodified with respect to its spatial profile, and then spatially filtered with a 50 micron pinhole in 1x Magnification (M = 1) telescope consisting of two 50

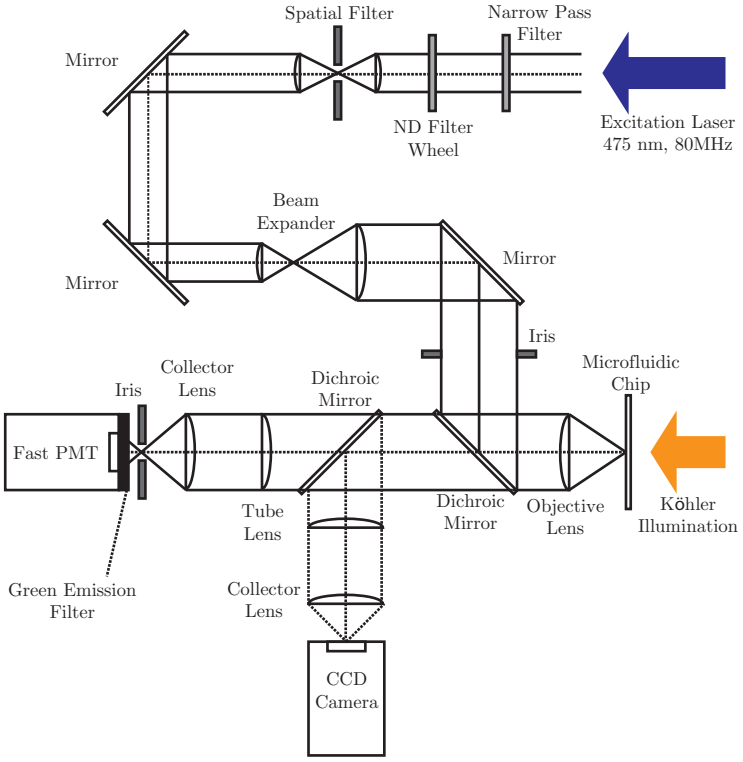

Figure 2.2: Full Schematic diagram of the prototype system.

mm focal length lenses. An M = 3 telescope (consisting lenses of f = -50 mm and f =150 mm) was used to expand the excitation beam waist to slightly overfill the objective aperture. An iris just behind the telescope was used to control the beam diameter and fill factor into the objective physical aperture. The spectroscopy of the preliminary investigations conformed to standard eGFP optical filtering [5, 18, 20], where the excitation is separated from any fluorescence emissions by a long pass dichroic filter (MD498, Thorlabs, USA) which had reflection and transmission bands at 452 - 490 nm and 505 - 800 nm respectively. An f = 50mm lens was used to focus the magnified fluorescence emission (after the tube lens) onto an iris and subsequently a fast PMH-100 photomultiplier tube (Becker and Hickl GmbH, Berlin, Germany) connected to a TCSPC counting module (SPC830, Becker & Hickl GmbH, Berlin, Germany). The filter configuration along the emission path consisted of a long-pass filter (RazorEdge 488nm ultra-steep long-pass edge filter, Semrock, Rochester, NY, USA) and an emission filter

525 ± 20 nm (D525/20m, Chroma Technology Corp, Rockingham, VT, USA). The long-pass filter (OD > 6 for $\lambda < 488$ nm) was used to eliminate/attenuate any bleed-through of the excitation laser from Rayleigh scattering from the chip and sample solution surfaces. Before the tube lens along the PMT path, a secondary dichroic mirror (MD498) was set up at 45 degree to the emission path. This was used to partially reflect the blue spectrum of the trans-Köhler illumination [46, 61] over the channel to a widefield imaging setup, to coarsely align the excitation profile to the channel.

The prototype spectrometer was occasionally able to capture over 10,000 samples in 10 minutes (fluorescent beads and cells) with average burst counts being more than 1000 photons. The photon economy was sufficient for mono fluorescence lifetime analyses (see chapter 3). However the system suffered from a systematic control over the beam positioning inside the channel which consequently affected the consistency of the BIFL screening (missed detections due to fluctuations of sample trajectories around the excitation beam in both lateral and axial directions). There was also a considerable spatial offset (both axially and laterally) in the beam position on the chip seen by a widefield image and the time-resolved detection. There was no automation mechanism to correct for the offset or beam re-positioning, other than manually adjusting the XYZ translational movement of chip until good fluorescence signals are detected. It was eventually realised that it would be useful to incorporate a pair of scanning mirrors to the time-resolved detection to obtain a FLIM image of the chip filled with a fluorescent solution. This is to be used as a pictorial reference for correcting for any offsets in the field-of-views between the two imaging modes. The excitation beam could also be positioned accurately across the field of view and ultimately the breadth of the chip, as revealed by a FLIM image at the micrometre scale. The beam re-positioning in axial directions can be corrected via a piezo-control of the objective. Simply put, this realisation is anticipated to improve the overall efficiency of the detection as well as giving rises to the ability to re-align the beam at the micrometre scale through a software interface (this will be discussed in full in chapter 3).

2.1.2 Optical Filtering

The spectroscopic information of the filter system along the excitation path is illustrated on Figure 2.3. The narrow-pass filter Z470/10x cleanly suppresses all wavelengths outside the transmission band in the 300 - 1200 nm range. The transmission wavelength at 470 nm fully lies within the reflection band of dichroic mirror MD498 at the 45 degrees incident angle.

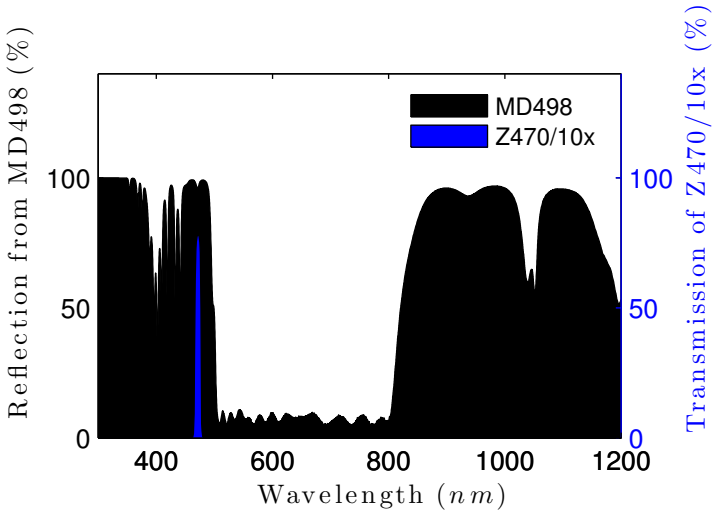

Figure 2.3: The optical filtering along the excitation path. The shaded blue area represents the transmission band by the narrow pass filter Z470/10x placed soon after the laser BDL-475. The amount of transmission can be observed from the secondary y-axis. The dark shaded area represents the reflection band of the dichroic mirror MD498 at 45 degree incident angle.

The spectroscopic information of the filter system along the emission path is illustrated on Figure 2.4. The emission filter, D525/20m, transmits light at 525 nm and another band of wavelengths above 1000 nm. The primary emission wavelength at 525 nm lies within the transmission band of MD498. While, the secondary emission band of D525/20m is also partially transmitted by the dichroic mirror. The long-pass edge filter (RazorEdge. with a cut-on wavelength of 488 nm) was used further to further suppress the long emission wavelength above 600 nm to less than 5% and further reduce any bleed through from Z470/10x. We

acknowledge that the long-pass filter allows a minor degree of transmission near 1200 nm, but the system is well shielded with hard cases to block out any room light from entering the fluorescence path.

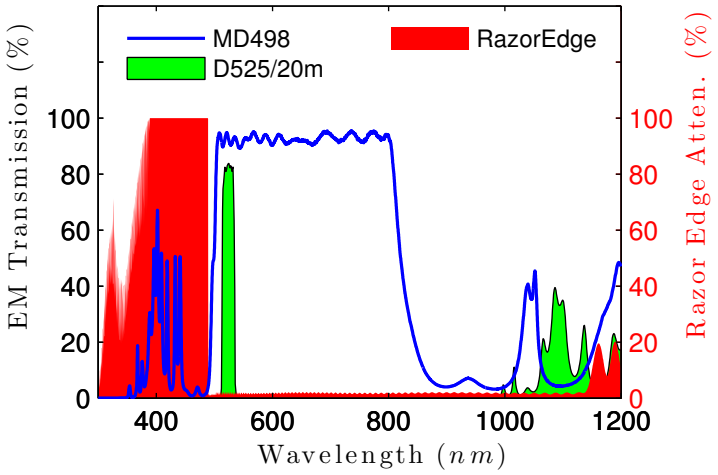

Figure 2.4: The optical filtering along the emission path. The blue line represents the transmission band by the dichroic mirror, MD498 at 45 degree. The shaded green area represents the transmission band of the emission filter 525/20m. The shaded red area represents the attenuation power of the long pass edge filter RazorEdge 488nm. The level attenuation power can be observed from the secondary y-axis.

2.1.3 The Development System

Following the proof of principality by the prototype, the fluidics system was incorporated into an automated high content screening platform [5,20], which has been used successfully for both FLIM and steady-state fluorescence anisotropy [46,61]. The system consists of two optical systems; a widefield epi-fluorescence imaging system with polarisation illumination and anisotropy collection in two wavelength channels (anisotropy detection can be bypassed to allow intensity imaging); and a fluorescence lifetime imaging system consisting of a laser scanning illumination with de-scanned detection [46,61] using time-correlated single photon counting. Here both sub-systems are considered in detail.

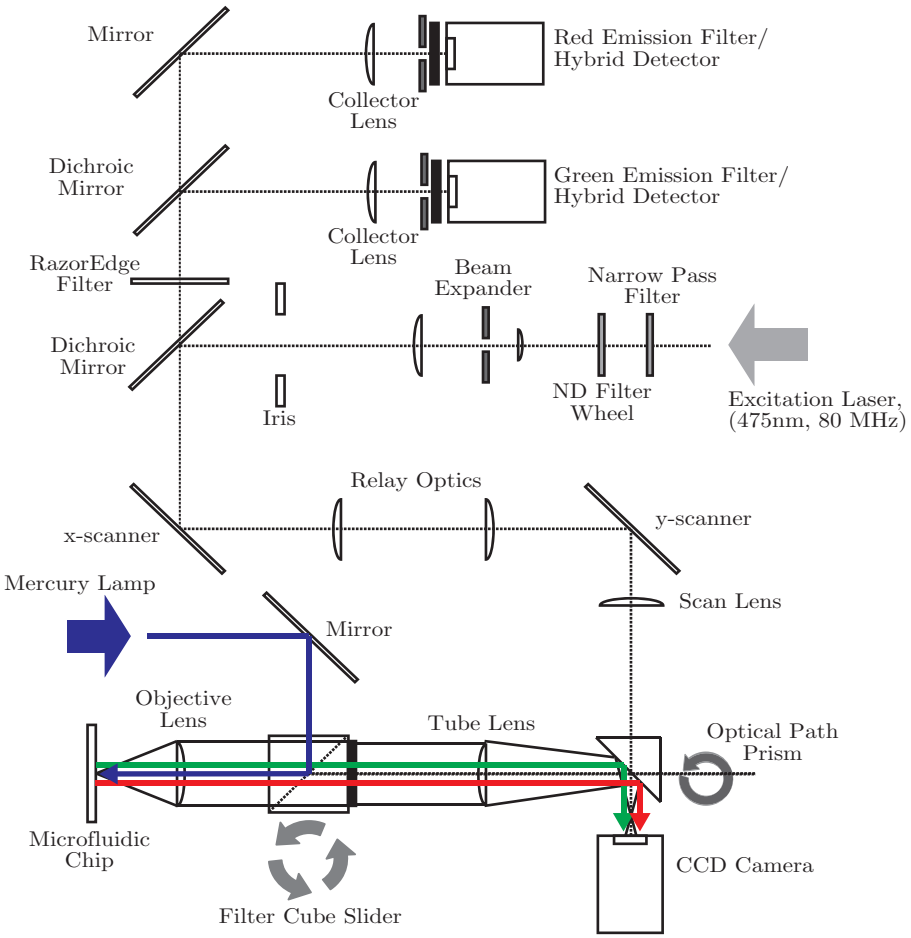

Figure 2.5: Overview of the automated high content screening system (Widefield Imaging Mode). Note the motorised optical prism (optical path selector), is rotated towards a CCD camera.

The widefield epi-fluorescence system is shown in Figure 2.5. The output from a liquid light guide coupled mercury lamp (Intensilight, Nikon, Tokyo, Japan) is collimated and reflected via a polarizing beamsplitter cube into a Khler epi-illumination system incorporating a half-wave plate to manipulate the input polarisation of the excitation. After excitation wavelength bandpass selection and reflection via a longpass dichroic the excitation is focused onto the pupil of an objective lens. The automated motorised filter cube slider (Figure 2.5) can hold three sets of spectroscopic optics (dichroic and emission filter). Two optics slots are explicit set for green and red emission (see Table 2.1).

	Filter Combination 1	Filter Combination 2	Filter Combination 3
Excitation Bandpass	465-495 nm. Centre Wavelength: 480 nm	530-560 nm. Centre Wavelength: 545 nm	Blank (Laser Transmission Path).
Dichroic (Longpass) Cut-on Wavelength	505 nm	570 nm	Blank (Laser Transmission Path)
Emission Bandpass	515-555 nm. Centre Wavelength: 535 nm	573-648 nm. Centre Wavelength: 610 nm	Blank (Laser Transmission Path)

Table 2.1: Fluorescence Filter Combination for widefield imaging system.

The last holder was left blank for the time resolved detection when the optical path prism in Figure 2.5 is switched to the laser confocal scanning microscope setup (see Figure 2.6). The tube lens from the laser-scanning path is shared in this configuration to focus the image from the object plane onto the active area of the single charge-coupled device (CCD) (Orca-ER, Hamamatsu, Shizuoka, Japan). In the anisotropy imaging configuration, a QuadView image splitter (Photometrics Ltd, UK) is used with the filter sets (filter combination 1 and 2 in Table 2.1) for green/red emission (eGFP/mRFP or CY3/CY5) and vertical/horizontal polarisation.

A dual-axis descanned confocal system with TSCPC detection was set up to enable FLIM (Figure 2.6). The excitation laser (BDL-475) and excitation filter (Z470/10X) are identical to the ones used in the prototype model. A gradient neutral density filter was used to control the power of the excitation on an ad hoc basis.

An M = 3 telescope (consisting lenses of f = 20 mm and f = 60 mm) was used to expand the excitation beam waist to slightly overfill the objective aperture. An iris just behind the telescope could be used to control the beam diameter and fill factor into the physical aperture of the objective. Following beam steering via the emission dichroic and a kinematic mirror, the excitation is incident on

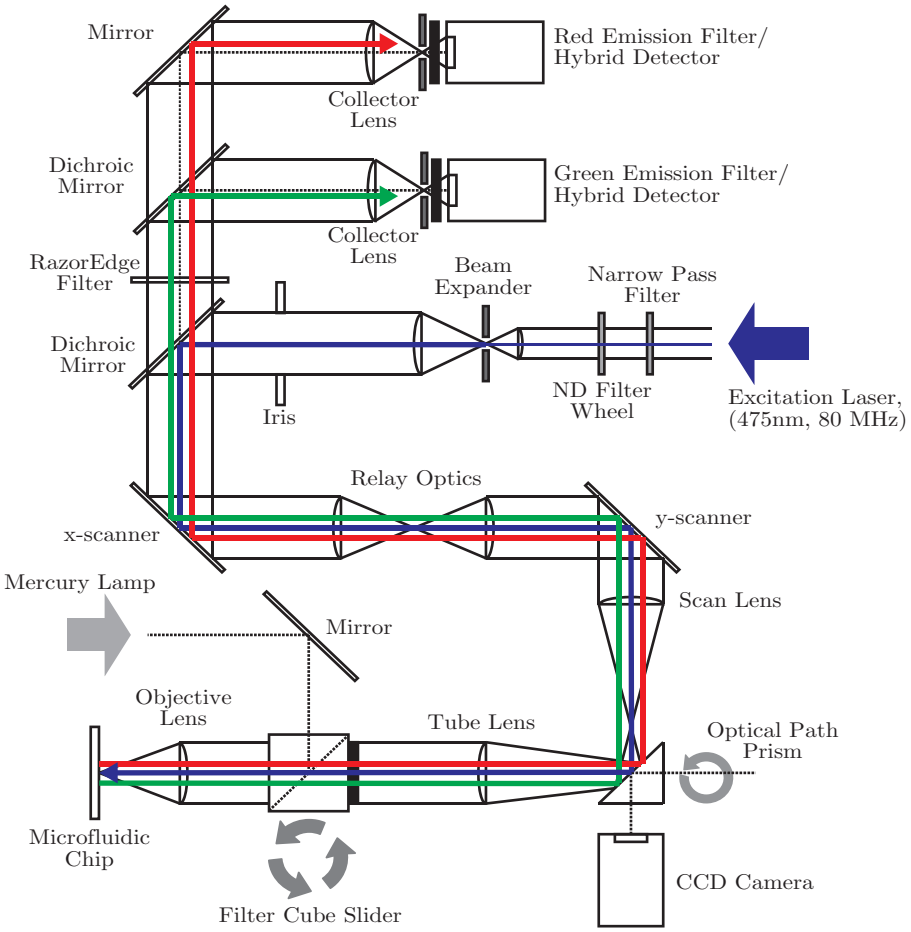

Figure 2.6: Overview of the automated high content screening system (Confocal Microscope).

the x-axis galvonometric scanner, an afocal set of relay optics (a pair of f = 50 mm) was included in the scanning arrangement to ensure that both galvanometer mirrors were in the conjugate telecentric planes of the microscope. Another reimaging lens system comprising of scan (f = 200 mm) and tube lenses (f = 200 mm) was formed between the y-axis scanning mirror and the back focal plane of the objective to transform the angular deflection off the scanning mirrors into the xy- position of the beam spot along the object plane. The emission passes the relay optics and is de-scanned via the galvanometers. The dichroic (MD470) and emission filters (D525/20m and RazorEdge - 488nm) along the emission path are identical to those used in the prototype.

2.1.4 Microscope Objective and beam profile

Commonly, either Nikon ELWD Plan Fluor 40x air objective (0.6 NA) or Nikon Plan Fluor 20x air objective (0.5 NA) was used to focus the excitation light into the sample (either for imaging or inside a fluidic channel). Emitted fluorescence was detected in the epi-configuration.

2.1.5 Detector and Single Photon Counter

Initially the system was developed using a fast photo-multiplier tube (PMH-100, Becker & Hickl GmbH, Berlin, Germany) for preliminary test experiments. Once the system was successfully characterized for the cell experiments, the detector was replaced by a more sensitive hybrid single-photon avalanche photodiode detector which has a better time resolution (HPM-100, Becker & Hickl GmbH, Germany, Berlin). The new detector combines a Hamamatsu R10467-40 GaAsP hybrid PMT tube with the preamplifier and the HT power supplies for the PMT operating voltages. The detectors were connected, depending on the experimental arrangement, via a 4-channel detector router (HRT-41, Becker & Hickl GmbH, Berlin, Germany). The router allowed the experiment in chapter 5, to use two HPM-100 detectors to detect fluorescence in both green and red channels. Time-correlated single photon counting detection was achieved with the SPC830 PCI BUS interface (SPC-830, Becker & Hickl GmbH, Berlin, Germany). It features a 12-bit ADC resolution with dead time of 125 ns and can effectively record photons up to 5 MHz (see Table 2.2 for other specifications).

Photon Counting Method	Time-tagging, continuous writing to disk
Macro Timer Resolution, internal clock	25 ns, 12 bit
Macro Timer Resolution, clock from SYNC input	10ns to 100ns, 12 bit
ADC Resolution / No. of Time Channels	12 bit / 4096
Dead Time	125 ns
FIFO buffer Capacity (photons)	8 million photons

Table 2.2: Main Specifications of the FIFO setting of SPC-830.

2.2 Development of Microfluidic System

The microfluidic system used for sample handling and automation, consists of 3 sub-systems the pump, fluidic network and disposable reservoir (beaker or plastic container).

The initial fluidic system consisted of a circular borosilicate capillary (Inner Diameter (ID) = 100 μm and Outer Diameter (OD) = 170 μm) and syringe pump (Aladdin, World Precision Instruments Inc, USA see Table 2.3 for further specifications).

Syringe Size	Up to 60 ml
Number of Syringes	1
Motor Type	Step Motor
Steps per Revolution	400
Mechanical Speed (Maximum/ Minimum)	3.06 cm per minute / 0.03 cm per minute
Pumping Rate	1.019 litre per hour (60 ml syringe), 5 μl per hour (1 ml syringe)
Maximum Force	25 lb (at the minimum speed), 10 lb (at the maximum speed)
Pumping Method	Injection / Withdrawal

Table 2.3: Technical Specification of Aladdin Pump.

Different interconnecting tubing (from pump-to-fluidic and from fluidic-to-reservoir), such as heat shrink or PTFE tubing (ID = 150 μm) sealed by epoxy glue to the syringe tip and capillary, were investigated, but none were satisfactory. They all suffered from leakage, sample clogging at the inlet, and development of backpressure which sometimes caused the luer taper syringe connector to eject from the syringe body.

The capillary tube was soon replaced by a plastic[1] microfluidic chip which has a similar footprint as the standard laboratory glass slide (01-0006-0019-02, microfluidic chipshop GmbH, Jena, Germany). The chip contained a single straight channel with a trapezoidal profile (base length = 120 μm x top length = 92 μm x height = 20 μm). The clearance holes at the inlet and outlet of the chip were 1 mm in diameter. The thickness of the base layer (optical layer for the excitation and emission) was 130 μm. The fluidic interface was established with Upchurch nanoports (N-126H, Idex Health & Science, Illinois, USA), at the in- and out-lets

[1]Topas®coc 92% light transmission, Refractive index 1.54 at 20 degree Celsius. For full details (`http://www.topas.com/products/topas-coc-polymers`.

of the chip (Figure 2.7). The connectors were sealed with the port proprietary adhesive epoxy ring. PEEK^{TM}(polyetheretherketone) tubing (ID = 0.2 mm, OD = 0.8 mm) (1575-12x, Idex Health & Science, Illinois, USA) was used as the interconnecting tubes between the chip and the input and output sources (see Figure 2.7).

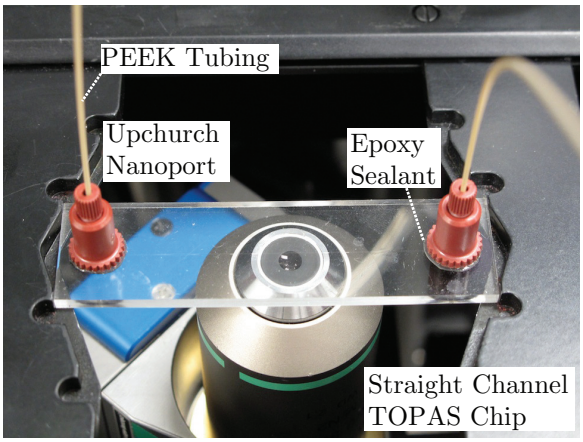

Figure 2.7: Fluidic interface of Topas Chip with upchurch nanoport.

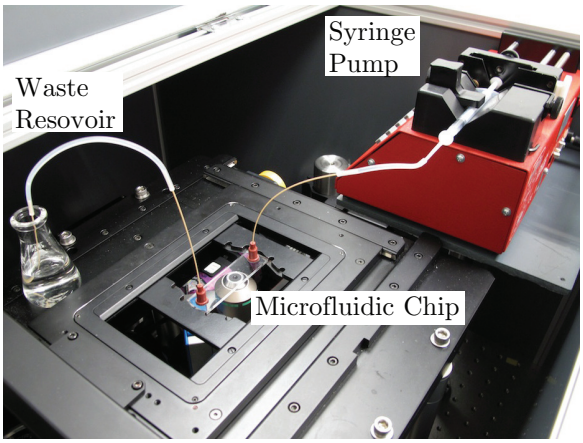

Figure 2.8: Overview of the preliminary fluidic network.

The Topas components had a limited success, as the backpressure often forced the Upchurch connector to come loose and developed severe leakages. Additional industrial epoxy was applied to the ports, but the sealant was too still too weak for the backpressure they normally experienced. Furthermore, the use of syringe

pump was problematic, as a slow delivery speed can cause samples to settle inside a syringe. Although this was addressed by using the pump in the withdrawing mode to allow sample solution to be continuously stirred with a magnetic stirrer, the air gaps from the leaky fluidic system often introduced air bubbles, which interrupted the flow operation at every attempt.

Eventually, a glass T-Junction Chip (3000086, Dolomite Microfluidic, Cambridge, UK) was used as a permanent platform to work on. The chip has an air-sealed connection and can be operated up to 30 bars of working pressure (see Table 2.4 for the specification).

Number of Input	2
Number of Output	1
Channel Cross-Section	100 μm x 110 μm (Depth x Width)
Channel Length After The T-Junction	278 mm (feed channels = 20 mm and 22 mm)
Channel Volume After The T-Junction	2.5 μl
Back Pressure From Water Flow at 100 μl/min	1.5 bar
Surface Roughness of The Channels	5 nm
Chip Size	45.0 mm x 15.0 mm
Top Layer Thickness	2.0 mm
Base Layer Thickness (Optical Layer)	150 μm
Operating Pressure	30 bar (Based on tests at 21 °C)
Material	Glass
Channel Coating	None (Hydrophillic)

Table 2.4: Specification of the T-Junction Chip.

The thin layer T-junction chip was specifically designed for micro-mixing applications, which contained two reagent input channels and a mixing length (meander) of 278 mm. For this application, the chip is used in a reverse configuration to make use of the single channel outlet, as the input source. The screening laser

was focused to the centre of the channel at the first turn of the meander.

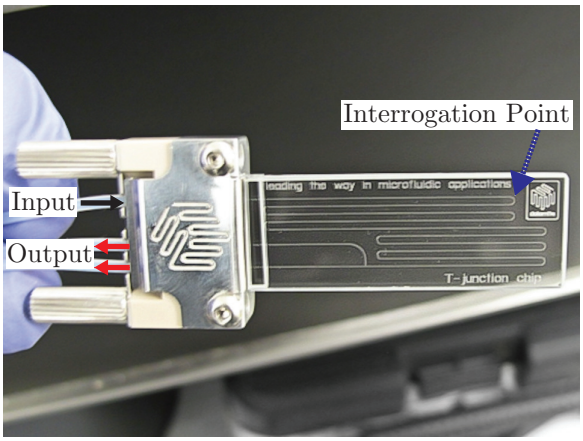

Figure 2.9: Image of the Image of thin layer T-junction chip.

The channel profile is uniform throughout the chip and has a slightly elliptical profile with axes of 100 μm and 110 μm in the x– and y–direction, respectively. The chip is suitable for a high numerical aperture objective, as the thickness of the thin layer (base layer) is 150 μm, and is similar to those of the industry standard of cover slips (145 - 170 μm). A fast response pressure pump (Mitos Pump, Dolomite Microfluidic, Cambridge, UK) was used to deliver samples to-and-from the chip with the polytetrafluoroethylene (PTFE) tubing (see Figure 2.10). The pump can supply the volumetric rate of nano- to milliliter per minute range, which is controlled by air pressure supply (a compressor). The range of pumping pressure is between 0 to 10 bar. The pump can be step-controlled by as small as 1 mbar step. A micro-magnetic flea was used inside a flat base sample vessel in the pressurized chamber of the pump with a low voltage magnetic stirrer, to keep the samples in suspension.

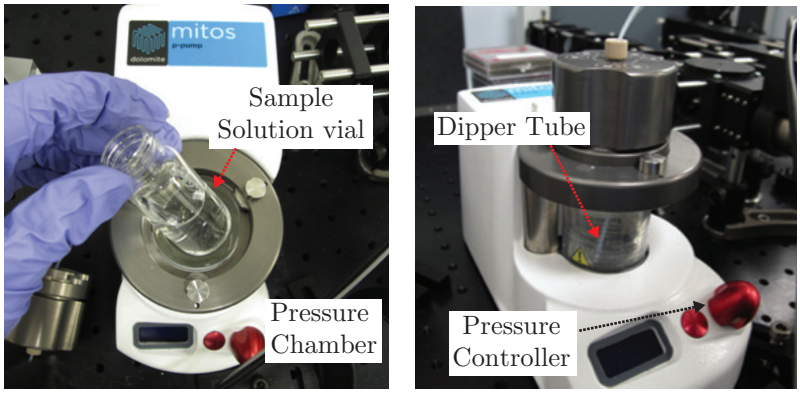

Figure 2.10: Overview of Mitos Pressure Pump. Image on the left demonstrates the loading of a sample solution to the pressurised chamber of the pump. While the image on the right shows the chamber being sealed with the interlocking cap. Notice the cap has a locking mechanism for the tubing at the top. The tube must be inserted into the chamber until it is fully submerged in the solution, so the pump can apply sheer force on the solution surface with a regulated air pressure (controlled by the red knob in front of the pump), until the solution is eventually driven into the tubing.

2.3 Method of Photon Detection and Analysis

2.3.1 First In First Out (FIFO) Mode

TCSPC in FIFO mode records fluorescent bursts and their decay profiles by measuring the photon density on the detector at a single photon resolution. The system ensures the usually large photon information is registered onto the analysing computer at as minimal loss as possible. This is achieved by relaying the stream of live data onto a fast and relatively large on-board solid-state memory (FIFO buffer), which then dumps the data onto the slower mechanical hard-disk of the computer. As long as the FIFO buffer is pre-allocated with adequate data memory for high throughput experiments (the maximum memory of SPC-830 can buffer up to 8 million photon events), the average photon information readout speed would be limited to the average hard disk writing speed allowing data to be stored up to any memory available on the hard disk. Despite the capability of TCSPC in FIFO mode to store large data, it is sensible to aim in containing

data to practical file sizes ($<$ 500MB) that have average useful readouts over 1000 events (i.e. bursts containing $>$ 1000 photons). These experiments can span approximately 20 minutes using practical cell throughput. The number of functional readouts from the 20 minute period is a good throughput indicator for any test or newly proposed flow assays. The previous high content screening milestone from the work within the group achieved approximately 1000 screens in half hour through anisotropy measurements [5, 20]. Anything below this limit would contradict the progressively demanding objective in the high throughput arena.

The principle, which TCSPC tags the time information is similar to the way the standard stopwatch operates - start, stop, and reset. The module repeatedly and sequentially records the arrival times of each detected photon relative to the period of the laser repetition and then tags them with two time labels, macrotime (the time difference between the photon detection and the beginning of the experiment) and microtime (the time difference between the photon detection and the triggering of the laser pulse immediately after it). In the case of dual-detection operations, TCSPC will additionally tag the routing channel number that the photons were recorded in.

The data is sequentially read out to the computer from the SPC on-board FIFO buffer memory. A histogram of the macrotimes will display a variation of photon flux over the course of the experiment, so that, fluorescent bursts and their occurrence times can be observed. Separate histograms of the microtimes from the corresponding photons in each burst will reveal the burst photon densities from the leading edges to the last photons of their decay profiles.

2.3.2 Single Photon Emission Criterion

The laser power needs to be conservatively set so that the probability of single photon detection within a signal period is much less than 1, or 0.01 to be more specific to avoid pulse pile-up. Practically, this can be achieved by attenuating the laser power whilst exciting fluorescent samples in question until the count

rate of the detector reduces below a hundredth of the total repetition rate, which is 800 kHz in this case.

2.3.3 Clocking Mechanism

TCSPC measures the temporal positions of detected single photons during laser pulse interval by digitizing the output voltage of the time-amplitude-convertor (TAC) with a 12-bit analogue-to-digital convertor, ADC. The time measurement is performed in the reversed start-stop configuration, where the detection event and the subsequent laser clock cycle signal are used as the starting and stopping triggers of the timing capacitor of TAC respectively. TAC works on the assumption that its timing capacitor charges up the voltage linearly until it is stopped by the reference signal, so that the output voltage is proportional to the elapsed time. For greater accuracy on the timing measurement, the amplified photoelectron signals from the detector are filtered by a constant-fraction discriminator (CFD). The CFD alleviates any amplitude-induced jitters of the signals from the single-photon peak height distribution of the PMT, by splitting each detected signal into two and delaying one of them by up to the rise time of the signal. The delayed signal is then inverted and then added to the un-delayed signal with the AND gate of the CFD, to mark the temporal position of the maximum signal amplitude with the zero crossing point of the summed signal. Additionally, the CFD can also be used to discriminate noise from the pre-amplifier that are below its threshold limit.

2.3.4 Maximising Photon Counts

TCSPC is by no means a 100% efficient process, despite its marked gain in the resolution from the frequency domain technique. Counting loss inherently occurs due to the finite digital processing time (or dead time) of ADC. Even if the TAC is successfully reset during this dead time, any photons arriving at the detector during the dead time will not be passed to the TAC/ADC electronics.

The SPC 830 module has a fixed digital system dead time of 125 ns and so the counting efficiency would rapidly drop off with higher instantaneous count rate

(see Figure 2.11). TCSPC caps off the maximum useful count rate at the 50% of the recording loss. This corresponds to an input rate reciprocal of the dead time, or 8 MHz in this case.

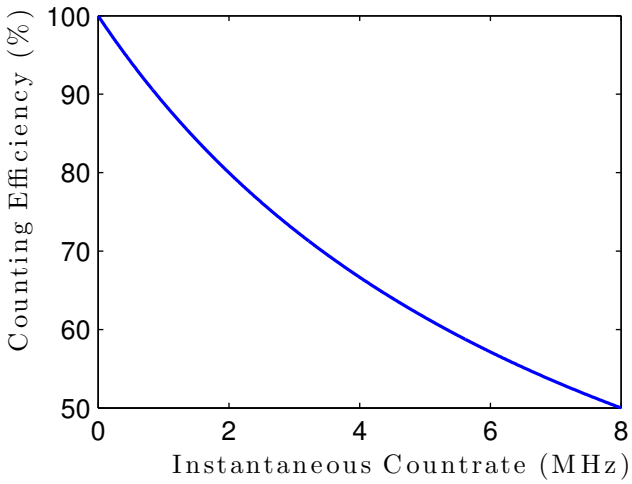

Figure 2.11: Photon Counting Efficiency of SPC-830.

Other sources of dead time can come from the latch delay of the router (the time which the SPC module, needs to de-multiplex the routing signals after the CFD is triggered by the multiplexed signal of the router) and the TAC resettling time. The discharge (or reset) rate of the TAC timing capacitor is proportional to the amount of charge stored in the capacitor. The rule of thumb for maintaining the TAC dead time and the completion of the AD conversion from different routing signals to be near- or coincident is that the TAC range and latch delay need to be kept below 100 ns interval separately. The TAC range and latch delay in this experimental setup are permanently set at 50 ns and 20 ns respectively and so whether it is a single or multiple detection experiment, the criterion above is satisfied. Furthermore, the counting efficiency of this acquisitions would normally approach 100% (as the laser power would be set in accordance to the single photon emission criterion and maintaining the average instantaneous count rate to less than 800 kHz).

2.3.5 Setting Up FIFO

When setting up a single photon counting system, it makes sense to try and isolate the single photon sensitive detector away from the scanning path of the excitation source and put a proper light shield around it. As previously mentioned in subsection 2.3.4, there are delays associated with the router and detector transit time as well as the cable length along the optical path of the CFD signals. Hence, it is imperative to compensate the SYNC optical path with an extra length of cable, until the correct reference pulse is shifted to a time after the detected photon. Since a 10 ns measurement window is used to record transient profiles, the sync signal theoretically needs to be delayed by the combination of the recording interval, detector transit- and a few ns TAC settling times. The cable compensation may not necessarily be carried out exclusively along the SYNC optical path, the CFD cable can also be shortened to adjust the temporal position of the signals.

2.3.6 BIFL Data Analysis

BIFL is a very powerful analysis method for high throughput screening. The principal of the technique is to identify fluorescence bursts over the course of an experiment, store their decay profiles, and then iteratively fit the transients with different types of fitting models (typically but not exclusively exponential), until the best convergence emerges. However, the temporal position of the bursts and their fluorescence lifetime are not the only parameters, which may be extracted from the data. The burst identification also allows sequential multi-parametric burst characteristic information to be recorded, such as the instantaneous count rate, burst height, burst width and burst integral intensity.

To analyse the data BIFL, conversion software was written in MatLab (Mathworks Incorporation, Massachusetts, USA), to translate FIFO data into a BIFL image and a separate double precision binary MatLab file containing the sequence of burst characteristic information. The reason for choosing the MatLab programming environment was to take advantage of the extensive built-in library of common mathematical functions. Any written source code can be shared and executed on any platform, as long as MatLab is compatible with those computers

(i.e. windows, mac and unix).

The SPC-830 hardware stores FIFO data in a proprietary binary format (.SPC) with intelligent event markers to reduce the general file size. For ease of access, the data is converted using a built in function within the SPC acquisition software into the basic American Standard Code for information interchange format (ASCII) (.dat, .txt, .asc, etc), to obtain the raw photon information before reading into MatLAb. The transformed data is normally 3 to 5 times the size of the SPC file, and so proper memory management in the programming has to be implemented to avoid the filling the physical memory (and subsequent programme slowdown/crash). The analysis computer was a 32-bit Windows machine and so the PC system is limited to 4 GB of RAM. A 32-bit Matlab installation can reserve a maximum of 1.5 GB for the workspace memory and so, when splitting the photon information into separate vectors from a 500-600 MB ASCII file, the intermediate variables during the computation can use up all the memory and prematurely halt the execution. Therefore block-processing and correct memory reservation for any outputs are the key programming factors to this algorithm.

In converting the data from the raw FIFO photon arrivals, the aim was to replicate the data format of standard FLIM images so that BIFL images remain compatible with existing fitting programs. Predominantly in our lab, the Time Resolved Imaging-2 (TRI-2) data analysis software package developed by Dr Paul Barber and co-workers [18] is used to analyse data. TRI2 is compatible with both $*$.SPC format from Becker & Hickl and the multi-dimensional image cytometry standard format (.ics). Due to the unnecessary complexity of converting to the $*$.SPC format, the ICS format was chosen as a file type to write the BIFL images for which there are well documented C-libraries and also supports lossless image compression. Although a 2D format is adequate to record the sequence of the entire acquisition, it would be cumbersome to visually observe the lifetime readouts in a single row or column of pixels. Therefore, the sequence of bursts is recorded onto a square image in a raster scan starting from the top-left hand corner. The side length of any BIFL image template is calculated by rounding up a square root of a total number of detection events. Once the sequence of

bursts is registered onto the blank template, any remaining pixels will be padded with zeroes. The grey value along the pixels in x and y directions will represent the intensities of each transient that are stored in the z-direction (see Figure 2.12).

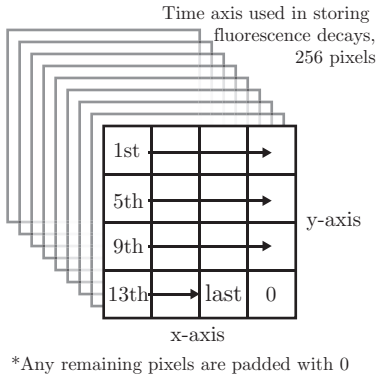

Figure 2.12: The file writing structure of BIFL data on the 3 dimensional ics format.

The BIFL conversion algorithm is dependent on 4 parameters: macrotime, microtime, detector channel number, and invalid photon flag.

Invalid photons can often happen during the dual-detection operation, when multiple photons from each detector are detected within the response time of the routing electronics and a null count is sent from the router. It may also occur when the sum of the TAC output exceeds the ADC conversion range or occasionally during the FIFO buffer overflows.

The BIFL conversion algorithm consists of the main following steps:

- Delete all the invalid photons
- Create a histogram of macrotime to display bursts along the time axis
- Find the average baseline of the signal
- Find the start and end positions of each burst
- Derive the intensity, height and width of each burst

- Reject bursts with intensity less than 200 photons
- Create 8-bit histograms from the photon microtimes in each burst to compute the transients (native 12-bit time resolution (2 ps) for data with >100 ps timing resolution is excessive)
- Sequentially save the transients in an .ics file

A successfully assembled $*$.ics file can be readily visualised by TRI-2. TRI-2 incorporates the rapid lifetime method (3-part integral), Levenberg-Marquardt least square, Bayesian, and Phasor algorithms for deriving the fluorescence lifetime of each pixel, spatial binned/integrated data or on a global basis. Further details of lifetime fitting are discussed in chapter 4.

2.4 Sample Preparation

2.4.1 Determining Optimal Sample Concentration

Cell analogues, 10 μm diameter green fluorescent beads (G1000, Duke Scientific, USA) were diluted with pure distilled water. Three different bead types had been used in total during this project, and so the G1000 beads will be referred to as Type I beads to differentiate them from the other two bead types used in later the experiments in chapter 3.

100 μl of Type I bead solution (nominal bead density = 1.8×10^7 beads per ml) was initially diluted with 5 ml of de-ionized water (1:1000 ratio) and then, further serially diluted 4 times in 2-fold (2.5 ml of stock transfer + 2.5 ml of de-ionized water) - see Table 2.5.

There is currently no hydro-dynamic focusing mechanism within the chip to deliver a stream of single cell samples to the interrogation point, and hence the optimal stock concentration was deduced on the basis of a good temporal separation between each detection event. The conjecture about the optimal single

Stock Number	Number of Beads / ml
1	360000
2	180000
3	90000
4	45000
5	22500

Table 2.5: Bead concentration per each stock.

sample delivery was drawn from observations of the burst graph from each stock (Figure 2.13). The data were acquired for 10 minutes at a constant flow-rate (air supply of 300 mbar) and excitation power of 25 μW. Burst data (macrotime) were binned into 500 μs intervals. Figure 2.13 displays burst concentrations of each stock in the first 10 second measurement window. The Figure clearly shows a trend in a reduction of burst numbers with increased dilution within the time frame, with exceptions of (b) and (c), where the density of the events look similar. The overall number of detected beads from the 10 minute acquisition of stock 1 to 5 were observed to be 36,218, 18699, 12365, 6921 and 749, respectively.

If the burst graphs of stock 2 and 3 from Figure 2.13 (b) and (c) were compared side by side, it could be observed that there are good temporal separations between bursts, with a relatively uniform height in stock 3. Therefore Stock number 3 was chosen as the optimal concentration to work on. This corresponds to a mixture of 5 μl of bead solution and 5 ml of de-ionised water. The performance of the bead stock will be demonstrated in full details in chapter 3, which also includes video footage to further support the conjecture formed on the basis of the temporal separation observed on the burst graphs in Figure 2.13.

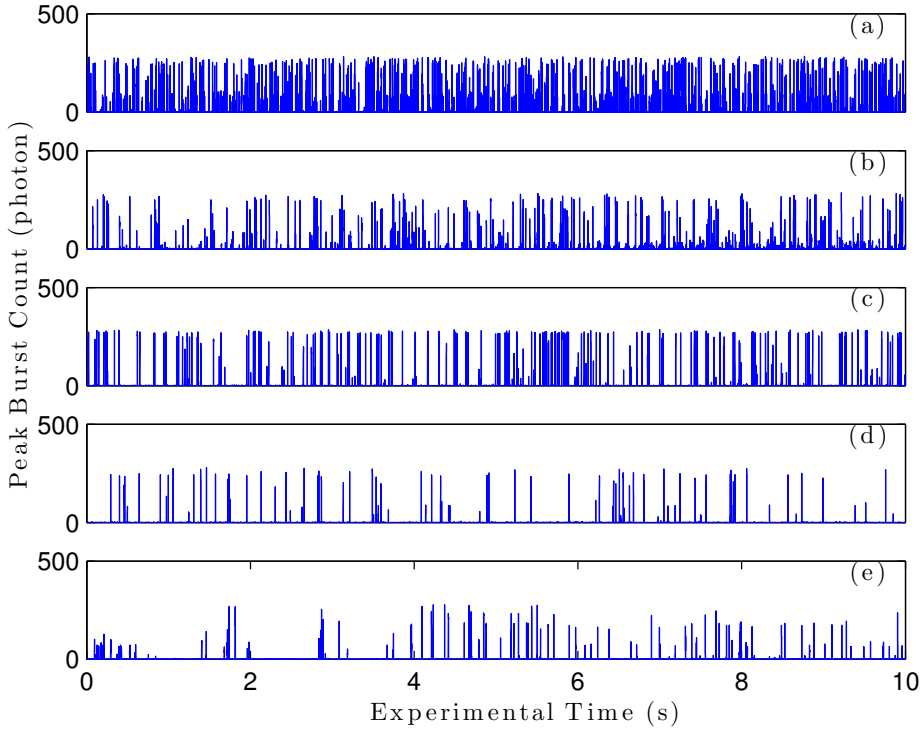

Figure 2.13: Burst Frequency plot within the first 10 seconds experimental acquisition, where a, b, c, d, and e represent the burst acquisition from stock 1 to 5, respectively.

2.5 Lifetime Analysis

2.5.1 Instrument Response Function

Fluorescence intensity data from a TCSPC system is a convolution product between the sample impulse response and instrument response functions IRF. IRF or the prompt signal is a pulse shape of an excitation pulse measured by the detection system. There is a significant importance in the accounting of IRF, as the response times (time resolution) of any real-life measurement systems are finite. Therefore a measured pulse shape will always be subject to some broadening, which can be several nanoseconds wide. Omission of IRF measurement, will add a degree of uncertainty in the time between the photon generation and the

moment which the photon arrives at the detector. The mathematical expression of the convolution is given as:

$$\begin{aligned} N(t) &= \int_{-\infty}^{t} I_{IRF}(t')\, F(t-t')\, \mathrm{d}t' \\ &= \int_{-\infty}^{t} I_{IRF}(t')\, exp\left(\frac{-(t-t')}{\tau}\right)\, \mathrm{d}t' \end{aligned} \tag{2.1}$$

Here $N(t)$ is the model decay, $F(t-t')$ is the decay function (or $exp\left(\frac{-(t-t')}{\tau}\right)$), $I_{IRF}(t')$ is the instrument response curve, t' is the time that IRF starts, and $I(t)$ is the measured decay data point at time t and τ is the lifetime of a fluorescent marker.

The instrument response was acquired by the using the laser reflection from the surface of the chip, with all the optical filtering removed from the emission path. Initially, a recording of the instrument response was attempted by acquiring scattering signals from glass particles, LUDOX®TM-50 colloidal silica (Sigma Aldrich, United States), but found the reflection from the chip to be too strong in relation to those signals. Figure 2.14 shows the prompt signal from the acquisition. It can be observed there is a secondary peak between 8 to 9 ns of the measurement window. This is likely to be the product of a small optical reflection from one of the components along the fluorescence emission path such as the dichroic mirror. This can be suppressed to good effect with the emission filter system mentioned in subsection 2.1.2.

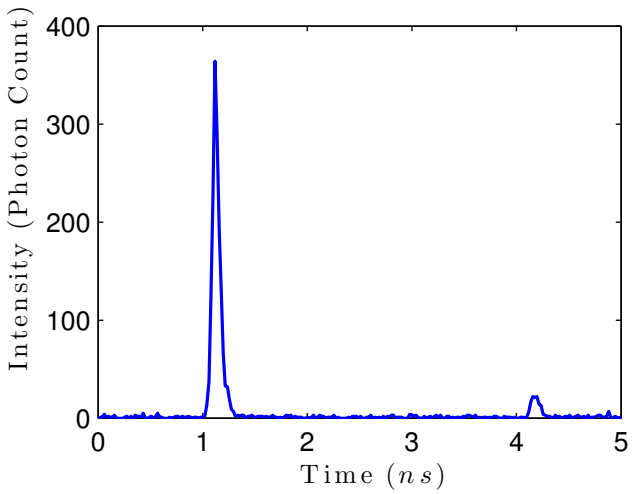

Figure 2.14: The instrument response function $I_{IRF}(t')$, acquired using the laser reflection from the fluidic chip.

2.5.2 Non-linear Least Square Analysis

Linear and non-linear Least square analysis is the most general and reliable method for determining the fitting accuracy of calculated data on the experimental data sets (provided the calculation is described by a correct mathematical model) [46].

Although fluorescence decays are a non-linear problem, the nature of TCSPC data still conveniently conforms to the prerequisites of the regression analysis for the best estimation [46].

The main requisites state that:

- The assumed fitting function is the correct mathematical model of the system
- The data points are all independent observations
- There is a sufficient number of data points so that the parameters are over-determined

- All the experimental uncertainty is in the dependent variable
- The uncertainties in the dependent variable are distributed like a Gaussian, centred on the correct value
- There are no systematic errors in either the dependent or independent variables

2.5.3 Data fitting (Non-linear Least Square Fitting)

For this application, the bi-exponential decay law is used as a standard fitting model in the analysis. This is based on the assumption that all observed transients will only be the results of fluorescence decays with or without interacted partners (Donor alone and Donor-Acceptor respectively). For a mono-exponential, the same equation is also used but with $\alpha_2 = 0$.

$$I_c(t) = Z + I_0 \int_{-\infty}^{\infty} I_{IRF}(t')\, I(t)\, (\alpha_1\, exp\left(\frac{-(t-t')}{\tau_1}\right) + \alpha_2\, exp\left(\frac{-(t-t')}{\tau_2}\right))\mathrm{d}t' \quad (2.2)$$

Here Z is the background signal, $I_{IRF}(t')$ is the instrument response function, I_0 is the peak intensity, α_1 and α_2 are the fractional proportions of the lifetimes τ_1 and τ_2 respectively, where $(\alpha_1 + \alpha_2 = 1)$.

To calculate a curve for a fit, the unknown parameters of each temporal decay intensity $I(t)$ such as the fractional contribution of each lifetime (α_i) and their associated lifetimes (τ_i) will be kept afloat and optimised with non-linear regression until they best-matches the recorded data from TCSPC. The optimisation is accomplished once the goodness-of-fit parameter, χ^2, reaches a minimum or is minimised to a tolerated value.

χ^2 is essentially the sum of the squared fitting residuals normalised by the data variance σ^2. The Poisson nature of TCSPC data can bias the value of χ^2 (or

specifically the variance) by a different number of collected photons per sample. Therefore it needs to be reduced (or normalised) to χ^2_R by the degree of freedom[2] of the optimisation. In this case, if only random errors were to contribute to the calculation of χ^2_R, then the value is expected to be centred around unity.

2.5.4 Custom Fitting Protocol

TRI-2 creates a decay curve by iteratively re-convoluting each assumed decay intensity with the instrument response function, correct for any with baseline offset, and then compared it with the measured data until χ^2_R reaches a minimum threshold. The program uses a modified Levenberg-Marquardt (MLM) algorithm to minimise χ^2_R [62] The initial parameters were estimated by the rapid lifetime determination (RLD) or three-part integral method [63, 64]. The RLD method is based on the fact that a good estimate of the lifetime of a single exponential decay can be obtained by performing three integrals over the decay curve. If the decay is complex and not mono-exponential in form, then the RLD would result in an average lifetime instead. The MLM algorithm uses these initial parameters and iterates the optimization step until χ^2_R becomes less than 1.5 or when 10 consecutive iterations cannot further reduce the χ^2_R values.

TRI-2 makes a small adjustment in the χ^2_R calculations by normalising the square of the residual with the assumed decay intensity instead of the measured data, to avoid a further bias in estimation especially when photon counts are low [64].

2.5.5 Systematic Errors

Systematic errors can exist in TCSPC data, when the excitation power becomes excessively high and exceeds the safe limit. Multiple photons emissions in a single laser period are likely to corrupt the clocking mechanism, as the first photon can arrive at the detector much sooner than the rest. Once the first photon is

[2]The number of parameters which are free to vary (number of variable parameters number of data points)

registered to stop the TAC signal, the detector will become blind for a hundred nanoseconds and so photons loss can occur which can distort the transient shape to appear as though it has a faster decay [46, 49, 61].

There are two kinds of pulse pile up effect, classic and inter pulse pile-ups [46, 49, 61]. Classic pile-up does not impose a significant concern to this experiment, as the effect is most likely to be observed in experiments with a kHz pulsed laser source. To put this into perspective, the relative change between the observed $\tau_{measured}$ and the real lifetimes τ_{real} cause by classic pile-up can be defined as:

$$\frac{\tau_{measured}}{\tau_{real}} \approx \left(1 - \frac{P}{4}\right) \tag{2.3}$$

Here P can be either thought of as the average number of photons being detected per laser period, or the probability of a single photon detection in a single excitation event. Note the expression is only valid for a small approximation up to a few photons.

As previously mentioned, for a single photon emission criterion, P should be approximately equal to 0.01. Let consider a case, where the count rate reaches 20% of the laser repetition rate (16 MHz or $P = 0.2$), the measured lifetime according to the approximation will only gain a change by a maximum of 5 per cent which is often tolerable. From hindsight, the maximum count rate observed in BIFL experiments was between 2×10^6 to 3×10^6 counts ($P = 0.025$ – 0.0375), which would correspond to change in lifetime of 1% from the real value.

On the other hand, inter-pulse pile-up is a problem of high-repetition rate experiments, and is applicable to this case. It is directly associated with the intrinsic counting loss of a TCSPC system. Inter pile-up causes signal distortions as the classic pile-up does. After a photon is detected, the system is blind for the start-stop time and the TAC/ADC dead time. The TAC/ADC dead time normally extends over several excitation cycles, and may eventually stop inside one of the pulse periods. This will cause that pulse period to become partially blinded. Should a photon continue falling within the blind period (early part) of

any partially blinded excitation cycle, then the efficacy of the count mechanism can become bias over time. The pile-up is naturally a Poissonian problem, where the statistical probability of a photon being detected in the blind period depends on the number of repetitions of the event. Hence it is normally negligible under a single photon criterion.

The relative size of the distortion depends on the ratio of the count rate to the signal repetition rate and can be estimated as follows:

$$\frac{P_{late} - P_{early}}{P_{late}} = \frac{\tau_{det}}{f_{rep}} \tag{2.4}$$

Here P_{early} is a probability of a photon detection in the blind period, P_{late} is a probability of a photon detection in the remaining time of the period, r_{det} is the detector count rate at the CFD input and f_{det} is the signal repetition rate.

However, the magnitude of the dead-time-related distortion does not depend on the dead time per se, but can be approximated by Equation 2.3 like the classic pile up. While the size of the distortion is predictable, the actual shape of the distortion is not. Furthermore, the length of dead time may vary depending on the TAC voltage of the detected photon, and the transition from the blind into the active state may cause some ripple in the TAC characteristic for a few ns. Therefore the temporal positions of any distortion are never fixed, making it difficult to correct for the inter pulse pile. In practice, the only safeguard to any pulse pile-up would be to monitor the count rate of the detector and ensure that it falls within the safe limit.

2.5.6 Phasor Approach

Phasor analysis can provide an alternative view of the fluorescence decay occurring at each pixel of FLIM image (i.e. the strength of any FRET interactions and number existed fluorescent species). The analysis was originally employed for the global analysis of frequency domain lifetime data [65, 66]. However it was later found that single frequency domain global analysis methods could also be applied to time-domain data to accurately t bi-exponential models [67, 68].

In phasor analysis, the lifetime data from each image pixel (FLIM or BIFL) is Fourier transformed into a coordinate pair called phasor. Phasor is essentially a polar coordinate, consisting of distance and phase relative to a fixed point and direction. Any fluorescence decay in a function image (FLIM or BIFL) with similar lifetimes will thus be transformed into phasors of close coordinate values.

Phasor Calculation Protocol

The mathematical expressions involved in the calculation of phasor coordinates are relatively simple in terms of the computational processing. It is possible to perform the transformation from either the intensity or the phase delay of the data points in relation to the laser pulse period. For this project, the coordinates are calculated by taking the means of both transformation methods.

Phasor Numerical Recipes

The s and g coordinates in the phasor plot corresponding to a given decay $I(t)$ are given by the following expressions:

$$g_{i,j}(\omega) = \int_0^\infty I_{i,j}(t)\cos(\omega t)\mathrm{d}t / \int_0^\infty I_{i,j}(t)\mathrm{d}t \tag{2.5}$$

$$s_{i,j}(\omega) = \int_0^\infty I_{i,j}(t)\sin(\omega t)\mathrm{d}t / \int_0^\infty I_{i,j}(t)\mathrm{d}t \tag{2.6}$$

Here ω is the laser repetition angular frequency or the angular frequency of light modulation, and the indexes i and j identify a pixel of the image.

Since any measured decay curve is a convolution between the IRF and fluorescence response function, the Fourier transformation of the convolution can thus be treated as the product between the Fourier transforms of the two functions. The IRF can thus be de-convolved from fluorescent signals by dividing every phasor with a Fourier Transform of the IRF.

If the decay is single exponential, then the coordinates of the phasor are given by:

$$g_{i,j}(\omega) = \frac{1}{1 + (\omega\tau)^2} \tag{2.7}$$

$$s_{i,j}(\omega) = \frac{\omega}{1 + (\omega\tau)^2} \tag{2.8}$$

In the case which in a pixel i and j we have the contribution of several exponential components, the coordinate g and s of the phasor are given by:

$$g_{i,j}(\omega) = \sum_k \frac{f_k}{1 + (\omega\tau_k)^2} \tag{2.9}$$

$$s_{i,j}(\omega) = \sum_k \frac{f_k\,\omega\tau_k}{1 + (\omega\tau_k)^2} \tag{2.10}$$

Here f_k is the intensity weighted fractional contribution of the component with lifetime τ_k.

Significance of Phasor Cluster Location

Single Exponential Phasor

This is best understood by considering an ideal case where the IRF of the system is a delta function, and then calculate each phasor (g, s) in terms of the phase delay within the modulation period (2π). This is carried out by averaging the cosine and sine function of the microtime data of each burst (c.f. time delay of a fluorescent photon from an exciting laser pulse) [1].

$$g = \frac{1}{N}\sum_{i=1}^{N} \cos\left(\frac{2\pi\tau_i}{P}\right) \tag{2.11}$$

$$s = \frac{1}{N}\sum_{i=1}^{N} \sin\left(\frac{2\pi\tau_i}{P}\right) \tag{2.12}$$

Here τ_i is the microtime time values of the photons in ns, P is the phasor period or the reciprocal of the laser repetition rate $\frac{1}{f}$, and N is the total number of

photon in a burst and f is the phasor frequency.

By extension, it is also possible to define the "fundamental" phasor coordinate of a photon with microtime τ as [1]:

$$g = \cos(2\pi f\tau) \tag{2.13}$$

$$s = \sin(2\pi f\tau) \tag{2.14}$$

These coordinates are known as the fundamental phasors, which represents the angular position of each lifetime within the modulated phasor period (0 to 2π), on a unit circle. The phasors are distributed along the circle starting from the zero degree plane in an anti-clockwise direction (see Figure 2.15).

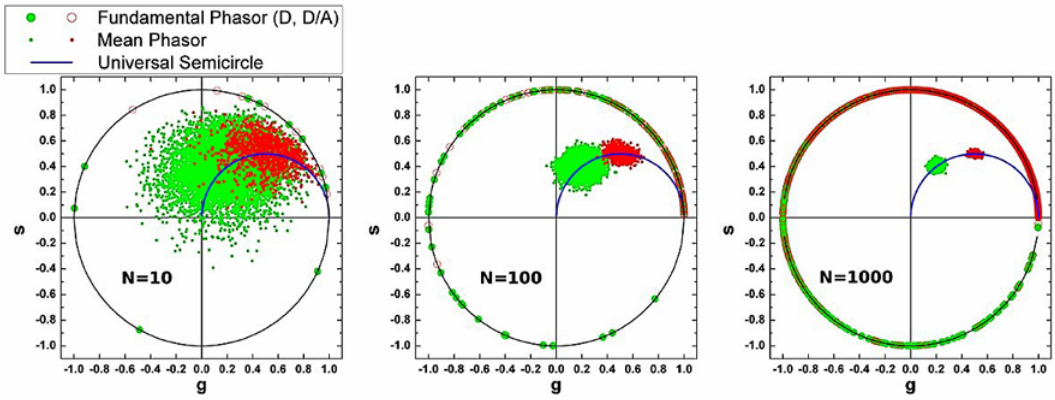

Figure 2.15: A illustration of the locations of the fundamental phasors and average phasors corresponding to simulated photons emitted by a species with lifetime of 4.6ns (plotted in green), and 2.3 ns (plotted red), using a laser repetition of 68 MHz [1] - Figure 5. Fundamental phasors (large circles) are located on the circumference of the unit circle, which corresponds to a delta function IRF. Average values of phasors from different numbers of photon N = 10, 100, or 1000 are located inside the disc on a universal semicircle (blue line) of radius 0.5 and centre (0.5, 0) [1].

The angular distribution of fundamental phasors between the 0 and 2π planes directly reflects the photon concentration of a transient from the time which fluorescence begins to decay until the end of the measurement window (approximately

from 2 to 10 ns in this project). The average phasor value corresponding to N number of photons along the unit circle is the expected to be localised within the top-right quadrant of the disc (a quadrant which contains the majority of photons in a burst). For a fast decay, the distribution of the phasors should diminish rapidly from the starting plane, as shown by the phasors with FRET interactions (open red circles on the unit disc on the rightmost panel of Figure 2.15). Similarly, a long decay will spread the phasor distribution to a larger angular range across the circle, depicted by the phasors with no FRET interactions (solid green circles on the unit disc on the rightmost panel of Figure 2.15).

Provided there are no systematic errors, the averaged phasor coordinates (g, s) from a lifetime image will centre within the first quadrant of the phasor circle around a specific coordinate (a centre point of distribution) defined in Equation 2.15 and Equation 2.16. The distribution of phasors is Poissonian and the 2D standard deviation on the 2D histogram plot will scale linearly with the signal-to-noise ratio ($N^{\frac{1}{2}}$).

The real useful phasor coordinate are calculated by taking an average of the fundamental phasors [1]:

$$g = \frac{1}{1 + (2\pi f\tau)^2} \tag{2.15}$$

$$s = \frac{2\pi f\tau}{1 + (2\pi f\tau)^2} \tag{2.16}$$

The concentration of fundamental phasors along the unit circle provides a simple intuition to predict the locations of averaged phasors on the universal semi-circle. Average phasors from fluorescence with short lifetimes will be located close to the starting plane (1, 0) (right hand side of the universal semi-circle) and the ones with long lifetimes will be located closed to the centre of the unit circle (0, 0) (left hand side of the universal semi-circle). A convenient landmark of the universal semi-circle lies within the coordinate (0.5, 0.5) of the unit circle. The point corresponds to a lifetime of $\tau = \frac{P}{2\pi}$ (which is approximately equal to 2 ns in this project, as the laser repetition rate used, is 80 MHz). Equation 2.15

and Equation 2.16 also provide a mean to compute lifetimes from the phasor coordinates by the following modified expression [1]:

$$\tau = \frac{1}{2\pi f}\left(\frac{s}{g}\right) \tag{2.17}$$

As long as the fluorescence decays from any dye is mono-exponential, the distribution of phasors will universally lie along a semicircle path within the quadrant spanning from (0, 0) to (1, 0) see Figure 2.15. An exact position (along the path) is dependent on the average lifetime (as previously mentioned).

Multi-exponential Phasors

Species with fluorescence decays described by multiple exponentials τ_i, with relative weights f_i can be shown to have phasor coordinates [1]:

$$g = \sum_i f_i \, g_i \tag{2.18}$$

$$s = \sum_i f_i \, s_i \tag{2.19}$$

Given that:

$$\sum_i f_i = 1 \tag{2.20}$$

Here the (g_i, s_i) and τ_i of each species are related by Equation 2.15 to Equation 2.17. In other words, phasors add linearly and as a result, combinations of two lifetime components fall on a straight line between the two components inside the semicircle area, as shown in Figure 2.16, with the position along that line determined by the relative weights of each component.

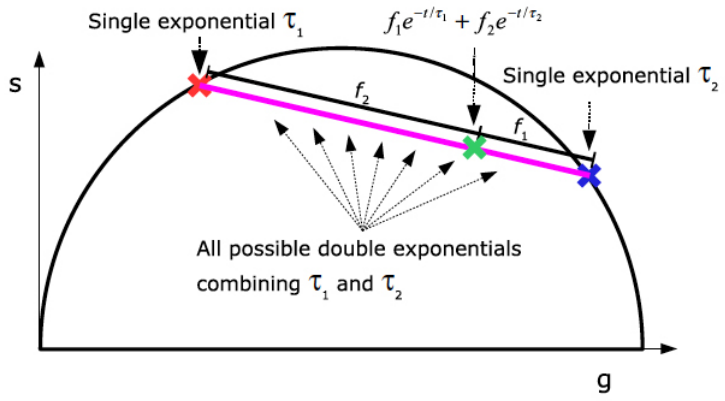

Figure 2.16: Multi-exponential Phasors Distribution [1].

Accounting for the IRF in Phasor Measurement

The phase ϕ and modulation m of the phasor are defined as [1]:

$$\phi = \tan^{-1}\left(\frac{s}{g}\right) \tag{2.21}$$

$$m = \sqrt{g^2 + s^2} \tag{2.22}$$

In the presence of an IRF, the measured and the real (expected) values of the phasor phase and modulation are related by:

$$\phi_{measured} = \phi_{real} + \phi_{IRF} \tag{2.23}$$

This simple geometric approach to handling the IRF is a particular strength of phasor analysis for both data analysis and instrument design. The computation of phasor analysis is faster than NL-MLM algorigthm which uses iterative deconvolution on every data point in fittings of every pixel. Phasor analysis performs the deconvolution operation only once and with simple algebra, resulting in a very rapid calculation of FLIM images.

Phasor analysis is appealing for the project, as it is fast and does not require powerful computational power. More importantly, the relationship between phasors

and Cartesian coordinates is reversible through Fourier transformation, making it convenient to select specific pixels (or lifetime populations) on a BIFL image from specific regions on a phasor plot. The phasor method was intended on being used as a graphical view on the data behaviour, in supplement to the standard analysis of lifetime data in MLM. Owing to the speed of the computation, phasor analysis could be proven useful in a future application such as sorting screened analytes, i.e a generation of sorting identifications through " 2D gating" on phasor plots.

Chapter 3

Fluid Dynamics in the Microfluidic Chip and Burst Detection

The development of cell screening assay in flow using the FIFO approach is a rigorous process. Cellular fluorescence expression produced by either a transfection or immunocytochemistry can markedly vary from case to case (from a few hundred to thousands photons per cell). Users must therefore use a sufficiently strong excitation power for a majority of the cells under investigation, to obtain meaningful data for a lifetime analysis. The standard non-linear least squares analysis such as the Levenberg-Marquardt algorithm [18, 62], requires a demanding photon economy for complex fits (approximately 10,000 photons for a bi-exponential model [5, 18, 62, 69, 70]). Due to the variation of fluorescence expression from cell-to-cell and the lack of cellular direction control in flow (as will be discussed in this chapter), an easy solution to the large inconsistency of photon emissions would be to increase the laser power until the average detected count rate from flowing cell exceeds the safe limit of TCSPC by approximately 5% (See chapter 2, subsection 2.3.2). This would of course cause some erroneous signal responses from TCSPC, but in a level which would be correctable in a post-analysis. The use of high power laser not only increases the probability of pulse pile-up, but it also highlights the signal impurities from the Rayleigh and

Raman Scattering of solvent molecules which would normally be undetected by traditional FLIM. In effect, the BIFL method requires high signal counts for short detection periods in order to ensure that individual cells are measured rapidly and the most efficient use of measurement time is employed. Simply put, if the cells under investigation could be arranged to arrive line astern with a minimal gap between them, the collection in terms of both cell numbers per unit time and photon counting rate would be optimised. Unfortunately, cells are not so well behaved in flow. In order to fulfil this a droplet type microfluidic chip [71–79] would be required to ensure that cell observations are repeated at defined intervals. However the droplet generation was not pursued as part of the thesis since a number of potential problems were foresaw in terms of droplet formation with a two component (cells + media) aqueous phase. In a real system beads and cells are distributed over the width of the fluidic for low flow rates and wide channels. This was particularly the case for initial investigations using fluidic chips with >0.5 mm channels. The obvious solution to this detection problem would be to borrow the phenomenon of hydrodynamic focusing from flow cytometry [80]. Hydrodynamic focusing (focusing of particles to the centre of the fluidic via the shear forces exerted on those particles by the flow) in microfluidics would ensure that most cells are directed to the centre of the probe region (see Figure 3.1), and this increases the useful detection efficiency (in terms of the fraction of all particles being detected and the maximum excitation/collection efficiency).

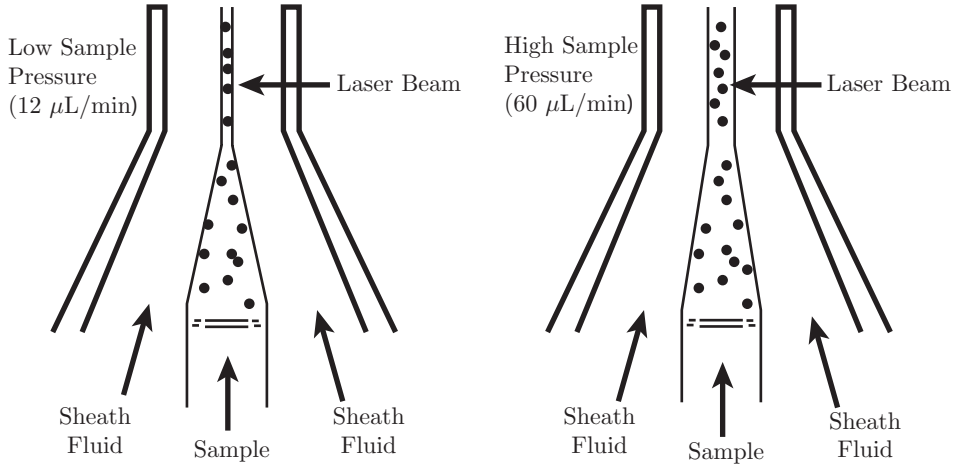

Figure 3.1: Demonstration of hydrodynamic focussing.

For this research, the increase in bulk velocity introduced by the sheath fluids, would reduce the sample dwell time in the focal volume and subsequently the photon population per sample. It will be shown below that without the focussing, the operational flow speed is somewhat limited. Enlarging the focal volume for such configuration would also not be sensible for TCSPC, as it could probe any other impurity fluorescence (such as dye leakages, or label-free proteins in solutions) during cell detections as well as degrading the single cell screening resolution of the system. Further sample dilution must be made to lengthen. the inter cell time during detection to tackle the issue, which would consequently result in a lower analytical throughput rate. Although there have been some attempts to photo-bleaching the impurity species in the flow cytometer sheath fluids upstream of the detection volume in [6,10], the sample stream itself is more likely to be contaminated with label-free proteins and cannot be pre-treated with the method. All in all, the proposal would add an unnecessary degree of complexity to the system, which is expensive and offers small rewards in return. Another feasible concept to combat the noise issue would be to employ a smaller detection volume with a higher NA objective. However the volumetric flow rate would need to be extremely low for any samples to yield sufficient photon counts. A microfluidic chip with smaller channel geometry, which has a sufficiently thin optical surface would be required so as to accommodate the pace of the flow and the smaller working distance of the objective. The disadvantages of such a channel config-

uration would be a reduction in the screening throughput; difficulty in sample injection due to sample settling in the slowen flow and channel clogging, The increased complexity of fabricating such a fragile chip if indeed feasible would inevitably prove to be an expensive undertaking.

In this project, the simplest combination of excitation and sample delivery methods was chosen; namely BIFL and the microfluidic chip discussed in chapter 2. BIFL can probe a variety of information from a particulate flow; the throughput level, fluorescence expression level, residence time in the volume, flow speed, and instantaneous count rate of the detector. Appropriate parameters can be cross-correlated on a fixed or ad hoc basis to determine the statistical probability of a single particle detection and more accurate fluorescent signals without extra hardware. The 100 μm x 110 μm channel profile of the fluidic chip allows for a relatively fast flow (see Table 3.1 and Table 3.3) with moderate backing pressure. This proves to be less prone to blockages at the input apertures by cellular debris. Particles can be screened relatively homogeneously through a line focus or a single spot in the case of the strongly labelled samples in faster flow; leaving the controlling parameter on the photon economy to just the flow speed itself, as will be shown later in subsection 3.2.1 (spot focus) and subsection 3.2.2 (line focus).

The proof-of-concept for FIFO BIFL in flow was validated using 3 types of spherical fluorescent beads, Type I [1], Type II [2] and Type III [3]. Type I (10 μm) and Type III (2 μm) beads are made of the same polystyrene material and labelled with the same green fluorescent dye (see footnote), whereas Type II (10 m) beads are made of Melamine Resin, and labelled with FITC.

This proof-of-concept is very extensive, and will broken into 2 chapters. This chapter describes the workflow in optimising the detection efficiency and alignment of the travelling samples to the excitation probe with hydro-focussing. The

[1]Type I beads 10 microns, Fluoro-Max Green Aqueous Fluorescent Polystyrene Particles. Excitation λ 468 nm / Emission λ 508 nm. (G1000, Thermo Scientific, USA).

[2]Type II beads 10 microns, FITC-dyed Micro Melamine Resin Particles. Excitation λ 490 nm / Emission λ 525 nm. (90287, Fluka, Switzerland).

[3]Type III beads 2 microns, Fluoro-Max Green Aqueous Fluorescent Polystyrene Particles.

following chapter (chapter 4) examines the characterisation of the lifetime detection system using Type I and II beads.

3.1 Introduction to Fluid Dynamics

In this introductory section, some fundamental fluid properties will be summarised to provide some understanding of the phenomenological properties of laminar flow in capillaries/microfluidics.

3.1.1 The Flow Mode Within Microfluidics

Flow behaviour can be generally be described by two modes of operation, laminar and turbulent flow [81, 82]. There are many ways to visualise the concepts of these modes, but it is appropriate in this context to discuss them in terms of flow lines and velocity vectors flow [2–4, 81, 82].

Fluid velocity is a vector quantity, and, because the fluid behaves as a continuum, a velocity field can be spatially and temporally segmented into infinite number of vector particles along a flow (See Figure 3.2). The line or curve, which joins all the velocity vectors together, is known as a streamline [2–4, 81, 82].

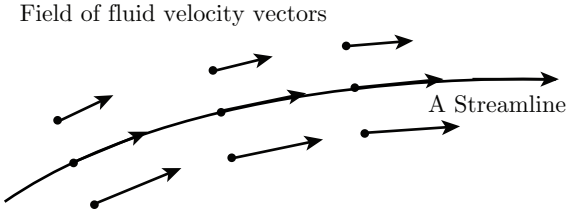

Figure 3.2: Diagrammatic representation of streamline (drawn by candidate).

Laminar flow is sometimes referred to as streamline flow, where fluid particles are travelling in definite observable streamlines throughout the flow journey. Contrarily, under a turbulent flow, there are no definite streamlines and so fluid particles

can freely move in irregular pattern with no definite layers.

The dynamics of a fluid in a pipe is characterised by the ratio between viscous and inertial force densities [2–4, 80–82]. When the inertial force is dominant, the fluid would flow in a normal behaviour (Newtonian) which can be controlled by using the fundamental law of conservation, such as the loss of momentum of fluid particles when they are rounding a corner, etc [2–4, 80–82]. On the other hand, when the viscous force begins to overwhelm the inertial force, the flow would become insensitive to any changes in resultant force, resulting in a streamline flow throughout the pipe, even in the meander configuration discussed in chapter 2. The ratio between the two forces is known as Reynolds number (Re), which is defined as [2–4, 80–82]:

$$Re = \frac{\rho U_0 L_0}{\eta} \tag{3.1}$$

Here ρ is fluid density, U_0 is average flow velocity, L_0 is the characteristic length (in the case of cylindrical channel this is given as the diameter) and η is fluid viscosity.

Laminar and turbulent flow is separated by a specific range of Re numbers. A flow is said to be laminar if $Re < 2300$ and turbulent when $Re > 4000$) [2–4, 80–82]. Re between 2300 and 4000 represents the transitional flow phase of the two modes [2–4, 80–82].

One of the main reasons for utilising microfluidics lies in the prominent laminar nature (non-turbulent) of its flow operation. The orderly, steady-state flow accommodates the FRET screening (see chapter 2) by maintaining the particulate sequence in a streamline throughout its journey through the chip at a near-uniform speed.

The general discussion on the transition between the laminar and turbulent flow regime due to an increase in flow speed is of little significance in the context of this thesis, as the T-junction chip has a sufficiently small, symmetrical and

homogenous channel profile, which provides low Reynolds number (laminar) flow at acceptable flow rates for the sample solutions that are employed.

For example: For a typical fluidic chip with a diameter of 100 μm flowing a solution of water (ρ = 1000 kgm^{-3}: η=0.001002 Pas), Equation 3.1 can be rearranged to derive a maximum flow speed at the laminar threshold (Re = 2300) to be 23.046 ms^{-1}. To make a transition to turbulent flow (Re > 4000) the flow velocity would have to exceed 40.08 ms^{-1}. The next section will show some typical velocity calculations based on pressure differential to show that the fluid velocity is always below the maximum Re value for laminar flow (i.e. Re < 2300).

3.1.2 Velocity Profile

A diagram summarising the velocity profiles in laminar and turbulent flow is shown in Figure 3.3. It can be observed that the streamlines across different parts of a flow cross-section do not have the same velocities. In general, the leading edge of a fluid will deform into a curved or parabolic surface when it is driven by an external force or pressure differential. This deformity is primarily caused by the shear viscous force exerted by an external boundary of the fluid acting against the flow. The peripheral area of the fluid that is in contact with the capillary wall is assumed to have zero velocity (no slip condition), while the neighbouring fluid area in which the motion of the fluid is affected and retarded by this viscous stress is known as the boundary layer. If the flow in the pipe is laminar, then the velocity gradient profile of the flow cross-section will be parabolic with the maximum velocity at the center being approximately twice as fast as the average bulk fluid velocity [reference]. In turbulent flow, the velocity profile will be partially curved (see Figure 3.3).

The fluid velocity can be predicted by solving Navier-Stoke Equation [2–4, 81, 82] with the assumption of a constant pressure gradient along the axial direction of the channel and a no slip boundary [2–4, 81, 82].

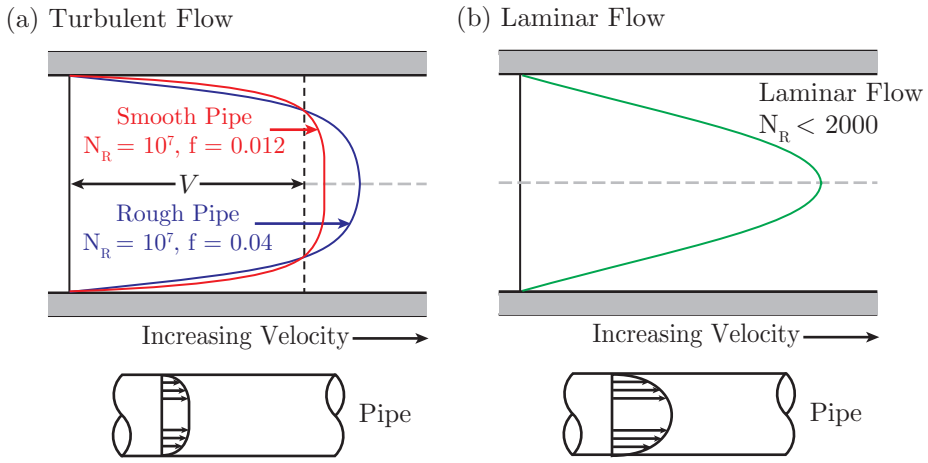

Figure 3.3: An illustration of a formation of velocity profile under a viscous stress [2–4] (images drawn by candidate).

$$V(r) = \frac{\Delta P R^2}{4\mu L}\left(1 - \left(\frac{r}{R}\right)^2\right) \tag{3.2}$$

Here $V(r)$ is the fluid velocity along the axial direction, r is the spatial or lateral position along the channel width, μ denotes the fluid kinematic viscosity, L the length of the micro-channel, ΔP is the pressure differential, and R is the radius of the tube. The typical operational pressure used in driving the flow in this experiment ranged from 0.1 bar to 2.0 bar of pressure. From Equation 3.2, the shape of the velocity profile can be predicted as shown in Figure 3.4 (assuming the pressure differential is equivalent to the driven pressure).

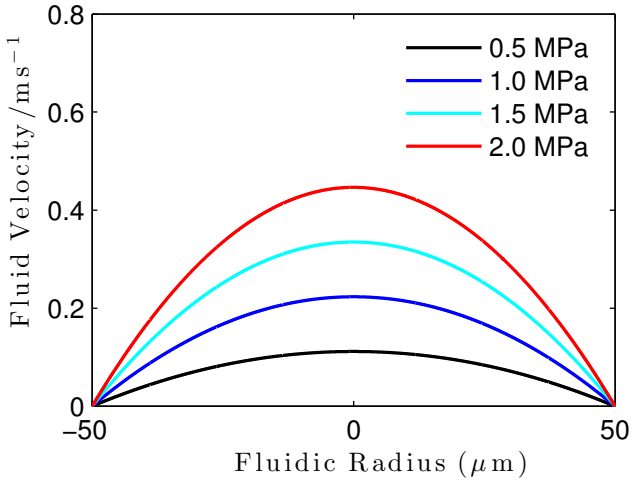

Figure 3.4: A simulation of the velocity profile due to the increase in flow pressure in the Dolomite micro-mixing chip, computed by Equation 3.2, where ΔP is the driven pressure in Pa, increase from 0 to 2 MPa by a 0.5 MPa step (0.5 bar step), $R = 50$ μm, $\mu = 1.002$ Pas, and r was computed in the range between -50 μm to 50 μm.

3.1.3 Additional Boundary Layers During Flow Operation

When a fluid flows past a surface for example a thin sheet of surface (see Figure 3.5), an additional boundary layer will develop and thicken as the fluid is travelling along the sheet. The boundary layer expands because the retardation from the frictional force has time to develop on layer-to-layer of the fluid in the form of shear stress towards the unaffected part of the flow. Even if this boundary layer is developed from a laminar flow, it can abruptly become turbulent if the growth of the layer becomes too large. In any case, the boundary layer will grow or expand downstream, until the flow passes by the body (the shearing motion engendered in the boundary layer is then degraded by viscous forces), or until it meets another boundary layer growing from some other surface, or until it reaches a free surface.

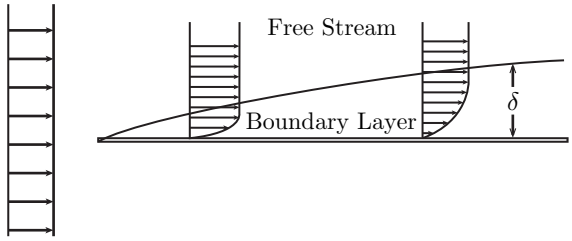

Figure 3.5: An illustration of an introduction of boundary layer, where δ is the thickness of the layer (drawn by candidate).

The concept of the boundary layer may seem a little off context in this chapter, but it can nevertheless provide a possible explanation on some of the random streamlines switching within a flow (in section 3.2). It was observed that samples (especially eukaryotic cells) tend to adhere and aggregate on the inner channel surface when they are driven by low pressure or not flushed out of the system properly. These aggregations can introduce a significant roughness to the fluidic wall (which can appear as bed bump in Figure 3.6) near or prior to the probe location. The time of occurrence and exact location of these aggregations are impossible to observe during data acquisitions, and so random streamline switching will inevitably occur. Although these unwanted samples could be cleaned up with a caustic chemical such as sodium hydroxide, several usages of the chemical will cause degradation to the wall surface and consequently some irregularities on the wall.

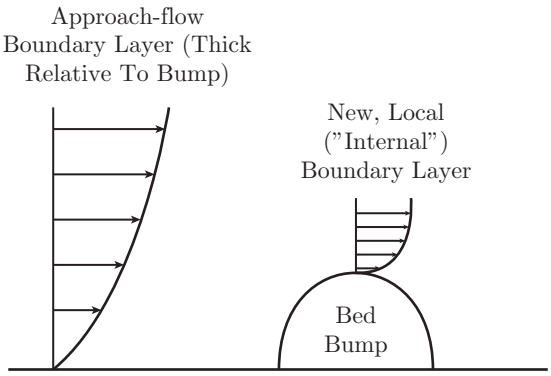

Figure 3.6: An illustration of additional boundary layer introduced by an obtruding object along a fluidic wall (drawn by candidate).

3.1.4 Streamline Switching

A simplistic diagram of streamlines in a curved portion of a flow channel is shown in Figure 3.7

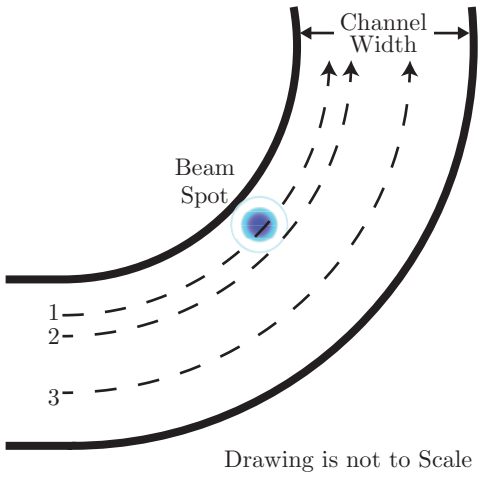

Figure 3.7: An illustration of streamlines within the flow channel (drawn by candidate).

As discussed in the previous section, each streamline possesses a different velocity depending on the lateral location. This would not be of major concern should the flow trajectories be restricted to a channel width comparable to those of the flow particles (10 μm or so). However, the Dolomite microfluidic chip[4] has a channel width approximately 10 times the size of typical eukaryotic cells, and so any streamlines of cells or cell analogues can be spatially distributed to a relatively wide area across the channel under low viscous force. Figure 3.8 and Figure 3.9 illustrate the preferential streamlines of Type I and Type II beads driven by equally moderate pumping pressure at 0.5 bar. Interestingly, the two bead types prefer to flow on a different side of the channel. Figure 3.8 shows that Type I beads (polystyrene) tend to flow towards the inner side of the bend (to the right of the crosshair). Contrarily, Type II beads (Melamine resin) distinctively flow towards the outside of the bend (left of the crosshair).

[4]Dolomite microfluidic: `http://goo.gl/0oxjnc`

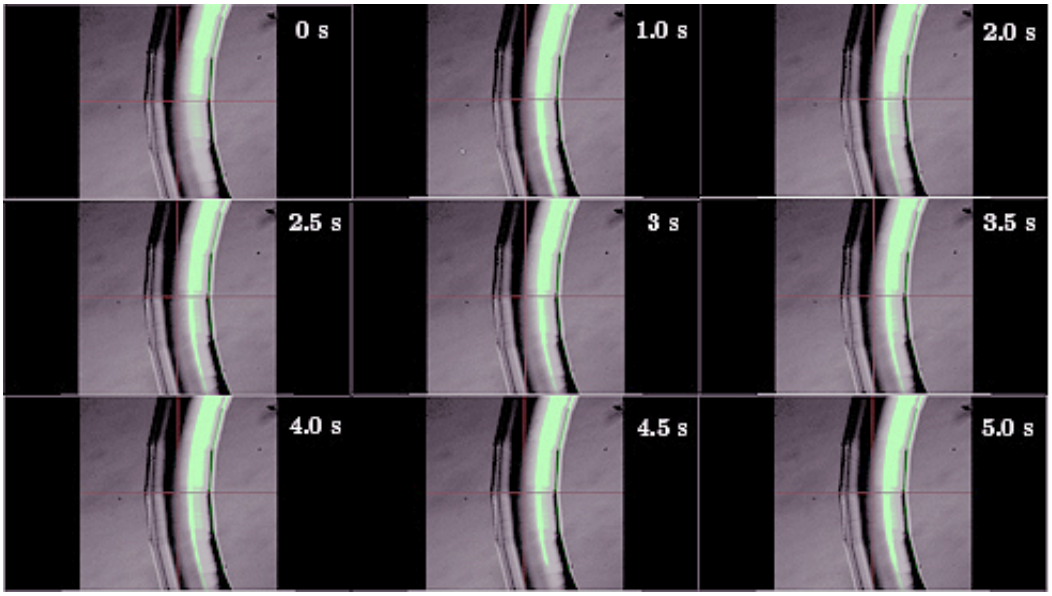

Figure 3.8: Time-lapse sequence of Type I beads in the microfluidic. A crosshair was computer generated and superimposed onto the video output as a positional reference. A full video footage can be found at `http://youtu.be/UsVKtx4K-yo`.

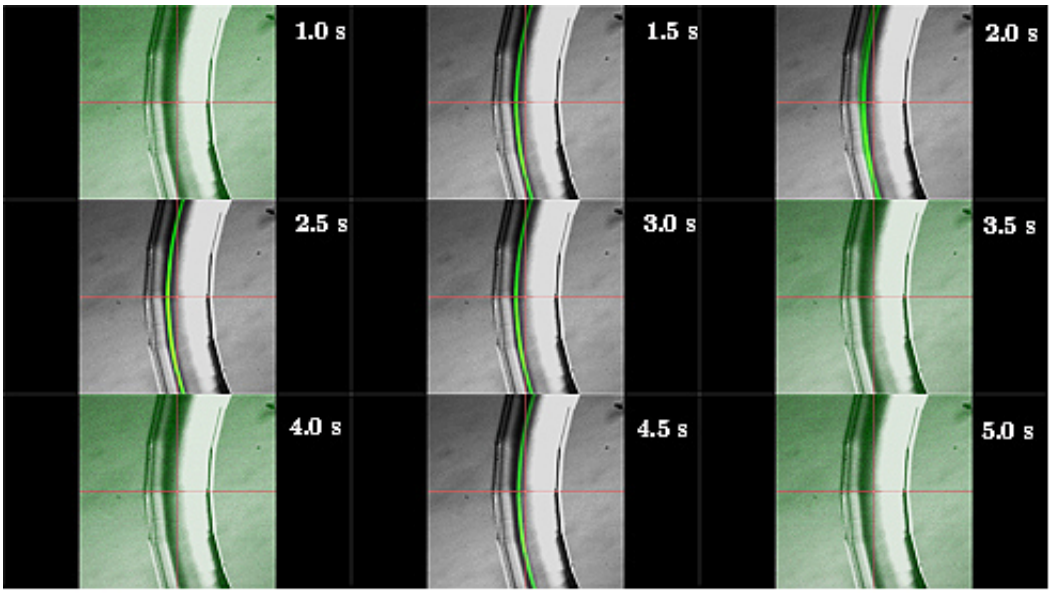

Figure 3.9: Time-lapse sequence of Type II beads in the microfluidic. A crosshair was computer generated and superimposed onto the video output as a positional reference. A full video footage can be found at `http://youtu.be/BO1-qJsM2xc`.

Notice the preferential streamlines in the videos; there were occasional lateral streamline switching or intensity changes around the same region (z-plane variation). Therefore, even if the probe is parked on the most travelled streamlines, some variations on the excitation intensity and the residence time are inevitable in an experiment. These fluctuations are expected to be reduced when the hydrodynamic focusing effect of the velocity profile becomes pronounced at high pumping pressure. The trajectories of the flow particles should switch towards the central region of the channel, as predicted by the velocity gradient profile (in Figure 3.3 and Figure 3.4). This focusing effect, however, will stand as a trade-off for signal-to-noise ratio since increased speed implies reduced burst width.

3.2 Experimental Work (Characterisation of Burst Characteristics)

The key consideration to the effectiveness of this high throughput BIFL project is weighted between the average sample photon collection efficiency and analytical throughput of the system (i.e. number of samples detected per minute). This section will guide through the workflow in deducing the best method of excitation for BIFL, in terms of the pumping pressure (average flow speed) and the merits of spot and line probes from cell analogues, 10 microns fluorescent beads (Type I). The result will include different representations of the burst characteristic readouts, such as burst integrated intensity and width to provide an outlook of the spatial distribution of streamlines at different pumping pressure (or viscous force). Typical burst characteristics from the raw burst data will also be included to provide an alternative mean of assessing the viability of flow speed on the number of photons collected per burst and as a confirmation on the BIFL ability to resolve fluorescent bursts at high flow rates.

The average excitation residence time (burst width) of the beads (from a single location measurement) will be used as a mean of optical velocimeter in flow.

$$\bar{V}_{sample} = \frac{\phi_{sample}}{\bar{t}_{res}} \tag{3.3}$$

$$Q_{sample} = \frac{10^3}{60}\pi ab\bar{V}_{sample} \tag{3.4}$$

Here $\bar{V}_{sample}, \phi_{sample}, \bar{t}_{res}$ are the average flow speed, diameter and mean burst width of the sample respectively. Alternatively, Q_{sample} is the bulk velocity of samples (expressed in litre per minute for direct analogy with volumetric flow rate), a and b are the channel diameters in the short and long axis respectively.

It is not the objective of this work to measure the exact velocities of the flow at different locations and assess if the steady-state flow is established in the chip or not. The accuracy of the bulk velocity measurement will be directly determined by the standard deviations of the burst width and integrated intensity distributions from each acquisition, which is sufficient in this case.

Type I beads were chosen for this investigation, as their mean diameters are comparable to those of typical eukaryotic cells, $\varnothing = 10$ μm and has a coefficient of variation less than 5%[5]. The beads are commercially made (Thermo Scientific, USA), and were internally dyed with green fluorescence (excitation = 468 nm / emission = 508 nm) by the proprietary Fireffli^{TM}technique, which claims to give them a saturated colour with no leaching to buffer media. This system characterisation takes the advantage of the particle uniformity, as will be shown by the burst characteristics results for subsection 3.2.1 for point illumination and subsection 3.2.2 for line focus.

3.2.1 Spot Probe

With a 20X objective (N,A, = 0.5), the diffraction limited focal volume and lateral diameter of the probe are approximately 10 fl and 1.2 microns respectively. A

[5]For Full details of the beads: `http://www.thermoscientific.com/ecomm/servlet/productsdetail_11152_L10535_87438_11963237_-1`

spot probe is ideal for this work, as the use of the femto-litre probe volumes would ensure that the background signals originated from autofluorescence of the media, Rayleigh scattering and Raman scattering are minimised [42]. The positioning of the probe was determined experimentally by the preferential streamline observed in FLIM, where an example is given in Figure 3.10. The image is normally acquired for approximately 5 minutes. The image in the figure shows that the particular samples are predominantly travelling through the centre of the channel. The beam can directly controlled by the scanning mirrors onto any position along the sample track developed on the FLIM image for the BIFL FIFO acquisition. In this case, the Type I bead solution was driven at an arbitrary low pumping pressure of 0.1 bar (1% of the pump pressure), The positioning of the beam remained spatially fixed with other operated pressure (0.2, 0.5, 0.8, 1.2 bar). The beam was positioned off-centre towards the inside the bend, around the streamlines observed in the time-lapse sequence (in Figure 3.8). The power of the beam is attenuated to 1 μW with an ND3 filter.

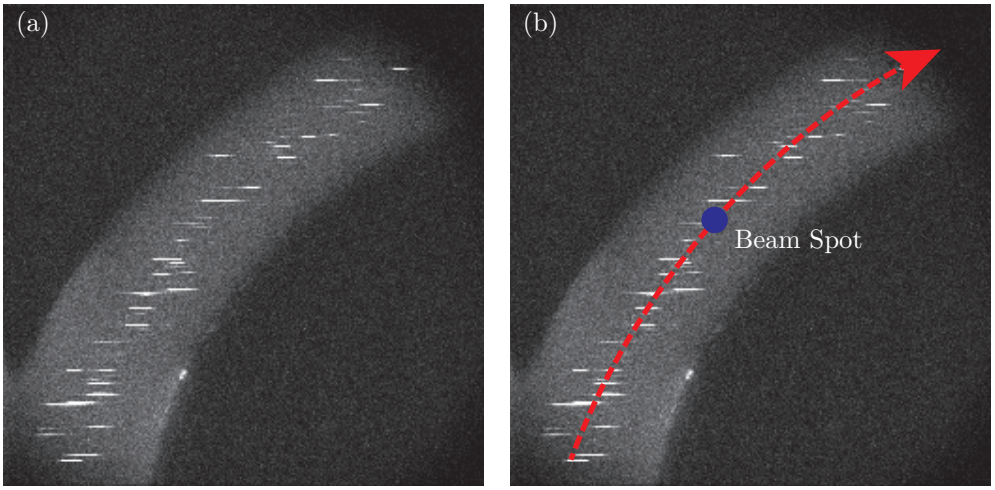

Figure 3.10: Observation of preferential streamline of a sample with FLIM. The picture in the figure was acquired for approximately 10 seconds, for illustrative purposes. As the beam spot is smaller the diameter of the bead, the beads would always be partially excited (in streaks) as each sample traverses through the channel in the field of view. Figure (a) and (b) are identical, where the sample trajectory was drawn and superimposed on top of (b), for illustrative purposes.

Burst Characteristics: Burst Width and Integral Intensity From Spot Excitation

Figure 3.11 and Figure 3.12 show histograms of burst widths (resident time in the excitation beam spot) and integrated intensities (number of fluorescence photons emitted during each sample excitation) of Type I bead at 5 different pumping pressures, 100, 200, 500, 800 and 1200 mbar, respectively. Figure 3.13 shows a summary of the integrated intensity distributions of the bead type from every pumping pressure. Figure Figure 3.11 and Figure 3.12 are meant for comparative purposes, and so the number of histogram bins was kept constant for every data set. As will be seen in the Figures and many others in this thesis, the probability distributions of the integrated intensity and burst width do vary distinctively between data sets. This can display very course information if the histograms do not effectively cover the ranges of critical data of each operational pumping pressure. Any data sets which are affected, will be resolved by placing inserts to reveal close-up observations around the specific centre values of each data set. The sample frequencies of the histograms on the inserts were normalised to the avoid confusions in the differences of sample numbers caused by different histogram ranges. Similarly, burst widths tend to have more discrete values, and so the number of bins used for the integrated intensity would be too excessive for the burst width histograms. Therefore the sample frequency of the burst widths were also normalised to avoid confusions caused by the change in the number of histogram bins.

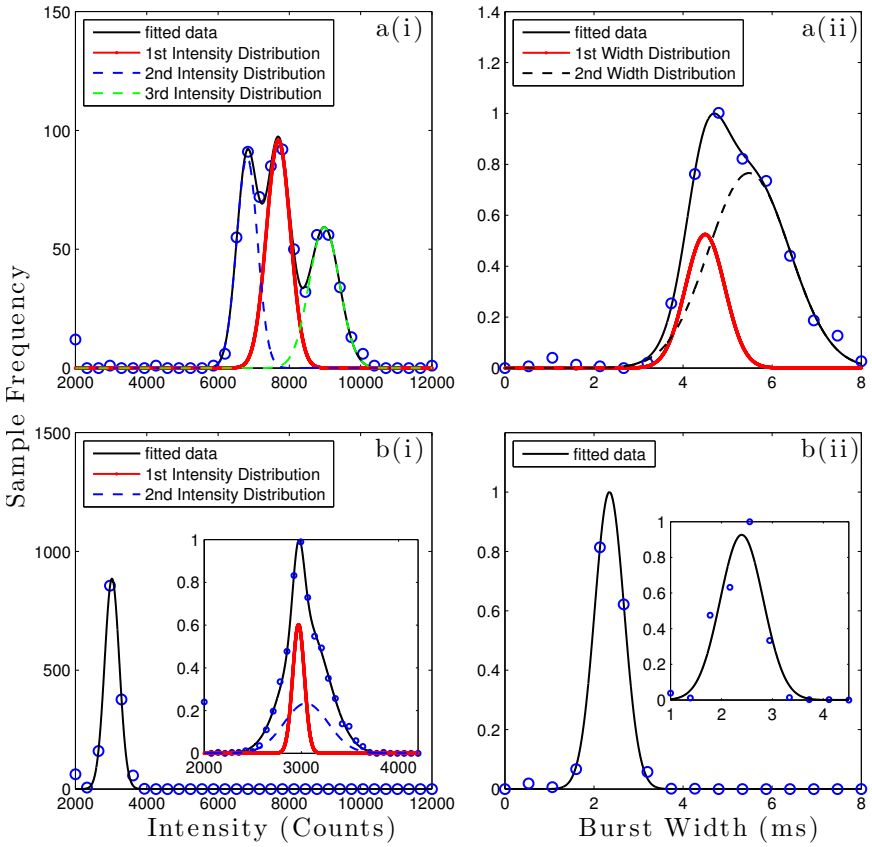

Figure 3.11: Histograms of integrated intensity (i) and burst width (ii) of Type I beads as a function of pumping pressure, c, d, and e correspond to 0.5, 0.8 and 1.2 bar of pumping pressure, respectively.

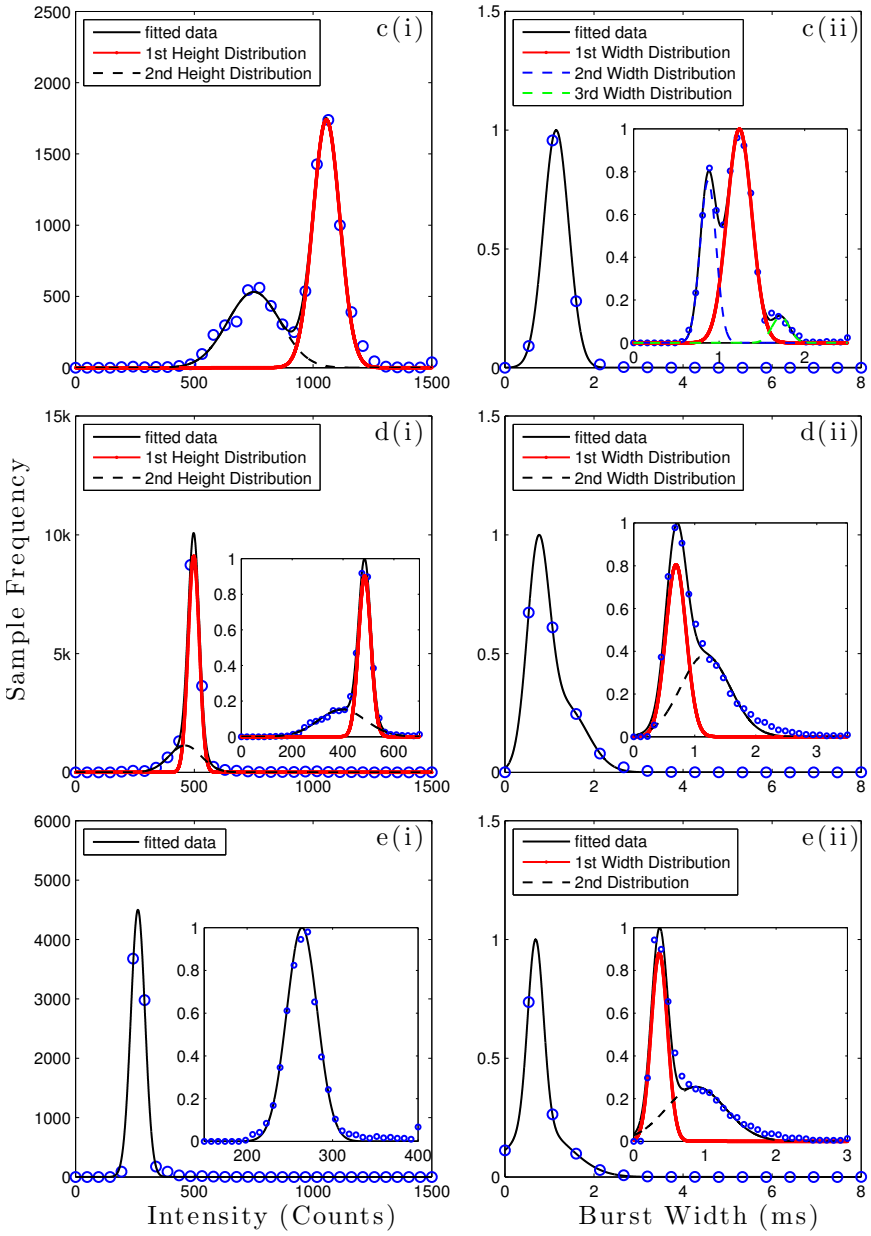

Figure 3.12: Histograms of integrated intensity (i) and burst width (ii) of Type I beads as a function of pumping pressure, where a and b corresponds to 0.1 and 0.2 bar of pumping pressure, respectively.

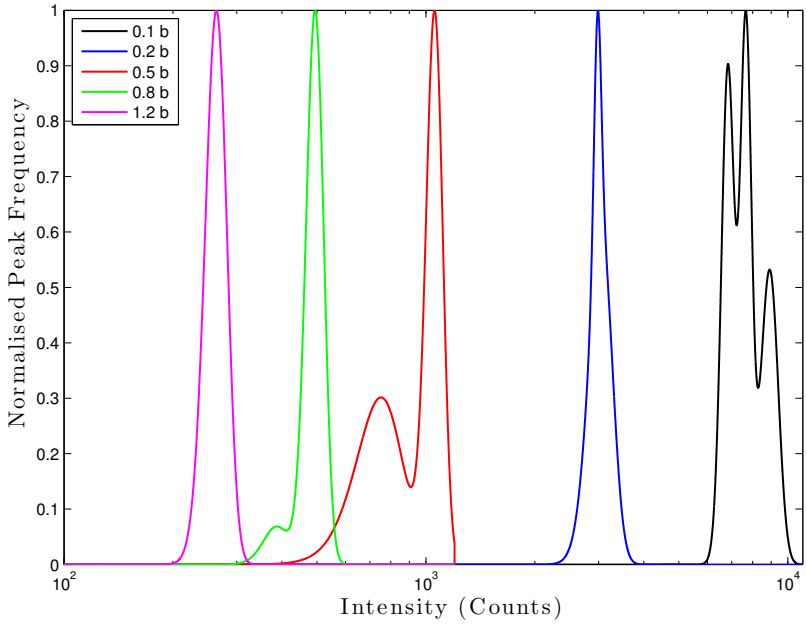

Figure 3.13: Integrated intensity of type I beads at 0.1 to 1.2 bar of pumping pressure.

Pumping Pressure (mbar)	Average Flow Rate ($nLmin^{-1}$)	Analytical Through-put (sample min^{-1})	Burst Width (ms)	Standard Deviation (ms)	Integral Intensity (Counts)	Standard Deviation (Counts)
100	0.32	11	4.495	0.6248	7693	474
200	0.60	25	2.398	0.4666	2097	85
500	1.16	141	1.237	0.2061	1027	86
800	2.08	254	0.6938	0.2367	485	34
1200	4.00	118	0.3604	0.1607	264	25

Table 3.1: The summary of burst Intensity and width with spot probe.

Generally, the data seems to be well behaved. The intensity data in Figure 3.11 demonstrates there are two to three intensity distributions at low pumping pressure (0.1 and 0.2 bar). This suggests that the streamlines were spatially dis-

tributed widely around the probe and experiencing different levels of excitation power. The distribution of trajectories supports the argument on the lack of shear stress acting on the solution very well. Since the particles could travel almost unconditionally under little influence of the velocity gradient. At 0.5 bar, the flow became better behaved and reduced to two streamlines within the channel, as observed in the two distinctive intensity distributions – the strongly and weakly excited populations, which can also be observed in the demonstration video provided in the caption of Figure 3.8. Beyond 0.5 bar (see Figure 3.13), the weakly excited population was progressively diminished until it eventually disappeared.

The integrated intensity exponentially drops off with pumping pressure, as depicted by the steady increment the semi log-plot (Figure 3.13). The throughput of the system showed signs of steady increases from a-d before dropping in the last operated pressure at 1.2 bar. The exponential trend in the integrated intensity decrease, the reductions in the weakly excited population from c(i) - e(i) and the analytical throughput in e(i) all seem to suggest that the increase in viscous force started to force the streamlines to migrate towards the centre of the channel and away from the probe in both axial and lateral directions.

The burst width distributions at low pumping pressure a(ii) - c(ii) with an exception of b(ii), are observed to be generally broad and have tendency to skew towards either side of the residence time. These characteristics conform well to the velocity gradient concept, as any weak out-of-plane excitation in the axial direction at low viscous flows can broaden the distributions towards the longer side of the timescale, while partial clipping of the beam in the lateral direction will have the same effect on the opposite side of the curves. At the higher end of the pressure supply, d(ii) - e(ii), the mixture of distributions was reduced into 2 populations. The flow channel profile of the chip is slightly oval, and so it is possible that at moderate pumping pressure, the streamline could reach the centre of the channel axis under the viscous force faster in one other direction, which is depicted by a progressive discretisation of the.integrated intensity distribution at a(i) – e(i). The reduction in the long residence time distribution at d(ii) – e(ii) also supports the evidence on the streamlines became more confined towards the

focal plane.

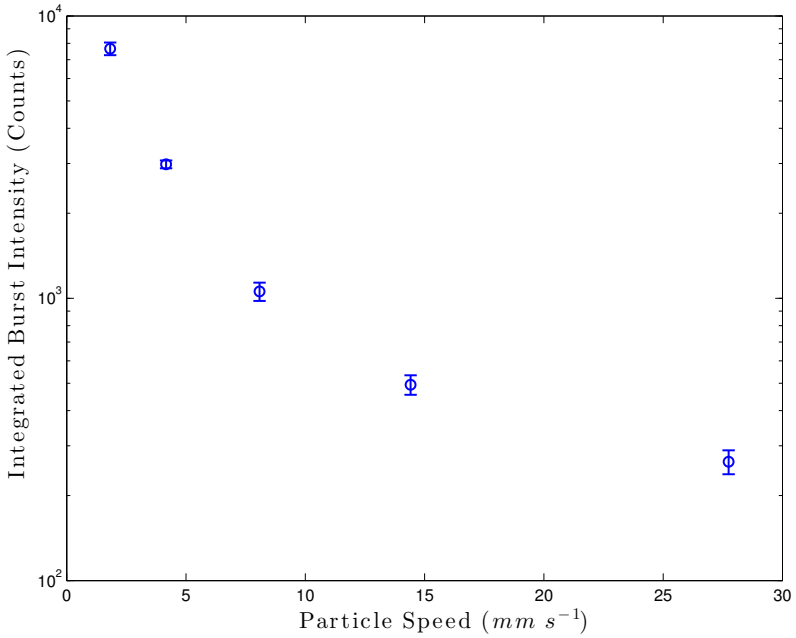

Figure 3.14: Integrated intensity of Type I beads as a function of the particle velocity.

The relationship between the average burst intensity with respect to the particle speed is observed to be double exponential. This just adds a further support on the change of streamline which moved away from the probe which was parked off-centre in the channel. If the velocity gradient becomes parabolic, then the streamlines around the channel centre are expected to gain twice the speed as those nearer to the channel wall. Therefore a combination of the extra gaining in speed at centre and the reduced excitation could cause the photon economy of each burst to be reduced at a double exponential rate with increasing pumping pressure.

Temporal Outlook of Streamline Switching

Temporal outlook on the streamline switching from each pumping pressure can be obtained by observing bulk variation in the peak fluorescence amplitudes with respect to time. The results from each pumping pressure are shown from Figure 3.15 to Figure 3.19. This data representation will be exclusive to the spot probe analysis, as the excitation method is less effective than a line probe, in terms of detecting the spatial distribution of streamlines across a relatively large channel.

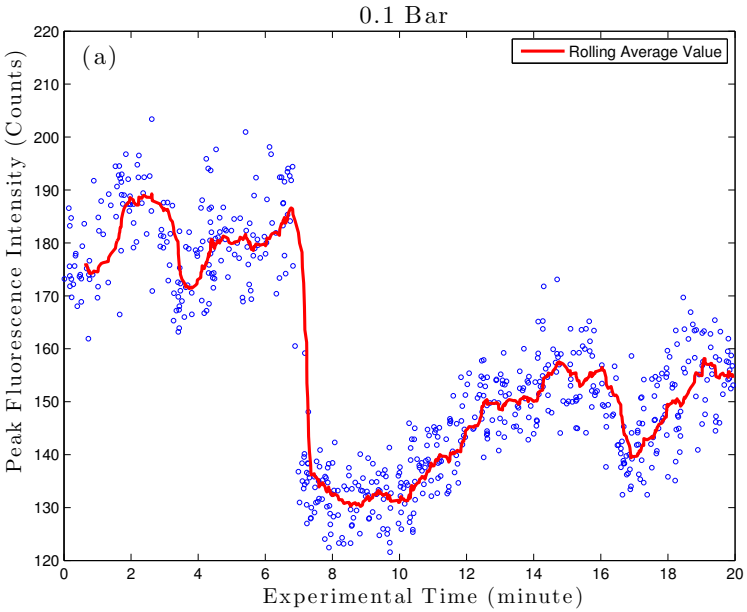

Figure 3.15: The homogeneity of peak fluorescence intensity during the course of the experiment at the BIFL acquisitions, operated at 0.1 bar of pressure.

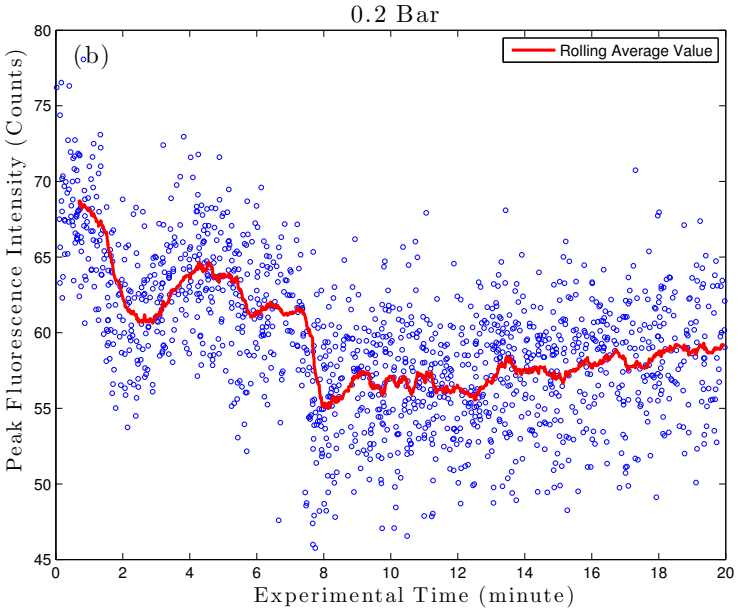

Figure 3.16: The homogeneity of peak fluorescence intensity during the course of the experiment at the BIFL acquisitions, operated at 0.2 bar of pressure.

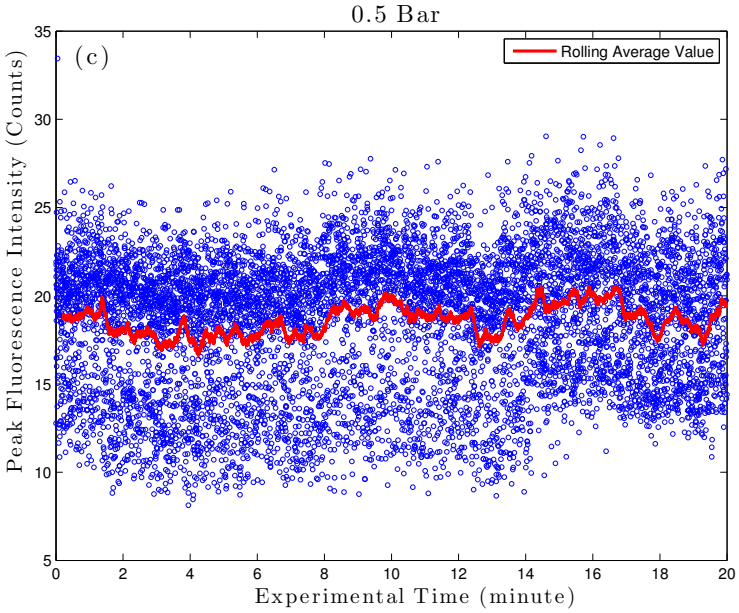

Figure 3.17: The homogeneity of peak fluorescence intensity during the course of the experiment at the BIFL acquisitions, operated at 0.5 bar of pressure.

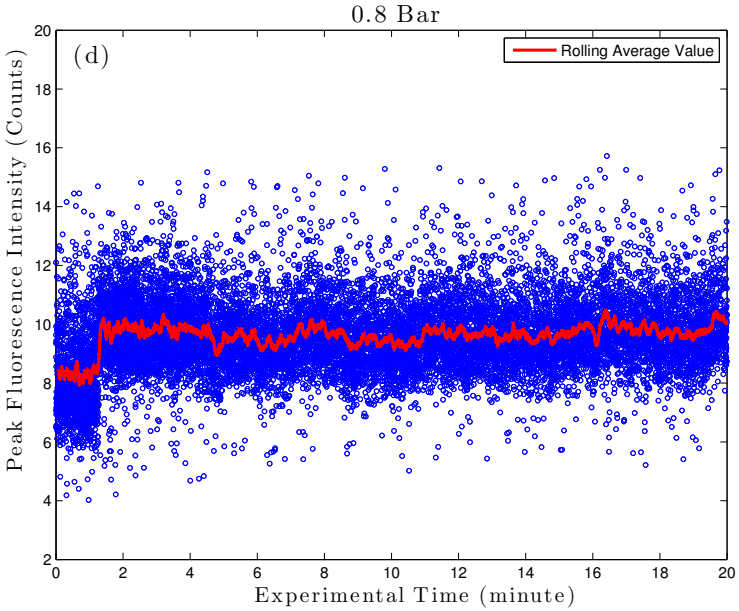

Figure 3.18: The homogeneity of peak fluorescence intensity during the course of the experiment at the BIFL acquisitions, operated at 0.8 bar of pressure.

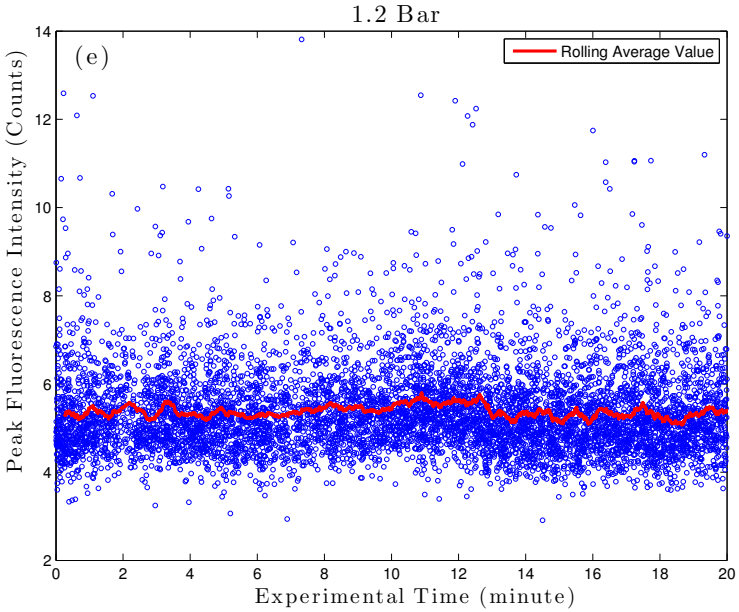

Figure 3.19: The homogeneity of peak fluorescence intensity during the course of the experiment at the BIFL acquisitions, operated at 1.2 bar of pressure.

At 0.1 bar Figure 3.15, the streamline underwent a clear shift at approximately 7^{th} minute of the acquisition, sufficiently suggesting that the trajectories are distinctively separated from the others. This bodes well with the suggestion that there is a large trajectory freedom under a little influence of velocity profile at low viscous force. The localised variations in each streamline cluster (depicted by the pseudo-random changes of fluorescent amplitude) were relatively large, and thus conform well to the Poisson nature of the relatively low number of events. At 0.2 bar Figure 3.16, switches took place approximately at the 2nd and 8th minute of the acquisition. The switching in this case is less drastic than the one at 0.1 bar. It is credible to deduce that the preferential streamlines are starting to aggregate around the probe volume at this point. At 0.5 bar Figure 3.17, the preferential routes were narrowed down to 2 clusters of streamlines flowing alongside one and another. The newly entered beads were continually injected into either track throughout the time course. Although judging by the data density, the track that the majority of the beads went through was closer to focal plane of the excitation beam. At 0.8 bar Figure 3.18, it is observed that the two streamlines were reduced into a single cluster and switched to another trajectory after a minute and remained well behaved for the duration of the experiment. The average increase in the peak intensity suggests that new streamline became closer to focal plane than previously. It was highlighted in the previous section that there was a drop in the analytical throughput due to the switching of streamline towards the central part of the channel. This can be observed in Figure 3.19 by the reduction of the data density comparing to the one at 0.8 bar. The relatively low peak intensity in this acquisition also provides a further explanation in the reduction of the throughput, as some portion of the total burst population may have been embedded in the background noise during the burst resolving process.

Typical Burst Characteristics

The most important aspect of BIFL lies within the ability to resolve the bursts at any flow rates. The information on the mean burst widths and intensities in the previous section will be used to find and display a burst from each data set

alongside its decay profile in this section in Figure 3.20 and Figure 3.21.

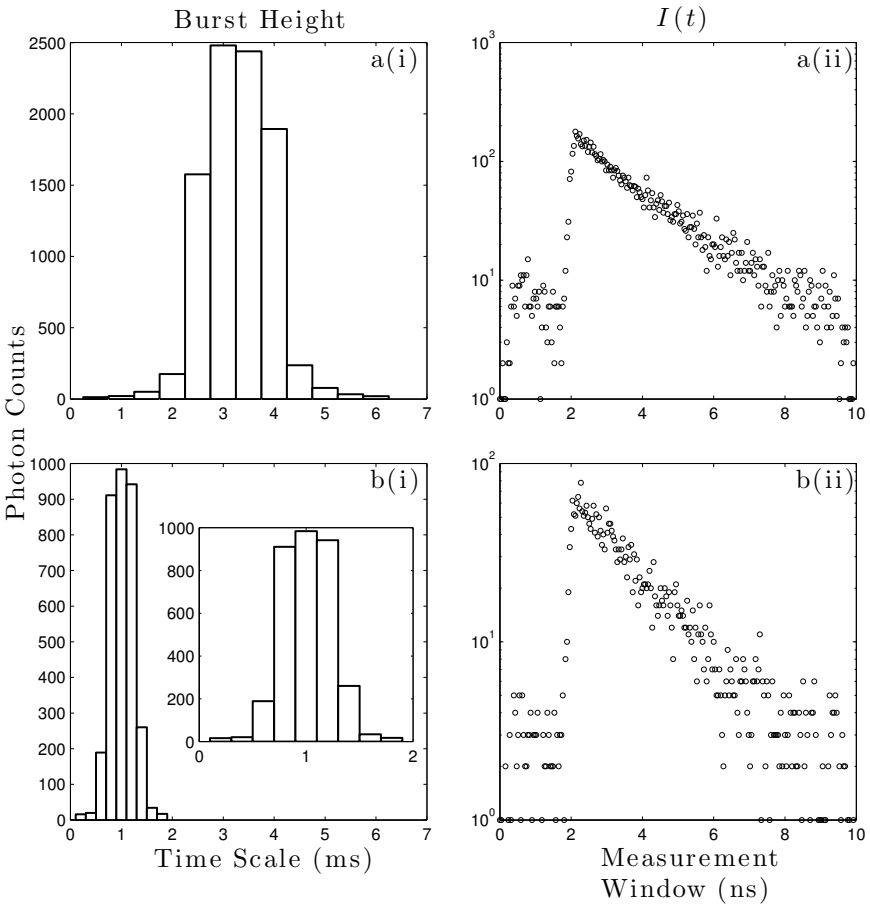

Figure 3.20: Typical burst characteristics of Type I beads with spot probe excitation. The histograms in the first column (i) represent the typical shape of the burst and the ones in the second column (ii) represent the intensity decay profile of the burst, where a and b represents the BIFL acquisitions at 0.1 and 0.2 bar of pumping pressure.

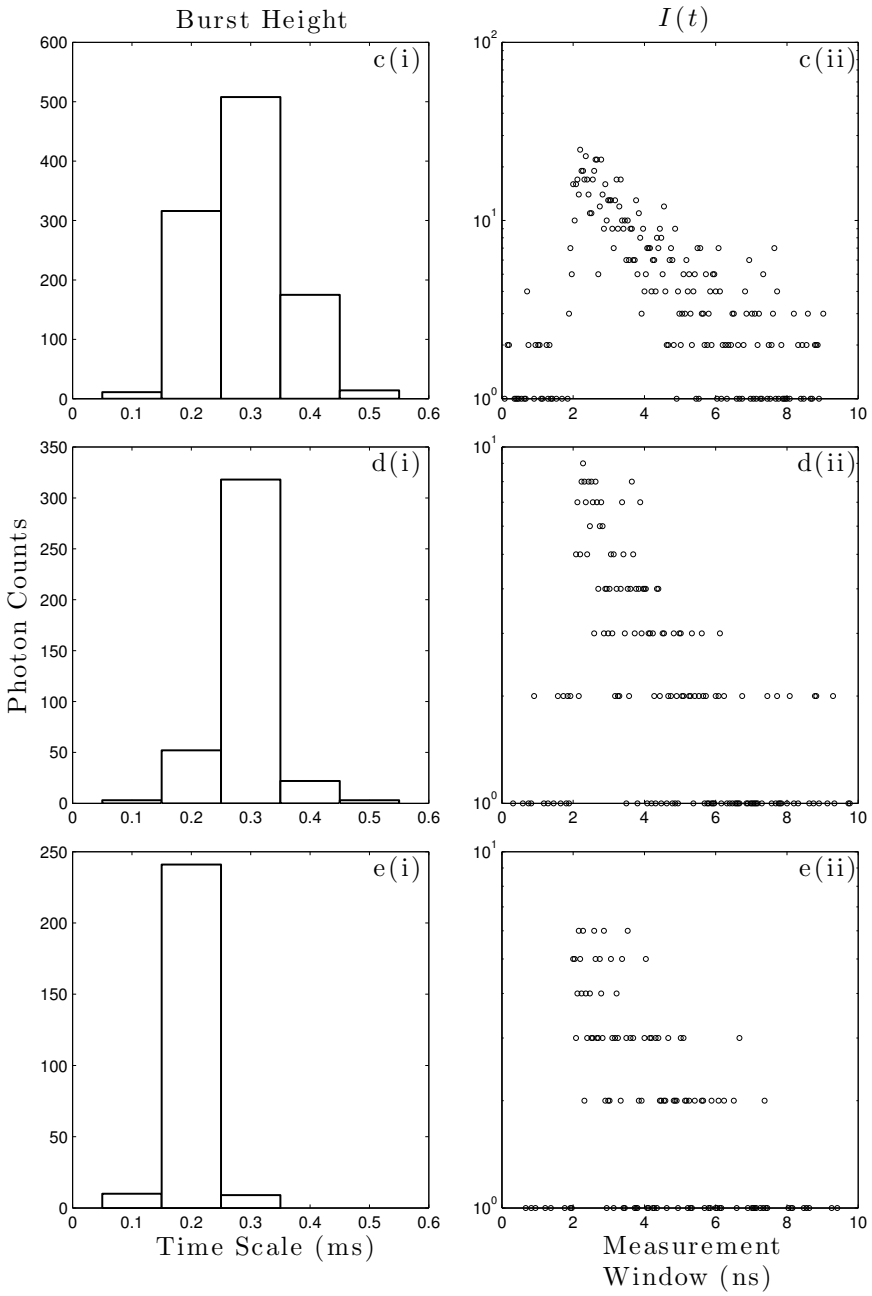

Figure 3.21: Typical burst characteristics of Type I beads with spot probe excitation. The histograms in the first column (i) represent the typical shape of the burst and the ones in the second column (ii) represent the intensity decay profile of the burst, where c, d, and e represents the BIFL acquisitions at 0.5, 0.8 and 1.2 bar of pumping pressure.

As expected, the reduction in the burst intensity and width were due to the gain in particle velocity with supply pressure. The average burst width of the beads was significantly shortened after 0.2 bar of pressure supply, and had to be plot on a different scale in Figure 3.21.

The signal-to-noise ratio (SNR) of the decay is given by $\sum_i \sqrt{n_i}$, where n_i is the number of photons detected in microtime bin i. SNR of fluorescence decays from each pumping pressure is summarised in Table 3.2.

Pumping Pressure (mbar)	SNR (1×10^3)
100	1.30
200	0.77
500	0.36
800	0.25
1200	0.1665

Table 3.2: The summary of the integrated SNR of Type I beads with spot probe excitation.

Burst profiles are (more or less) symmetrical, which is somewhat expected from a signal which is a convolution of the beam profile and the cross-section of a bead. The SNR dropped from 1.30×10^3 after 100 mbar of pressure and quickly deteriorate to approximately 170 at 1.2 bar of pressure. The significance of the SNR will be described in details in the next chapter. It is interesting to note that recent high profile work on flow cytometry has concentrated in recovering cell burst profiles in an attempt to obtain spatial or compartmentalisation data for protein markers [57].

Summary of Spot Probe Excitation

Overall, the data was well behaved. The only caveat to the spot excitation profile would be the switching of streamlines at high pumping pressure. Although the excitation beam could be re-positioned relative to the new streamlines after each

pressure adjustment, the systematic characterisation of the samples and automation of the system would be compromised.

The notable trade-off in the experiment was between the spatial reduction of a streamline distribution and the total photon collection per sample, at high flow rates. The homogeneity of burst characteristics from those flow rates would open door for other experiments such as high throughput particle counting and sizing, or monitoring of dye labelling efficiency, but fell short below this 1000 photons target (see subsection 2.5.3 in chapter 2).

It was observed that the microfluidic chip tends to be fully or partially clogged up at various parts of the channel over time, most notably around the inlet, T-junction and bends of the channel. The additional boundary layers introduced by these composites can still abrupt and influence the trajectory of the streamline even if the cluster size is reduced. Therefore it could force the samples away of the focal volume and reduce the range of operational pumping pressure even further.

The obvious proposal to tackle the issue would be to utilise a line probe across the channel. This would alleviate the need to re-position the probe to match any drifts in streamlines under any circumstances or for other sample types. Type I have behaved well so far, but this does not necessary guarantee the same outcomes from other sample types which have different mass. The line profile would also be suitable for detecting smaller particles, which would otherwise be difficult to detect with a spot probe due to the relative width and intensity of the channel.

3.2.2 Line Focus Excitation

This section will investigate the feasibility of a line focus across the microfluidic channel. The focus will be achieved by focusing one axis of the excitation beam profile with a cylindrical lens (f = 150 mm) before the first pair of relay optics in the instrument setup (see section 2.2 in chapter 2). The lens is mounted onto

a rotatable lens holder for adjustments of the line orientation. A consideration which needs to be taken on board is the implication of focal volume enlargement, as this would introduce a trade-off between the noise and the gain in analytical throughput with a more uniform excitation power. The attraction to this method lies within the ability to keep the pumping pressure relatively low to allow more photon collection per sample, irrespective to their streamlines.

The power of the beam is increased from the spot probe case to approximately 25 μW with an ND 1.6 filter due to the lower power density across the larger beam area.

Burst Parameter Characteristics Width and Integral Intensity

Burst width and integrated intensity of Type I beads excited by line excitation at 25 μW is summarised in Figure 3.22, Figure 3.23 and Figure 3.24, below.

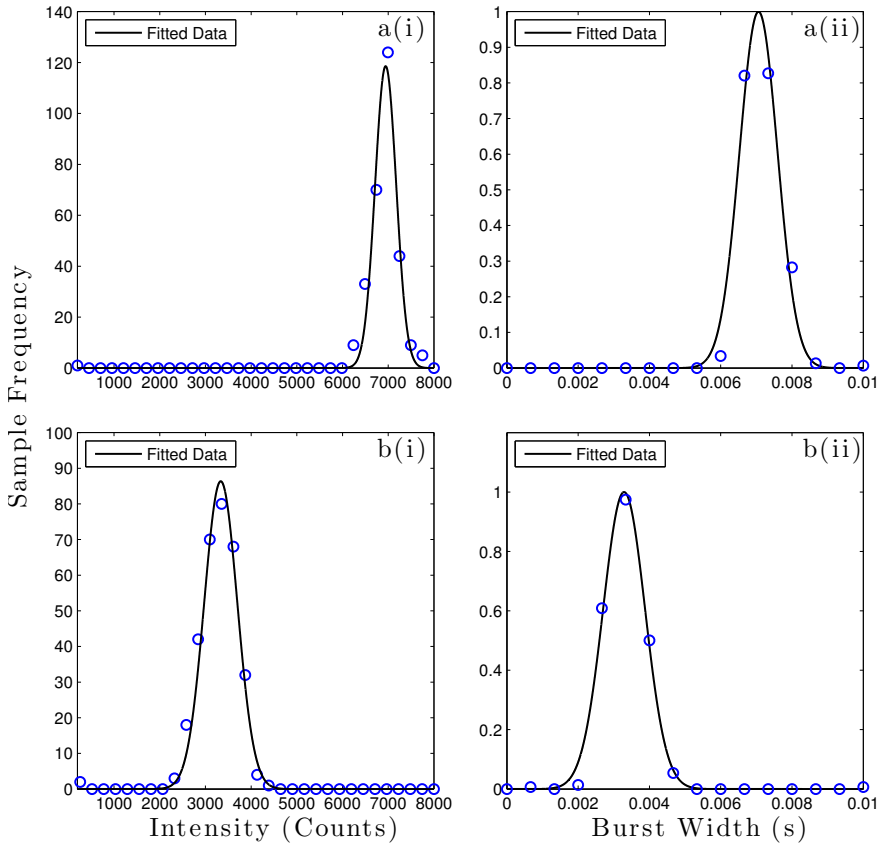

Figure 3.22: Histograms of integrated intensity (i) and burst width (ii) of Type I beads as a function of pumping pressure with line probe excitation, where a and b correspond to 0.2, and 0.5 bar of pumping pressure respectively.

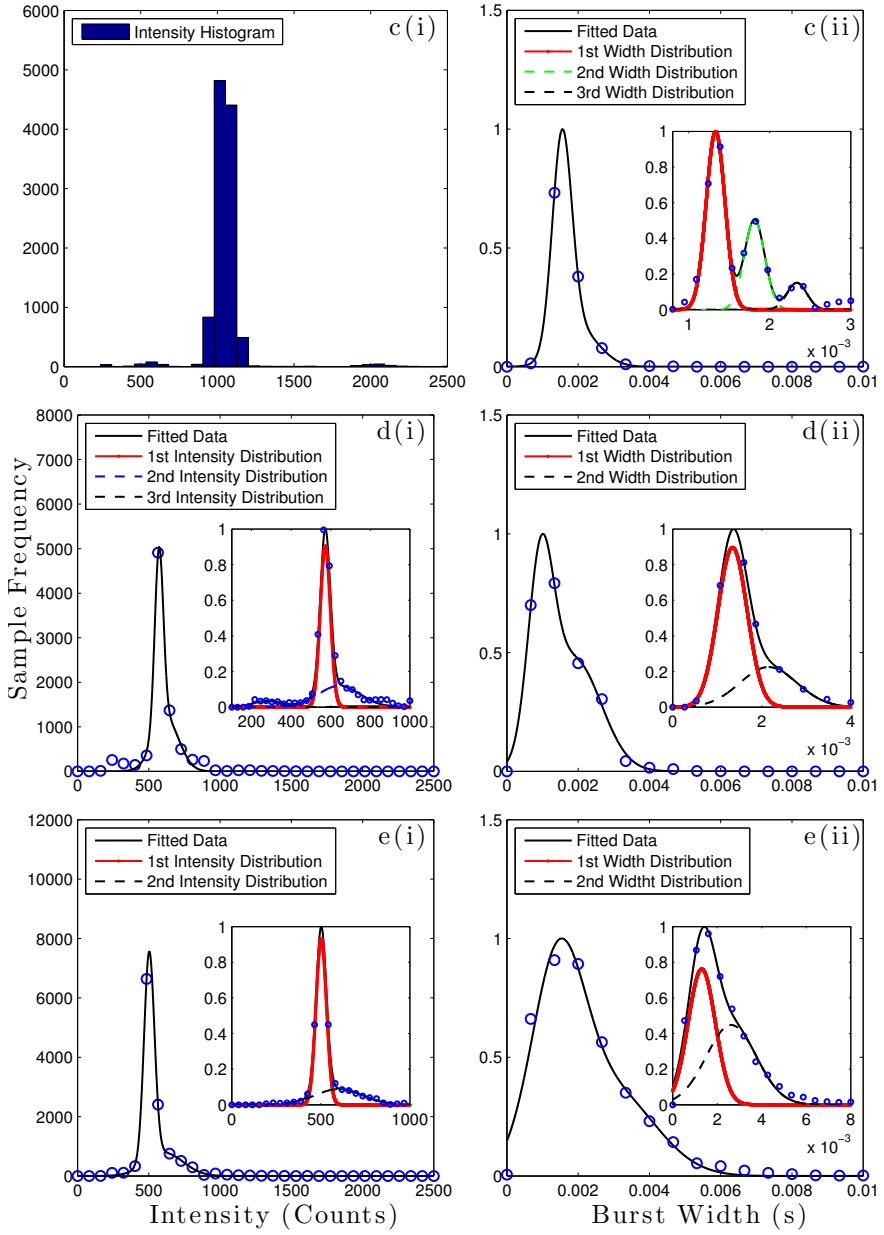

Figure 3.23: Histograms of integrated intensity (i) and burst width (ii) of Type I beads as a function of pumping pressure with line probe excitation, where c, d and e corresponds to 1.0, 1.5, and 1.8 bar of pumping pressure, respectively. Note c(i) was represented by an unfitted histogram as the features were difficult to observe with a dot plot around 600 and 2000 counts marks.

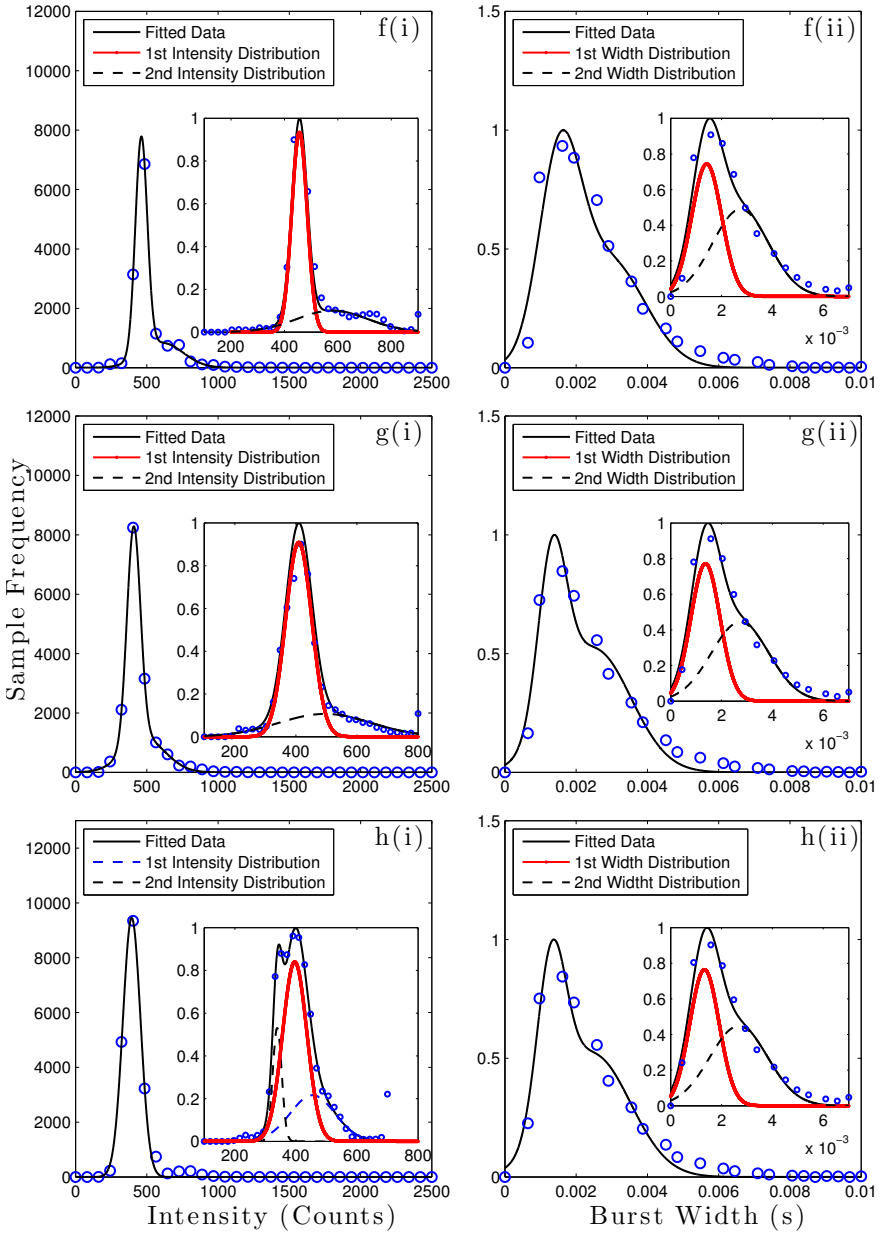

Figure 3.24: Histograms of integrated intensity (i) and burst width (ii) of Type I beads as a function of pumping pressure with line probe excitation, where f, g and h corresponds 2.0, 2.3 and 2.5 bar of pumping pressure, respectively.

Pumping Pressure (mbar)	Average Flow Rate ($nLmin^{-1}$)	Analytical Through-put (sample min^{-1})	Burst Width (ms)	Standard Deviation (ms)	Integral Intensity (Counts)	Standard Deviation (Counts)
200	0.020	5	7.061	0.7557	6944	328
500	0.044	5	3.289	0.8317	3335	512
1000	0.080	183	1.811	0.1775	945	76
1500	0.067	138	1.345	0.4649	572	43
1800	0.110	189	1.308	0.8650	502	52
2000	0.102	224	1.418	0.8327	456	41
2300	0.105	281	1.370	0.8105	409	60
2500	0.108	319	1.331	0.8151	339	20

Table 3.3: The summary of burst Intensity and width with line probe.

From Figure 3.22, Figure 3.23 and Figure 3.24 and Table 3.3, the line excitation was observed to give better behaved results than those of the spot probe due to reduced sensitivity to streamline switching (or rather that streamlines are detected with similar probabilities regardless of radial position). At low pressure (a(i) and b(i)), a clear cluster of streamlines was observed through a relatively even intensity distribution. The width of the intensity distribution slowly begins to increase when the pressure was increased from 0.2 to 0.5 bar. At 1.0 bar, a sign of streamline switching began to emerge, as there are developments of small distributions around the 600 and 2000 counts marks. The interesting features of this acquisition are the approximate doubling of the median intensities in each distribution. It can be assumed that the streamlines on either side of the major streamline cluster are approximately twice as slow and twice as fast respectively. At 1.5 bar, the result shows a merging between the three distributions, indicating that newly injected samples began to migrate from cluster-to-cluster of streamlines. At 1.8 bar, the streamlines seem to merge into two even distributions, where one representing a cluster of streamlines centred somewhere between the inside curve and the centre of the channel and another shifting towards the lower intensity values (or faster streamline) near the centre of the channel. As usual,

this is assumed on the basis that the speed of streamline towards the centre is faster than those locating near the boundary layer. Interestingly, from f(i) - h(i), the streamline distribution seems to behave in a similar way to those of d(i) - f(i), where plateau of small intensities (which consists of a broad range intensity values) were formed, and then collapse into two distinctive distributions, before breaking off into two or more intensity distributions again. This possibly suggests that the streamline distribution is undergoing switching again (either towards the more central position or outside of the channel). Remember that Type I beads tend to flow towards the inner side of the bend at low flow pressure (see subsection 3.1.4 or the footage online at `http://youtu.be/UsVKtx4K-yo`).

The burst width results portray the behaviour of the intensity plots accurately in this experiment. At low pressure a(ii) and b(ii), the burst width distributions were relatively even, which equally reflected in the behaviour of the corresponding intensity plots in a(i) and b(i). At 1.0 bar, where 3 streamlines had developed, the burst width distribution showed 3 clear burst width clusters. The number of samples in each cluster was progressively reduced with longer burst width. At higher pressure (>1.0 bar; (d(ii) to h(ii)), the burst width distributions broadly consist of two populations, where one is centred around 1.5 - 1.8 ms and another around 3 ms. This provides strong evidence on the flow speed in the boundary layer, which should be twice as slow as at the centre of the channel.

Integrated Intensity as a function of speed

The average integrated intensity of the data from each pumping pressure is plotted as a function of the particle speed is shown in Figure 3.25.

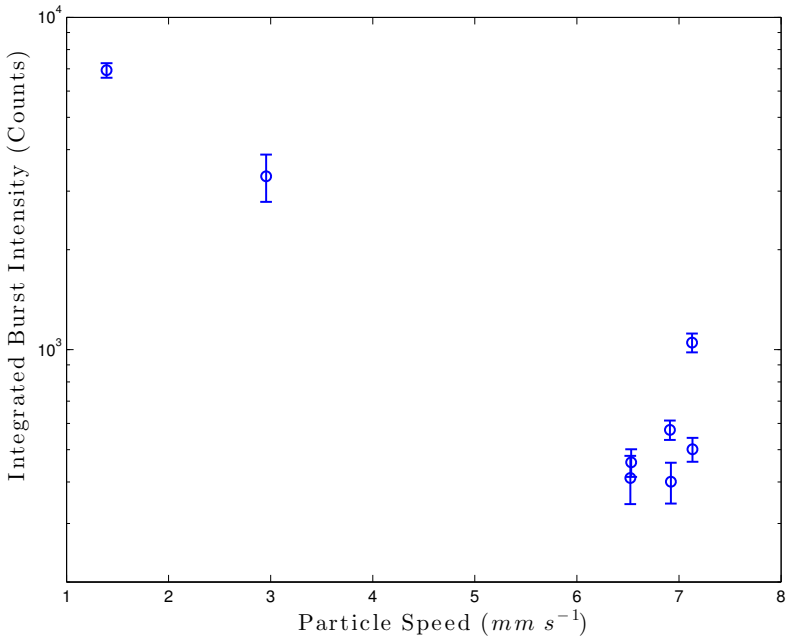

Figure 3.25: Integrated intensity of type A beads as a function of the travelling speed.

From Figure 3.25, the particle speeds at the higher end of pressure supply were prone some to errors. Notice at higher pressure, the speed of the particle increased markedly. This possibly represents the shift of streamlines from the boundary to the faster centre layers of the channel. The average burst intensity with respect to the particle speed is observed to be strongly and negatively correlated in this case. The burst widths were likely to be the product of the full beam excitation, and so would provide a more accurate representation of the particle speed in flow.

Typical Burst Characteristics

The burst statistics from the previous section were used work out the typical burst characteristics (burst shape) of the data acquired by the line focus excitation, are shown in Figure 3.26, Figure 3.27 and Figure 3.28 below. The typical SNR of bursts for each pumping pressure is then summarised in Table 3.4.

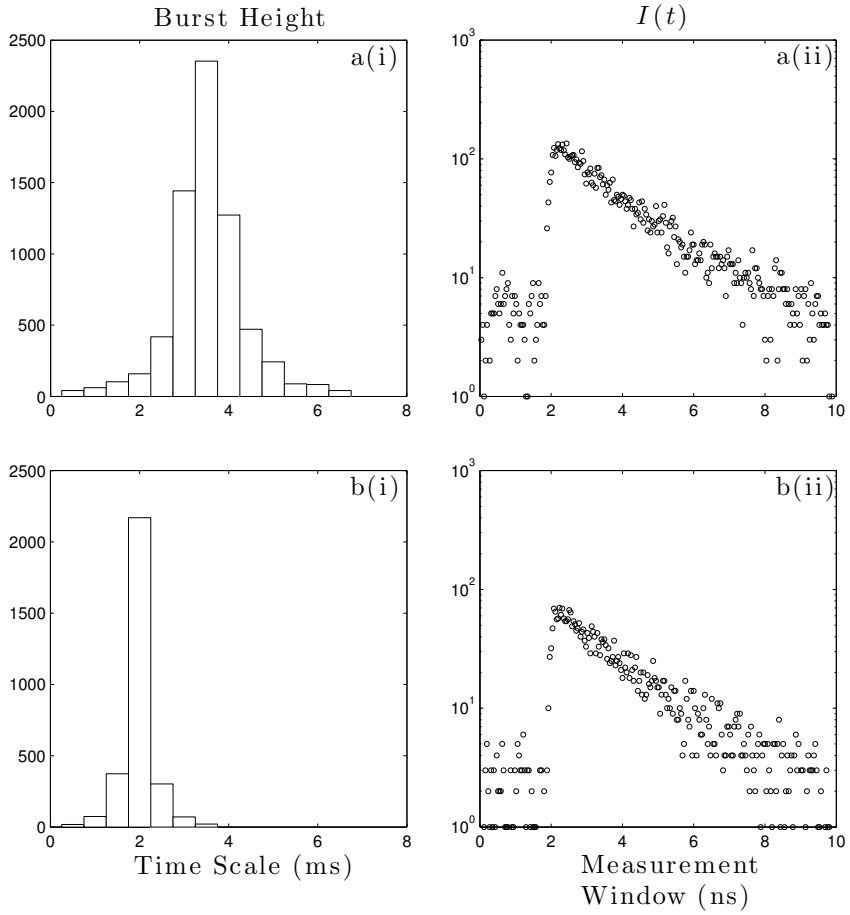

Figure 3.26: Typical burst characteristics of Type I beads with the line focus excitation. The histograms in the first column (i) represent the typical shape of the burst and the ones in the second column (ii) represent the intensity decay profile of the burst, where a and b represent the BIFL acquisitions at 0.2 and 0.5 bar of pumping pressure.

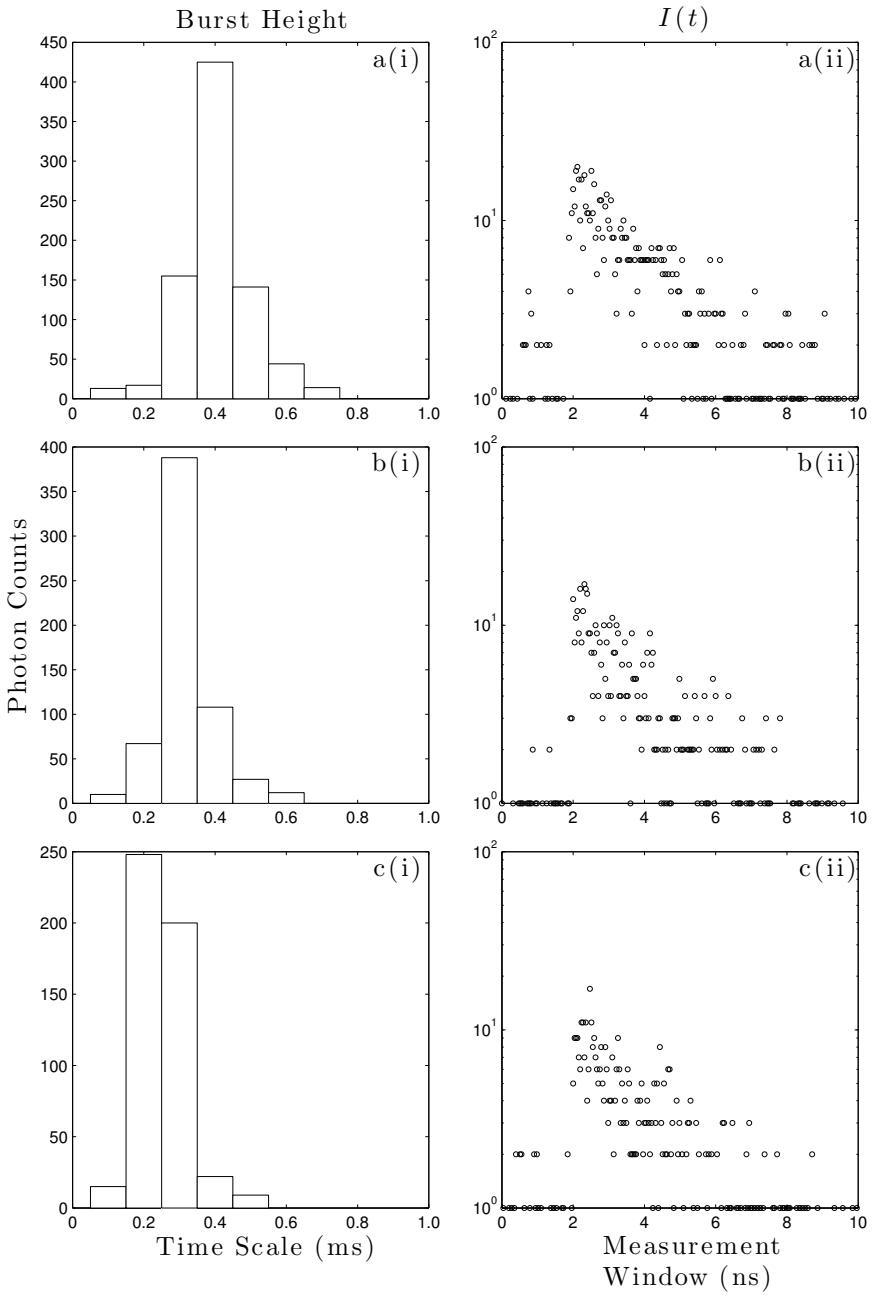

Figure 3.27: Typical burst characteristics of Type I beads with the line focus excitation The histograms in the first column (i) represent the typical shape of the burst and the ones in the second column (ii) represent the intensity decay profile of the burst, where c, d and e represent the BIFL acquisitions at 1.0, 1.5 and 1.8 bar of pumping pressure. Note the scale of the burst height in the first column is different from the one in Figure 3.26.

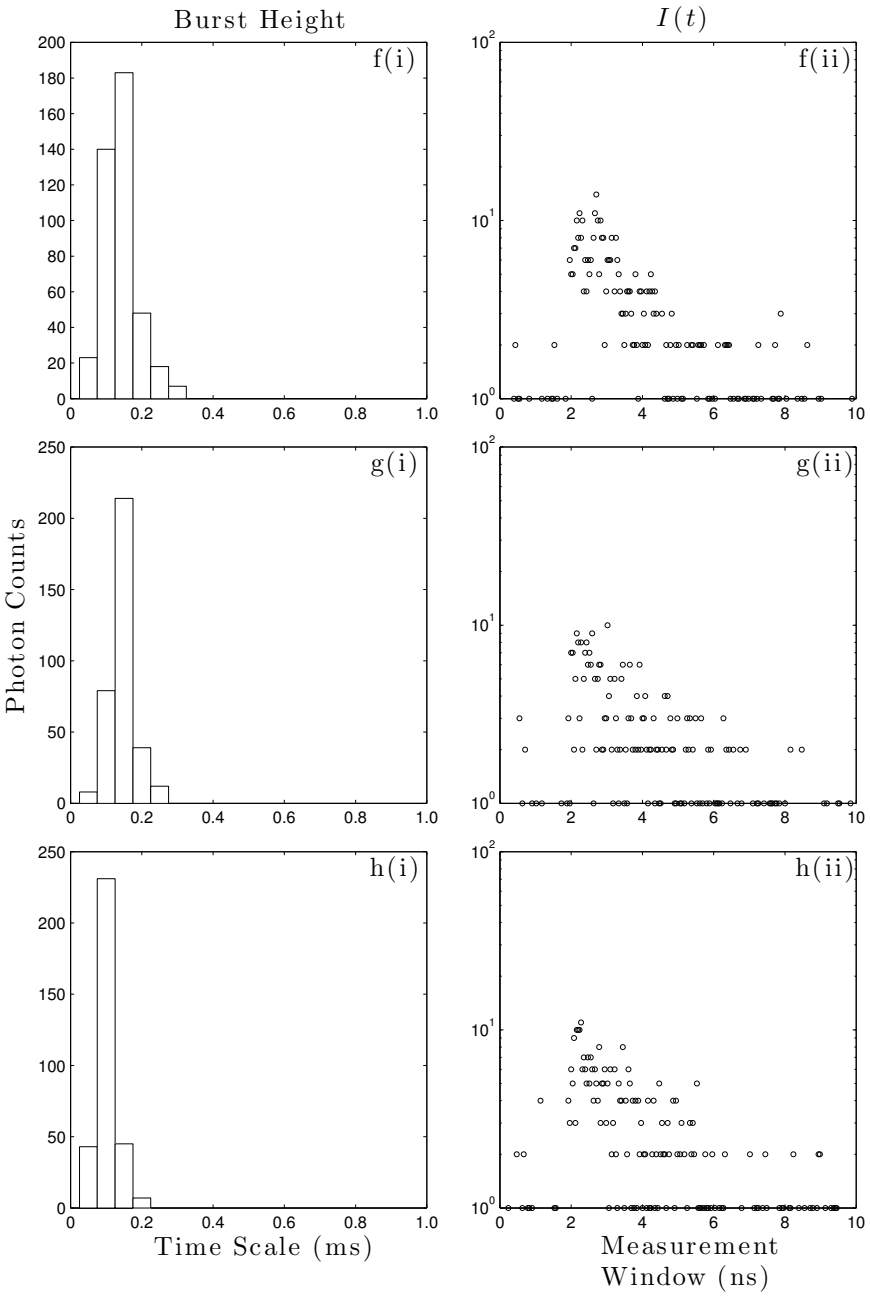

Figure 3.28: Typical burst characteristics of Type I beads with the line focus excitation The histograms in the first column (i) represent the typical shape of the burst and the ones in the second column (ii) represent the intensity decay profile of the burst, where f, g and h represent the BIFL acquisitions at 2.0, 2.3 and 2.5 bar of pumping pressure. Note the scale of the burst height in the first column is different from the one in Figure 3.26.

Pumping Pressure (mbar)	SNR (1×10^3)
200	1.12
500	0.58
1000	0.35
1500	0.30
1800	0.25
2000	0.38
2300	0.23
2500	0.21

Table 3.4: The summary of the integrated SNR of Type I beads with spot probe excitation.

The data in the first column shows that the average burst shape is progressively getting smaller from Figure 3.26 (a) to Figure 3.28 (h). In Figure 3.26, the burst height saw a relatively slow change over the increasing flow rate, from approximately 2.3×10^3 counts to 200 counts, The burst widths can be observed to have curtailed by a similar extent (refer to Table 3.3 for more details). Figure 3.26 shows a decrease from approximately 3.5 to 2 ms. Figure 3.27 shows a decrease from 0.4 to 0.3 and 0.2 ms. Most of the burst width characteristics in Figure 3.28 shows the burst width to be centring around 0.1 ms

There is a big improvement on the SNR compares to the spot focus excitation in Table 3.2. However the laser power was increased from 1 μW to 25 μW in this case in an attempt to increase the power density across a larger beam area, and so it is likely to pay some contributions to the improvement. In all fairness, the increase in particle speed with higher operational pumping pressure show signs of stagnation in Figure 3.25 after the particles reached the average travelling speed of approximately 7 mms^{-1}. This possibly suggests that the flow operation is now operated in the more exponential rather than linear regime. Whether the streamline is going change, or become hydrodynamically focussed to the centre of the channel in this flow regime, the line excitation does hold up to the change very well. This is supported by the increase in the analytical throughput (see

Table 3.3) and the steady SNR around pumping pressure between 1.8 to 2.5 bar (see Table 3.4)).

In the interest of brevity, 0.5 bar was chosen as an operational pumping pressure to directly compare the typical burst characteristics from the two excitation types, which are shown in Figure 3.29.

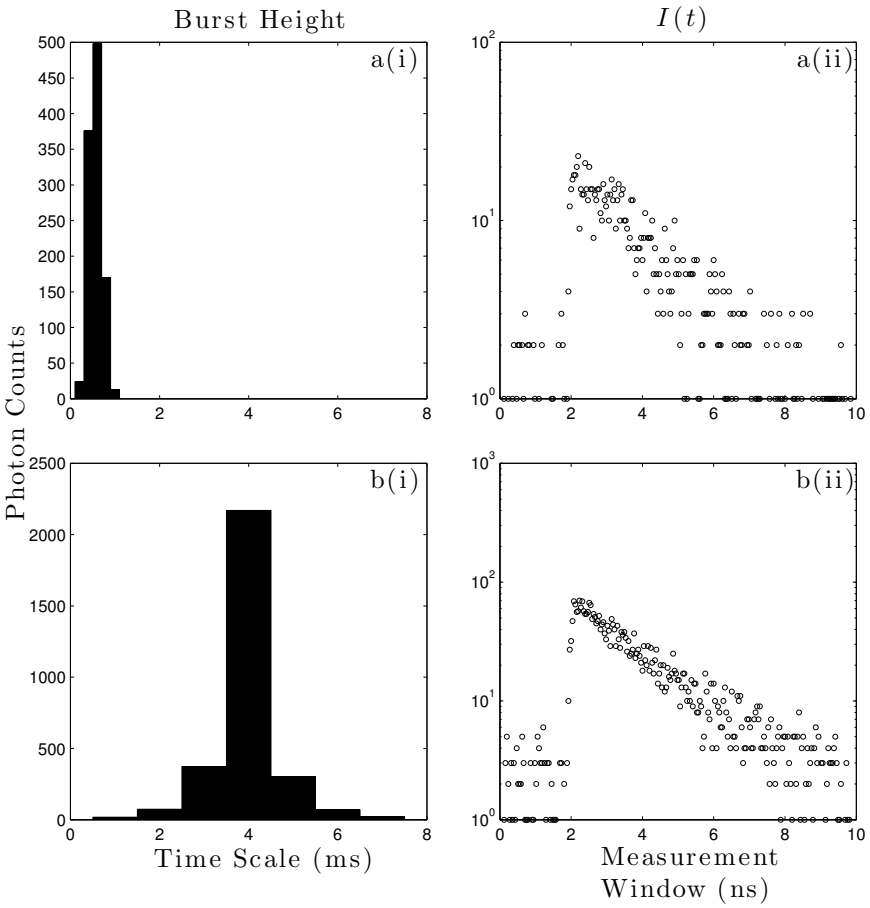

Figure 3.29: Typical burst characteristics of Type I beads with spot and line probe excitation The histograms in the first column (i) represent the typical shape of the burst and the ones in the second column (ii) represent the intensity decay profile of the burst, where a and b represent the BIFL acquisitions from the spot and line excitation, respectively.

The fluorescence data shows a well-defined decay shape over a large range of pumping pressure. It is possible that the increase in power would have some contribution in the improvement, but more importantly, the number of cleanly excited samples (full beam irradiation) was significantly increased as depicted by the reduction of burst width populations to a single discrete value.

Summary of Line Probe Excitation

The validity and merit of the line focus excitation has been very positive. Shift in streamlines could be observed in the burst intensity histograms very clearly. This illustrated the trajectory-dependent speed of flow particles across the cross-section of the channel, as discussed in the theoretical section.

Although a discussion on the lensing effect from the inner wall of the channel has not been mentioned, the possibility or its effect on the outcome is acknowledged. This is because it could prevent the excitation beam from completely intersecting the channel. The only way to observing the line profile in the channel would be to set up another wide-field microscope on the other side of the chip. However this would be difficult, as the current microscope is inverted. The pair of the scanning mirrors and its associated optics in the de-scanned path is also essential for the positioning of the excitation beam in the channel adding another widefield detection along the path to observe the line focus profile would be time consuming and may not justify the need for a system re-configuration which has been complexly co-aligned for the existing widefield and fluorescence lifetime imaging modes.

The results have been very informative. The fact that the switching of streamline clusters across a large range of pumping pressure could be observed, strongly indicated that the line focus excitation sufficiently covered the breadth of the channel.

3.2.3 Small Particle Detection

The screening ability of the line probe on small particles will be tested by Type III beads ($\varnothing$= 2 μm). The material and dye of the beads are the identical to those of Type I ($\varnothing$= 10 μm). Therefore the number of fluorescent molecules contained within a given particle will be proportionally reduced accordingly to the size. The bead solution was serially diluted to obtain a similar concentration as the previous investigation (16,000 beads per ml).

The pumping pressure was kept relatively low (<0.5 bar) for the system to collect a sufficient amount of photons per sample. Figure 3.30 shows a sample footage of the beads in flow. From the image sequence, it could be observed that multiple beads were sometimes travelling through the focal volume. However there were only a few instances of this in the video attached to the caption of Figure 3.30. and so further dilutions were not attempted in light for keeping the same sample concentration to one of Type I beads, for comparative purposes. The sample dilution process was very extensive, due to the high number of beads contained in solution.

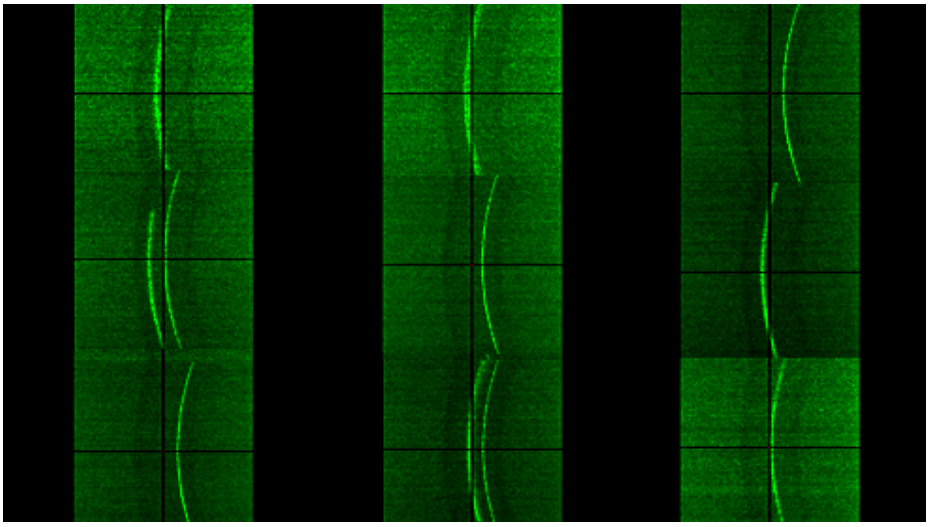

Figure 3.30: A random video image sequence of the Type III beads at 100 mb of pressure. The spatial distribution of the trajectories are spreaded out widely within the channel, but the pumping pressure in the illustrated video is less compared to the previous videos. A full video footage can be found at `http://youtu.be/HjqO4kdu6jQ`.

Burst Chracteristics: Burst Width and Integral Intensity From Line Excitation

The burst characteristics of Type III beads are summarised in Figure 3.31 and Figure 3.32.

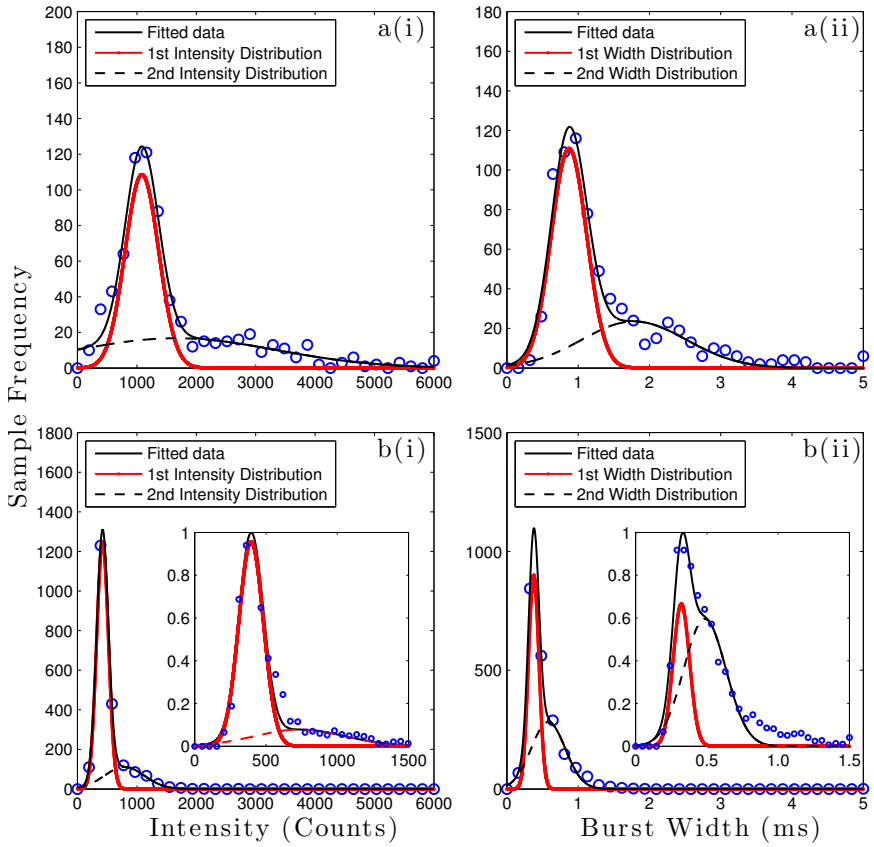

Figure 3.31: Histograms of integrated intensity (i) and burst width (ii) of Type III beads as a function of pumping pressure, where a and b corresponds to 0.05 and 0.1 bar of pumping pressure, respectively.

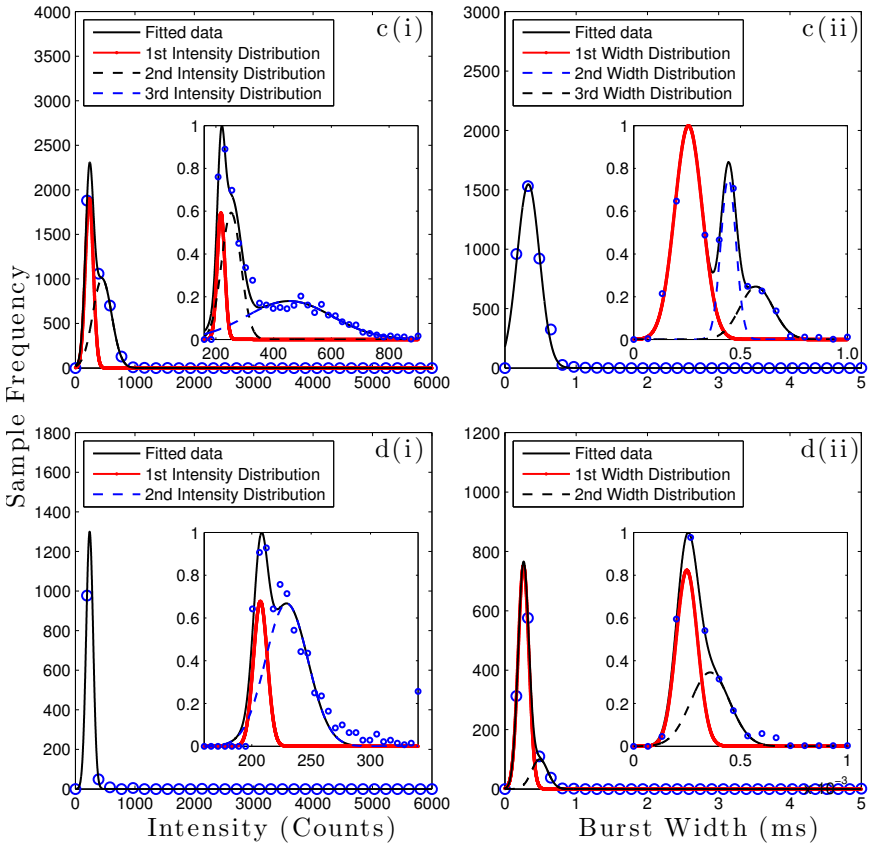

Figure 3.32: Histograms of integrated intensity (i) and burst width (ii) of Type III beads as a function of pumping pressure, where c and d corresponds to 0.2 and 0.5 bar of pumping pressure, respectively.

Pumping Pressure (mbar)	Average Flow Rate ($nLmin^{-1}$)	Analytical Through-put (sample min^{-1})	Burst Width (ms)	Standard Deviation (ms)	Integral Intensity (Counts)	Standard Deviation (Counts)
50	1.653	12	0.871	0.035	1084	399
100	4.486	35	0.321	0.081	396	122
200	5.603	63	0.257	0.092	217	18
500	5.783	117	0.249	0.071	229	22

Table 3.5: The summary of burst Intensity and width of Type III beads with line probe.

By and large, Type III beads also behaved similarly to the Type I. The only exception is the case at 50 mbar (0.005% of the total pumping pressure). There seems to be a strong evidence of simultaneous detection of closely spaced samples, from the in- and out-of-excitation planes, in the broadness of the secondary burst intensity and width distributions. It is very unrealistic for a fraction of the secondary width distribution of Type III beads at 50 mbar to have the same residence time as most of Type I beads, at 200 mbar (Figure 3.22 b(ii)). Although there is a 4-time reduction in pressure in this experiment (contributed to the increasing of burst width), Type III beads are smaller than Type I by a factor of 5 (contributed to the decreasing of burst width). Furthermore, Type III beads are smaller (since they have a fraction of the volume of the Type I); they can enter the fluidic chip very easily without clogging or fouling the input. This allowed more samples to enter the system at a minute pumping pressure at several trajectory-dependent speeds (as illustrated in the video). It is possible to deduce that the sample solution is under-diluted, and is especially obvious when the beads are travelling at a near diffusion rate (detection in the boundary and centre layers). Without a strong formation of streamlines, the inter-burst time needs to be extended to minimise the probability of multiple bead detection.

In short summary, only a significant difference in the particle velocity between 50 and 100 bar of pumping pressure was observed. This indicates that a terminal

velocity is reached rapidly for the Type III beads. Initially, the force transferred to the particle by the fluid must be greater than the viscous drag. When these forces are balanced a terminal velocity will be reached. This appears to occur at much lower pressure for the Type III beads compared to the Type I. This is to be expected since the volume of the Type III is a factor of 100 smaller than the Type I.

Integral Intensity as a function of speed

Figure 3.33 shows the integrated intensity of Type III beads as a function of particle velocity. Errors are generally large and the integrated intensity decreases at a low proportion at the highest pressure. It is possible that once the inter burst time is shortened, multiple beads in the preferential streamline distribution are likely to be detected simultaneously.

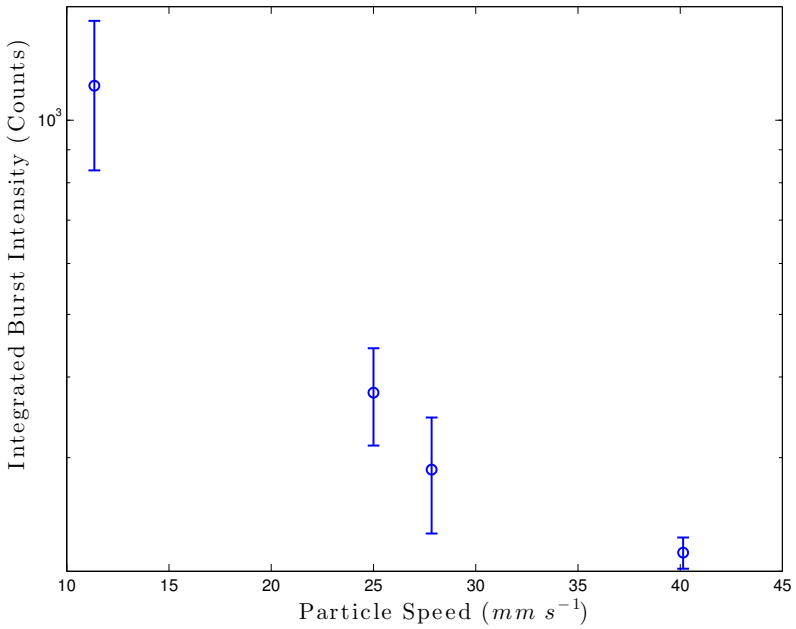

Figure 3.33: Integrated intensity of Type III beads as a function of the particle velocity.

Typical Burst Characteristics for Type III Beads With Line Focus

The typical burst characteristics of Type III beads are shown in Figure 3.34 and Figure 3.35.

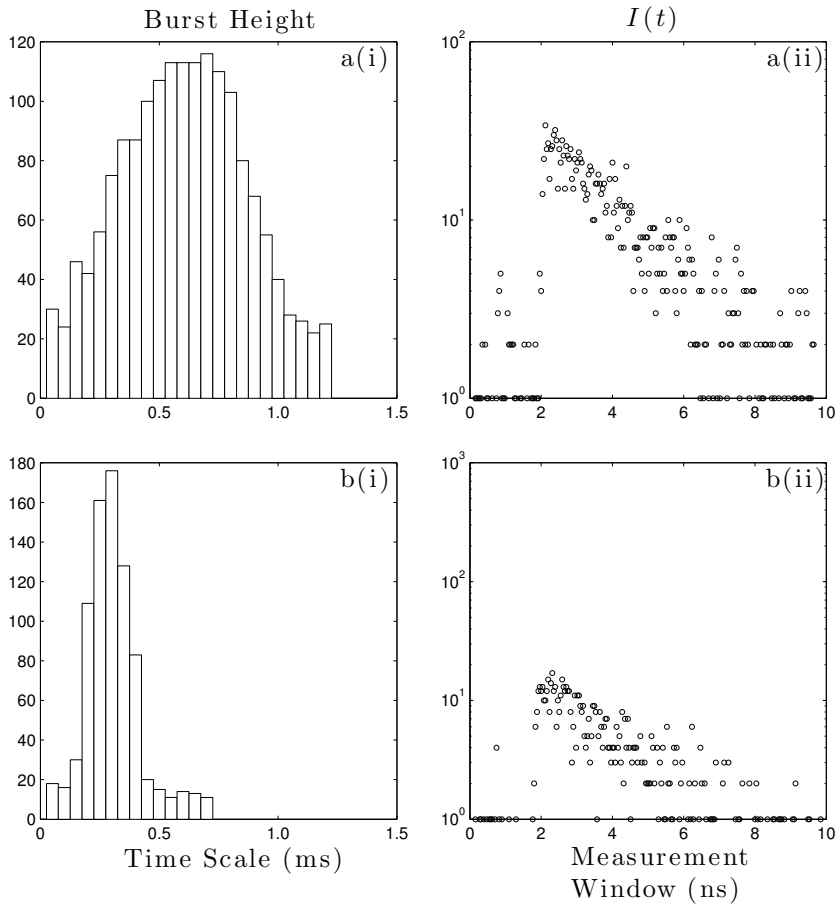

Figure 3.34: Typical burst characteristics of Type III beads. The histograms in the first column (i) represent the typical shape of the burst and the ones in the second column (ii) represent the intensity decay profile of the burst, where a and d represents the BIFL acquisitions at 0.05 and 0.1 bar of pumping pressure respectively.

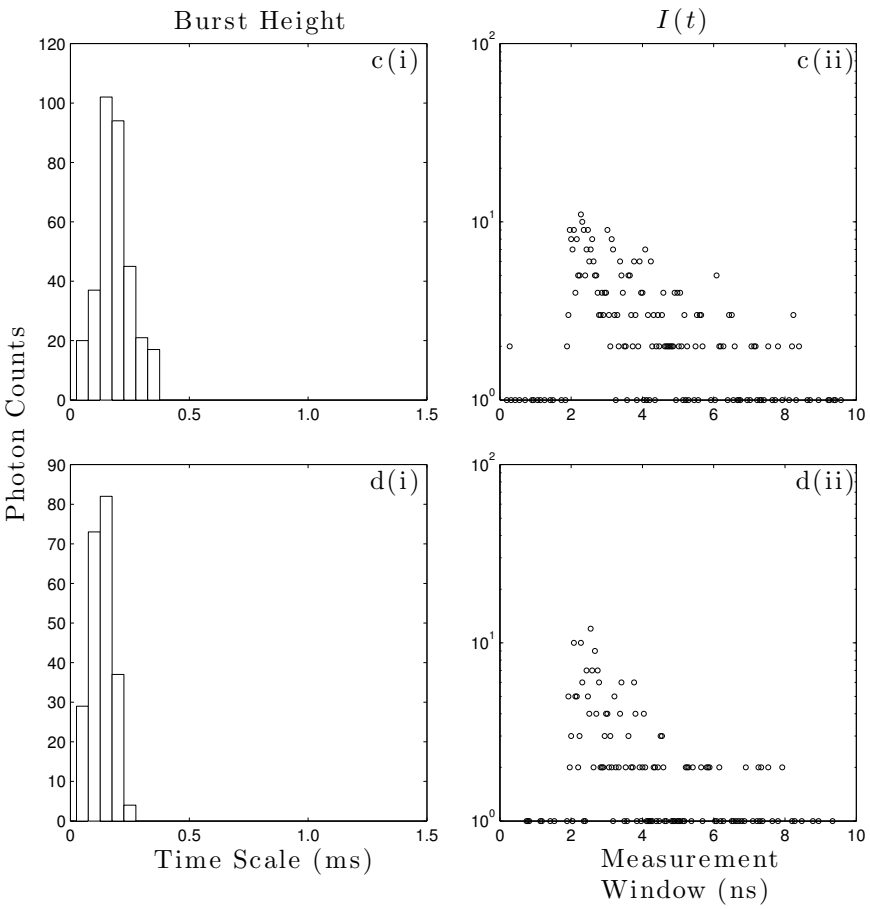

Figure 3.35: Typical burst characteristics of Type III beads. The histograms in the first column (i) represent the typical shape of the burst and the ones in the second column (ii) represent the intensity decay profile of the burst.where c and d represents the BIFL acquisitions at 0.2 and 0.5 bar of pumping pressure respectively.

Pumping Pressure (mbar)	SNR
50	442
100	240
200	151
500	142

Table 3.6: The summary of the SNR of Type I beads with spot probe excitation.

Typical bursts are well behaved on the sub millisecond regime. The bursts are progressively shortened, but the outline of the fluorescence decay can still be observed at 0.5 bar. From Table 3.6, it could be seen that the SNR of the beads is much lower compared to the ones of Type I beads in subsection 3.2.2.

Summary of Small Particle Detection

The line focus excitation was able to sufficiently detect samples which are 5 times smaller than typical eukaryotic cells. Despite being limited to a low operational range of pumping pressure, the fact that fluorescence signals of Type III beads showed similar SNR to those acquired from Type I beads at more than 0.5 bar of pumping pressure (see Table 3.4), is clearly a positive outcome. This opens a possibility for more demanding detection such as T-cells ($\varnothing$= 5 - 10 microns) in the future.

The typical burst width of Type III beads is less than 1 ms, with an exception of the lowest pumping pressure. It is possible to speculate at this point that it may be sufficient for the system to distinguish Type III from Type I beads on the basis of burst widths in the case of mixed bead investigation (see subsection 3.2.4).

3.2.4 Particle Sizing

The results from the previous section demonstrated the probing ability in detecting sub-millisecond residence time of small particles with good photon population at low flow rates. This realistically gave rise to a possibility of particle sizing in

this large channel environment. For this investigation, a 1 to 1 mixture of Type I and III beads will be used to validate the concept. The mixture was diluted with de-ionised water by 10-fold[6] to attempt in increasing the inter-burst time of the samples.

Contour Analysis of Burst Width and Integral Intensity

Figure 3.36 is a density plot of particle detections with a mixed Type I and III bead solutions, at 0.1, 0.2, 0.35, 0.5 and 0.8 bar of pumping pressure, respectively

[6]1ml of Type I + 1ml of Type III+ 8ml of de-ionized water

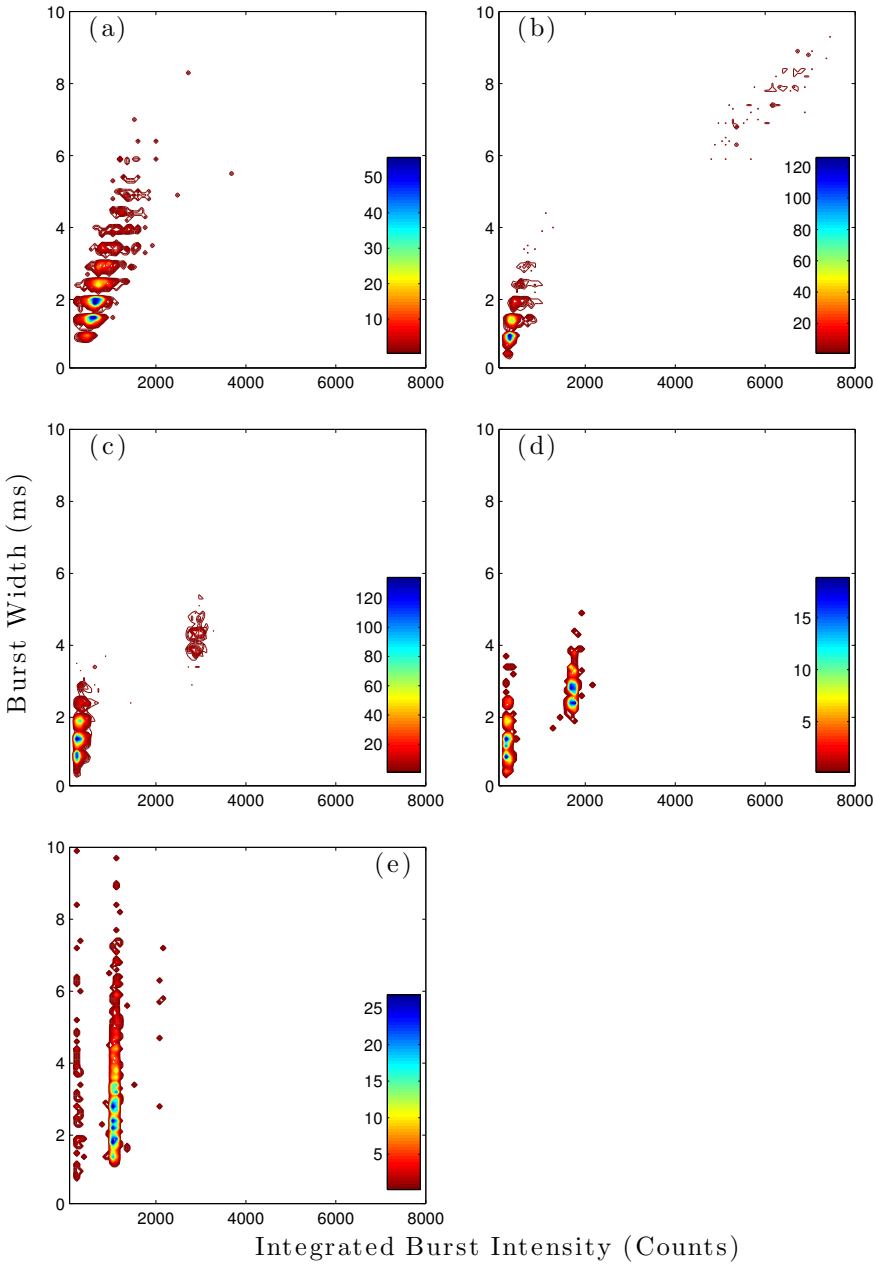

Figure 3.36: Typical burst characteristics of Type III beads. The histograms in the first column (i) represent the typical shape of the burst and the ones in the second column (ii) represent the intensity decay profile of the burst.where c and d represents the BIFL acquisitions at 0.2 and 0.5 bar of pumping pressure respectively.

There was evidence of oversampling of burst width histogram data through segmentation of contours in the burst width axis, as the data from each pumping pressure were computed on the same time scale. In Figure 3.36 (a), only a single cluster of beads is observed when the solution is pumped at low pressure which, based on data from section 3.2.3 almost certainly consists of only Type III beads. This indicates that at low pressure there is a differential in the loading probability for the beads into the microfluidic chip which may be due to number density or the differential buoyancy of the beads. In Figure 3.36 (b) it can be speculated that the two clusters of data correspond to two different bead types, where Type III beads lie within the cluster close to the origin between 0-4ms burst width and <1000 photons per burst, and Type I beads dispersed around 6000 photons per burst and with a burst width in the range 6–10 ms. With increasing pump pressure a decrease in burst width and integrated intensity was observed for both bead types, which is consistent with data in the previous sections. At 800 mbar, an anomalous behaviour is evident since, whilst there are distinct differences in the intensity of the two bead types (certainly assuming that the two observed populations are from the two bead types), there is a significant distribution in the values for burst width for the Type III beads (cluster closest to the y axis).

The increase in throughput (as dictate by the size of the clusters) of the heavy particles at higher pumping pressure demonstrates the differences in sample buoyancies in solution very well. At 500 mbar, the burst width distribution of Type I beads (as dictated by the length of the contour along the burst width axis) begins to lengthen again. At this point, the average intensity of Type III beads is already significantly reduced to below a few hundreds counts. A large portion of Type III bead population could either be diminished and becomes embedded in the noise or more realistically were co-detected with Type I beads which resulted in anomalously lengthy residence time distributions in both bead populations. The same argument is also hold true for the data behaviour at 800 mbar in (e). However, clear detection between beads of Type I or III could be undertaken purely on the basis of intensity since there is at least a 10-fold difference in intensity between the clusters in Figure 3.36 (e).

The burst characteristic information from Figure 3.36 will be explicitly summarised in Figure 3.37 to Figure 3.42 below. Figure 3.37 and Figure 3.38 shows the integrated intensity of what was concluded to be Type I beads, while Figure 3.39 shows the burst width distribution of the bead type. Similarly, Figure 3.40 and Figure 3.41 represent the integrated intensity, and Figure 3.42 shows the burst width distribution of Type III beads, respectively.

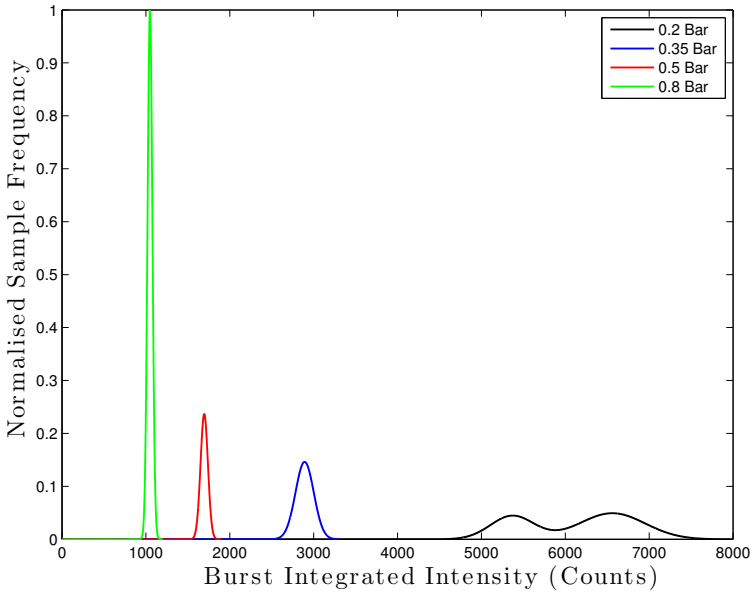

Figure 3.37: Explicit burst integrated intensity plot of Type I beads.

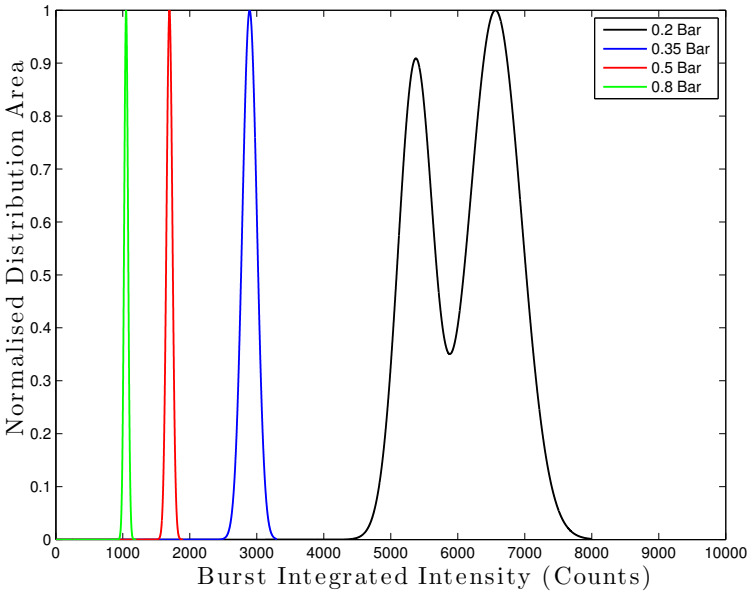

Figure 3.38: Explicit burst integrated intensity plot of Type I beads (normalised area distribution).

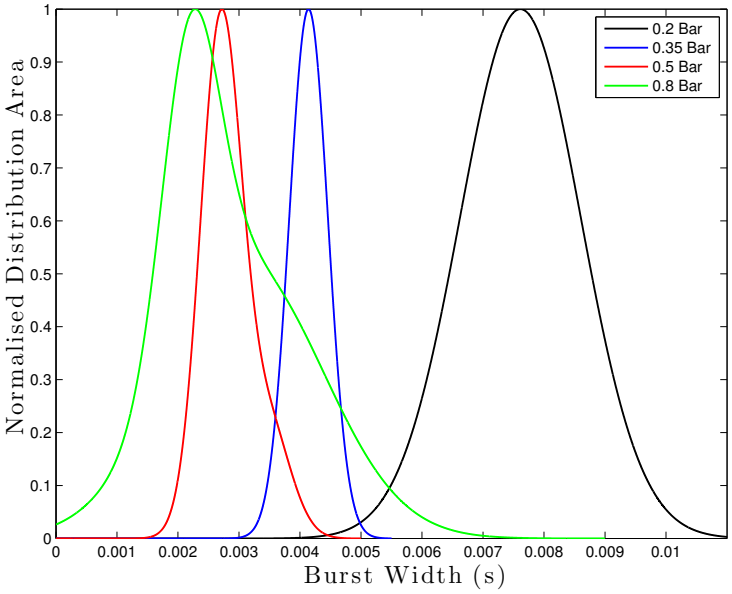

Figure 3.39: Explicit burst width plot of Type I beads (normalised area distribution).

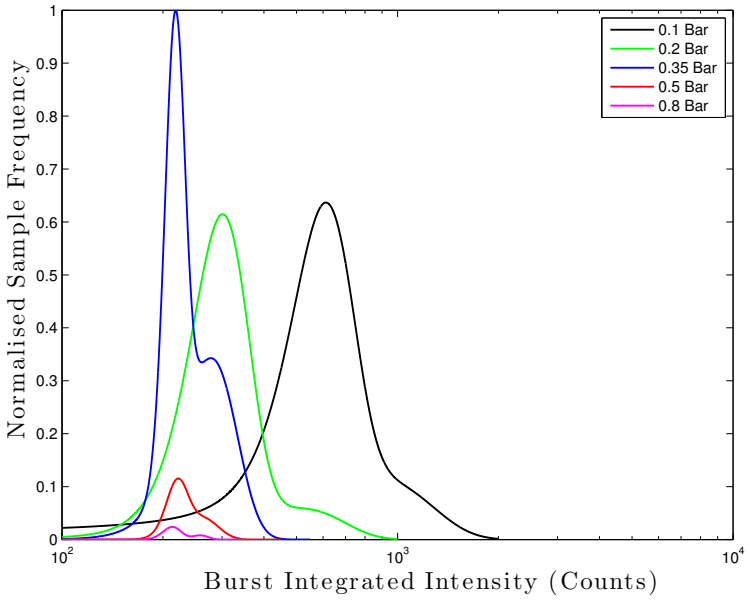

Figure 3.40: Explicit burst integrated intensity plot of Type III beads.

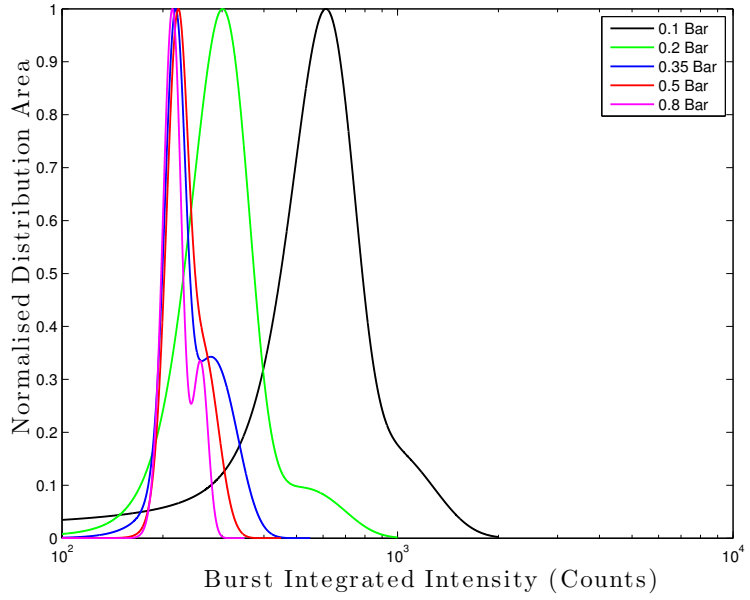

Figure 3.41: Explicit burst integrated intensity plot of Type III beads (normalised area distribution).

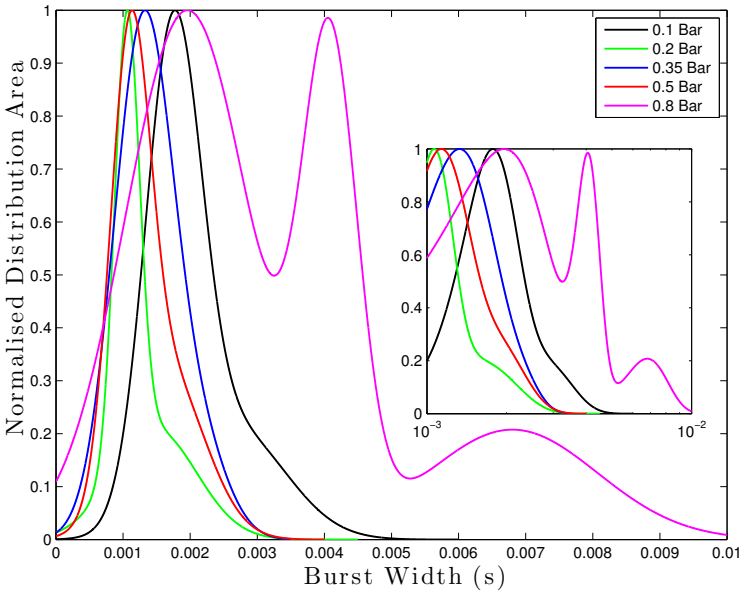

Figure 3.42: Explicit burst width plot of Type III beads (normalised area distribution).

Finally, the thumbnail sequence in Figure 3.43 below, provides further evidence in the simultaneous detection of Type I and III beads, to the data in Figure 3.36 to Figure 3.42. This video demonstrates typical flow behaviour of the mixture at 100 mbar. It can be observed that there are some Type III overtaking Type I beads. Therefore It is possible that once a continuum of Type I bead streamlines is established within the channel at high pressure, a torrential flow of Type III beads can constantly overtaking the heavier particles, which sometimes resulted in a range of particle number being co-detected (as observed in the large distribution of anomalous burst widths at (d) and (e) in Figure 3.36).

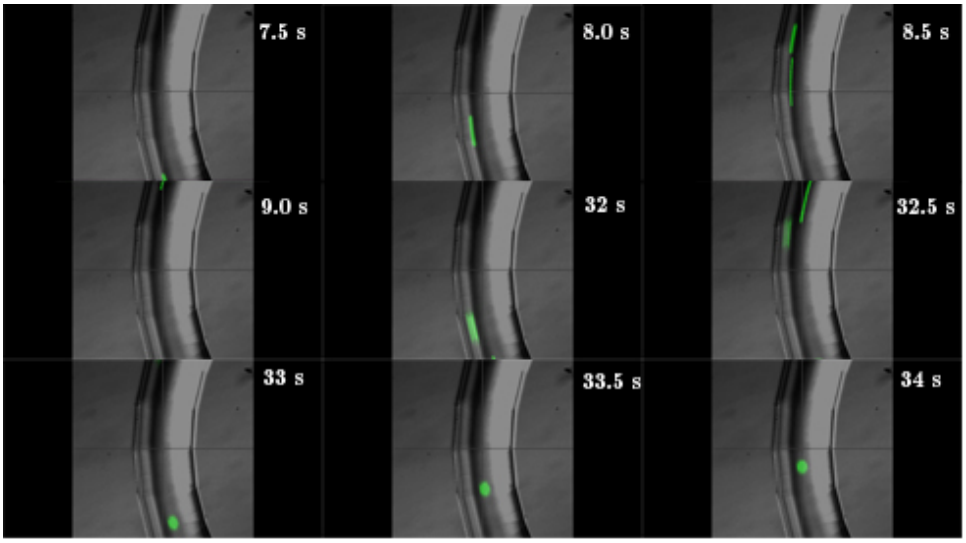

Figure 3.43: Time-lapse sequence of the mixed bead types. A full video footage can found at `http://youtu.be/1Sqfyrd3BdM`.

3.2.5 Summary of Chapter 3

This chapter has shown the workflow for aligning fluorescent sample to the probe within our chip, without hydro-focussing facility. It has been shown the ability in the detecting particle of different sizes, as well as understanding the implication of the pumping pressure on the change in streamlines for the travelling samples. The knowledge on the burst parameters will be used to control the flow operation for FIFO BIFL acquisition in the next chapter, which will extensively guide through the workflow of FIFO BIFL processing methodology, with Type I and Type II beads.

Chapter 4

Lifetime Analysis of Cell Analogues

This chapter will show the workflow in deriving burst integrated fluorescence lifetime data for two bead types with two distinct fluorescence lifetimes, in a solution under flow. Analysis was carried out with non-linear modified Levenberg-Marquardt (NL-MLM) fitting algorithm and the application of phasor analysis to time-domain data. Both types of readout were compared and studied for correlations and consistencies and the use of either as the sorting mechanism was demonstrated and discussed in details.

Initially, FLIM images of the two bead types were acquired as the experimental reference for the lifetime of BIFL data and interrogated with the two analysis methods. BIFL images from Type I and Type II fluorescent beads were acquired separately and then in a mixed solution, The lifetime analysis were performed and discussed in the context of the lifetimes found from the respective FLIM image and the burst characteristics of the data. An important aspect of the mixed population experiment is to ensure the two samples receive sufficient excitation power for sufficiently intense fluorescence emission for the lifetime analysis. As previously shown in chapter 3, controlling of the streamline to the excitation point has been optimised in our large microfluidic channel without the benefit of hydrodynamic focussing. However, different sample types (beads with different

dyes) possess different quantum yields and streamlines and so it is also important to calibrate the laser power per sample type in preparation for a mixed population acquisition.

To give a general indication of the brightness of the two bead types (as will be shown in full details in section 4.2 and section 4.3), Type I and Type II beads require approximately 25 nW[1] and 10 μW[2] respectively for excitation of FLIM images to achieve a similar intensity level ($\ll 1,000$ counts) (see section 4.1 and section 4.2). As always the laser power was set to excite the samples within the safe count limit to avoid pulse-pile up ($<$ 800,000 counts/second) (see subsection 2.5.5, chapter 2). The preliminary goal of the investigation was to serially increase the excitation power until the dimmer Type II beads are able to achieve the average integral intensity above 1000 counts (per bead. i.e. in a single pass through the focal volume). Simply put, the final excitation power used in the mixed population experiment must be intense enough to meaningfully excite the dimmer beads in the mixed sample solution for the NL-MLM analysis to analyse the lifetimes of both beads properly. Additionally, the pulse pile-up effect on the lifetimes of the two beads will be evaluated, due to the serial increase in power (if any).

All the histograms of lifetime and phasor co-ordinates in this chapter will be fit with a Gaussian Model [83]. If any case requires a double Gaussian mixture for the fit, then the average value of the parameter will be weighted by the fractional contribution of each data population[3]. Should the histograms of lifetime distribution of either bead type are not normally distributed around a single value (showing 2 or more peaks and/or irregular skews in either directions),then the data will still be coarsely fit with a double Gaussian mixture model, to crudely assess the lifetimes or ignoring anomalous fractions of the data (an obvious example can be observed in Figure 4.53).

[1] Approximately 25×10^{-6}% of the full laser power (1 mW)

[2] 1% of the full laser power

[3] Mean Value $= \frac{A_1 x_1^2 + A_2 x_2^2}{A_1 x_1 + A_2 x_2} = f_1 x_1 + f_2 x_2$, where A is the peak value, x is the parameter in question, and f is the fractional contribution of each Gaussian distribution. The number in the subscript denotes the population number.

4.1 FLIM Analysis (Type I Beads)

In this section, the FLIM data of Type I beads is investigated, on the pixel-by-pixel and integrated basis (sum of the transient signal from every useful pixel) at the correct excitation power (where the fluorescent photons were counted at the instantaneous count rate of less than 800,000 photons per second at the detector). The FLIM image was acquired for 5 minutes at the excitation power of approximately 25 nW.

Figure 4.1 below shows the intensity image and its corresponding histogram of the beads from the FLIM acquisition.

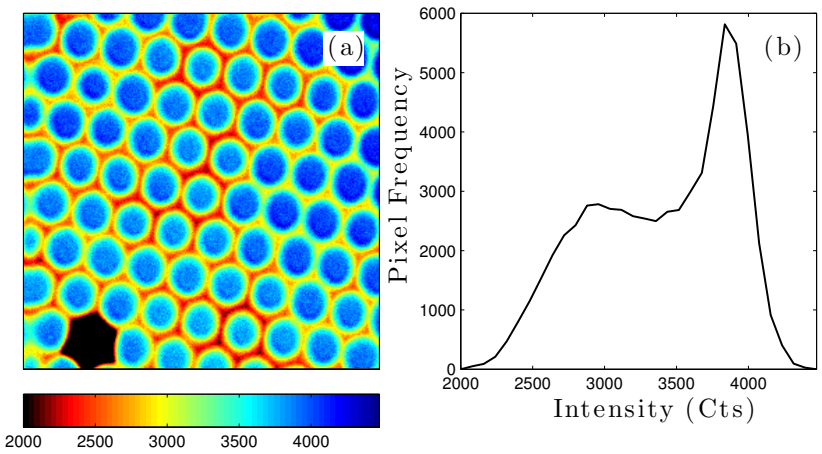

Figure 4.1: Intensity image of Type I beads (a), and its corresponding histogram (b)

From the Figure, the beads show the strongest brightness at the centre of the beads (approximately 3,900 photon counts), and weaker brightness around the peripheries of the beads sitting at out-of-planes, ranging from 2,000 to 3,500 photon counts. The disparity in the intensities across the beads is unsurprising, since the single-photon laser scanning FLIM system is not arranged with a confocal and so the resolution of the image is subjected to some out-of-plane excitations.

4.1.1 Average Lifetime Data Calculation of Individual Useful Pixels (Type I Beads)

This section reports the analysis of lifetimes of Type I beads by NL-MLM and phasor analysis. The results in the section will be used as the experimental reference for the BIFL experiment in section 4.4.

NL-MLM Analysis (Type I Beads)

The FLIM image corresponding to the intensity data shown in Figure 4.1 and the corresponding lifetime histogram of Type I beads, excited at 25 nW is presented in Figure 4.2.

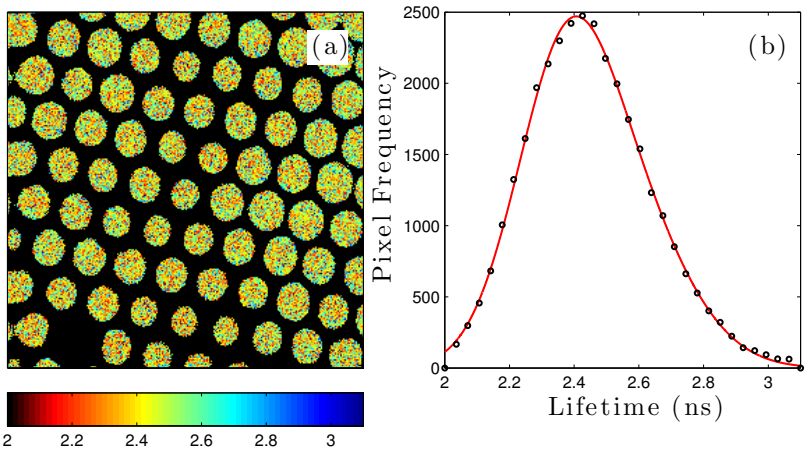

Figure 4.2: (a) FLIM image of Type I beads, calculated and processed by NL-MLM. (b) Lifetime histogram for image in (a).

A_1	τ_1	σ_1	A_2	τ_2	σ_2	Ave. τ	Ave. σ
1719	2.36	0.21	1064	2.55	0.27	2.44	0.24

Table 4.1: The table of summary for the lifetime fitting for Type I bead by NL-MLM (FLIM). The average lifetime of the control was calculated by a double Gaussian mixture model, where A_1 and A_2 are the fractional contributions from the number of pixel of the image, τ_1 and τ_2 are the mean lifetimes measured in ns, and σ_1 and σ_2 are the standard deviations of each sub-population in ns. Ave. τ and Ave. σ reprensents the average lifetime and the associated standard deviation in ns respectively.

For the data in Figure 4.2, the number of photons available is sufficient for NL MLM and phasor analysis in order to calculate the average lifetime on a pixel-by-pixel basis to good effect. Note that the differences in photon counts between the core and periphery of the beads show no noticeable change in fluorescence lifetime, since the mono-exponential fit by NL-MLM is reasonably robust as long as the photon count of each pixel is greater than 1000 and the TCSPC operation is operated within the safe limit (see subsection 2.5.2, chapter 2). The lifetime distribution (Figure 4.2 (b)) of Type I beads were marginally positively skewed, but can be approximated by the double Gaussian mixture very accurately. The data for histogram fitting of lifetimes is given in Table 4.1. The average lifetime of the beads was calculated from the fit to be 2.44 ± 0.24 ns.

Phasor Analysis (Type I Beads)

The contour plot of the phasors of Type I beads excited at 25 nW and the histograms of each phasor co-ordinate (u and v) are shown in Figure 4.3.

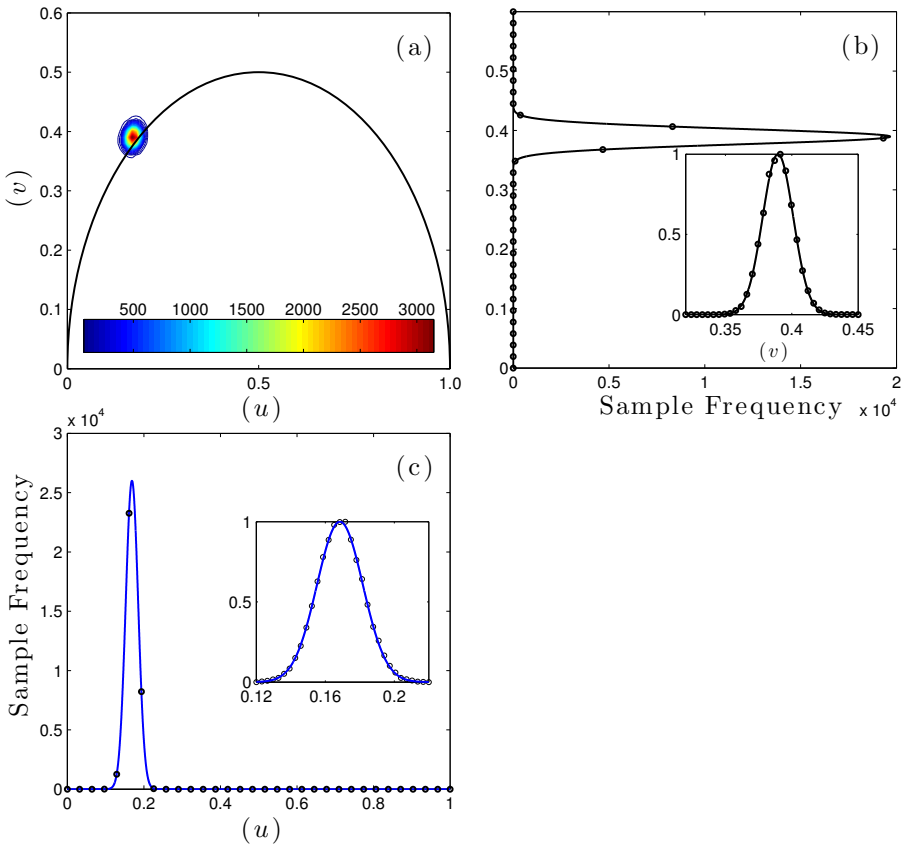

Figure 4.3: Summary of phasor analysis of FLIM image of Type I beads, where (a) shows the contour plot of phasors concentration, and (b) and (c) shows the phasors distribution along the v-axis and u-axis, respectively.

It can clearly be seen from Figure 4.3 that the phasor analysis of Type I beads shows the phasors from each FLIM pixel to be evenly distributed at coordinates ($u = 0.169 \pm 0.019, v = 0.390 \pm 0.016$, see Table 4.2 and Table 4.3) on the phasor graph. The phasor distribution lies on to top of universal semi-circle, which indicates the mono-exponential nature of the decay, as previously described in the theoretical background.

A	u	σ
3169	0.169	0.019

Table 4.2: Summary of the Gaussian fit for the u–coordinate of Type I beads (FLIM) from the inset of Figure 4.3 (c), where A is the peak height of the distribution, u is the centre value, and σ is the standard deviation of the distribution.

A	v	σ
4747	0.390	0.016

Table 4.3: Summary of the Gaussian fit for the v–coordinate of Type I beads (FLIM) from Figure 4.3 (b), where A is the peak height of the distribution, v is the centre value, and σ is the standard deviation of the distribution.

The Fourier transformation of the phasors on the FLIM image along with the corresponding lifetime histogram is shown in Figure 4.4.

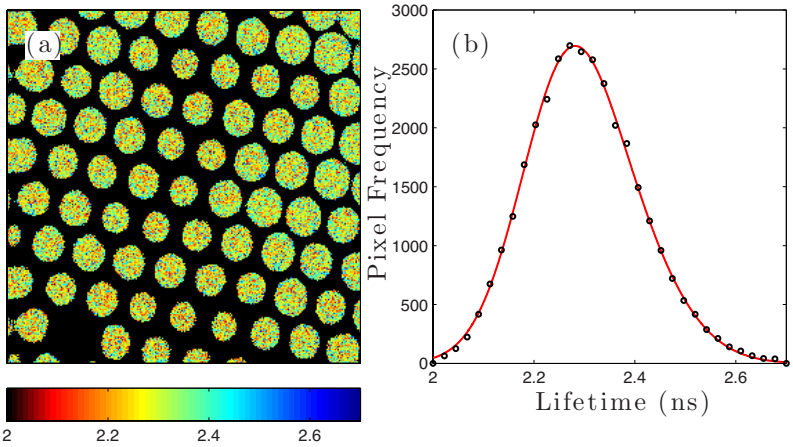

Figure 4.4: (a) FLIM image of Type I beads, which is calculated and processed by NL-MLM. (b) Lifetime histogram for image in (a).

A_1	τ_1	σ_1	A_2	τ_2	σ_2	Ave. τ	Ave. σ
1895	2.26	0.13	1073	2.36	0.16	2.29	0.14

Table 4.4: Table of summary of the lifetime fitting parameters by FT(Phasor) from Figure 4.4 (b). The average lifetime of the control was calculated by a double Gaussian mixture model, where A_1 and A_2 are the fractional contributions from the number of pixel of the image, τ_1 and τ_2 are the mean lifetimes measured in ns, and σ_1 and σ_2 are the standard deviations of each sub-population in ns. Ave. τ and Ave. σ reprensents the average lifetime and the associated standard deviation in ns respectively.

The phasor diagram (frequency domain data) is the Fourier transformation of the lifetime decay(s) (temporal domain data), and so the inverse transformation of the phasor coordinates will simply retrieve the original temporal domain data back. The inverse transformation of the phasors in this case shows that the beads have an average lifetime of 2.29 ± 0.14 ns (see Figure 4.4 (b)). Using a mixture of Gaussians, it was calculated that the average lifetime derived from the phasor method is 140 ps shorter than that obtained by NL-MLM analysis. However, the associated standard deviation is also lower by approximately 40%.

4.1.2 Integrated Transient Profile of FLIM image (Type I Beads)

Analysis of the accumulated transient profile from all bursts is a good first-stop lifetime check when resolving the lifetime of FLIM or BIFL data. The ensemble information can report any anomalous behaviour that the system was experiencing during the experiment. Any obscured or hidden features of individual transients may be accumulated and appear in the result. Additionally the summation of transients will give well-defined transient characteristics, such as the temporal position of the start, peak and tail of the signal, for a better de-convolution of real transient signal. In this section, the accumulated transient profile of every active FLIM pixel will be analysed and compared to the average lifetime of the individual pixels.

The integrated transient profile of FLIM image of Type I beads will be fit with a mono-exponential model of the NL-MLM in section 4.2.2 and Fourier Transformation of the phasors in section 4.2.2.

NL-MLM Analysis (FLIM: Type I Beads)

Figure 4.5 shows the integrated temporal transient of the data for Type I beads, fitted with a mono-exponential model by the NL-MLM algorithm.

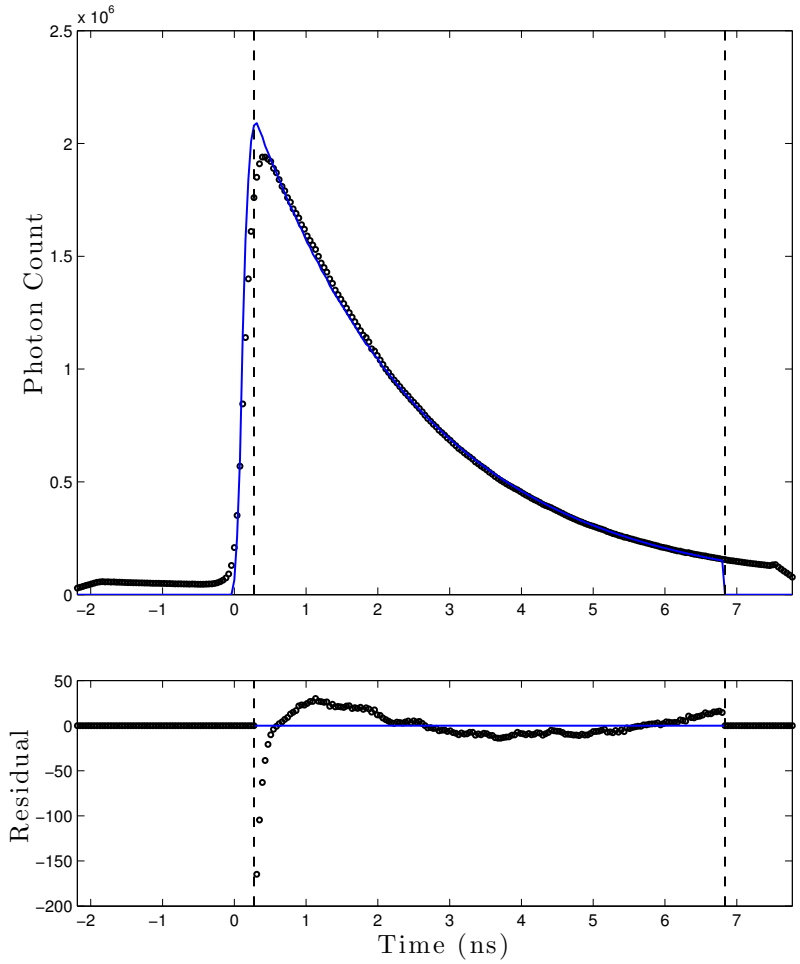

Figure 4.5: Integrated transient profile of Type I beads. The transient is fitted with the mono-exponential model by the NL-MLM algorithm.

Z	A	τ	χ^2_R / d.f.
11250	2.23E+06	2.40	410

Table 4.5: Summary of the mono-exponential fit by NL-MLM on the integrated transient profile of Type I beads, where Z is the baseline level, A is the peak amplitude and τ is the lifetime of the transient in ns. χ^2_R is the goodness of fit parameter.

The full spectroscopic information nor the dye detail was not enclosed by the product, but it is clearly evident from Figure 4.5, that both the goodness of fit parameter ($\chi^2_R \gg 1$) and the residuals that the data does not fit at all well to a single exponential. The bead samples were drawn directly from a commercial package without being washed, and may contain a small amount of dispersant[4] which is mildly fluorescent. This is not surprising, since the fluorophore adsorbed onto the beads is in a complex chemical environment.

The count rate for a single raster scan was kept below 1×10^4 counts per second to avoid pile-up. Fit parameters are summarised in Table 4.5 for completeness. The lifetime of this accumulated transient is calculated to be 2.40 ns. This is comparable to the average lifetime of each individual pixel by the same analysis method at 2.44 ± 0.24 ns, which was different by approximately 40 ps. Whilst fitting the data to a bi-exponential model yields significantly better fits, this is not practical on a pixel by pixel basis due to lack of photons, so this analysis is taken no further. In addition, the influence of any background signal in the solution starts to become significant when every pixel is integrated and it is possible that this is partially responsible for the more complex decay observed in Figure 4.5.

Phasor Analysis (FLIM: Type I Beads)

Figure 4.6 shows the integrated transient profile of the Type I bead data fit by the Fourier transformation of the phasors.

[4] `http://goo.gl/exlFWm`

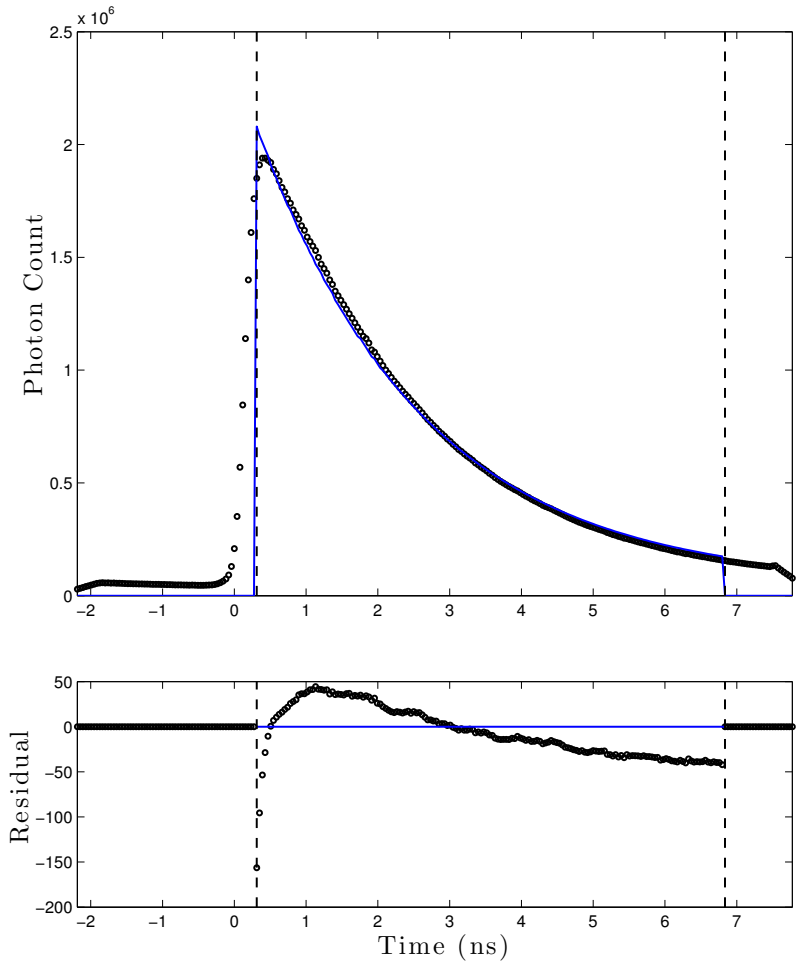

Figure 4.6: Integrated Transient profile of Type I beads, where the transient is calculated by the Fourier Transformation of the phasors.

u	v	τ_p	τ_m	τ	χ^2_R / d.f.
0.169	0.393	2.42	2.19	2.31	951

Table 4.6: Summary of the lifetime calculation from the integrated transient profile of Type I beads by Fourier Transformation of the phasors, where u and v are the centre values of the corresponding axes. τ_p is the lifetime component calculated from the phase delay of the modulated signal waveform from the modulated excitation laser rate in ns, τ_m is the lifetime component calculated from the demodulation between the two modulated waveforms in ns. τ is the average of the two lifetime components in ns and χ^2_R is the goodness of fit (or calculation) parameter of the Fourier transformation of the phasors.

As for the data in Figure 4.6, there is significant error in the fit from the analysis. However, the phasor analysis only takes an account of the phase delays between the modulated data points and the modulated laser repetition and here the modelling assumes a single exponential decay. The average lifetime of the integrated transient is calculated to be 2.31 ns. This is very close to the average lifetime value of the individual pixel data at 2.29 ± 0.14 ns.

4.2 FLIM analysis (Type II Beads)

This section will investigate the lifetime of Type II in the same analysis structure as for Type I in section 4.1. Figure 4.7 represents the intensity image and its corresponding histogram of Type II beads from the FLIM acquisition.

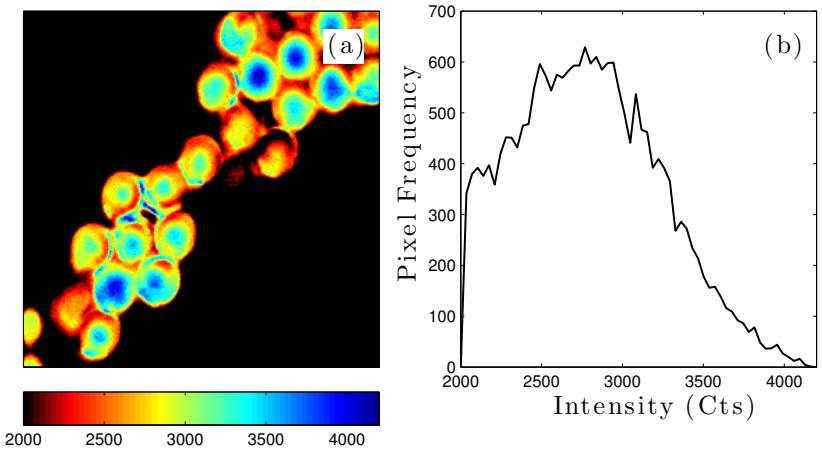

Figure 4.7: Intensity image of Type II beads (a), and its corresponding histogram (b)

From Figure 4.7, Type II beads were observed to be considerably dimmer than Type I beads, as the laser power had to be increased by 3 orders of magnitude to 10 μW, to yield a similar average intensity as the FLIM image of Type I beads. The brightness of the beads varied from one to another to a small degree. Overall, the photon counts of the beads across the image are above 1,000 counts. This should give a comparable fitting accuracy to the one of Type I beads.

4.2.1 Individual Pixel Lifetime Data (Type II Beads)

NL-MLM Analysis (Type II Beads)

Figure 4.8 shows lifetime image (a) and its corresponding lifetime histogram (b) of Type II beads, excited at 10 μW fit using the NL-MLM fitting algorithm.

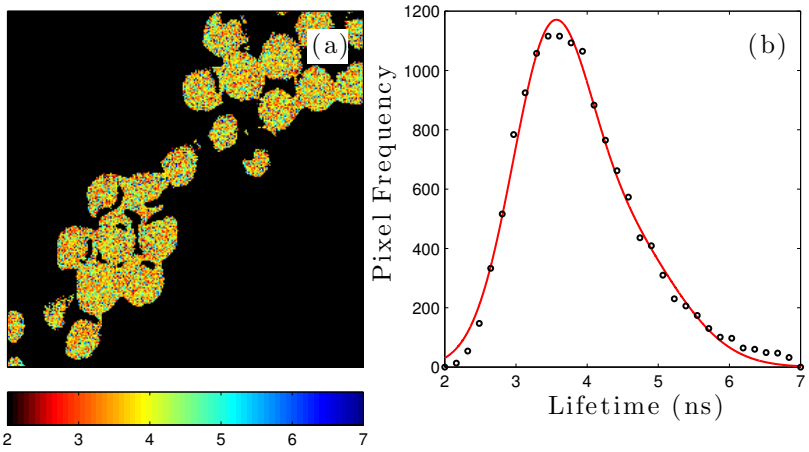

Figure 4.8: (a) FLIM image of Type II beads, which is calculated and processed by NL-MLM. (b) Lifetime histogram for image in (a).

A_1	τ_1	σ_1	A_2	τ_2	σ_2	Ave. τ	Ave. σ
901	3.46	0.76	460	4.37	1.17	3.82	0.94

Table 4.7: The table of summary for the lifetime fitting of Type II bead by NL-MLM (FLIM). The average lifetime of the control was calculated by a double Gaussian mixture model, where A_1 and A_2 are the fractional contributions from the number of pixel of the image, τ_1 and τ_2 are the mean lifetimes measured in ns, and σ_1 and σ_2 are the standard deviations of each sub-population in ns. Ave. τ and Ave. σ reprensents the average lifetime and the associated standard deviation in ns respectively.

NL-MLM analysis shows that the average lifetime of the Type II bead is calculated to be 3.82 ± 0.94. This is 1.4 ns longer than the lifetime of Type I beads. The lifetime distribution is positively skewed to larger degree in comparison to the distribution of Type I bead. The false colour image in Figure 4.8 (a) shows that the two lifetime components listed in Table 4.7 are ubiquitous all over the surfaces of the beads, where the concentration of one lifetime component (green pixel) is lower than the another (orange pixel) by approximately half (see Table 4.7). It is possible that the FITC dyes on the Type II beads contain 2 lifetime components as the Figure suggests – FITC is extremely environmentally sensitive and so this is a reasonable assumption.

Phasor Analysis (Type II Beads)

Phasor analysis was used to analyse the transient data forType II beads and is summarised in Figure 4.9.

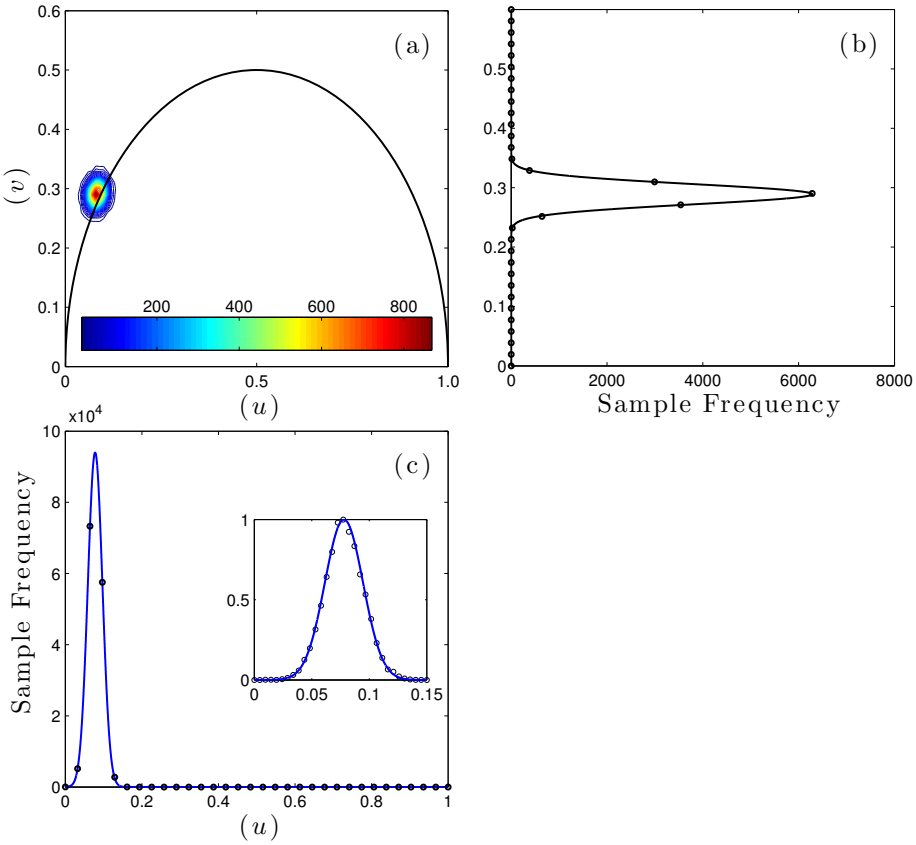

Figure 4.9: Summary of phasor analysis of FLIM image of Type II beads, where (a) shows the contour plot of phasors concentration, and (b) and (c) shows the phasors distribution along the u-axis and v-axis, respectively.

A	u	σ
1608	0.078	0.023

Table 4.8: Summary of the Gaussian fit for the u–coordinate of Type II bead (FLIM) (see the inset of Figure 4.9 (c)), where A is the peak height of the distribution, u is the centre value, and σ is the standard deviation of the distribution.

A	v	σ
6282	0.289	0.024

Table 4.9: Summary of the Gaussian fit for the v–coordinate of Type II bead (FLIM) (see Figure 4.9 (b)), where A is the peak height of the distribution, v is the centre value, and σ is the standard deviation of the distribution.

The phasor analysis should also give a supportive view of the number of the lifetime components present for the data. As stated in the theoretical introduction, the phasors would only be evenly aggregated in one cluster on the universal semicicle, if the decay of FITC exhibits mono-exponential behaviour. As can clearly be observed, the phasors are approximately evenly distributed at $(0.078 \pm 0.023, 0.289 \pm 0.024)$. They also lie on top on the universal semi-circle. Figure 4.10 shows the lifetime image, calculated by the Fourier transformation of the phasors in Figure 4.9 (a).

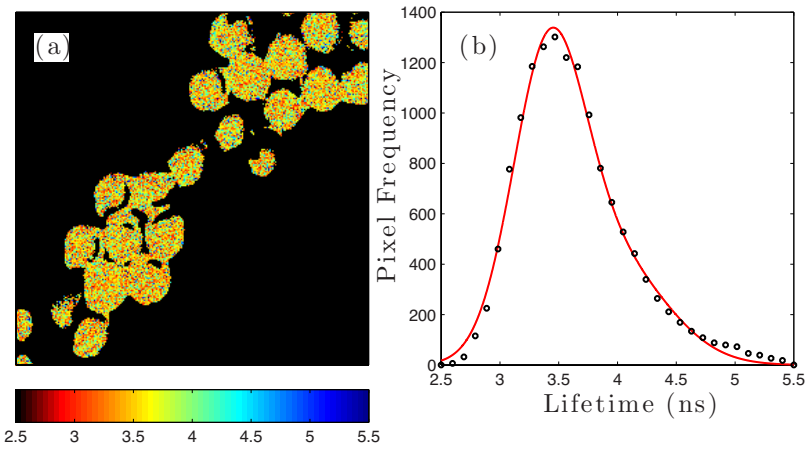

Figure 4.10: (a) FLIM image of Type II beads, which is calculated and processed by NL-MLM. (b) Lifetime histogram for image in (a).

A_1	τ_1	σ_1	A_2	τ_2	σ_2	Ave. τ	Ave. σ
1105	410	3.40	3.93	0.43	0.67	3.57	0.52

Table 4.10: The table of summary for the lifetime fitting of Type II bead (FLIM: FT(Phasor)). The average lifetime of the control was calculated by a double Gaussian mixture model, where A_1 and A_2 are the fractional contributions from the number of pixel of the image, τ_1 and τ_2 are the mean lifetimes measured in ns, and σ_1 and σ_2 are the standard deviations of each sub-population in ns. Ave. τ and Ave. σ reprensents the average lifetime and the associated standard deviation in ns respectively.

The Fourier transformation of the phasors calculated the lifetime of Type II beads to be 3.57 ± 0.52. This lifetime value is lower than that calculated by NL-MLM, by approximately 260 ps. The lifetime distribution is positively skewed as in the NL-MLM case. Since the phasor distribution lies on top on the universal semi-circle, the positive skew on the lifetime distribution will be accepted as the natural characteristics of the beads, for the analysis of BIFL data in section 4.4. The average standard deviation calculated by the Fourier transformation of phasors is approximately 45% lower than the one calculated by NL-MLM. This is comparable and consistent to the reduction found in the Type I beads, at 40%

4.2.2 Integrated Transient Profile (Type II Beads)

NL-MLM Analysis (Type II Beads)

Figure 4.11 shows the integrated transient profile of the FLIM image, fit with the mono-exponential model by the NL-MLM algorithm.

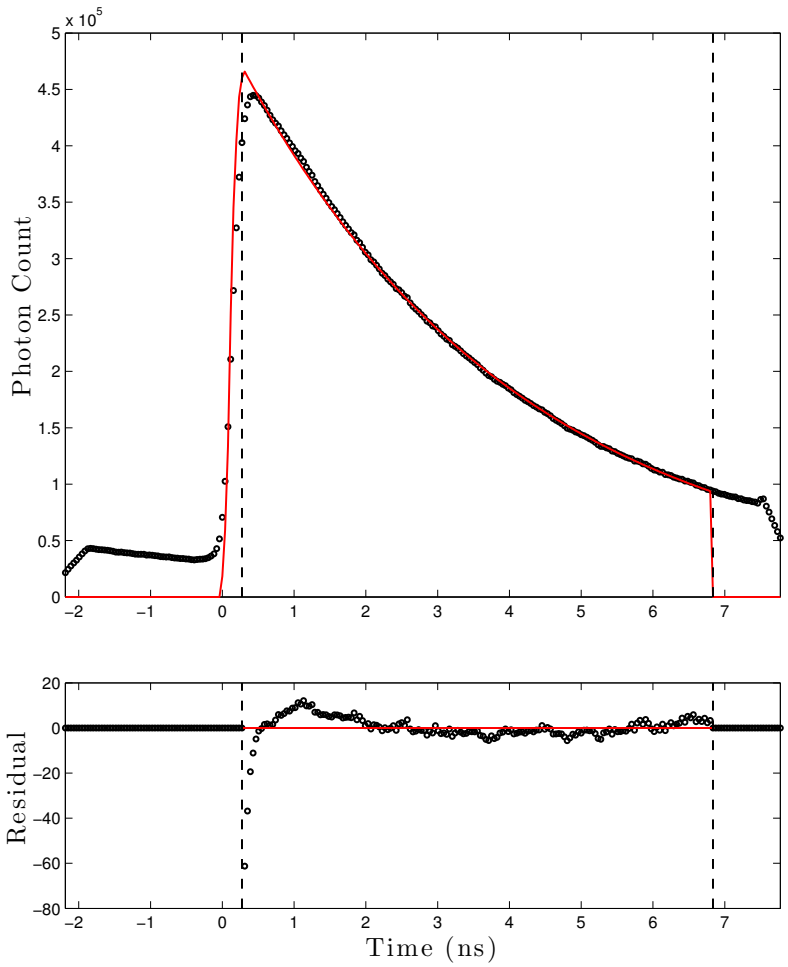

Figure 4.11: Integrated transient profile of Type II beads. The transient is fit to a mono-exponential model by the NL-MLM.

Z	A	τ	χ^2_R / d.f.
6854	479480	3.90	49

Table 4.11: Summary of the mono-exponential fit by NL-MLM on the integrated transient profile of Type II beads, where Z is the baseline level, A is the peak amplitude and τ is the lifetime of the transient in ns. χ^2_R is the goodness of fit parameter.

As for the Type I data, the integrated transient is not fit well to a mono-exponential due to contamination and/or underlying complexity in the transient decay of the dye adsorbed onto the beads. In the interests of brevity, no additional analysis was performed. The lifetime of the accumulated transient is comparable the average lifetime of individual pixel, with a shift in the lifetime in just 70 ps.

Phasor Analysis (Type II Beads)

Figure 4.12 shows the integrated transient profile of the Type II bead data fit by the Fourier transformation of the phasors.

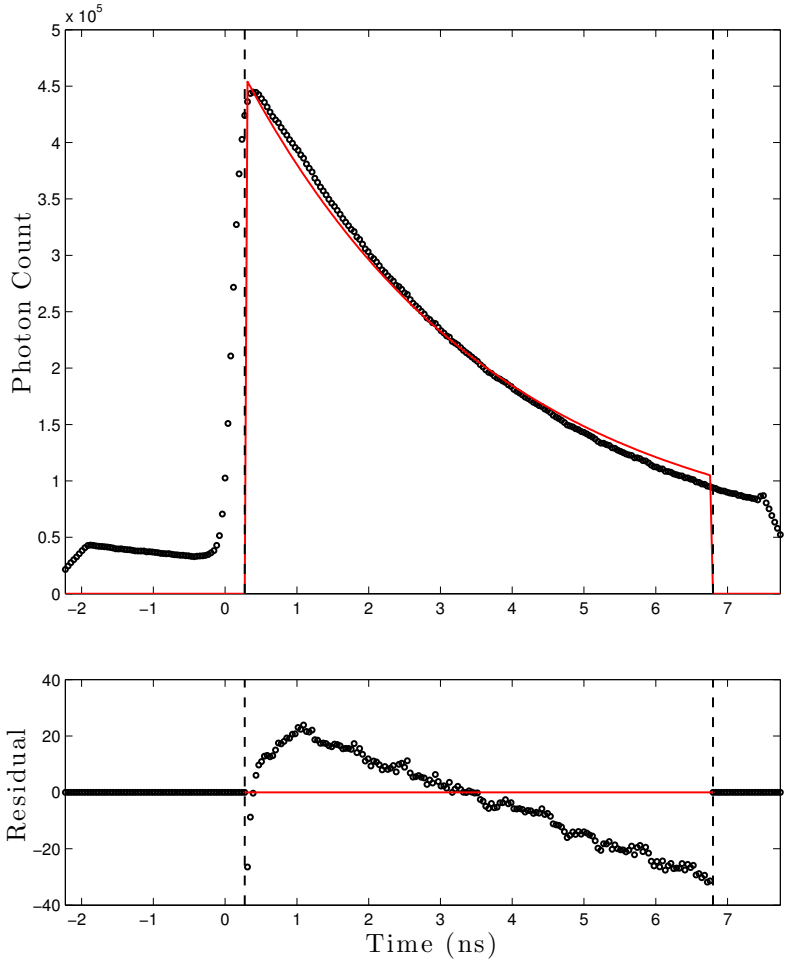

Figure 4.12: Integrated Transient profile of Type II beads, where the transient is calculated by the Fourier Transformation of the phasors.

u	v	τ_p	τ_m	τ	χ^2_R / d.f.
0.079	0.290	3.81	3.27	3.54	258

Table 4.12: Summary of the lifetime calculation from the integrated transient profile of Type II beads by Fourier Transformation of the phasors, where u and v are the centre values of the corresponding axes. τ_p is the lifetime component calculated from the phase delay of the modulated signal waveform from the modulated excitation laser rate in ns, τ_m is the lifetime component calculated from the demodulation between the two modulated waveforms in ns. τ is the average of the two lifetime components in ns and χ^2_R is the goodness of fit (or calculation) parameter of the Fourier transformation of the phasors.

As for the Type I data, the integrated transient is not fit well to a mono-exponential due to contamination and/or underlying complexity in the transient decay of the dye adsorbed onto the beads. In the interests of brevity, no additional analysis was performed. The lifetime of the integrated transient profile of Type II beads was calculated to be 3.54 ns. Again, this is in close agreement with the average lifetime calculated from the data pixel with the same method at 3.57 ± 0.52 ns.

4.3 Flow Experiment: Burst and Transient Characteristics (Type I Beads)

Data for Type II beads in flow were acquired prior to Type I to determine the required excitation range for later direct comparison and mixture analysis, hence the data collected for Type I beads suffered (in some cases significant pulse pulse-up (as will be seen). This section will show the burst characteristic readouts such as burst width, average burst integral intensity and the instantaneous count rate of the detector during the detection of each burst of Type I beads in the flow system, for each pre-set of the laser powers – 0.011 mW, 0.03 mW, 0.10 mW, and 0.16 mW respectively (Attenuation settings are listed in Table 4.13). The average burst integral intensity will give an indication of the accuracy of the fit which can be expected from the bursts, while the instantaneous count rate will report the level of the photon pile-up effect, as well as, the level of counting loss

which the system may experience during the burst detection.

ND (O.D.)	Percentage of laser transmission (%)	Excitation Power (mW)
2.0	1.00	0.01
1.5	3.16	0.03
1.0	10.0	0.10
0.8	15.8	0.16

Table 4.13: Summary of the laser power used in the flow experiment, where ND(O.D.) is the optical density of neutral density filter used for the power attenuation.

From the previous section, the lifetime fitting of integrated fluorescence profiles of both bead types can be observed to yield very close values to the average lifetimes of individual functional pixels of the respective FLIM images (despite the extremely poor fit to the data). The integrated transient profile analysis will be used in tandem with the burst characteristics information, to evaluate the effect of the laser power on the shape of the decays of each bead type (pulse pile-up effect). The decay rates of the integrated fluorescent profiles of the burst data will be directly compared in relation to the experimental reference from the FLIM image of each bead type.

Every aspect of the burst characteristics will be summarised in a single figure per each laser power setting, followed by graphs of integrated transient profile (analysed by NL-MLM and Fourier Transformation of phasors).

The bead solution was pumped at 220 mbar of pumping pressure in every acquisition, with the exception of the 0.16 mW case, where the pumping power was increased to 500 mbar. The power setting was excessively high for the excitation of the beads in flow. FIFO buffer memory overflow warnings were displayed

during the acquisition at the 220 mb operation, and so it was decided to reduce the residence time of the beads in the focal volume by increasing the flow speed thereby reducing the data rate to acceptable levels for the FIFO transfer.

4.3.1 Burst Characteristics of Type I Beads at 0.01 mW of Excitation Power

Data for burst characteristics of Type I beads excited at 0.01 mW of excitation power is collated in Figure 4.13. The bead solution was pumped at 220 mb of pressure and the data was acquired for 10 minutes.

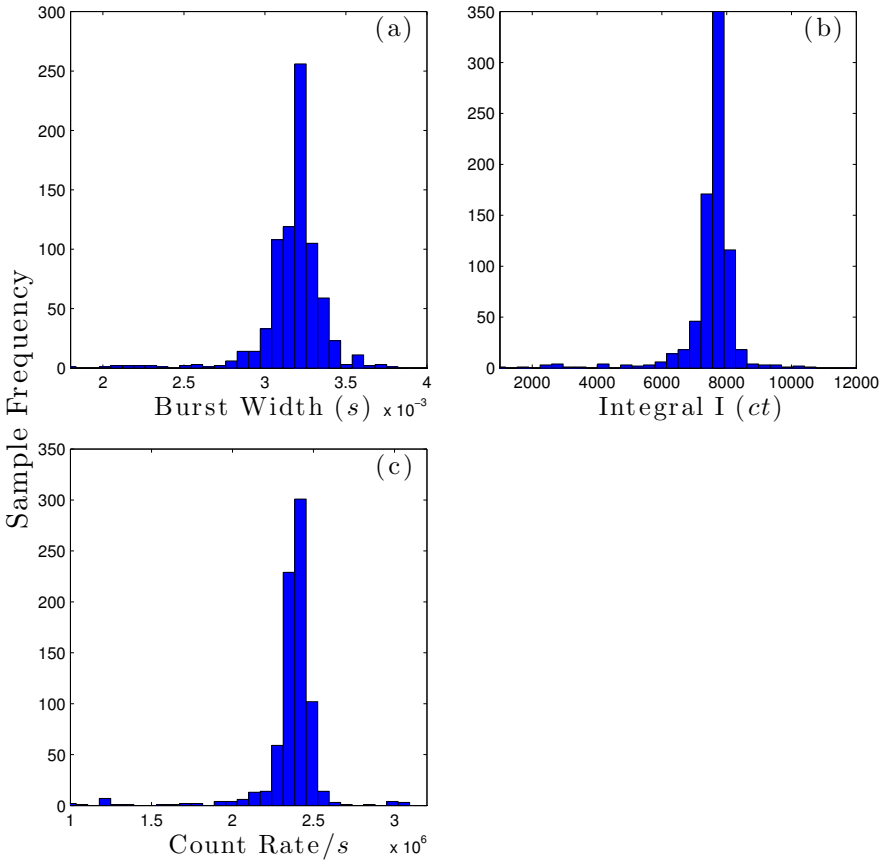

Figure 4.13: Burst characteristics of Type I beads at 0.01 mW of excitation power, where (a), (b), and (c) represents the burst widths, integral intensities, instantaneous count rates during each burst detection respectively.

As can be observed from Figure 4.13, the average burst width of the beads is approximately 3.2 ms. This value is a close reproduction of the burst width result shown in Figure 3.9 in chapter 3 (same bead type examined at 200 mb), which suggests that the acquisition is fully reproducible. With this power setting, the system was able to count the integral burst intensity of the beads on average $\sim$ 8,000 photons. As shown in subsection 4.1.2, the fluorescence profile of Type I beads showed a mono-exponential behaviour. The average burst integral intensity from this flow acquisition satisfies and far exceeds the photon number threshold (1,000 counts) for the mono-exponential model of NL-MLM analysis, and hence

this should give the fitting process an accurate lifetime determination, which will be shown in greater detail in subsection 4.3.2. The instantaneous burst count rate, however, is exceeding the self-imposed limit of 0.01 photons per excitation event of 800 kHz to give an observed burst photon counting rate of $\sim$ 2.4 MHz. This will be taken into the account with the analysis with the integrated profile analysis below.

4.3.2 Integrated Lifetime Analysis of Type I beads at 0.01 mW of Excitation Power

Fitting with NL-MLM Algorithm

The integrated transient profile of the bursts acquired at 0.01 mW of excitation power and fitted with a mono-exponential decay by the NL-MLM algorithm is shown in Figure 4.14.

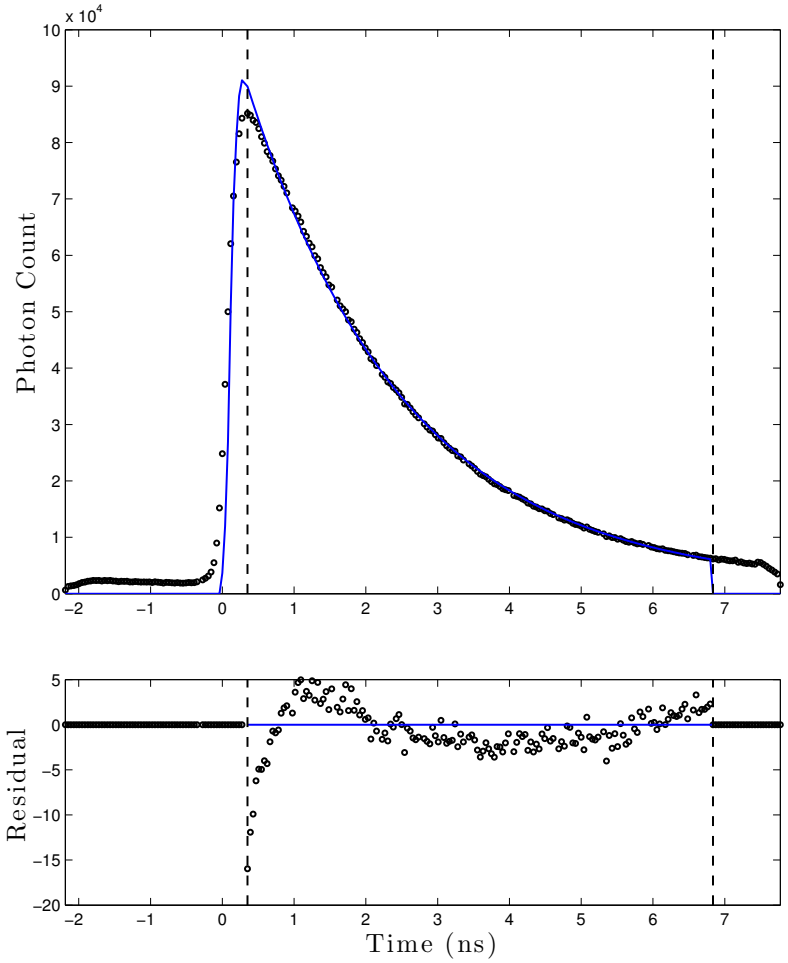

Figure 4.14: Integrated Transient profile of Type I beads. The transient is fit to a mono-exponential model by the NL-MLM.

Z	A	τ	χ^2_R / d.f.
11250	2.23E+06	2.40	410

Table 4.14: Summary of the mono-exponential fit by NL-MLM on the integrated transient profile of Type I beads (Burst Mode) excited at 0.01 mW, where Z is the baseline level, A is the peak amplitude and τ is the lifetime of the transient in ns. χ^2_R is the goodness of fit parameter.

The integrated analysis of Type I beads by NL-MLM shows that lifetime is cal-

culated to be 2.20 ns. This is 230 ps shorter than the experimental reference, analysed from FLIM data for the Type I beads. This reduction in lifetime is somewhat an anecdotal evidence for the pulse pile-up effect and has to be examined with the results at different power setting for a more conclusive judgement. The transient shows the same multi-exponential characteristic as observed previously but the analysis is taken no further in the interests of brevity.

Fitting with Fourier Transformation of Phasors

Figure 4.15 shows the integrated transient profile of the bursts acquired at 0.01 mW of excitation power where the fit to the data is calculated by the Fourier transformation of the phasors.

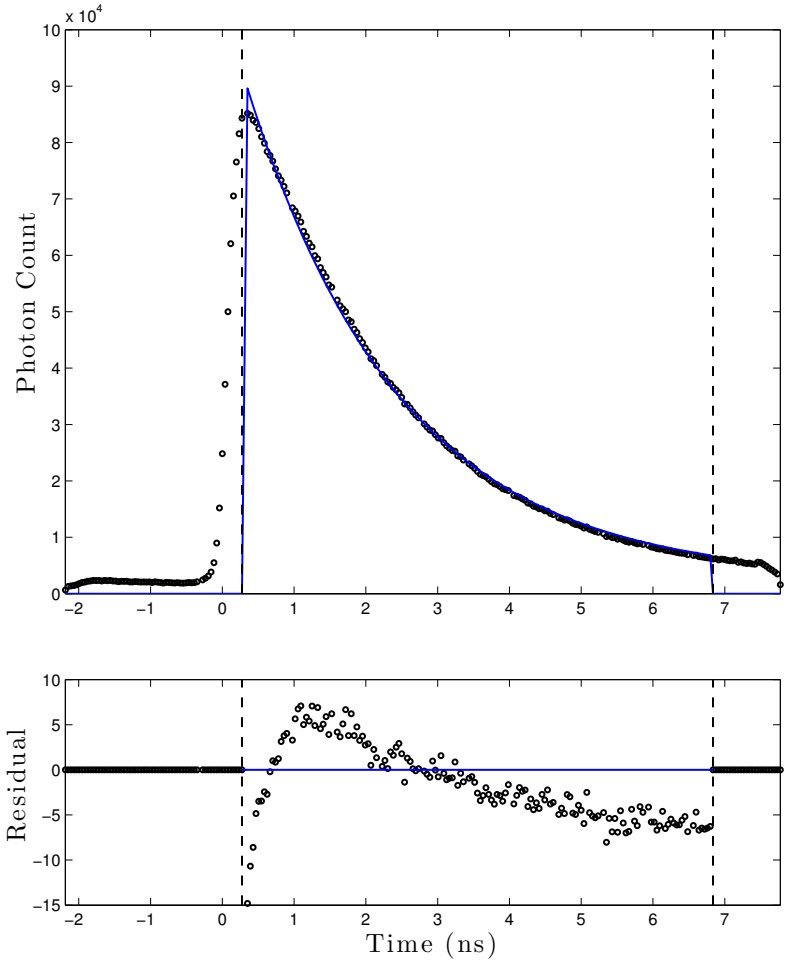

Figure 4.15: Integrated Transient profile of Type I beads calculated by the Fourier Transformation of the phasors.

u	v	τ_p	τ_m	τ	χ^2_R / d.f.
0.190	0.406	2.22	2.07	2.14	28

Table 4.15: Summary of the lifetime calculation from the integrated transient profile of Type I beads by Fourier Transformation of the phasors (Burst Mode) excited at 0.01 mW, where u and v are the centre values of the corresponding axes. τ_p is the lifetime component calculated from the phase delay of the modulated signal waveform from the modulated excitation laser rate in ns, τ_m is the lifetime component calculated from the demodulation between the two modulated waveforms in ns. τ is the average of the two lifetime components in ns and χ^2_R is the goodness of fit (or calculation) parameter of the Fourier transformation of the phasors.

The integrated lifetime of Type I beads was calculated to be 2.14 ns. This is 170 ps shorter than the experimental reference. The transient shows the same multi-exponential characteristic as observed previously but the analysis is taken no further in the interests of brevity.

4.3.3 Burst Characteristics of Type I Bead at 0.03 mW of Excitation Power

Data for burst characteristics of Type I beads excited at 0.03 mW of excitation power is collated in Figure 4.16. The bead solution was pumped at 220 mbar of pressure and the data was acquired for 10 minutes.

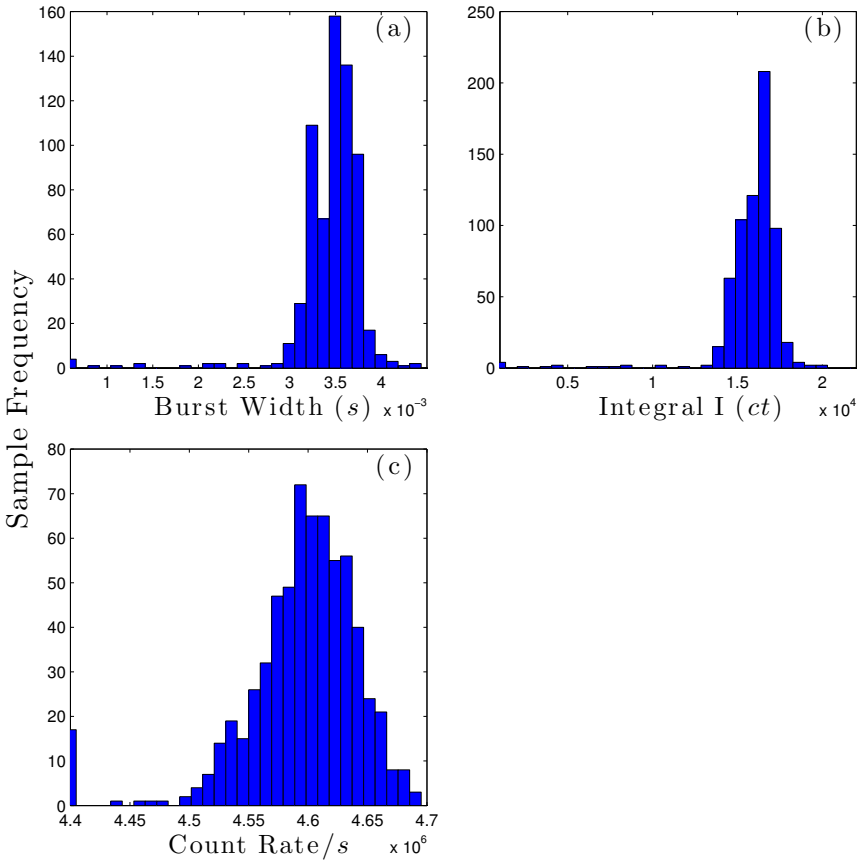

Figure 4.16: Burst characteristics of Type I beads at 0.03 mW of excitation power, where (a), (b), and (c) represents the burst widths, integral intensities, instantaneous count rates during each burst detection, respectively.

The burst width of the beads was observed to have increased from the previous power setting to 3.5 ms. However, the 300 μs shift is small and the change in the average burst width is probably due to the statistical nature or hysteresis from any change in the flow environment, it is also possible that airy disc pattern is becoming more apparent, which would appear as the expansion of the beam waist at the focal plane. This will be examined with the results of the higher power settings. The average integral burst intensity of the beads now reaches approximately 1.6×10^4 photon counts, but at the same time, the average instantaneous count rate also becomes considerably higher, at 4.6×10^6. It is important to

acknowledge that this instantaneous count rate will cause the photon counting efficiency of SPC–830 to be reduced to approximately 65% (see Figure 2.12 in chapter 2).

4.3.4 Integrated Lifetime Analysis of Type I beads at 0.03 mW of Excitation Power

Fitting with NL-MLM Algorithm

The integrated transient profile of the bursts acquired at 0.03 mW of excitation power and fitted with a mono-exponential decay by the NL-MLM algorithm is shown in Figure 4.17.

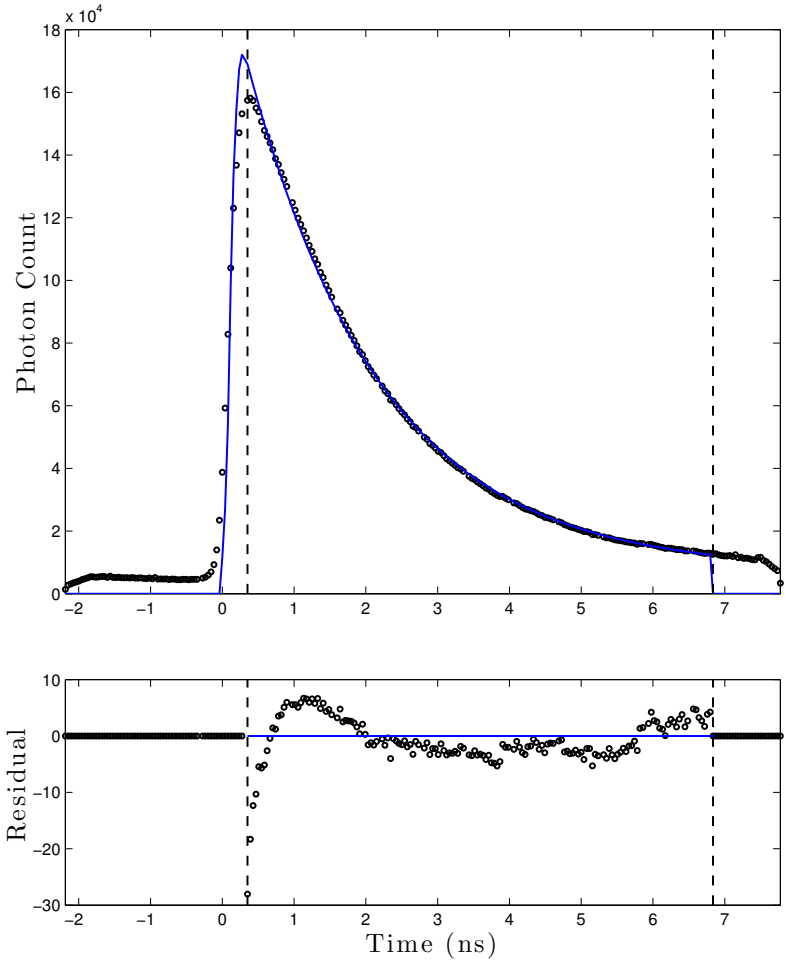

Figure 4.17: Integrated Transient profile of Type I beads. The transient is fitted a mono-exponential model by the NL-MLM.

Z	A	τ	χ^2_R / d.f.
7370	180859	1.86	33

Table 4.16: Summary of the mono-exponential fit by NL-MLM on the integrated transient profile of Type I beads (Burst Mode) excited at 0.03 mW, where Z is the baseline level, A is the peak amplitude and τ is the lifetime of the transient in ns. χ^2_R is the goodness of fit parameter.

The lifetime of Type I beads is now calculated to be 1.86 ns. The goodness of

fit parameter also becomes larger compared to the 0.01 mW case. The transient shows the same multi-exponential characteristic as observed previously. However, the reduction in average lifetime due to pile-up becomes considerable at this level of excitation power. When comparing the data in Figure 4.17 with the prompt signal (see Figure 2.13 in chapter 2), it can be observed that the secondary peak of the excitation now starts to bleed through the emission filtering system at 6 ns of the processing window (or 8 ns in real time, as shown in Figure 2.12 in chapter 2).

4.3.5 Fitting with Fourier Transformation of Phasors

Figure 4.18 shows the integrated transient profile of the bursts acquired at 0.03 mW of excitation power where the fit to the data is calculated by the Fourier transformation of the phasors.

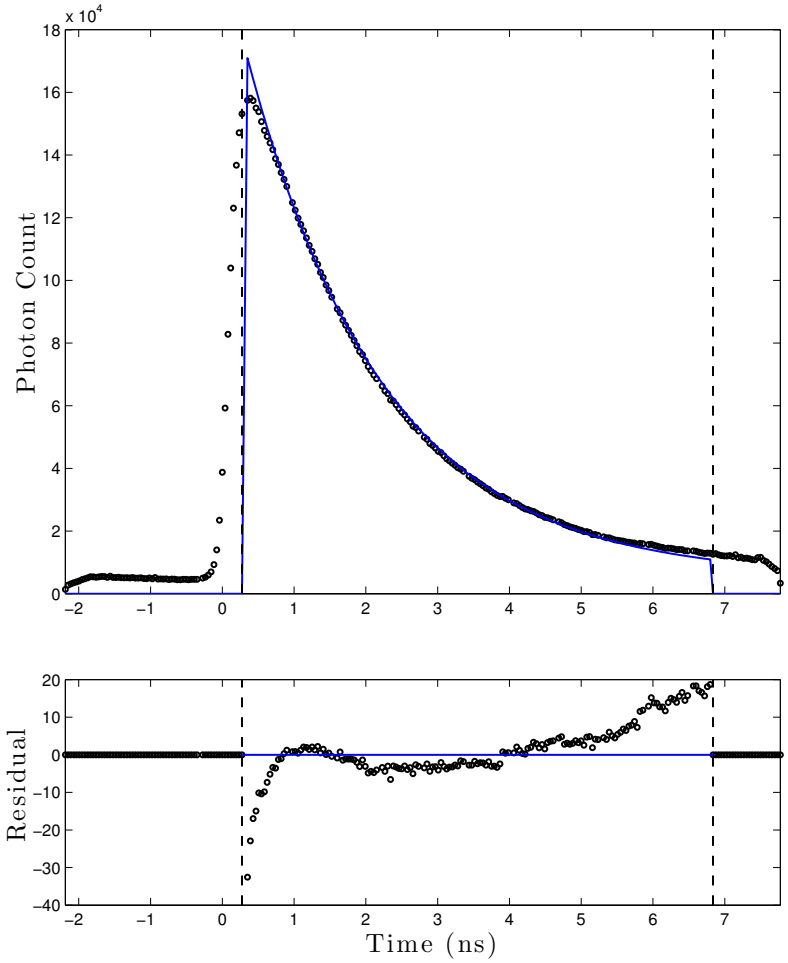

Figure 4.18: Integrated Transient profile of Type I beads. The transient is calculated by the Fourier Transformation of the phasors.

u	v	τ_p	τ_m	τ	χ^2_R / d.f.
0.230	0.413	1.87	1.93	1.90	76

Table 4.17: Summary of the lifetime calculation from the integrated transient profile of Type I beads by Fourier Transformation of the phasors (Burst Mode) excited at 0.03 mW, where u and v are the centre values of the corresponding axes. τ_p is the lifetime component calculated from the phase delay of the modulated signal waveform from the modulated excitation laser rate in ns, τ_m is the lifetime component calculated from the demodulation between the two modulated waveforms in ns. τ is the average of the two lifetime components in ns and χ^2_R is the goodness of fit (or calculation) parameter of the Fourier transformation of the phasors.

The lifetime of the integrated transient is calculated to be 1.90 ns, this is 410 ps shorter the experimental reference. However, the calculation seems very robust, despite the small secondary excitation at the tail of the transient. Even if there is a strong secondary excitation, the lifetime of the transient should still be minimally affected, as the phase delay between the data points and the stopping trigger of TCSPC would remain the same (provided that the local environment of the fluorophore remains unchanged throughout the first and secondary excitation).

4.3.6 Burst Characteristics of Type I Bead at 0.10 mW of Excitation Power

Data for burst characteristics of Type I beads excited at 0.10 mW of excitation power is collated in Figure 4.19. The bead solution was pumped at 220 mbar of pressure and the data was acquired for 10 minutes.

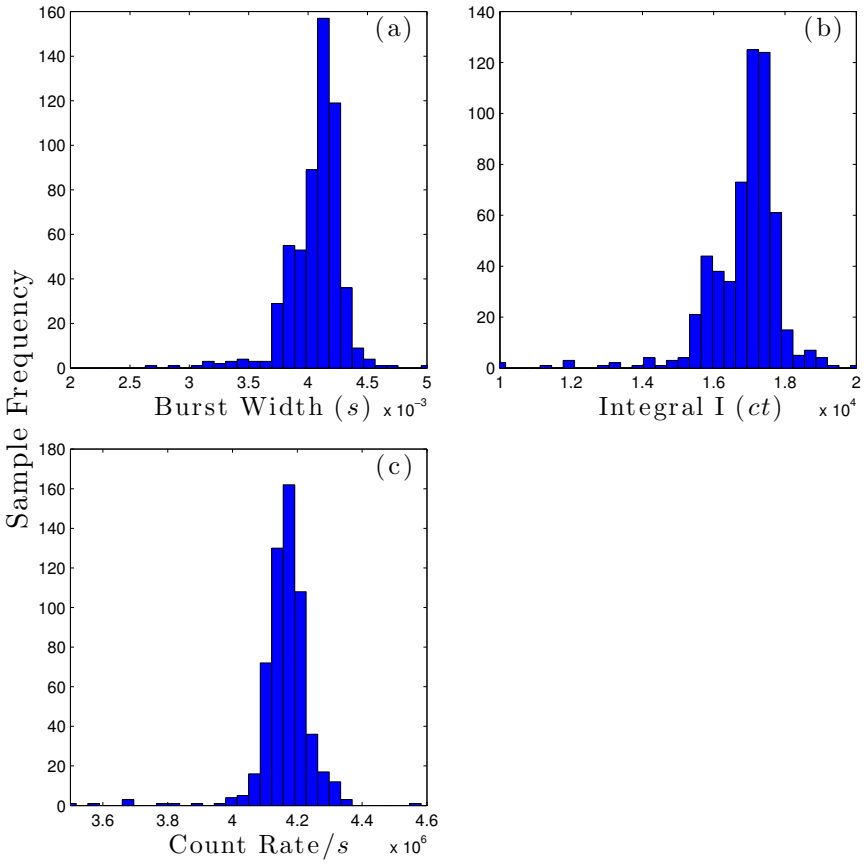

Figure 4.19: Burst characteristics of Type I beads at 0.10 mW of excitation power, where (a), (b), and (c) represents the burst widths, integral intensities, instantaneous count rates during each burst detection respectively.

From Figure 4.19, the average burst width of the beads now increases to approximately 4.1 to 4.2 ms. Hence the evidence on the expansion of the beam waist by the Airy Disc pattern seems increasing likely. There seem to be two populations of integrated intensity at the 1.6×10^4 and 1.75×10^4 photon counts in this acquisition. Interestingly, the instantaneous burst count rate is reduced from the previous from the power setting. It is likely that the reduction in photon counting efficiency begins to have an observable effect. With the reduction of the counting efficiency, it is possible that the degradation begins to counteract the increasing rate of the instantaneous photon counts resulting in a lesser number of photon

being counted at the TCSPC card. The shape of the integrated transient profile in Figure 4.21 and Figure 4.22 will be closely inspected for further evidence.

4.3.7 Integrated Lifetime Analysis of Type I beads at 0.10 mW of Excitation Power

Fitting with NL-MLM Algorithm

The integrated transient profile of the bursts acquired at 0.10 mW of excitation power and fitted with a mono-exponential decay by the NL-MLM algorithm is shown in Figure 4.20.

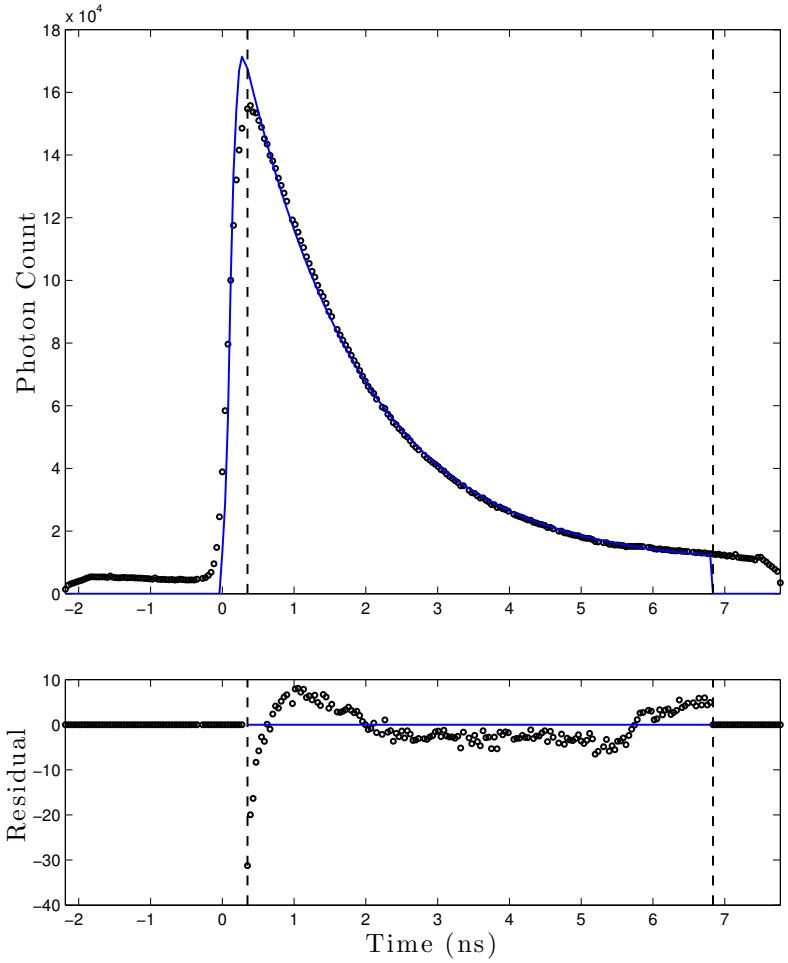

Figure 4.20: Integrated Transient profile of Type I beads. The transient is fitted a mono-exponential model by the NL-MLM.

Z	A	τ	χ^2_R / d.f.
9000	179930	1.65	39

Table 4.18: Summary of the mono-exponential fit by NL-MLM on the integrated transient profile of Type I beads (Burst Mode) excited at 0.10 mW, where Z is the baseline level, A is the peak amplitude and τ is the lifetime of the transient in ns. χ^2_R is the goodness of fit parameter.

The lifetime of integrated transient profile of Type I beads is now calculated to

be 1.65 ns, approximately 750 ps shorter than the experimental reference. From the residual plot, the tail of the transient shows a more pronounced excitation by the secondary peak of the prompt signal, in comparison to the previous power setting. From the residual plot, it can be observed that the fitting of NL-MLM took account of the secondary excitation in the lifetime derivation. The fit is clearly influenced by the secondary excitation. This will be shown in the summary in subsection 4.4.8 for further details.

Fitting with Fourier Transformation of Phasors

Figure 4.21 shows the integrated transient profile of the bursts acquired at 0.10 mW of excitation power where the fit to the data is calculated by the Fourier transformation of the phasors.

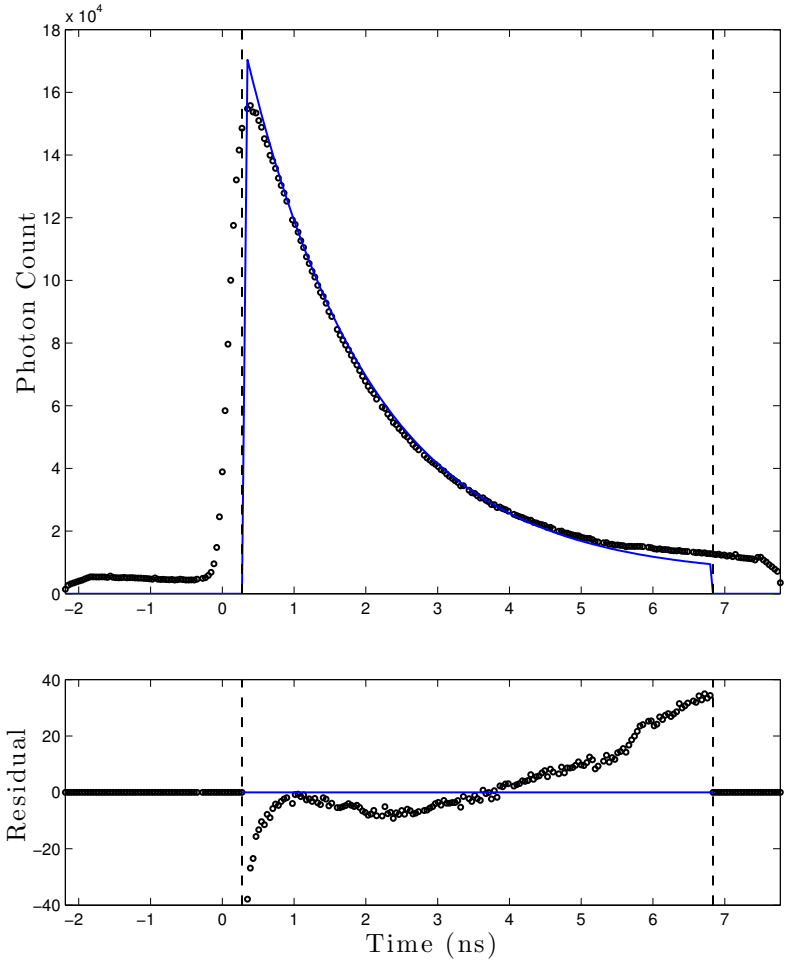

Figure 4.21: Integrated Transient profile of Type I beads. The transient is calculated by the Fourier Transformation of the phasors.

u	v	τ_p	τ_m	τ	χ^2_R / d.f.
0.262	0.420	1.66	1.82	1.74	218

Table 4.19: Summary of the lifetime calculation from the integrated transient profile of Type I beads by Fourier Transformation of the phasors (Burst Mode) excited at 0.10 mW, where u and v are the centre values of the corresponding axes. τ_p is the lifetime component calculated from the phase delay of the modulated signal waveform from the modulated excitation laser rate in ns, τ_m is the lifetime component calculated from the demodulation between the two modulated waveforms in ns. τ is the average of the two lifetime components in ns and χ^2_R is the goodness of fit (or calculation) parameter of the Fourier transformation of the phasors.

The lifetime of the transient calculated to be 1.74 ns. Again, despite the terrible fit to the data (especially towards the tail of the transient) does not seem to influence the lengthening of lifetime data.

4.3.8 Burst Characteristics of Type I Bead at 0.16 mW of Excitation Power

Data for burst characteristics of Type I beads excited at 0.16 mW of excitation power is collated in Figure 4.22. The bead solution was pumped at 220 mbar of pressure and the data was acquired for 10 minutes.

This power setting is now extremely high. However the burst characteristics of this data set cannot be directly compared to other data set at different power settings. The conjecture from the burst characteristic results of other power settings already shows that the power settings used in the experiment are too high for the excitation of the bead. From hindsight, the beads were only acquired at this level of power, as the power is sufficient to excite the dimmer Type II beads meaningfully. The burst characteristic and lifetime results will be used as the experimental reference for the mixed population experiment.

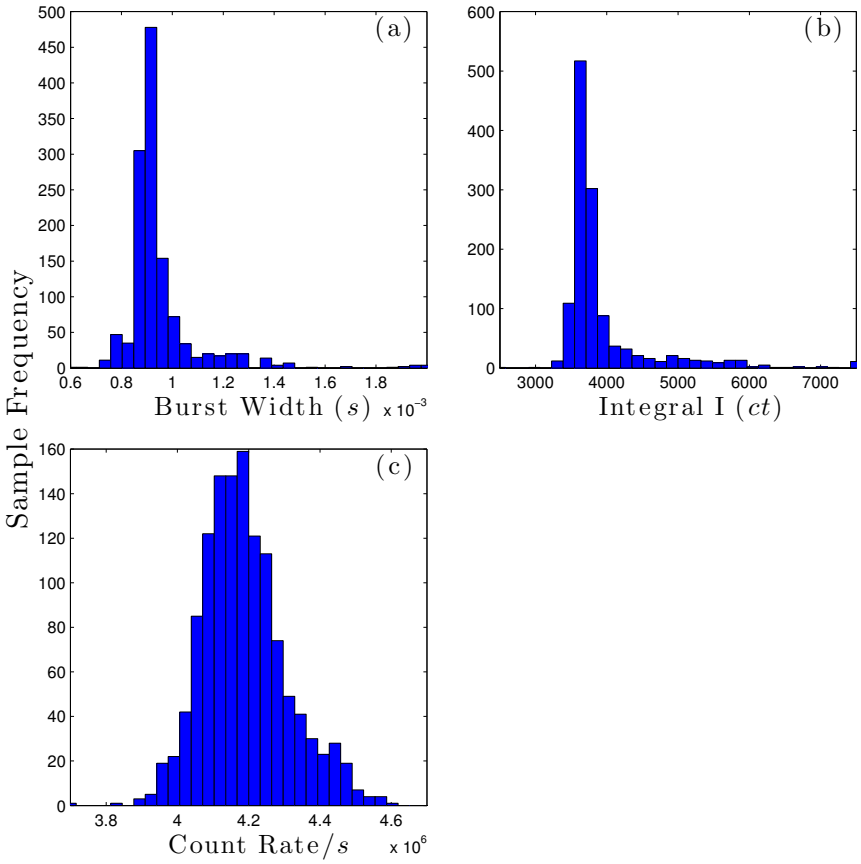

Figure 4.22: Burst characteristics of Type I beads at 0.16 mW of excitation power, where (a), (b), and (c) represents the burst widths, integral intensities, instantaneous count rates during each burst detection, respectively.

Due to the increase in pumping pressure, the average burst width now drops to 0.9 ms. Similarly, the average integral intensity now drops to approximately 3.8×10^3 counts. The instantaneous burst count rate profile is comparable to the one of the 0.10 mW case, at approximately 4.1×10^6 counts per second.

4.3.9 Integrated Lifetime Analysis of Type I beads at 0.16 mW of Excitation Power

Fitting with NL-MLM Algorithm

The integrated transient profile of the bursts acquired at 0.16 mW of excitation power and fitted with a mono-exponential decay by the NL-MLM algorithm is shown in Figure 4.23.

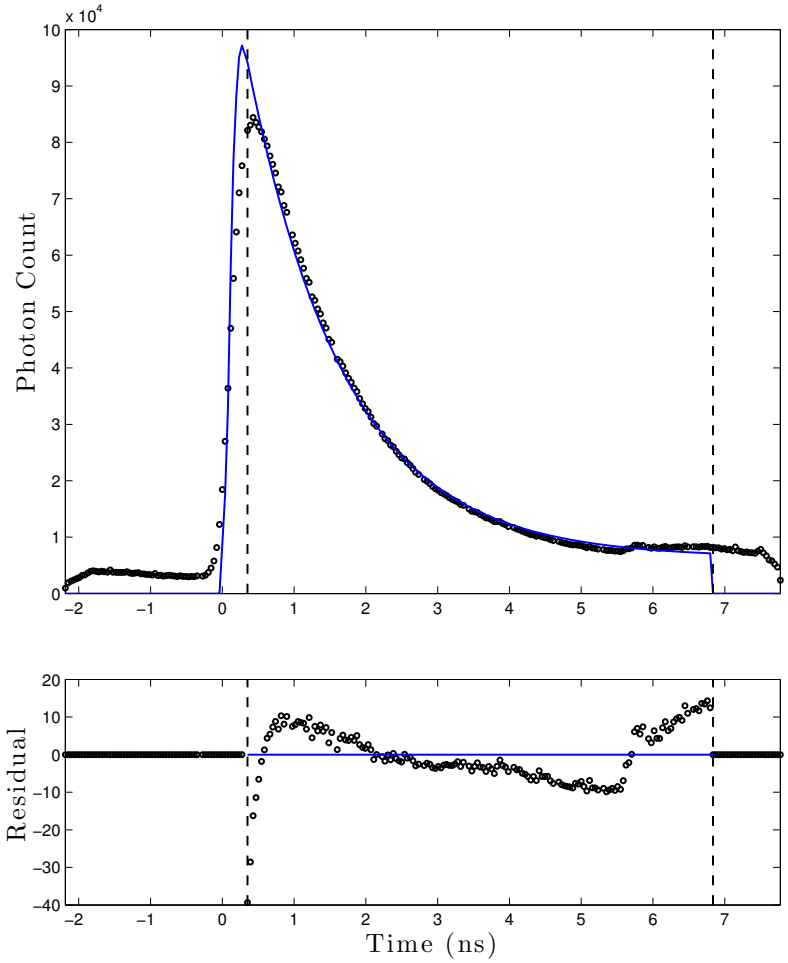

Figure 4.23: Integrated Transient profile of Type I beads. The transient is fitted a mono-exponential model by the NL-MLM.

Z	A	τ	χ^2_R / d.f.
6382	102449	1.35	74

Table 4.20: Summary of the mono-exponential fit by NL-MLM on the integrated transient profile of Type I beads (Burst Mode) excited at 0.16 mW, where Z is the baseline level, A is the peak amplitude and τ is the lifetime of the transient in ns. χ^2_R is the goodness of fit parameter.

The lifetime of the integrated transient is now calculated to be 1.35 ns by NL MLM. This is 1.05 ns faster than the experimental reference. As expected, the decay profile is significantly quenched and the secondary excitation at 6 ns of the processing window becomes the most pronounced at this power setting. The characteristics of the transient will be accepted and used as the experimental control for the mixed population experiment.

Fitting with Fourier Transformation of Phasors

Figure 4.21 shows the integrated transient profile of the bursts acquired at 0.16 mW of excitation power where the fit to the data is calculated by the Fourier transformation of the phasors.

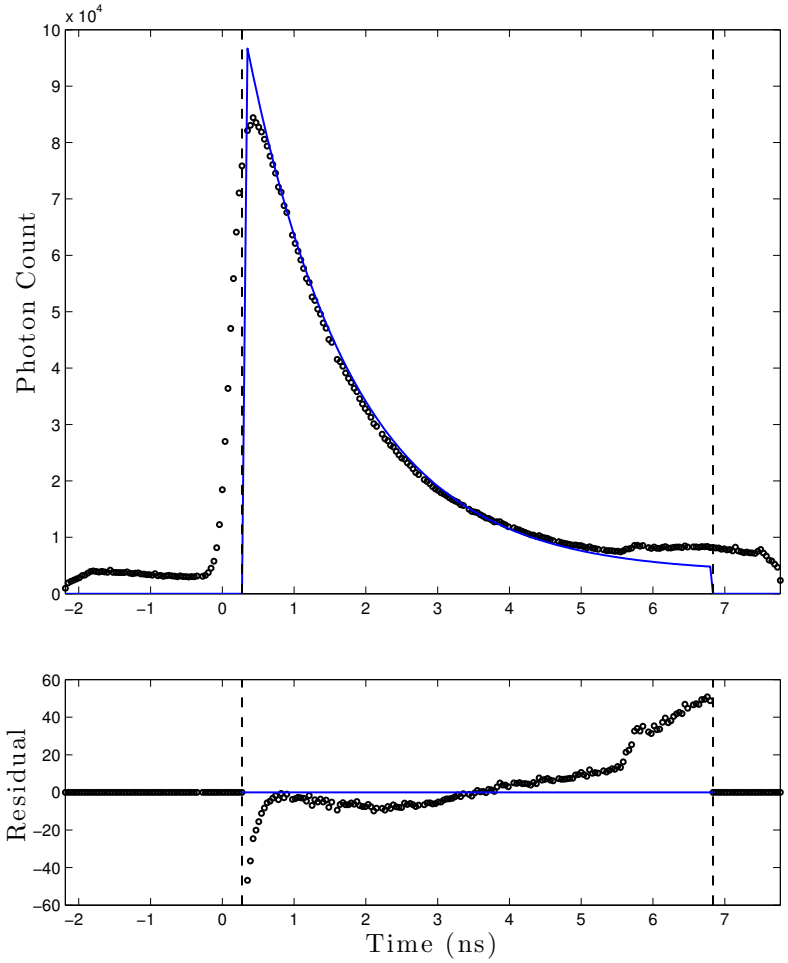

Figure 4.24: Integrated Transient profile of Type I beads. The transient is calculated by the Fourier Transformation of the phasors.

u	v	τ_p	τ_m	τ	χ^2_R / d.f.
0.332	0.436	1.36	1.59	1.48	382

Table 4.21: Summary of the lifetime calculation from the integrated transient profile of Type I beads by Fourier Transformation of the phasors (Burst Mode) excited at 0.16 mW, where u and v are the centre values of the corresponding axes. τ_p is the lifetime component calculated from the phase delay of the modulated signal waveform from the modulated excitation laser rate in ns, τ_m is the lifetime component calculated from the demodulation between the two modulated waveforms in ns. τ is the average of the two lifetime components in ns and χ^2_R is the goodness of fit (or calculation) parameter of the Fourier transformation of the phasors.

The lifetime of the transient of Type I bead is calculated to be 1.48 ns, 830 ps faster the experimental reference. The calculation of the transient ignored the secondary excitation, as shown in the previous cases.

4.3.10 Summary of Integrated Transient Data of Type I

As mentioned in the introduction, the accumulated transient profile is only observed for recognising the shape of the transient at different power settings. In terms of deriving the average lifetimes of the beads, this will be calculated from the basis of individual pixels instead.

As shown in subsection 4.3.1 to subsection 4.3.9, the use of high laser power increases the probability of detecting optical reflections within the system and scattered excitation from the beads to bleed through the emission filtering system at 6 ns of the processing window. The integrated transient analysis was able to pick up the characteristic by taking the advantage of the Poissonian nature of the TCSPC data[5] and sum up the photons of every burst in the pre-set time bins of the transient data. As a consequence, the additional excitation causes the mono-exponential behaviour (confirmed by subsection 4.1.2 and subsection 4.3.2) to spuriously gain additional lifetime component (see Figure 4.25). From the Figure, a progressive reduction of the decay rate of Type I beads is observable

[5]Each observable photon is an independent measurement

through the increase of the excitation power. It can be seen that the presence of the secondary excitation of near the 6 ns of the processing window is having a strong influence on the decay rate. If a transient were to show a mono-exponential behaviour, then a straight-line slope can be expected along the decay. The plot in blue (0.03 mW), cyan (0.10 mW) and red (0.16 mW) clearly shows that the effect on the increase in power (and subsequently a decrease in the counting efficiency) can falsely simulate the presence of additional lifetime component, and reduce the lifetime from the norm, which is very similar to FRET interaction. This will be closely investigated in detail with the phasor analysis of individual BIFL pixel.

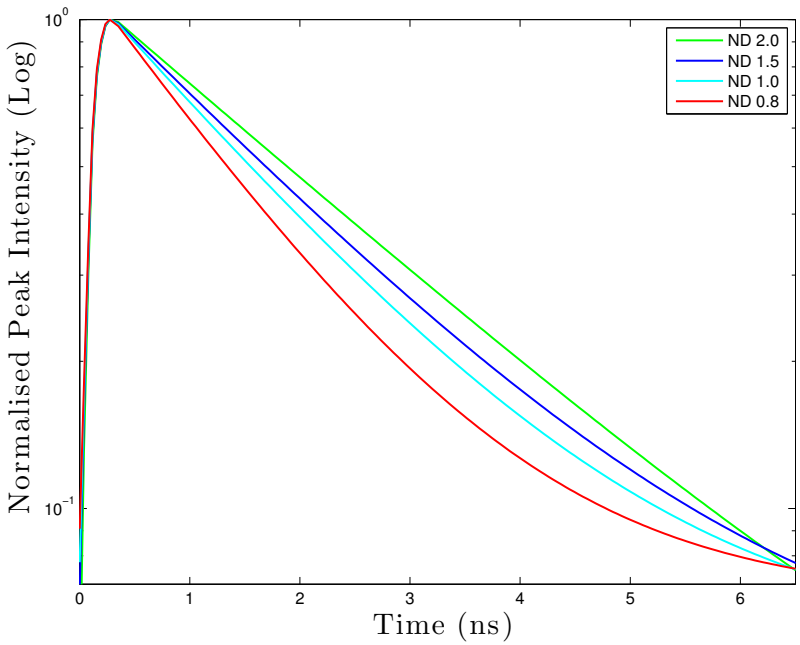

Figure 4.25: Summary of mono-exponential fits by NL-MLM on the integrated transients of Type I beads, where ND is the optical density of the neutral density used in the controlling of the laser excitation power (see Table 4.22 below).

ND	Power (mW)	Z	A	τ	χ^2_R / d.f.
2.0	0.01	1350	97421	2.21	15
1.5	0.03	7370	180859	1.86	33
1.0	0.10	9000	179930	1.65	39
0.8	0.16	6382	102449	1.35	74

Table 4.22: Summary of the mono-exponential fit by NL-MLM on the integrated transient profile of Type I beads (Burst Mode), per power setting, where Power is the excitation power in mW, Z is the baseline level, A is the peak amplitude, τ is the lifetime of the transient in ns and χ^2_R is the goodness of fit parameter.

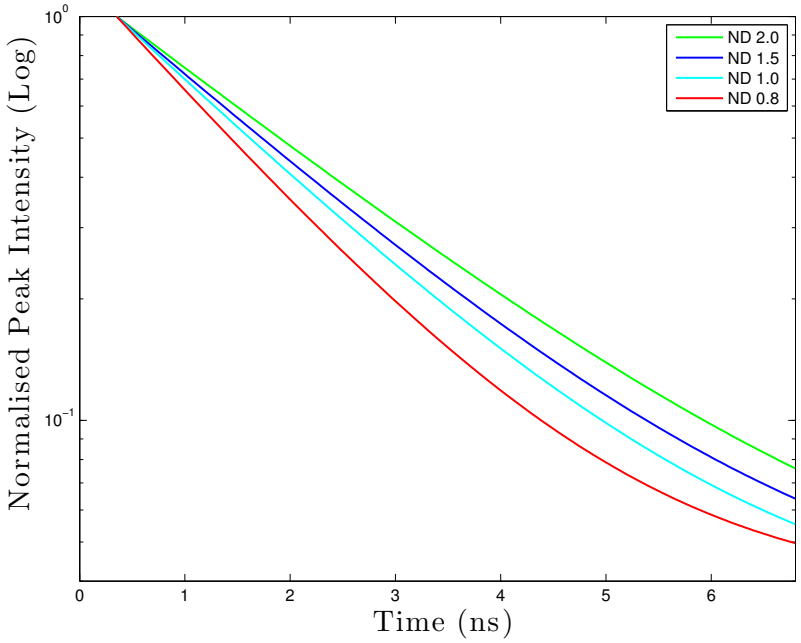

Figure 4.26: Summary of calculated transient profiles Type I beads by Fourier Transformation of phasors, where ND is the optical density of the neutral density used in the controlling of the laser excitation power (see Table 4.23 below).

ND	Power (mW)	u	v	τ_p	τ_m	τ	χ^2_R / d.f.
2.0	0.01	0.190	0.406	2.22	2.07	2.14	28
1.5	0.03	0.230	0.413	1.87	1.93	1.90	76
1.0	0.10	0.262	0.420	1.66	1.82	1.74	218
0.8	0.16	0.332	0.439	1.36	1.59	1.48	382

Table 4.23: Summary of the lifetime calculation from the integrated transient profile of Type I beads by Fourier Transformation of the phasors (Burst Mode), per power setting, where Power is the excitation power in mW, u and v are the centre values of the corresponding axes. τ_p is the lifetime component calculated from the phase delay of the modulated signal waveform from the modulated excitation laser rate in ns, τ_m is the lifetime component calculated from the demodulation between the two modulated waveforms in ns. τ is the average of the two lifetime components in ns and χ^2_R is the goodness of fit (or calculation) parameter of the Fourier transformation of the phasors.

From Figure 4.26, the effect of the multi-exponential decay on the phasor analysis is less subtle than the NL-MLM, but follows the same trend as in Figure 4.25. In order to gain a more complete picture of the pile-up behaviour by the excessive increase in power, the phasor distribution in the phasor analysis of each BIFL pixel will be closely examined in the following section (section 4.4).

4.4 Flow Experiment: Burst-generated Lifetime Data (Type I Beads)

In this section, the lifetime of Type I beads will be calculated on the individual pixel basis. NL-MLM and phasor analysis of Type I beads will be shown explicitly for each power setting listed in Table 4.13. For the NL-MLM fitting method, the corresponding BIFL image with a false colour scale will be used to represent the lifetime of the bursts, alongside the histogram of those lifetimes. The phasor analysis will first introduce a contour plot of the phasors and histograms of the u and v coordinates, before showing the lifetime of the bursts from Fourier transformation of the phasors with the same representation of BIFL image, and

the corresponding lifetime histogram as the NL-MLM section.

4.4.1 NL-MLM Analysis (Type I Beads) at 0.01 mW

Figure 4.27 shows the BIFL image and the corresponding lifetime histogram of Type I beads, excited at 0.01 mW. The bead solution was pumped at 220 mbar of air supply.

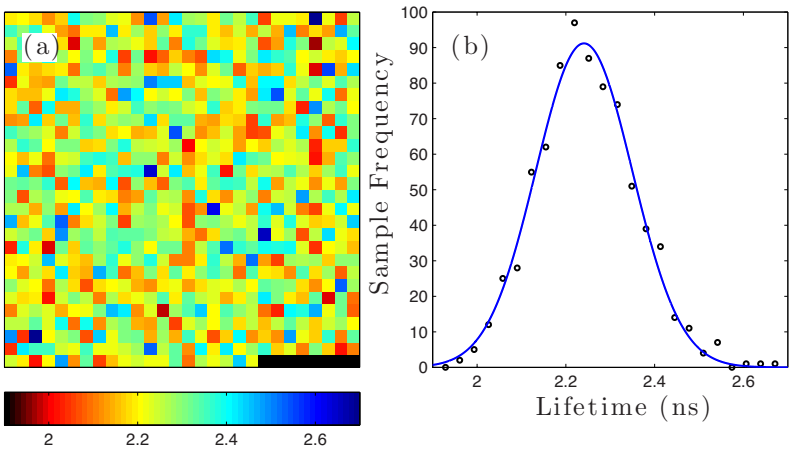

Figure 4.27: (a) A successfully analysed BIFL image (28 by 28 pixels) containing the lifetime of 776 bursts, by NL-MLM. (b) The corresponding lifetime histogram of the BIFL data in (a).

A	τ	σ
91	2.24	0.15

Table 4.24: Summary of the lifetime fitting parameters of Type I beads excited at 0.01 mW (see Figure 4.27 (b)), where A is the peak height of the distribution, τ is the lifetime in ns, and σ is the standard deviation of the distribution in ns.

Within 10 minutes, 776 bursts were acquired. The average lifetime of Type I beads at this power setting was calculated to be 2.24 ± 0.15 ns. This is 200 ps shorter than calculated from FLIM acquisition at 2.44 ± 0.24 ns. The small pulse

pile-up is relatively reasonable, as the average instantaneous count rate of the acquisition was approximately 2.4×10^6 counts per second corresponding to $\sim$0.03 photons per excitation event.

4.4.2 Phasor Analysis (Type I Beads) at 0.01 mW

Figure 4.28 shows the contour plot of the phasors for Type I beads excited at 0.01 mW, the histograms of each phasor co-ordinates (u and v).

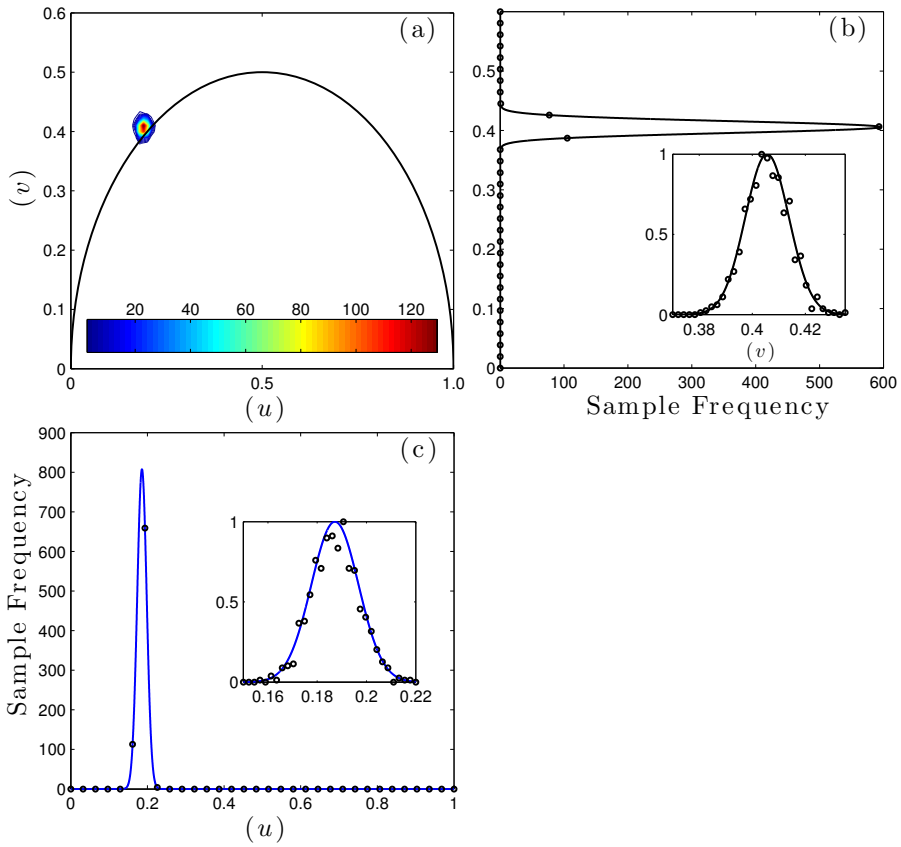

Figure 4.28: (a) Contour plot of phasors from the BIFL image (28 by 28 pixels) containing 776 bursts. (b) Main and inset panels show the corresponding v–coordinate distribution of the phasors. (c) Main and inset panels show the corresponding u–coordinate distribution of the phasors.

A	u	σ
73	0.187	0.014

Table 4.25: Summary of the Gaussian fit for the u–coordinate of Type I beads (BIFL) excited at 0.01 mW (see Figure 4.28 (c)), where A is the peak height of the distribution, u is the centre u-coordinate, and σ is the standard deviation of the distribution.

A	v	σ
79	0.406	0.012

Table 4.26: Summary of the Gaussian fit for the v–coordinate of Type I beads (BIFL) excited at 0.01 mW (see Figure 4.28 (b) (inset)), where A is the peak height of the distribution, v is the centre v-coordinate, and σ is the standard deviation of the distribution.

The Fourier transformation of the phasors in the BIFL image format and the corresponding lifetime histogram is shown in Figure 4.29.

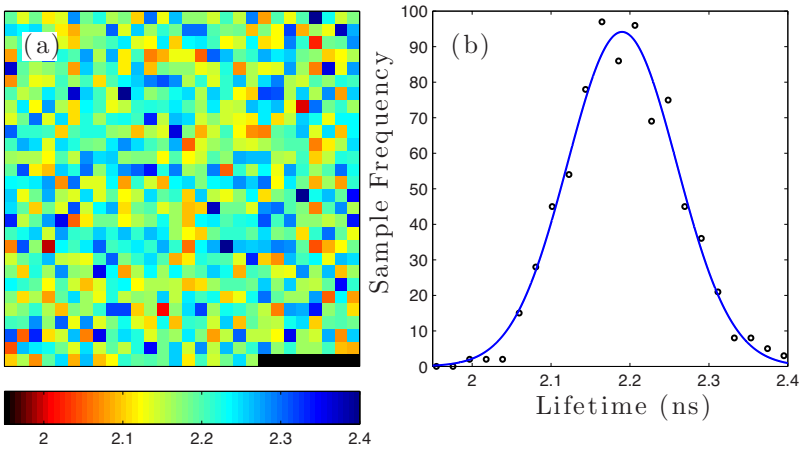

Figure 4.29: (a) A successfully calculated BIFL image by Fourier Transformation of phasors (28 by 28 pixels) containing the lifetime of 776 bursts. (b) The corresponding lifetime histogram of the BIFL data.

A	τ	σ
94.17	2.19	0.10

Table 4.27: Summary of the lifetime fitting parameters of Type I beads (BIFL) excited at 0.01 mW by FT(Phasor) (see Figure 4.29 (b)), where A is the peak height of the distribution, τ is the lifetime in ns, and σ is the standard deviation of the distribution in ns.

From Figure 4.28, the phasors of Type I beads were evenly distributed at coordinates $(0.187 \pm 0.014,\ 0.406 \pm 0.012)$ of the contour plot. This is relatively

close to those of the FLIM image at $(0.169 \pm 0.019, 0.390 \pm 0.016)$. The phasors also aggregate on top of the universal semi-circle, and so despite the difference in the centre u–coordinate (which will influence the calculation of lifetime) between the FLIM and flow experiments, the lifetime is still characterised by the mono-exponential decay at this power setting. From Figure 4.29, the average lifetime of the beads was calculated to be 2.19 ± 0.10 ns. This is 100 ps shorter than the FLIM acquisition at 2.29 ± 0.14 ns.

4.4.3 NL-MLM Analysis (Type I Beads) at 0.03 mW

Figure 4.30 shows the BIFL image and the corresponding lifetime histogram of Type I beads, excited at 0.03 mW.

Within 10 minutes, 653 bursts were acquired. The average lifetime of Type I beads at this power setting was calculated to be 1.88 ± 0.08 ns. This is 560 ps shorter than calculated from FLIM acquisition at 2.44 ± 0.24 ns. The pulse pile-up is now having significant effect on the reduction of lifetime, as the average instantaneous count rate of the acquisition was approximately 4.6×10^6 counts per second (0.06 photons per excitation). The average integral intensity of the burst was 1.6×10^4 photon counts and consequently results in a significant decrease in the standard deviation of the lifetime, by 158 ps in relation to the FLIM acquisition.

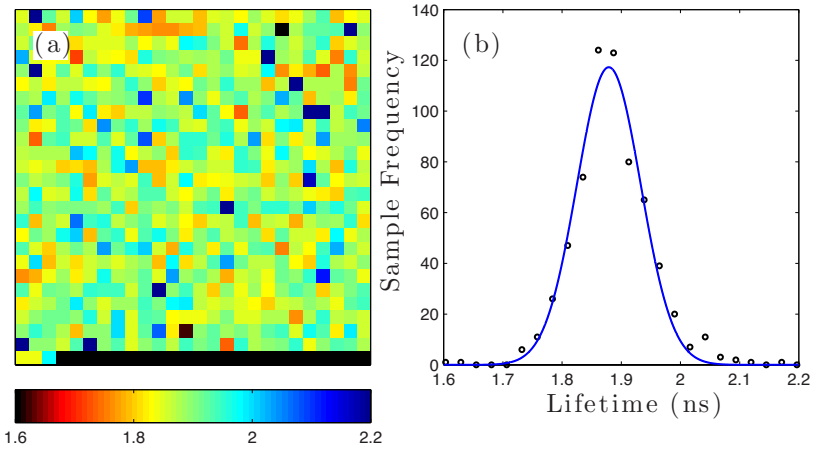

Figure 4.30: (a) A successfully analysed BIFL image (26 by 26 pixels) containing the lifetime of 653 bursts, by NL-MLM. (b) The corresponding lifetime histogram of the BIFL data.

A	τ	σ
117	1.88	0.076

Table 4.28: Summary of the lifetime fitting parameters of Type I beads (BIFL) excited at 0.03 mW by NL-MLM (see Figure 4.30 (b)), where A is the peak height of the distribution, τ is the lifetime in ns, and σ is the standard deviation of the distribution in ns.

4.4.4 Phasor Analysis (Type I Beads) at 0.03 mW

Figure 4.31 shows a contour plot of phasors of type I beads, excited at 0.03 mW, the histograms of each phasor co-ordinates (u and v). The Fourier transformation of the phasors in the BIFL image format along with the corresponding lifetime histogram is shown in Figure 4.32.

From Figure 4.31, the phasors of Type I beads were approximately, evenly distributed at co-ordinates (0.228 ± 0.010, 0.413 ± 0.008) of the contour plot. The centre u and v coordinates are considerably different from those of the FLIM image (0.169 ± 0.019, 0.390 ± 0.016). The phasors begin to aggregate just inside

of the universal semi-circle, and so a small simulation of the lifetime quenching, due to the degradation in the counting efficiency and pile-up can be expected here.

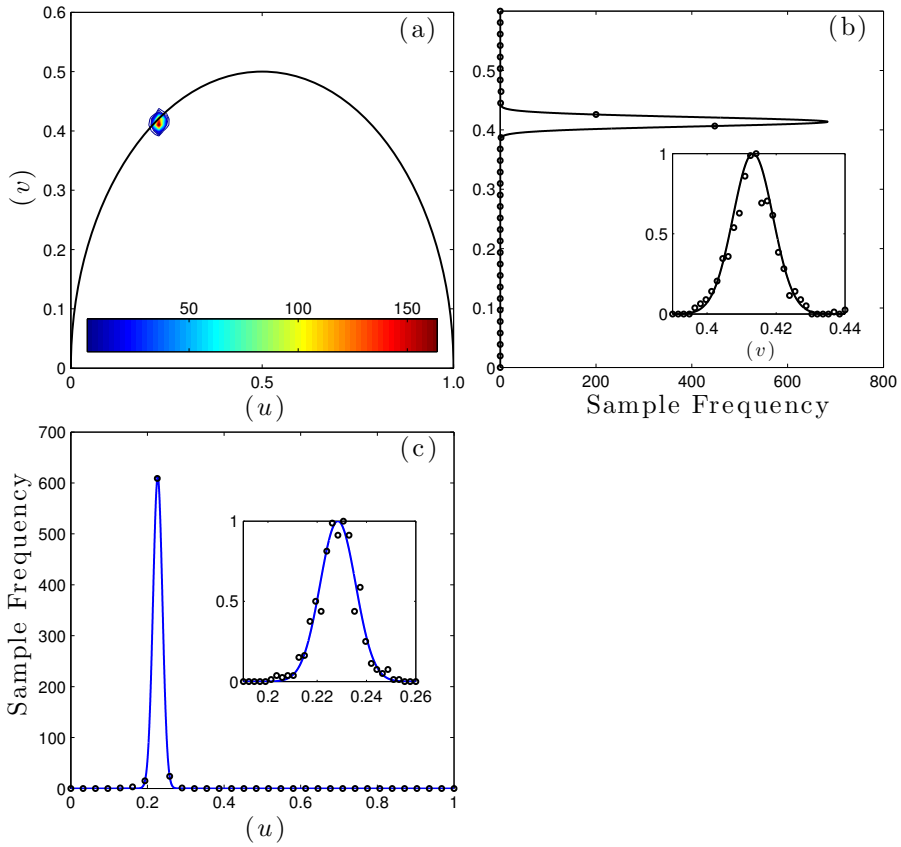

Figure 4.31: (a) A Phasor Analysis of BIFL image (26 by 26 pixels) containing 653 bursts. (b) Main and inset panels show the corresponding v–coordinate distribution of the phasors. (c) Main and inset panels show the corresponding u–coordinate distribution of the phasors.

A	u	σ
78	0.228	0.010

Table 4.29: Summary of the Gaussian fit for the u–coordinate of Type I beads (BIFL) excited at 0.03 mW (see Figure 4.31 (c)), where A is the peak height of the distribution, u is the centre u-coordinate, and σ is the standard deviation of the distribution.

A	v	σ
71	0.413	0.008

Table 4.30: Summary of the Gaussian fit for the v–coordinate of Type I beads (BIFL) excited at 0.03 mW (see Figure 4.31 (b) (inset)), where A is the peak height of the distribution, v is the centre v-coordinate, and σ is the standard deviation of the distribution.

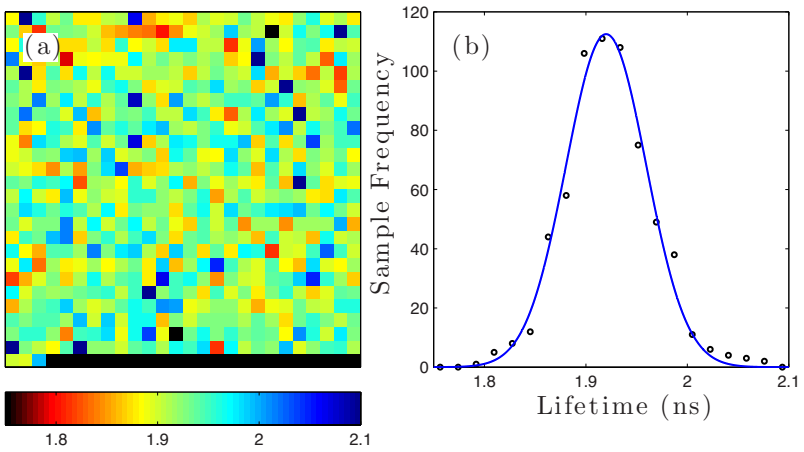

Figure 4.32: (a) A successfully calculated BIFL image by Fourier Transformation of phasors (28 by 28 pixels) containing the lifetime of 776 bursts. (b) The corresponding lifetime histogram of the BIFL data.

A	τ	σ
113	1.92	0.06

Table 4.31: Summary of the lifetime fitting parameters of Type I beads (BIFL) excited at 0.03 mW by FT(Phasor) (see Figure 4.32 (b)), where A is the peak height of the distribution, τ is the lifetime in ns, and σ is the standard deviation of the distribution in ns.

From Figure 4.32, the average lifetime of the bead was calculated to be 1.92 ± 0.06 ns. This is 370 ps shorter than the FLIM acquisition at 2.29 ± 0.14 ns.

4.4.5 NL-MLM Analysis (Type I Beads) at 0.10 mW

Figure 4.33 shows the BIFL image and the corresponding lifetime histogram of Type I beads, excited at 0.10 mW.

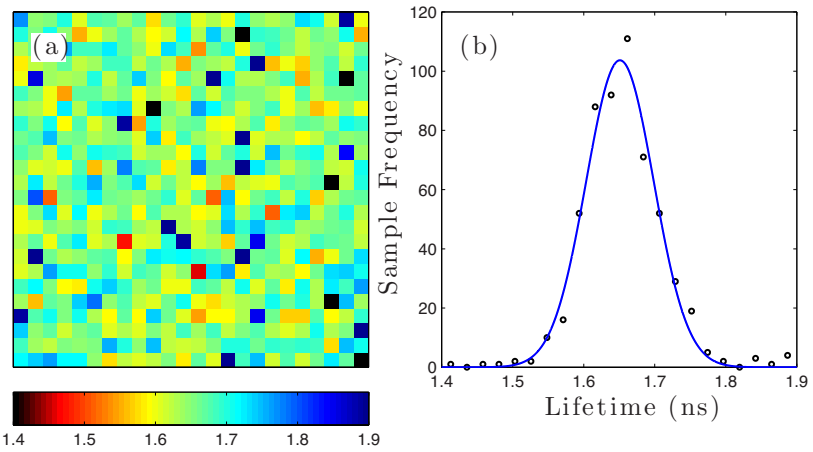

Figure 4.33: (a) A successfully analysed BIFL image (24 by 24 pixels) containing the lifetime of 575 bursts, by NL-MLM. (b) The corresponding lifetime histogram of the BIFL data.

A	τ	σ
104	1.65	0.07

Table 4.32: Summary of the lifetime fitting parameters of Type I beads excited at 0.10 mW by NL-MLM (see Figure 4.33 (b)), where A is the peak height of the distribution, τ is the lifetime in ns, and σ is the standard deviation of the distribution in ns.

Within 10 minutes, 575 bursts were acquired. The average lifetime of Type I beads at this power setting was calculated to be 1.65 ± 0.07 ns. This is 789 ps shorter than calculated from FLIM acquisition at 2.44 ± 0.24 ns. The pulse pile-up is now having significant effect on the reduction of lifetime, despite a 0.4×10^6 count drop in the average instantaneous count rate from the previous case, at 0.03 mW of excitation power. As mentioned in the burst characteristics analysis in subsection 4.4.5, it is possible that the degradation of TCSPC photon counting efficiency begins to counteract the increasing rate of the instantaneous photon counts. However this will be investigated in the phasor analysis in following section (subsection 4.4.6) in more details. The average integral intensity of the burst consists of two populations at 1.6×10^4 and 1.75×10^4 counts and consequently results in a further drop in the standard deviation of the lifetime, by 171 ps in relation to the FLIM acquisition.

4.4.6 Phasor Analysis (Type I Beads) at 0.10 mW

Figure 4.34 shows a contour plot of phasors of type I beads excited at 0.10 mW, the histograms of each phasor co-ordinates (u and v). The Fourier transformation of the phasors in the BIFL image format along with the corresponding lifetime histogram is shown in Figure 4.35.

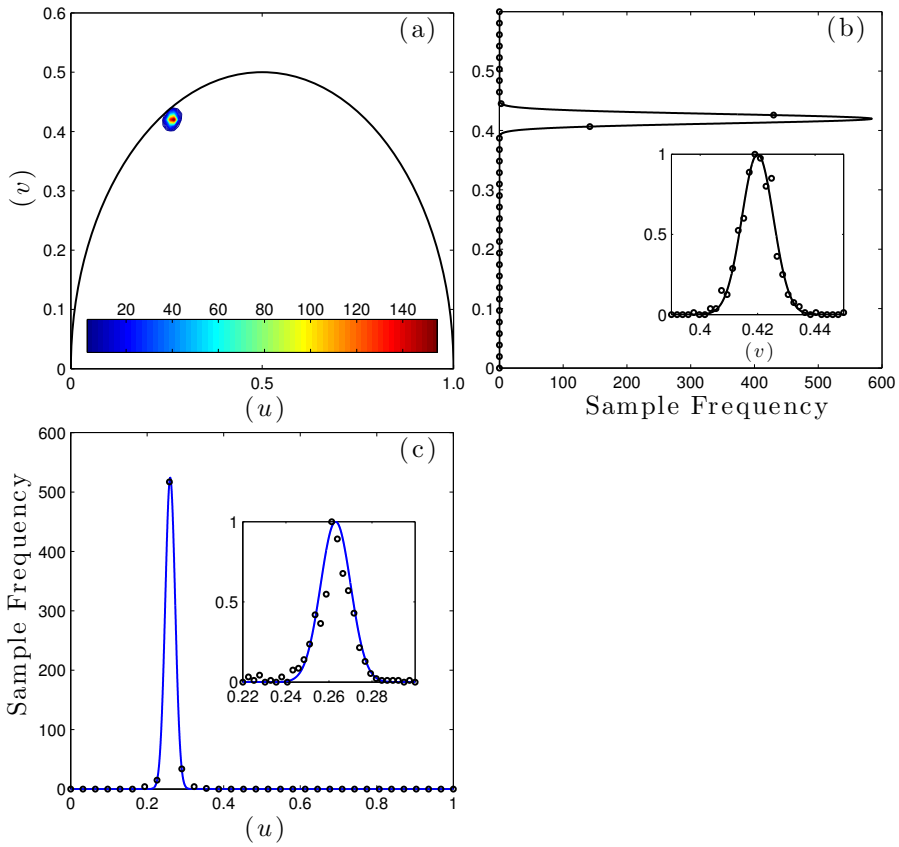

Figure 4.34: (a) A Phasor Analysis of BIFL image (24 by 24 pixels) containing 575 bursts. (b) Main and inset panels show the corresponding v–coordinate distribution of the phasors. (c) Main and inset panels show the corresponding u–coordinate distribution of the phasors.

A	u	σ
79	0.263	0.010

Table 4.33: Summary of the Gaussian fit for the u–coordinate of Type I beads (BIFL) excited at 0.10 mW (see Figure 4.34 (b) (inset)), where A is the peak height of the distribution, u is the centre u-coordinate, and σ is the standard deviation of the distribution.

A	v	σ
80	0.420	0.008

Table 4.34: Summary of the Gaussian fit for the v–coordinate of Type I beads (BIFL) excited at 0.10 mW from Figure 4.34 (c), where A is the peak height of the distribution, v is the centre v-coordinate, and σ is the standard deviation of the distribution.

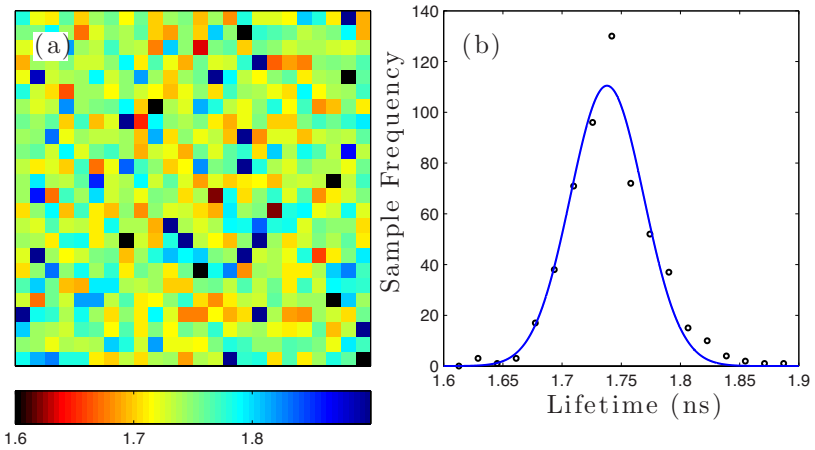

Figure 4.35: (a) A successfully calculated BIFL image by Fourier Transformation of phasors (24 by 24 pixels) containing the lifetime of 575 bursts. (b) The corresponding lifetime histogram of the BIFL data.

A	τ	σ
111	1.74	0.04

Table 4.35: Summary of the lifetime fitting parameters of Type I beads excited at 0.10 mW by FT(Phasor) (see Figure 4.35 (b)), where A is the peak height of the distribution, τ is the lifetime in ns, and σ is the standard deviation of the distribution in ns.

From Figure 4.34, the phasors of Type I beads were approximately, evenly distributed at co-ordinates $(0.263 \pm 0.010,\ 0.420 \pm 0.008)$ of the contour plot. The centre u and v coordinates are further different from those of the FLIM image $(0.169 \pm 0.019,\ 0.390 \pm 0.016)$. The phasor cluster now fully resides inside of the

universal semi-circle, and so lifetime quenching, due to the degradation in the counting efficiency can be confidently assumed here.

From Figure 4.35, the average lifetime of the bead was calculated to be 1.74±0.04 ns. This is 550 ps shorter than the FLIM acquisition at 2.29 ± 0.14 ns.

4.4.7 NL-MLM Analysis (Type I Beads) at 0.16 mW

Figure 4.36 shows the BIFL image and the corresponding lifetime histogram of Type I beads, excited at 0.16 mW. The bead solution was pumped at 500 mb of air supply (approximately twice as much from the previous cases), to avoid excessive pulse pile-up and FIFO overflow problem.

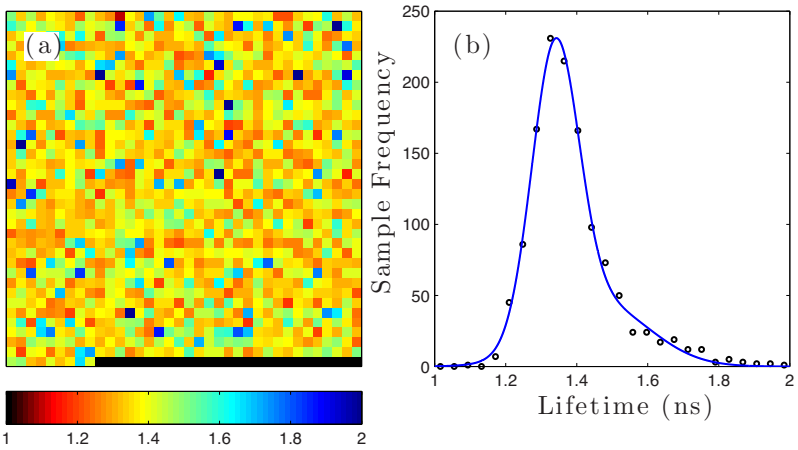

Figure 4.36: (a) A successfully analysed BIFL image (36 by 36 pixels) containing the lifetime of 1269 bursts, by NL-MLM. (b) The corresponding lifetime histogram of the BIFL data.

A_1	τ_1	σ_1	A_2	τ_2	σ_2	Ave. τ	Ave. σ
202	1.34	0.09	43	1.47	0.20	1.36	0.13

Table 4.36: Summary of the lifetime fitting parameters of Type I beads excited at 0.16 mW by NL-MLM (BIFL) (see Figure 4.36 (b)) . The average lifetime of the control was calculated by a double Gaussian mixture model, where A_1 and A_2 are the fractional contributions from the number of pixel of the image, τ_1 and τ_2 are the mean lifetimes measured in ns, and σ_1 and σ_2 are the standard deviations of each sub-population in ns. Ave. τ and Ave. σ reprensents the average lifetime and the associated standard deviation in ns respectively.

Within 10 minutes, 1,269 bursts were acquired. This is approximately twice the throughput from the previous cases, and is consistent to the doubling of pumping pressure in this acquisition. The shape of the lifetime histogram is positively skewed, but can be fitted with a double Gaussian mixture model to good effect. The ratio of the fractional contribution from each Gaussian distributed population is approximately 5:1. The dominating population has an average lifetime of 1.34 ± 0.09 ns, while the subordinate population has an average lifetime of 1.47 ± 0.20 ns. The weighted average lifetime between the two populations was calculated to be 1.36 ± 0.13 ns. This is 1.08 ns shorter than calculated from FLIM acquisition at 2.44 ± 0.24 ns. The pulse pile-up is by far having strongest effect on the reduction of lifetime of the beads in this case, due to this excessively high power setting.

4.4.8 Phasor Analysis (Type I Beads) at 0.16 mW

Figure 4.37 shows a contour plot of phasors of type I beads excited at 0.16 mW, the histograms of each phasor co-ordinates (u and v). The Fourier transformation of the phasors in the BIFL image format along with the corresponding lifetime histogram is shown in Figure 4.38.

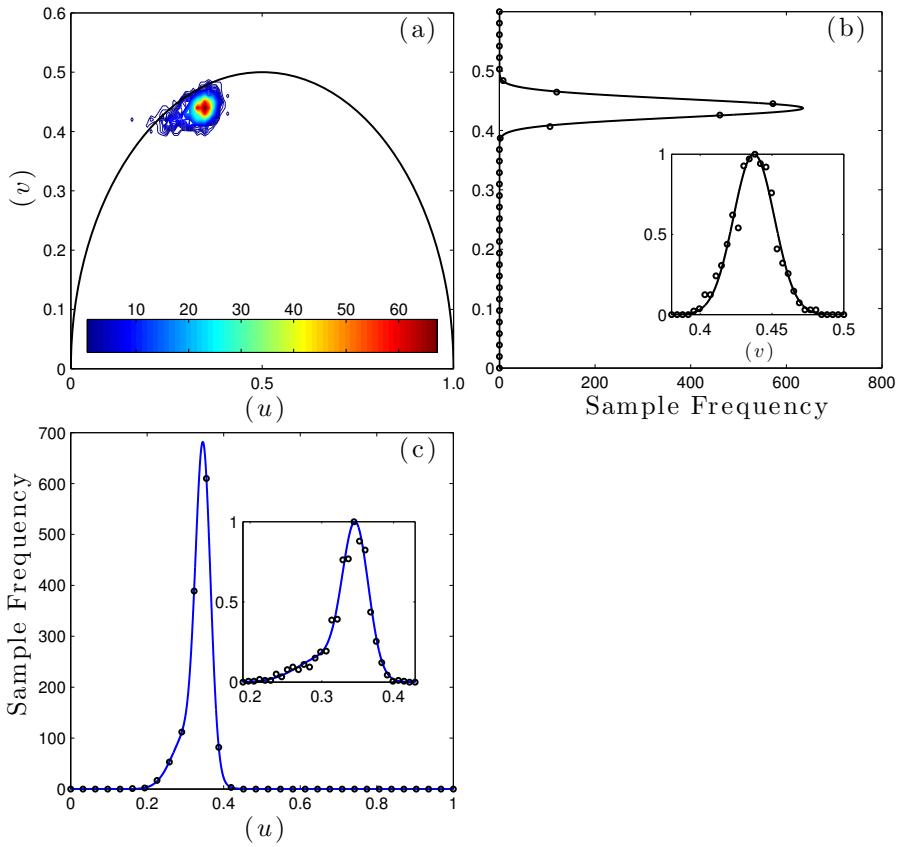

Figure 4.37: (a) A Phasor Analysis of BIFL image (36 by 36 pixels) containing 1269 bursts. (b) Main and inset panels show the corresponding u–coordinate distribution of the phasors. (c) Main and inset panels show the corresponding v–coordinate distribution of the phasors.

A_1	u_1	σ_1	A_2	u_2	σ_2	Ave. u	Ave. σ
161	0.347	0.025	28	0.305	0.052	0.341	0.033

Table 4.37: Summary of the Gaussian fit for the u–coordinate of Type I beads (BIFL) excited at 0.16 mW (see Figure 4.37 (b) (inset)). The approximate centre u–coordinate of Type I beads (Ave. u) and its error (Ave. σ) were calculated by a double Gaussian mixture model, where A_1 and A_2 are the fractional contributions from the number of pixel of the image, u_1, u_2, σ_1 and σ_2 are the centre u–coordinates and standard deviations of each sub-population respectively.

A	v	σ
136	0.437	0.020

Table 4.38: Summary of the Gaussian fit for the v–coordinate of Type I beads (BIFL) excited at 0.16 mW (see Figure 4.37 (c)), where A is the peak height of the distribution, v is the centre v-coordinate, and σ is the standard deviation of the distribution.

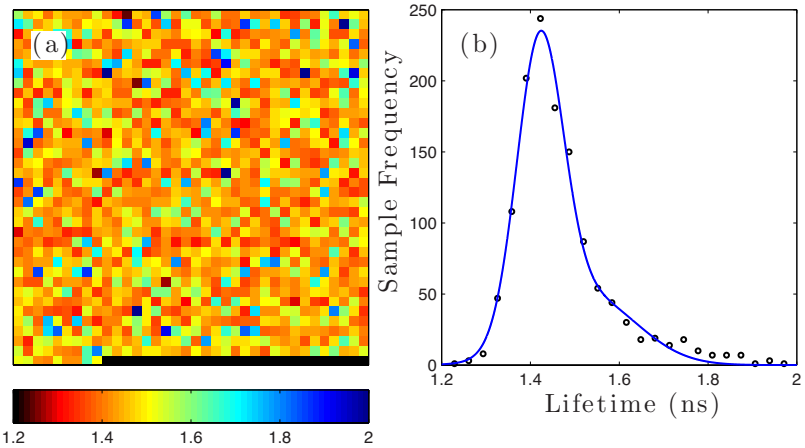

Figure 4.38: (a) A successfully calculated BIFL image by Fourier Transformation of phasors (28 by 28 pixels) containing the lifetime of 776 bursts. (b) The corresponding lifetime histogram of the BIFL data.

A_1	τ_1	σ_1	A_2	τ_2	σ_2	Ave. τ	Ave. σ
1206	1.42	0.07	47	1.53	0.16	1.44	0.10

Table 4.39: The table of summary for the lifetime fitting for Type I bead by NL-MLM (BIFL) (see Figure 4.38 (b)). The average lifetime of the control was calculated by a double Gaussian mixture model, where A_1 and A_2 are the fractional contributions from the number of pixel of the image, τ_1 and τ_2 are the mean lifetimes measured in ns, and σ_1 and σ_2 are the standard deviations of each sub-population in ns. Ave. τ and Ave. σ reprensents the average lifetime and the associated standard deviation in ns respectively.

From Figure 4.37 (a), the phasor plot of Type I beads clearly shows the skewed cloud of the phasor cluster. This suggests there are multiple bead populations,

which perhaps experienced different levels of excitation power. As extensively highlighted in chapter 3, an increase in pumping pressure can result in a change of streamlines. Hence some beads could travel in the streamlines away from the probe, while others still travel in lines close to the probe. The excessively high laser power illuminates much of the channel. Any bead regardless of the streamlines it travels in will likely to be excited to some extent, where the relative distance of the streamline to the probe will dictate the power absorption. Figure 4.37 (c) shows the average u–coordinates is negatively skewed. The ratio of the fractional contribution from each Gaussian distributed population is approximately 6:1. The dominating population has a centre u coordinate of 0.347 ± 0.025, while the subordinate population has a centre u coordinate of 0.305 ± 0.052. The average centre u coordinate between the two populations was calculated to be 0.342 ± 0.032.

The centre v–coordinate of the phasor is 0.437 ± 0.020. The coordinate pair $(0.342 \pm 0.033,\ 0.437 \pm 0.020)$ is significantly different from those of the FLIM image at $(0.169 \pm 0.019,\ 0.390 \pm 0.016)$. The skewed phasor cluster resides relatively far inside of the universal semi-circle compare to previous cases.

From Figure 4.37 (b), the average lifetime distribution of the beads was positively skewed. This is a close mirror reflection of the histogram of the u coordinate. The ratio of the fractional contribution from each Gaussian distributed population is approximately 4:1. The dominating population has an average lifetime of 1.42 ± 0.07, while the subordinate population has an average lifetime of 1.53 ± 0.16. The average lifetime between the two populations was calculated to be 1.44 ± 0.10 ns. This is 850 ps shorter than the FLIM acquisition at 2.29 ± 0.14 ns.

4.5 Flow Experiment: Burst and Transient Characteristics (Type II Beads)

This section will show the burst width, integral burst intensity and instantaneous count rate of the bursts of the Type II beads, excited at 0.03 mW, 0.10 mW and

0.16 mW respectively. The excitation at 0.01 mW (the same power setting which was used in the FLIM section) was insufficient in exciting the beads in flow and hence the related result will be omitted from the section.

The results will be summarised in the same layout structure as section 4.4. The bead solution was pumped at 250 mbar of pressure in every acquisition, with the exception of the 0.16 mW case, where the pumping pressure was increased to 500 mbar to replicate a similar flow condition to Type I beads at the same power. The power setting will be used to excite the mixed bead population, and so the results in this investigation and the one of Type I beads will be used as the experimental reference for the mixed population experiment. The average photon yield of the beads is generally low, and so the chance of misdetection from the streamlines near the probe can be high. The stock concentration of the beads was increased from 5 μl to 10 μl for the 5 ml sample dilution, to increase the number of streamlines in and around the probe.

4.5.1 Burst Characteristics of Type II Bead at 0.03 mW of Excitation Power

Figure 4.39 collates the burst characteristics of Type II beads excited at 0.03 mW power. The bead solution was pumped at 250 mbar of pressure and the data was acquired for 10 minutes.

The average burst width of the beads is approximately 1.4 ms, and is different from the Type I beads at 3.2 ms. This number is credible, since the materials of the beads are distinctively different. The average integral intensity consists of 2 populations, approximately centring at 250 and 380 counts. However both populations are insufficient for the mono-exponential model of NL-MLM analysis, as will be shown in further details in subsection 4.6.1. The average instantaneous burst count rate moderately centring at approximately 2.5×10^5 counts per second, which is well below the safe count limit at 8.0×10^5 counts per second.

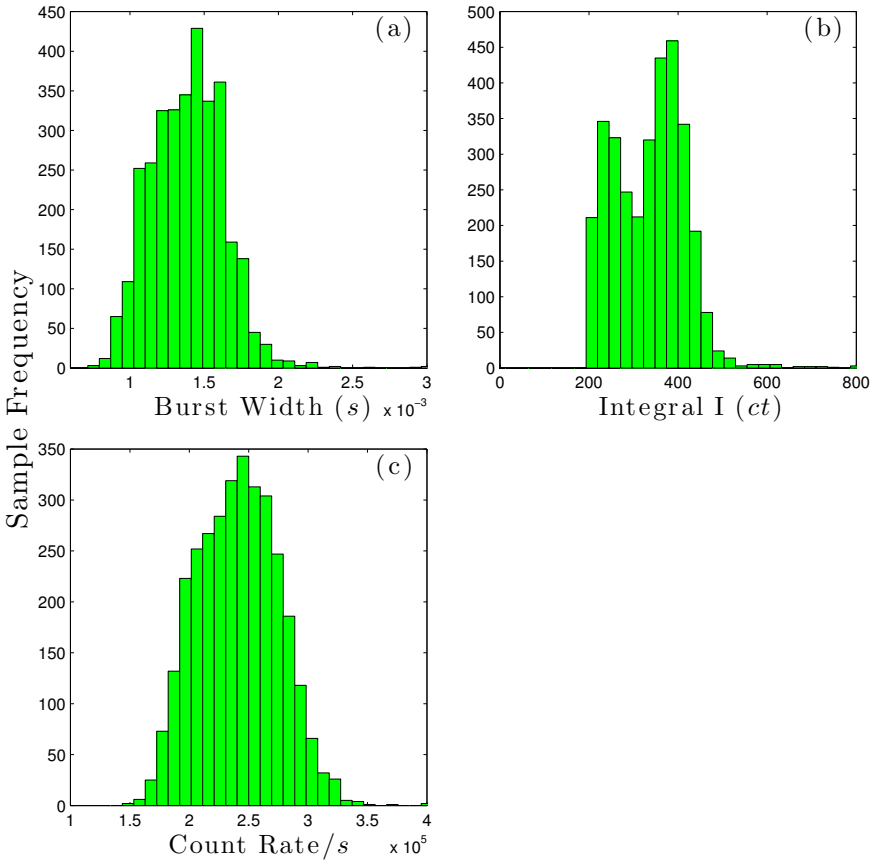

Figure 4.39: Burst characteristics of Type II beads at 0.03 mW of excitation power, where (a), (b), and (c) represents the burst widths, integral intensities, instantaneous count rates during each burst detection, respectively.

4.5.2 Integrated Lifetime Analysis of Type II beads at 0.03 mW of Excitation Power

Fitting with NL-MLM Algorithm

The integrated transient profile of the bursts acquired at 0.03 mW of excitation power and fitted with a mono-exponential decay by the NL-MLM algorithm is shown in Figure 4.40.

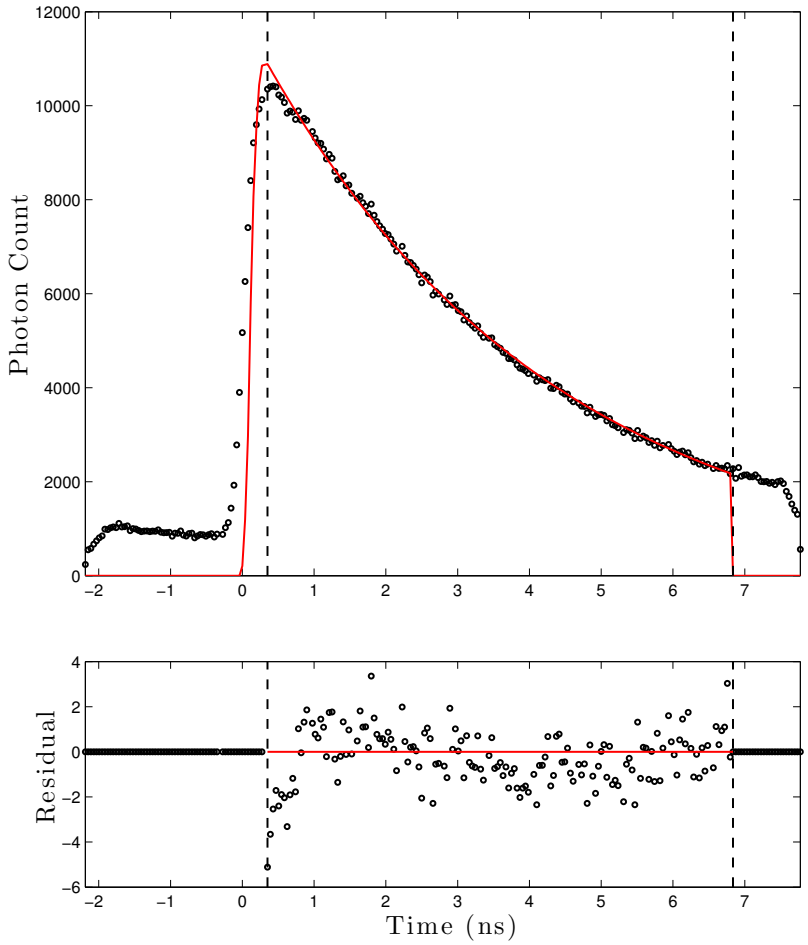

Figure 4.40: Integrated Transient profile of Type II beads. The transient is fitted a mono-exponential model by the NL-MLM.

Z	A	τ	χ^2_R / d.f.
-69	11537	4.07	2.86

Table 4.40: Summary of the mono-exponential fit on the integrated transient profile of Type I beads by NL-MLM (Burst Mode) excited at 0.03 mW, where Z is the baseline level, A is the peak amplitude and τ is the lifetime of the transient. χ^2_R is the goodness of fit parameter.

The integrated analysis of Type II beads by NL-MLM shows that lifetime is fit to

be 4.07 ns. This is 170 ps longer than the one analysed from the FLIM image at 3.90 ns. With the support of the modest instantaneous count rate and closeness of the lifetime to the experimental reference, it is safe to conclude that these data were free from the pulse pile-up effect.

Fitting with Fourier Transformation of Phasors

Figure 4.41 shows the integrated transient profile of the bursts acquired at 0.03 mW of excitation power where the fit to the data is calculated by the Fourier transformation of the phasors.

The integrated lifetime of Type II beads was calculated to be 3.62 ns. This is 80 ps longer than the experimental reference at 3.54 ns. As for all the integrated data the multi-exponential nature of the fit is quite evident for these data and perhaps more pronounced than the NL-MLM fit since this is a calculation rather than a fit and does not include convolution of the prompt with the fit.

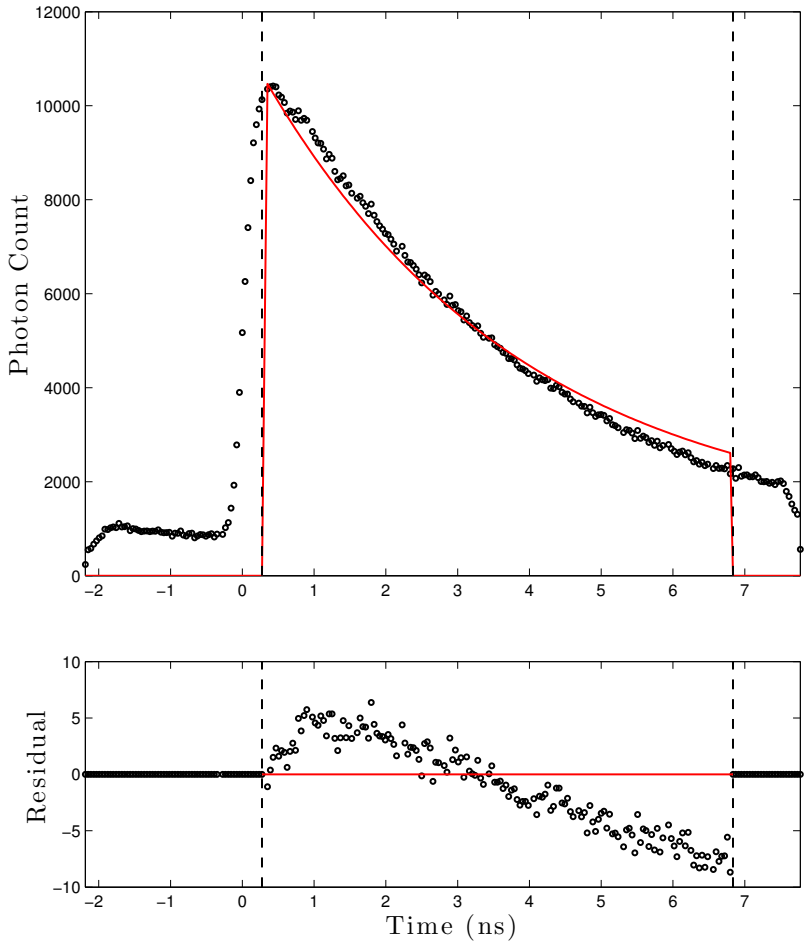

Figure 4.41: Integrated Transient profile of Type II beads calculated by the Fourier Transformation of the phasors.

u	v	τ_p	τ_m	τ	χ^2_R / d.f.
0.077	0.303	4.10	3.16	3.63	19

Table 4.41: Summary of the lifetime calculation from the integrated transient profile of Type II beads by Fourier Transformation of the phasors (Burst Mode) excited at 0.03 mW, where u and v are the centre values of the corresponding axes. τ_p is the lifetime component calculated from the phase delay of the modulated signal waveform from the modulated excitation laser rate in ns, τ_m is the lifetime component calculated from the demodulation between the two modulated waveforms in ns. τ is the average of the two lifetime components in ns and χ^2_R is the goodness of fit (or calculation) parameter of the Fourier transformation of the phasors.

4.5.3 Burst Characteristics of Type II Bead at 0.10 mW of Excitation Power

Figure 4.42 collates the burst characteristics of Type II beads excited at 0.10 mW power. The bead solution was pumped at 250 mbar of pressure and the data was acquired for 20 minutes.

The average burst width of the beads consisted of 2 populations, centring approximately at 1.2 ms, and 1.4 ms where the latter is more broadly distributed than the former. The average integral intensity has improved from the previous case and now consists of 2 populations, approximately centring at 450 and 700 counts. This is similar to the characteristics of the burst width histogram, as the latter population is more broadly distributed than the former. However both integral intensity populations are still insufficient for the mono-exponential model of NL-MLM analysis, as will be show in further details in subsection 4.6.3. The average instantaneous burst count rate now centres at approximately 4.2×10^5 counts per second, but is still below the safe count limit at 8.0×10^5 counts per second.

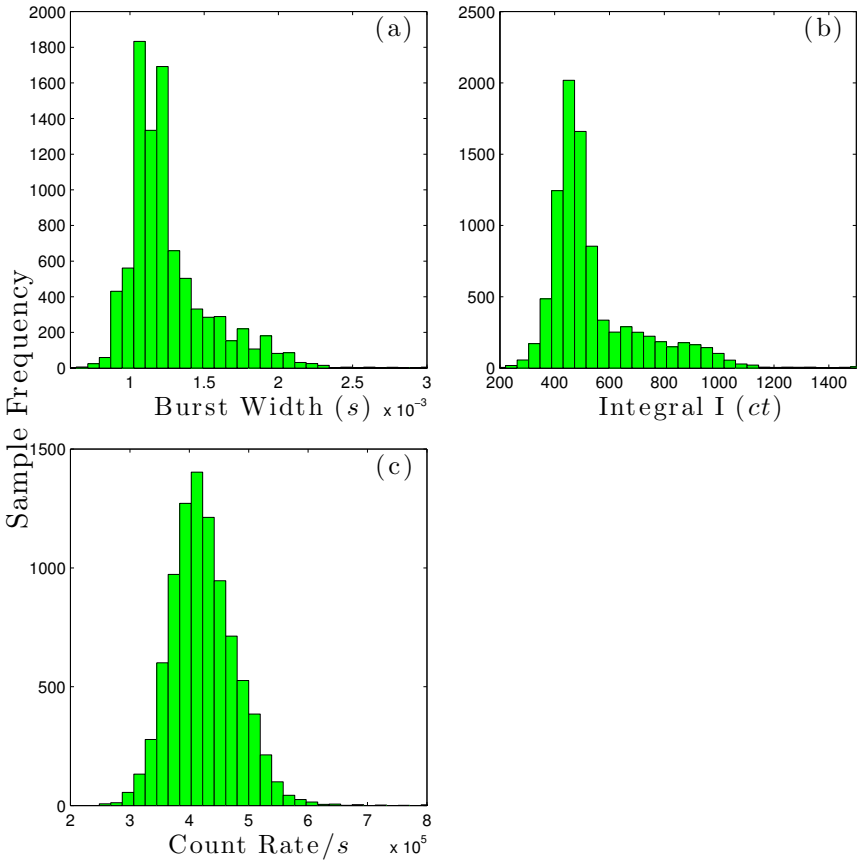

Figure 4.42: Burst characteristics of Type II beads at 0.10 mW of excitation power, where (a), (b), and (c) represents the burst widths, integral intensities, instantaneous count rates during each burst detection, respectively.

4.5.4 Integrated Lifetime Analysis of Type II beads at 0.10 mW of Excitation Power

Fitting with NL-MLM Algorithm

The integrated transient profile of the bursts acquired at 0.10 mW of excitation power and fitted with a mono-exponential decay by the NL-MLM algorithm is shown in Figure 4.43).

Z	A	τ	χ^2_R / d.f.
-65	51121	4.03	10

Table 4.42: Summary of the mono-exponential fit by NL-MLM on the integrated transient profile of Type II beads (Burst Mode) excited at 0.10 mW, where Z is the baseline level, A is the peak amplitude and τ is the lifetime of the transient in ns. χ^2_R is the goodness of fit parameter.

The integrated analysis of Type II beads by NL-MLM shows that lifetime is calculated to be 4.03 ns. This is 130 ps longer than analysed from the FLIM image at 3.90 ns. The instantaneous count rate range of the data was also within the single photon count limit of TCSPC. The lifetime of the transient is has the same characteristic as all the integrated data and the experimental reference.

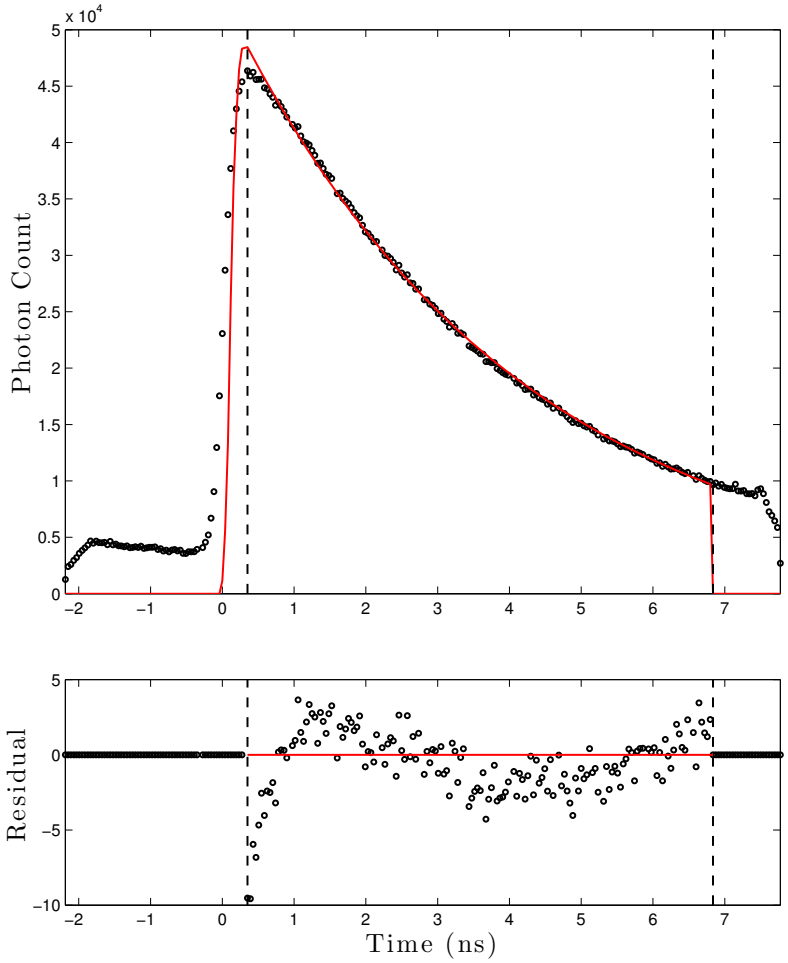

Figure 4.43: Integrated Transient profile of Type II beads. The transient is fitted a mono-exponential model by the NL-MLM.

Fitting with Fourier Transformation of Phasors

Figure 4.44 shows the integrated transient profile of the bursts acquired at 0.10 mW of excitation power where the fit to the data is calculated by the Fourier transformation of the phasors.

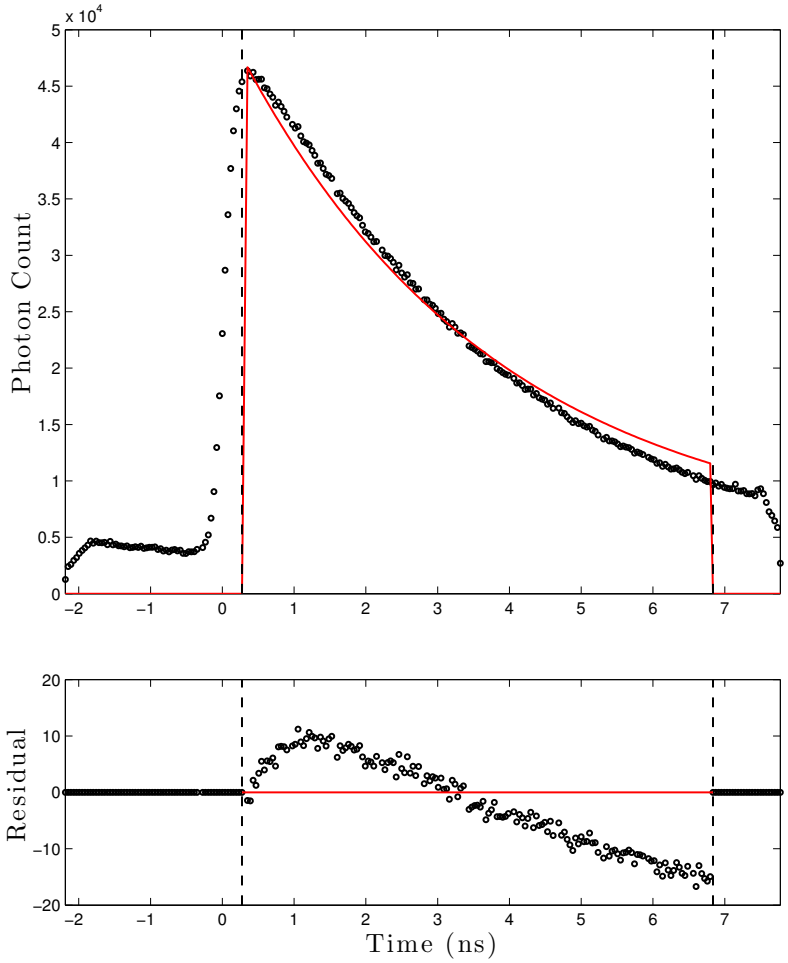

Figure 4.44: Integrated Transient profile of Type II beads calculated by the Fourier Transformation of the phasors.

u	v	τ_p	τ_m	τ	χ^2_R / d.f.
0.078	0.303	4.06	3.15	3.60	74

Table 4.43: Summary of the lifetime calculation from the integrated transient profile of Type II beads by Fourier Transformation of the phasors (Burst Mode) excited at 0.10 mW, where u and v are the centre values of the corresponding axes. τ_p is the lifetime component calculated from the phase delay of the modulated signal waveform from the modulated excitation laser rate in ns, τ_m is the lifetime component calculated from the demodulation between the two modulated waveforms in ns. τ is the average of the two lifetime components in ns and χ^2_R is the goodness of fit (or calculation) parameter of the Fourier transformation of the phasors.

The integrated lifetime of Type II beads was calculated to be 3.60 ns. This is 60 ps longer than the experimental reference at 3.54 ns. Transient is subject to the same multi-exponential characteristic as previously shown.

4.5.5 Burst Characteristics of Type II Bead at 0.16 mW of Excitation Power

Figure 4.45 collates the burst characteristics of Type II beads excited at 0.16 mW power. The bead solution was pumped at 500 mbar of pressure and the data was acquired for 10 minutes.

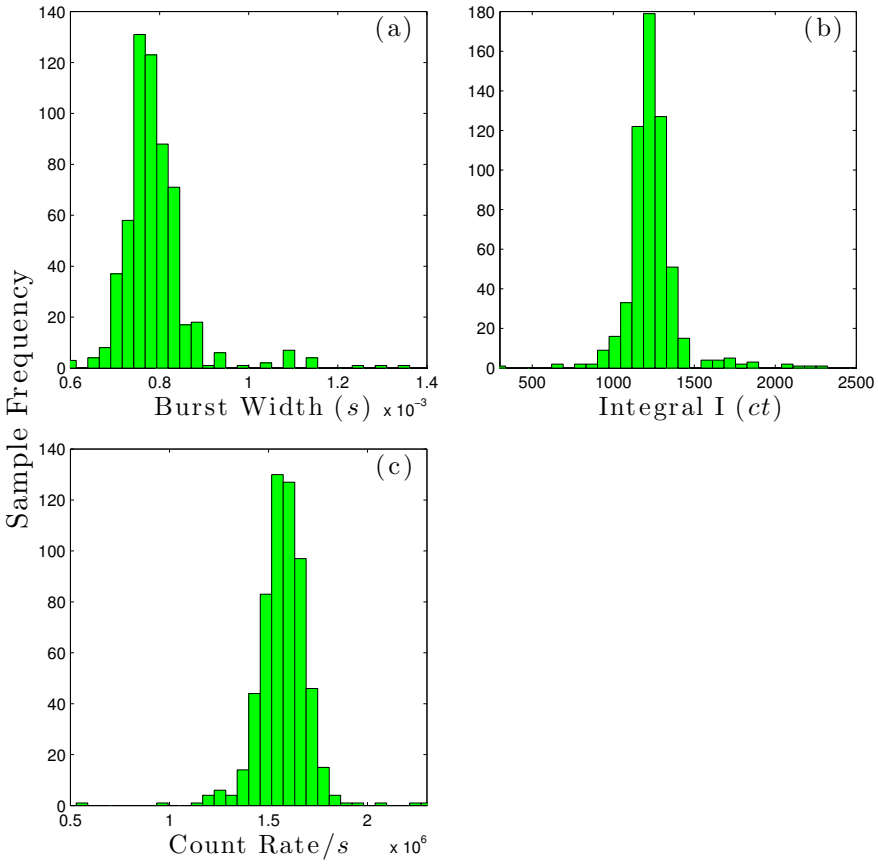

Figure 4.45: Burst characteristics of Type II beads at 0.16 mW of excitation power, where (a), (b), and (c) represents the burst widths, integral intensities, instantaneous count rates during each burst detection, respectively.

The average burst width of the beads is centred at approximately 0.75 ms. The reduction in the burst width was the direct result of the increase in the flow pressure. Interestingly, as the pressure was increased from 250 mb to 500 mb, the reduction of burst width fell by approximately half. The flow rate seems to be operating in the linear regime.

The average integral intensity has improved from the 0.10 mW case and now reaches above the 1000 count threshold for the fit of mono-exponential model by NL-MLM algorithm, as will be shown in further details in subsection 4.6.5. The

average instantaneous burst count rate, however, now reaches beyond the counting limit for modest pile-up, approximately 1.6×10^6 Hz. This will be discussed in the lifetime analysis in subsection 4.6.1, subsection 4.6.3 subsection 4.6.5.

4.5.6 Integrated Lifetime Analysis of Type II beads at 0.16 mW of Excitation Power

Fitting with NL-MLM Algorithm

The integrated transient profile of the bursts acquired at 0.16 mW of excitation power and fitted with a mono-exponential decay by the NL-MLM algorithm is shown in Figure 4.46.

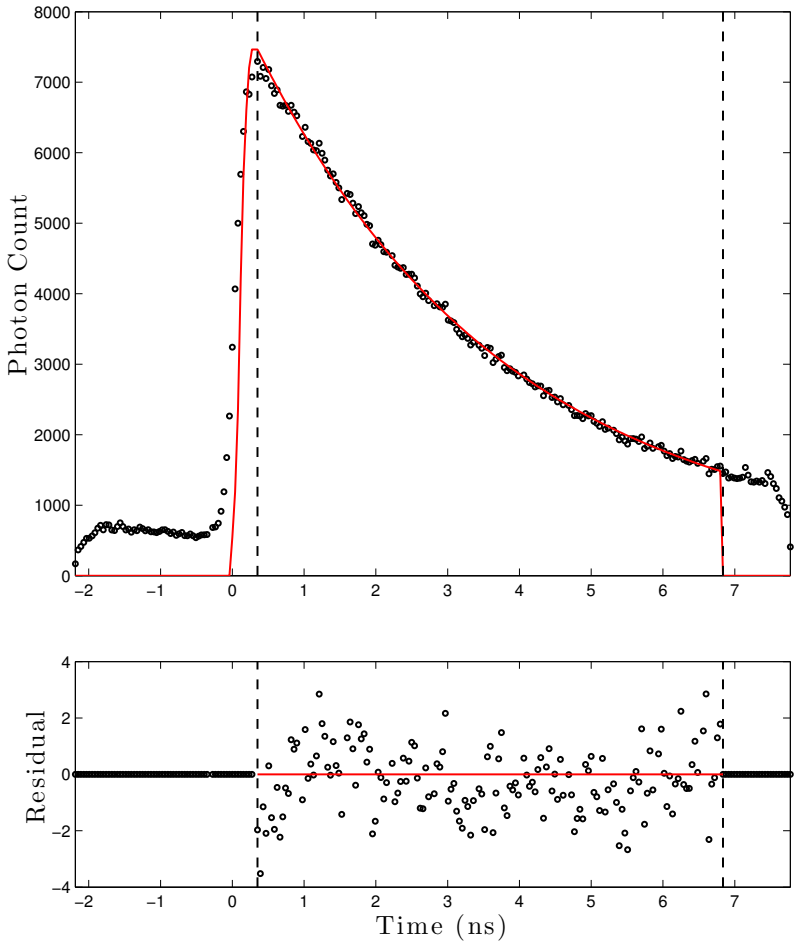

Figure 4.46: Integrated Transient profile of Type II beads. The transient is fitted a mono-exponential model by the NL-MLM.

Z	A	τ	χ^2_R / d.f.
364	7541	3.49	2.22

Table 4.44: Summary of the mono-exponential fit by NL-MLM on the integrated transient profile of Type II beads (Burst Mode) excited at 0.16 mW, where Z is the baseline level, A is the peak amplitude and τ is the lifetime of the transient in ns. χ^2_R is the goodness of fit parameter.

The integrated analysis of Type II beads by NL-MLM shows that lifetime is cal-

culated to be 3.49 ns. This is 410 ps shorter than the one analysed from the FLIM image at 3.90 ns. Since the average instantaneous count rate range of the data was beyond the (self-imposed) 0.01 s^{-1} single photon count limit of TCSPC, a small pulse pile-up and reduction in the lifetime was expected in this case anyway. The transient is remarkably well behaved and appears to be more-or-less mono-exponential, this is perhaps simply a reflection that the data does not contain as high a photon count (by an order of magnitude) as some of the previous data.

Fitting with Fourier Transformation of Phasors

Figure 4.47 shows the integrated transient profile of the bursts acquired at 0.16 mW of excitation power where the fit to the data is calculated by the Fourier transformation of the phasors.

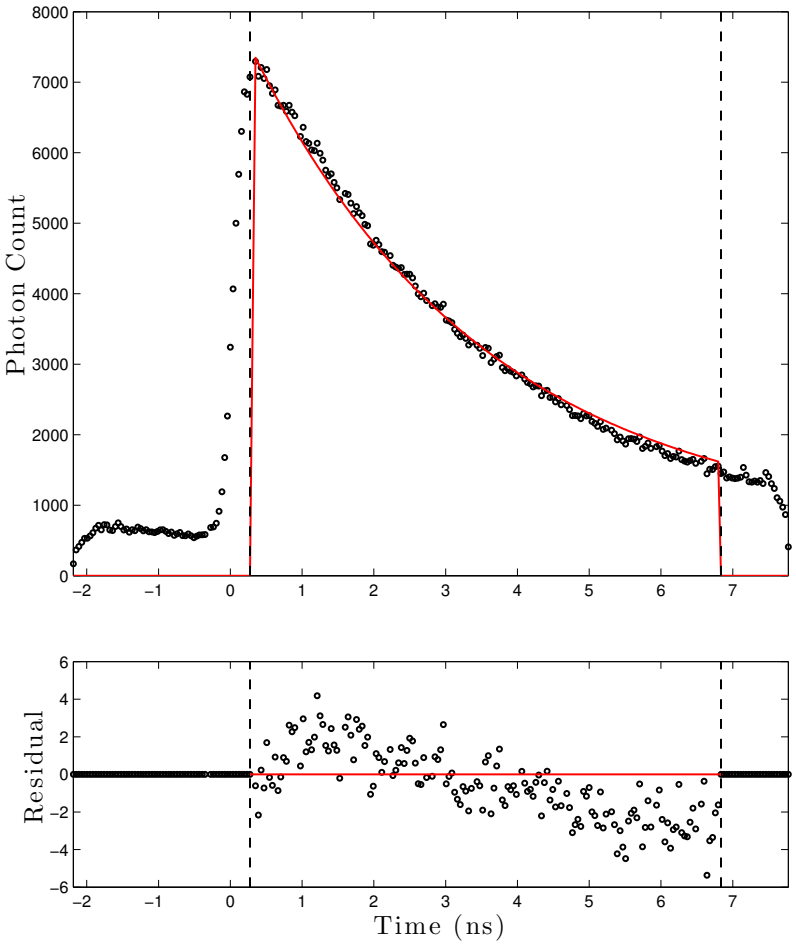

Figure 4.47: Integrated Transient profile of Type II beads calculated by the Fourier Transformation of the phasors.

u	v	τ_p	τ_m	τ	χ^2_R / d.f.
0.091	0.306	3.51	3.08	3.30	5

Table 4.45: Summary of the lifetime calculation from the integrated transient profile of Type II beads by Fourier Transformation of the phasors (Burst Mode) excited at 0.16 mW, where u and v are the centre values of the corresponding axes. τ_p is the lifetime component calculated from the phase delay of the modulated signal waveform from the modulated excitation laser rate in ns, τ_m is the lifetime component calculated from the demodulation between the two modulated waveforms in ns. τ is the average of the two lifetime components in ns and χ^2_R is the goodness of fit (or calculation) parameter of the Fourier transformation of the phasors.

The integrated lifetime of Type II beads was calculated to be 3.60 ns. This is 250 ps shorter than the experimental reference at 3.54 ns. Interestingly, the calculation of the fit in this case, carries the smallest misfit compare to other phasor analysis at 0.03 mW and 0.10 mW although there is clearly a systematic error in the fit.

4.5.7 Summary of Integrated Transient Data of Type II beads

From this section, Type II beads were observed to be significantly less bright than Type I beads. The average instantaneous count rates of the detector from different excitation powers were usually within the safe count limit of 0.01 $\times$ repetition rate, with the exception of 0.16 mW excitation. However, accurate lifetime analysis in the average integral burst intensities were also hampered to less than or just above 1000 counts (as will be seen in section 4.6). The decay rate of the beads showed no signs of secondary excitation at 6 ns of the processing window, although it can be assumed that if acquisition were performed for longer the secondary peak would eventually climb out of the noise. The fits for the integrated transients of Type II beads are summarised in Figure 4.48 for the fit with NL-MLM algorithm and in Figure 4.49 for the calculation by the Fourier Transformation of phasors.

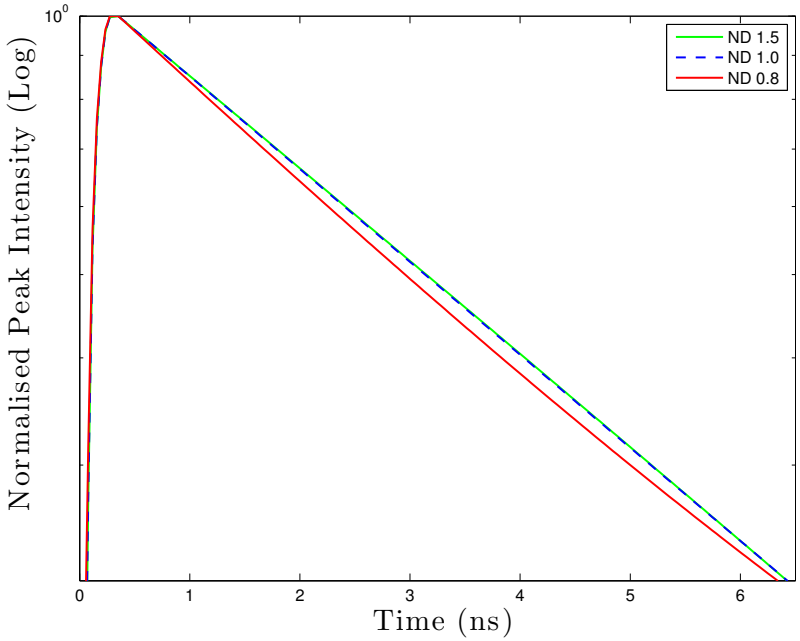

Figure 4.48: Summary of mono-exponential fits by NL-MLM on the integrated transients of Type II beads, where ND is the optical density of the neutral density used in the controlling of the laser excitation power (see Table 4.47 below).

ND	Power (mW)	Z	A	τ	χ^2_R / d.f.
1.5	0.03	364	7541	3.49	2.22
1.0	0.10	-65	51121	4.03	9.88
0.8	0.16	-69	11537	4.07	2.86

Table 4.46: Summary of the mono-exponential fit by NL-MLM on the integrated transient profile of Type II beads (Burst Mode), per power setting, where Power is the excitation power in mW, Z is the baseline level, A is the peak amplitude, τ is the lifetime of the transient in ns and χ^2_R is the goodness of fit parameter.

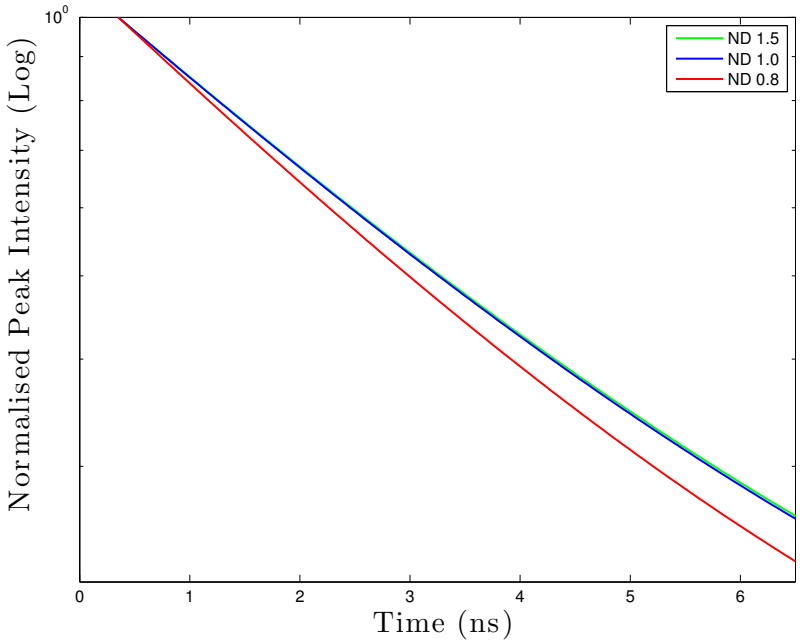

Figure 4.49: Summary of calculated transient profiles Type II beads by Fourier Transformation of phasors, where ND is the optical density of the neutral density used in the controlling of the laser excitation power (see Table 4.47 below).

ND	Power (mW)	u	v	τ_p	τ_m	τ	χ^2_R / d.f.
1.5	0.03	0.091	0.306	3.51	3.08	3.30	5
1.0	0.10	0.078	0.303	4.06	3.15	3.60	74
0.8	0.16	0.077	0.303	4.10	3.16	3.63	19

Table 4.47: Summary of the lifetime calculation from the integrated transient profile of Type I beads by Fourier Transformation of the phasors (Burst Mode), per power setting, where Power is the excitation power in mW, u and v are the centre values of the corresponding axes. τ_p is the lifetime component calculated from the phase delay of the modulated signal waveform from the modulated excitation laser rate in ns, τ_m is the lifetime component calculated from the demodulation between the two modulated waveforms in ns. τ is the average of the two lifetime components in ns and χ^2_R is the goodness of fit (or calculation) parameter of the Fourier transformation of the phasors.

As the acquisitions at the excitation power of 0.03 mW and 0.10 mW were free from the pulse pile-up effect, it could be seen from Figure 4.47 and Figure 4.48 that the shapes of the transients are very similar and yielded lifetime values similar to the experimental reference of the respective FLIM image. However the. small pulse-pile up effect associated with the 0.16 mW excitation can be tolerated, as the lifetimes of the beads calculated by both NL-MLM (3.49 ns) and Fourier transformation of phasors (3.29 ns) are distinctively different from those of the Type I beads at the same excitation power (NL-MLM = 1.35 ns, FT (Phasors) = 1.48 ns). Remember also that whilst there is modest pulse pile-up for both bursts, in the context of screening and sorting, the absolute lifetime is of only passing significance since it is the differences that are actually the most important.

4.6 Flow Experiment: Burst-generated Lifetime Data (Type II beads)

In this section, the lifetime of Type II beads will be calculated on the individual pixel basis. NL-MLM and phasor analysis of Type II beads will be shown explicitly for each power setting listed in section 4.5.

For the NL-MLM fitting method, the corresponding BIFL image with a false colour scale will be used to represent the lifetime of the bursts, alongside the histogram of those lifetimes. The phasor analysis will first introduce a contour plot of the phasors and histograms of the u and v coordinates, before showing the lifetime of the bursts from Fourier transformation of the phasors with the same representation of BIFL image and the corresponding lifetime histogram as the NL-MLM section.

4.6.1 NL-MLM Analysis (Type II beads) at 0.03 mW

Figure 4.50 shows the BIFL image and the corresponding lifetime histogram of Type II beads, excited at 0.03 mW. The bead solution was pumped at 250 mb of

air supply and the data was acquired for 10 minutes.

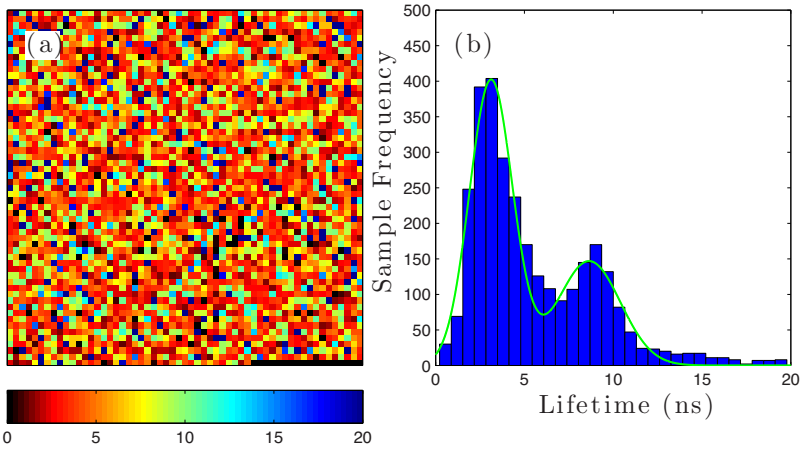

Figure 4.50: A successfully analysed BIFL image (57 by 57 pixels) containing the lifetime of 3231 bursts, by NL-MLM. (b) The corresponding lifetime histogram of the BIFL data.

A_1	τ_1	σ_1	A_2	τ_2	σ_2
402	3.12	1.72	147	8.64	2.49

Table 4.48: Summary of the lifetime fitting parameters of Type II beads excited at 0.03 mW by NL-MLM (BIFL) (see Figure 4.49 (b)). The average lifetime of the control was calculated by a double Gaussian mixture model, where A_1 and A_2 are the fractional contributions from the number of pixel of the image, τ_1 and τ_2 are the mean lifetimes measured in ns, and σ_1 and σ_2 are the standard deviations of each sub-population in ns.

The increase in the stock concentration is clearly evident in the BIFL acquisition. This is approximately 4 to 5-fold improvement in the number of bursts detected from the Type I beads. As previously described in subsection 4.5.1, the average integral intensity of the beads is approximately 250 - 400 counts. This has a direct impact on the lifetime histogram in Figure 4.49 (b), as the lifetime of the beads varied on a very large range between 0 ns and 20 ns, and consists of two populations. The ensemble histogram in the Figure could not be fitted with the

fitted algorithm within 10 successive iterations, and so was manually fit on the basis of the characteristics of the graph.

The mean lifetime of the major distribution was calculated to be 3.12 ± 1.72 ns. This is approximate 700 ps different from the experimental reference at 3.82 ns. Furthermore, the shape of the lifetime distribution in the experimental control showed that the lifetime of the beads is naturally, positively skewed, even when the acquisition was well-controlled in terms of the excitation power and photon economy per active pixel. The manual fit in Figure 4.49 (b) did not take an account of the skew in the shape of the dominating lifetime distribution, which would otherwise shift its weighted average lifetime.

The integrated transient of the data in subsection 4.5.2 showed that the lifetime of the beads was almost identical to the reference, and so it can be confirmed that the detection was solely from the Type II beads. However, because the individual photon population of each bead is low, the calculations of lifetime per individual bead are correspondingly inaccurate. The standard deviation of the beads is also very large (>1 ns). Anecdotally, when photon count of any bead is low, NL-MLM tends to calculate its lifetimes to be anomalously long. This is evident in the second population, where the average lifetime was calculated to be 8.64 ± 2.49 ns. It is not clear of the origin for the long fluorescence lifetime although it is almost certainly contamination by a long lived fluorescent molecule or particle (such as Qdot532 which has a similar lifetime). One merit, which could taken from the data is that despite the averagely low integral intensity of the beads (<500 counts), the average lifetime of either population in Figure 4.49 (b) is distinctively different from the one of Type I beads at the same excitation power.

4.6.2 Phasor Analysis (Type II beads) at 0.03 mW

Figure 4.51 shows a contour plot of phasors of Type II beads, excited at 0.03 mW, the histograms of each phasor co-ordinates (u and v). The Fourier transformation of the phasors is shown in the BIFL image format along with the corresponding

lifetime histogram in Figure 4.52.

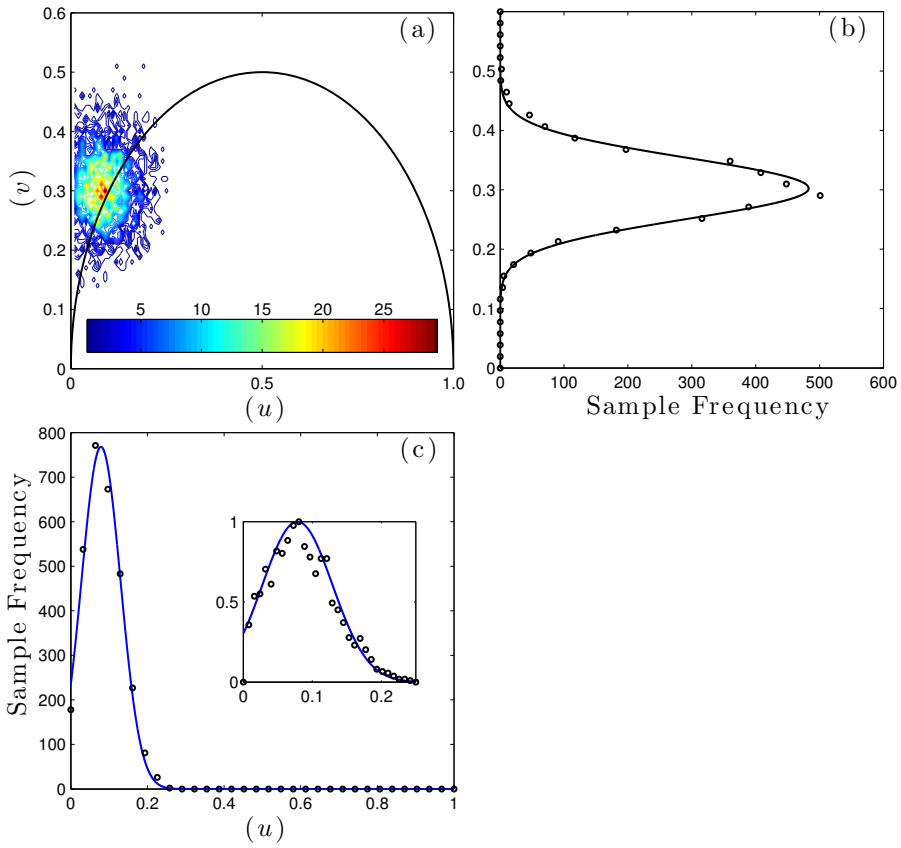

Figure 4.51: (a) Contour plot of phasors from the BIFL image (57 by 57 pixels) containing 3231 bursts. (b) The main panel shows the corresponding v–coordinate distribution of the phasors. (c) The main and inset shows the corresponding u–coordinate distribution of the phasors.

A	u	σ
195	0.079	0.072

Table 4.49: Summary of the Gaussian fit for the u–coordinate of Type II beads (BIFL) excited at 0.03 mW (see Figure 4.51 (c)), where A is the peak height of the distribution, u is the centre u-coordinate, and σ is the standard deviation of the distribution.

A	v	σ
483	0.302	0.073

Table 4.50: Summary of the Gaussian fit for the v–coordinate of Type II beads (BIFL) excited at 0.03 mW (see Figure 4.51 (b)), where A is the peak height of the distribution, v is the centre v-coordinate, and σ is the standard deviation of the distribution.

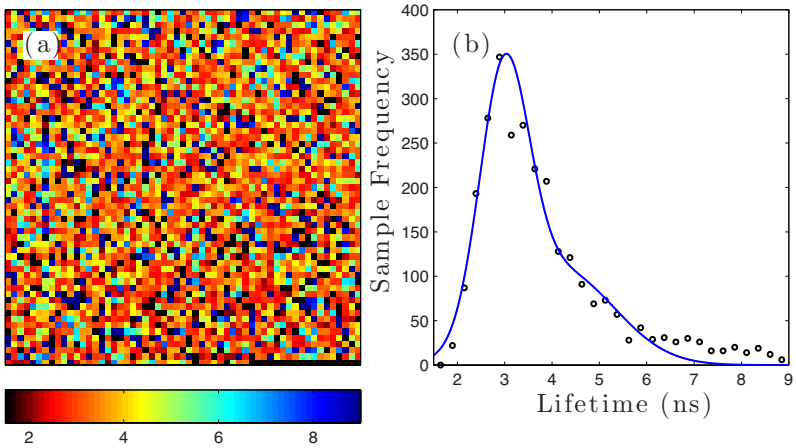

Figure 4.52: (a) A successfully calculated BIFL image by Fourier Transformation of phasors (57 by 57 pixels) containing the lifetime of 3231 bursts. (b) The corresponding lifetime histogram of the BIFL data.

A_1	τ_1	σ_1	A_2	τ_2	σ_2	Ave. τ	Ave. σ
289	2.99	0.73	105	4.19	1.61	3.39	1.12

Table 4.51: The table of summary for the lifetime fitting for Type II bead by FT(Phasor) (BIFL) excited at 0.03 mW (see Figure 4.52 (b)). The average lifetime of the control was calculated by a double Gaussian mixture model, where A_1 and A_2 are the fractional contributions from the number of pixel of the image, τ_1 and τ_2 are the mean lifetimes measured in ns, and σ_1 and σ_2 are the standard deviations of each sub-population in ns. Ave. τ and Ave. σ reprensents the average lifetime and the associated standard deviation in ns respectively.

From Figure 4.51, the phasors of Type II beads were evenly distributed at co-ordinates $(0.079 \pm 0.072,\ 0.302 \pm 0.072)$ of the contour plot. The co-ordinate

pair is close to that of the FLIM image at $(0.078 \pm 0.023, 0.290 \pm 0.024)$. The degree of resemblance between the two sets of co-ordinates is actually very good, considering the standard deviations of each centre co-ordinates are very large in this case. As previously mentioned in the theoretical introduction, the averaging of the phase delays from the modulated data points of each individual transient, would become more accurate on the phasor graph with higher photon counts. In this case, the integral photon counts of the beads are all below 500 counts, and so the result in Figure 4.51 actually reports the practical limit and robustness of the phasors method very well.

The phasors are also centred on the universal semi-circle as for the experimental reference. From Figure 4.52, the lifetime distribution of the beads is positively skewed and is much better behaved than the NL-MLM analysis. Although the result is not as clean as the experimental reference, due to the large spread of phasors, the average lifetime of the beads was nonetheless calculated to be 3.39 ± 1.12 ns. This is 180 ps shorter than the FLIM acquisition at 3.57 ± 0.52 ns (by the same analysis method). This is relatively good, considering the available photons.

4.6.3 NL-MLM Analysis (Type II beads) at 0.10 mW

Figure 4.53 shows the BIFL image and the corresponding lifetime histogram of Type II beads, excited at 0.10 mW. The bead solution was pumped at 250 mb of air supply and the data was acquired for 20 minutes. The acquisition time was increase to 20 minutes, as the 0.03 mW data could determine the lifetime of the beads relatively well, given the low photon count. With the gain in power, the increase in throughput was predicted to provide a more robust analysis in this case.

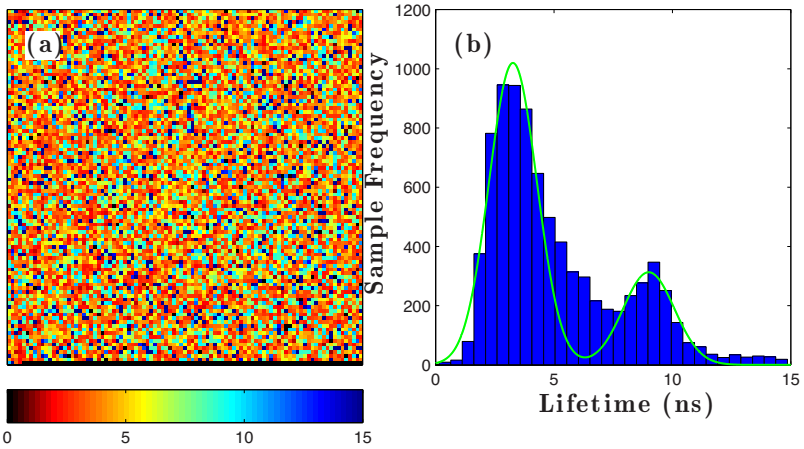

Figure 4.53: A successfully analysed BIFL image (95 by 95 pixels) containing the lifetime of 8934 bursts, by NL-MLM. (b) The corresponding lifetime histogram of the BIFL data.

A_1	τ_1	σ_1	A_2	τ_2	σ_2
1020	3.27	1.43	313	9.00	1.53

Table 4.52: Summary of the lifetime fitting parameters of Type II beads excited at 0.10 mW by NL-MLM (BIFL) (see Figure 4.53 (b)). The average lifetime of the control was calculated by a double Gaussian mixture model, where A_1 and A_2 are the fractional contributions from the number of pixel of the image, τ_1 and τ_2 are the mean lifetimes measured in ns, and σ_1 and σ_2 are the standard deviations of each sub-population in ns.

The result in Figure 4.53 (b) could not be fit within the fitting iteration of the program, and so the data was manually fit on the basis of the graph characteristics. Although the lifetime distribution of beads calculated by the NL-MLM algorithm still shows double peaks as for the 0.03 mW case, it could be seen that the dominant population closely resembles to the distribution of the experimental reference in Figure 4.10, where the distribution is positively skewed over a similar time scale (ignoring the minor distribution centring at $\sim$ 9 ns). There is no straightforward means to sort the two lifetime distributions from the data, other than cutting off the data beyond 8 ns. The artefact of the NL-MLM on the low photon counts operation has to be accepted; otherwise the use of the phasor

analysis has to be rigorously resorted to instead. The mean lifetime of the manual fit on the dominant distribution was calculated to be 3.27 ± 1.43 ns. The positive skew on the distribution, which was omitted from the fit would have shifted the weighted average value to be closer to the experimental reference at 3.82 ns.

4.6.4 Phasor Analysis (Type II beads) at 0.10 mW

Figure 4.53 shows a contour plot of phasors of Type II beads, excited at 0.10 mW, the histograms of each phasor co-ordinates (u and v). The Fourier transformation of the phasors in the BIFL image format along with the corresponding lifetime histogram is given in Figure 4.53.

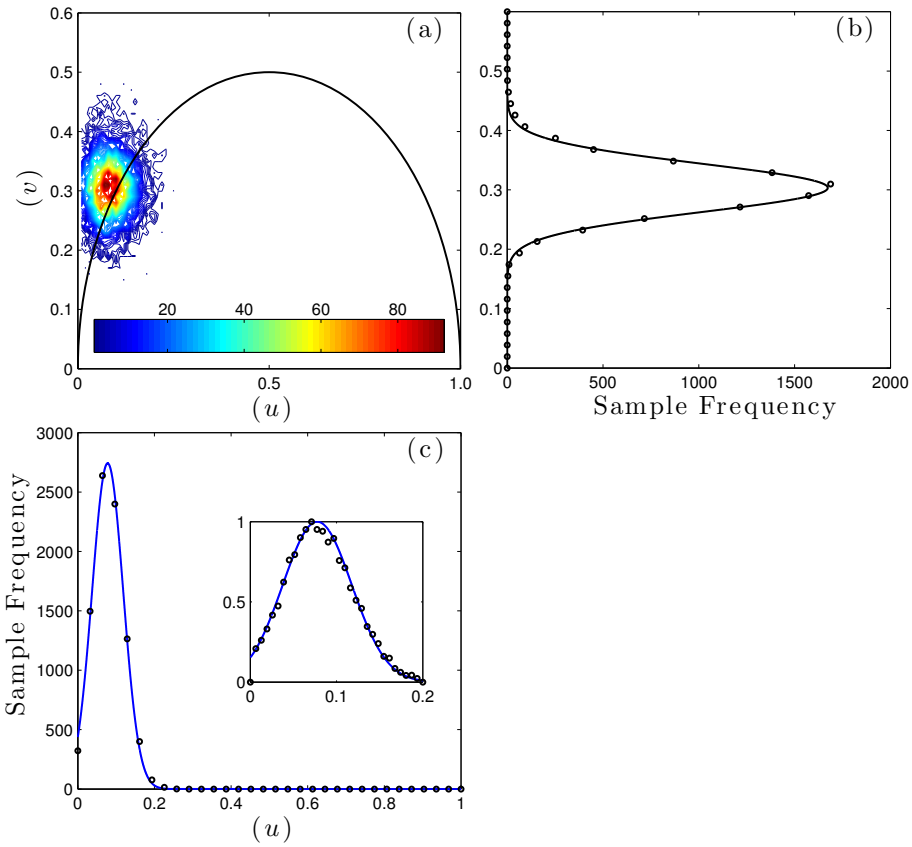

Figure 4.54: (a) Contour plot of phasors from the BIFL image (57 by 57 pixels) containing 3231 bursts. (b) The main panel shows the corresponding v–coordinate distribution of the phasors. (c) The main and inset shows the corresponding u–coordinate distribution of the phasors.

A	u	σ
561	0.078	0.057

Table 4.53: Summary of the Gaussian fit for the u–coordinate of Type II beads (BIFL) excited at 0.10 mW (see Figure 4.54 (c)), where A is the peak height of the distribution, u is the centre u-coordinate, and σ is the standard deviation of the distribution.

A	v	σ
1673	0.303	0.058

Table 4.54: Summary of the Gaussian fit for the v–coordinate of Type II beads (BIFL) excited at 0.10 mW (see Figure 4.54 (b)), where A is the peak height of the distribution, v is the centre v-coordinate, and σ is the standard deviation of the distribution.

From Figure 4.54, the phasors of Type II beads were evenly distributed at co-ordinates $(0.078 \pm 0.057,\ 0.303 \pm 0.058)$ of the contour plot. The co-ordinate pair is very close that of the FLIM image at $(0.078 \pm 0.023,\ 0.290 \pm 0.024)$. The improvement in the burst integral intensity sees the spread of the phasors reduced compared to lower power data sets. The centre of the phasor distribution is also centred on the universal semi-circle.

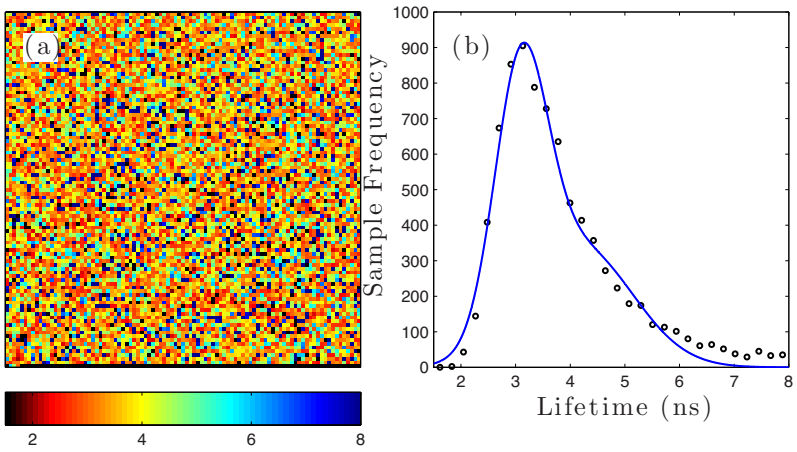

Figure 4.55: A successfully calculated BIFL image by Fourier Transformation of phasors (95 by 95 pixels) containing the lifetime of 8934 bursts. (b) The corresponding lifetime histogram of the BIFL data.

A_1	τ_1	σ_1	A_2	τ_2	σ_2	Ave. τ	Ave. σ
728	3.09	0.68	335	4.18	1.38	3.51	1.01

Table 4.55: The table of summary for the lifetime fitting for Type II bead by FT(Phasor) (BIFL) excited at 0.10 mW (see Figure 4.55 (b)). The average lifetime of the control was calculated by a double Gaussian mixture model, where A_1 and A_2 are the fractional contributions from the number of pixel of the image, τ_1 and τ_2 are the mean lifetimes measured in ns, and σ_1 and σ_2 are the standard deviations of each sub-population in ns. Ave. τ and Ave. σ reprensents the average lifetime and the associated standard deviation in ns respectively.

From Figure 4.55 (b), the lifetime distribution of the beads is positively skewed. The average lifetime of the beads was calculated to be 3.51 ± 1.01 ns. This is 60 ps shorter than the FLIM acquisition at 3.57 ± 0.52 ns (by the same analysis method), which is clearly within experimental error.

4.6.5 NL-MLM Analysis (Type II beads) at 0.16 mW

Figure 4.56 shows the BIFL image and the corresponding lifetime histogram of Type II beads, excited at 0.16 mW. The bead solution was pumped at 500 mb of air supply and the data was acquired for 10 minutes, replicating the same condition as the one of Type I beads at the same power setting.

The increase in flow speed seems to change the position of the streamlines, which resulted in the reduction of the throughput, compared to subsection 4.4.7. Nonetheless, the program can now fit the lifetime distribution with the Gaussian model as shown in Figure 4.56 (b). The weighted average lifetime of the beads was calculated to be 3.70 ± 1.26 ns. This is 120 ps shorter than the experimental reference at 3.82 ns. The average instantaneous count rate of the data was above the safe count rate of TCSPC, and so a small reduction in the measured lifetime is expected.

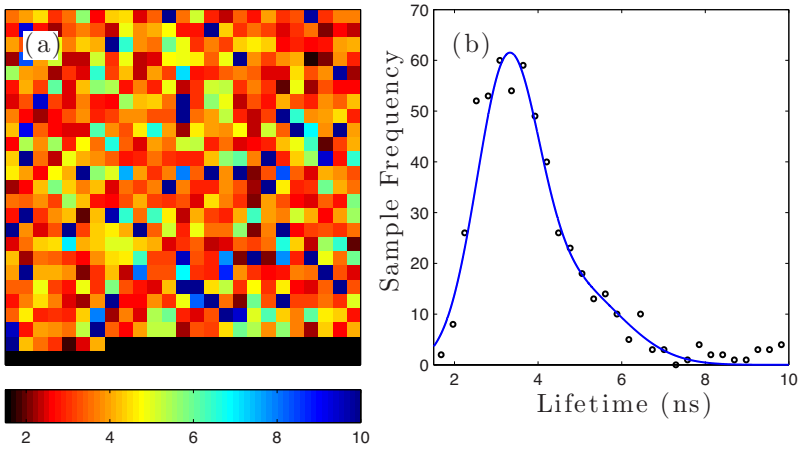

Figure 4.56: A successfully analysed BIFL image (25 by 25 pixels) containing the lifetime of 582 bursts, by NL-MLM. (b) The corresponding lifetime histogram of the BIFL data.

A_1	τ_1	σ_1	A_2	τ_2	σ_2	Ave. τ	Ave. σ
54	3.25	1.04	15	4.77	1.72	3.70	1.26

Table 4.56: The table of summary for the lifetime fitting for Type II bead by NL-MLM (BIFL) excited at 0.10 mW (see Figure 4.56 (b)). The average lifetime of the control was calculated by a double Gaussian mixture model, where A_1 and A_2 are the fractional contributions from the number of pixel of the image, τ_1 and τ_2 are the mean lifetimes measured in ns, and σ_1 and σ_2 are the standard deviations of each sub-population in ns. Ave. τ and Ave. σ reprensents the average lifetime and the associated standard deviation in ns respectively.

4.6.6 Phasor Analysis (Type II beads) at 0.16 mW

Figure 4.57 shows a contour plot of phasors of Type II beads, excited at 0.10 mW, the histograms of each phasor co-ordinates (u and v). The Fourier transformation of the phasors in the BIFL image format along with the corresponding lifetime histogram is given in Figure 4.57.

From Figure 4.57, the phasors of Type II beads were evenly distributed at co-ordinates $(0.090 \pm 0.037,\ 0.305 \pm 0.039)$ of the contour plot. The co-ordinate is

comparable to the experimental reference at $(0.078 \pm 0.023, 0.290 \pm 0.024)$. The centre u co-ordinate is marginally shifted to the right in relation to the reference. This will result in a decrease in the calculated lifetime, as supported by the evidence of the instantaneous count rate of the data. The phasors are also centred on the universal semi-circle as for the experimental reference.

From Figure 4.58, the lifetime distribution of the beads is positively skewed. The average lifetime of the beads was calculated to be 3.31 ± 1.12 ns. This is 260 ps shorter than the FLIM acquisition at 3.57 ± 0.52 ns.

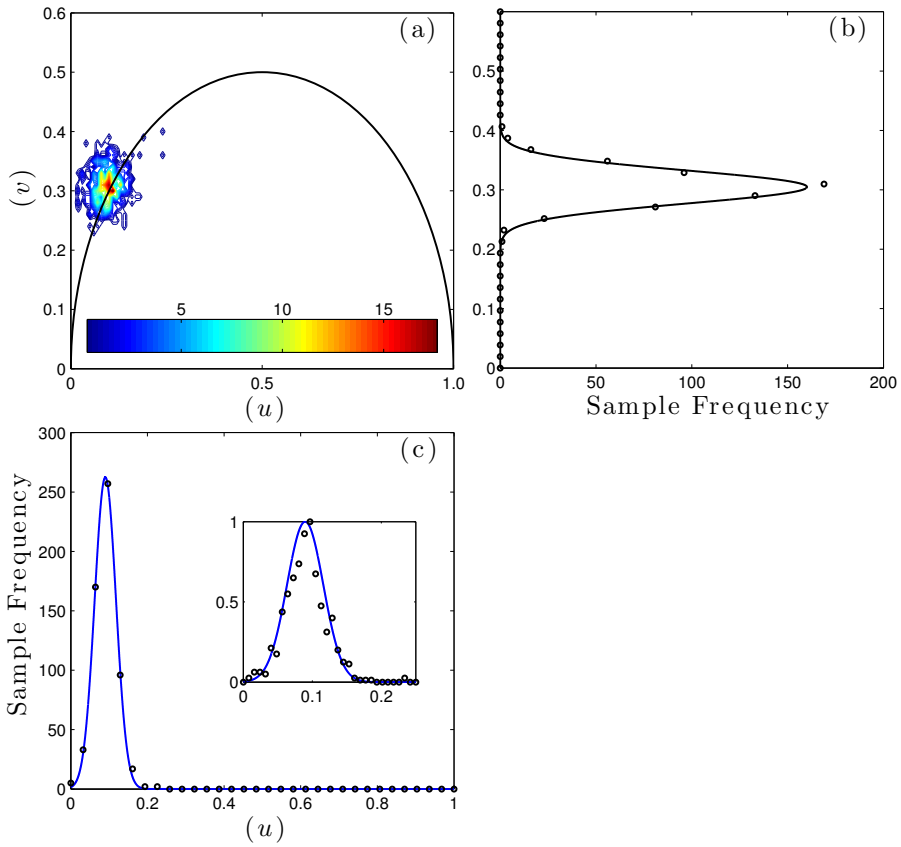

Figure 4.57: (a) Contour plot of phasors from the BIFL image (57 by 57 pixels) containing 3231 bursts. (b) The main panel shows the corresponding v–coordinate distribution of the phasors. (c) The main and inset shows the corresponding u–coordinate distribution of the phasors.

A	u	σ
69	0.090	0.037

Table 4.57: Summary of the Gaussian fit for the u–coordinate of Type II beads (BIFL) excited at 0.10 mW (see Figure 4.57 (c)), where A is the peak height of the distribution, u is the centre u-coordinate, and σ is the standard deviation of the distribution.

A	v	σ
160	0.305	0.039

Table 4.58: Summary of the Gaussian fit for the v–coordinate of Type II beads (BIFL) excited at 0.10 mW (see Figure 4.57 (b)), where A is the peak height of the distribution, v is the centre v-coordinate, and σ is the standard deviation of the distribution.

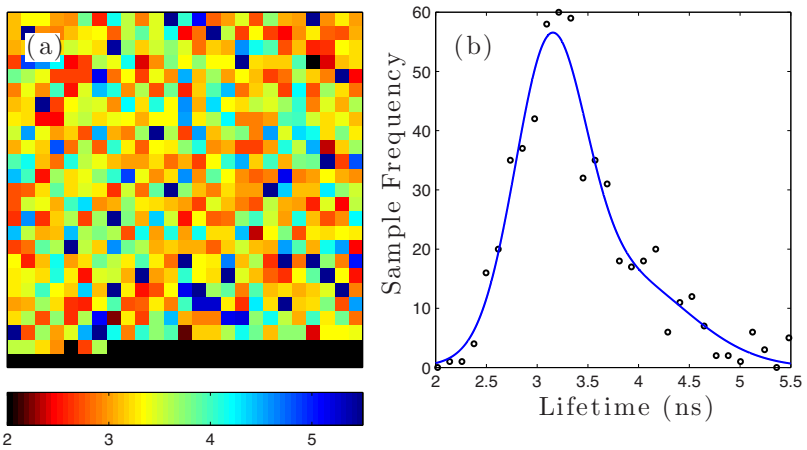

Figure 4.58: (a) A successfully calculated BIFL image by Fourier Transformation of phasors (25 by 25 pixels) containing the lifetime of 582 bursts. (b) The corresponding lifetime histogram of the BIFL data.

A_1	τ_1	σ_1	A_2	τ_2	σ_2	Ave. τ	Ave. σ
47	3.12	0.48	16	3.78	0.97	3.31	0.68

Table 4.59: The table of summary for the lifetime fitting for Type II bead by FT(Phasor) (BIFL) excited at 0.10 mW (see Figure 4.58 (b)). The average lifetime of the control was calculated by a double Gaussian mixture model, where A_1 and A_2 are the fractional contributions from the number of pixel of the image, τ_1 and τ_2 are the mean lifetimes measured in ns, and σ_1 and σ_2 are the standard deviations of each sub-population in ns. Ave. τ and Ave. σ reprensents the average lifetime and the associated standard deviation in ns respectively.

4.6.7 Summary of BIFL data of Type I and Type II beads

The two bead types are observed to be distinctively different in brightness. At the time of the investigation, the phasor analysis was not available and the analysis was solely relied on the NL-MLM algorithm. The importance of achieving the 1,000 counts was essential for the fitting algorithm, as shown in subsection 4.6.1 and subsection 4.6.3. Therefore the power had to be serially increased until satisfactory result is achieved at 0.16 mW. With hindsight, the phasor method would be sufficient in resolving the mixed population at 0.03 mW. The centre co-ordinates of phasors of Type I and Type II at the power setting are 0.228 ± 0.010, 0.413 ± 0.008 and 0.079 ± 0.072, 0.302 ± 0.073, respectively. On investigation of Figure 4.31 and Figure 4.51, the spreads of the phasors for each bead type do not overlap one and another. There was no need to saturate the detector with higher excitation powers.

However, as it was already determined that a power of 0.16 mW was required for NL-MLM, the results from the power setting will be used as the experimental references to the mixed population acquisition excited at the same power setting. Table 4.60 below, summarises the lifetimes and phasor co-ordinates of Type I and 2 beads at the power setting.

	τ (ns) - by NL-MLM	u	v	τ (ns) by FT(Phasors)
Type I	1.36	0.342	0.437	1.44
Type II	3.70	0.090	0.305	3.31

Table 4.60: Summary of lifetimes (fit by NL-MLM and FT(Phasor)) and phasor co-ordinates of Type I and II beads excited at 0.16 mW.

4.7 Mixed Beads Experiment (Type I and II Beads)

The burst characteristics and fluorescence profiles of each bead type have been shown, for each power setting, in previous the sections thus far. Hence, it would be useful to further investigate the mixed bead population of the 2 bead types, at 0.16 mW of excitation power and 500 mbar of pump pressure. In this section, burst characteristics, integrated transient profile and burst integrated lifetime of the mixed population will first be shown, before demonstrating the use of phasors as the means for sorting and separating the bead types. Upon successful sorting, the data will be crosschecked by explicitly examining the burst characteristics, integrated transient profile, and burst integrated lifetime of each sorted population. As shown in the video footage in chapter 3, each bead type was observed to possess its own streamline on different sides of the channel. The excitation beam was parked at centre of the channel in an attempt to capture as many beads as possible from both bead types, and accept some loss in the integrated intensities of the beads as a compromise.

4.7.1 Burst Characteristics of Mixed Bead at 0.16 mW of Excitation Power

Figure 4.59 collates the burst characteristics of the mixed beads population excited at 0.16 mW of excitation power. The bead solution was pumped at 500 mbar of air supply and the data was acquired for 40 minutes.

From Figure 4.59, each burst parameter consists of two distinct populations, where the frequency of one data population is approximately 3 times that of the other. The burst width characteristics in Figure 4.59 (a) shows the burst width distributions are approximately centred at 0.25 and 1.1 ms, respectively. The separate investigations of Type I and II beads in the previous sections showed the respective burst width distributions to be centring approximately between 0.8 – 0.9 ms, at this pumping rate. Here, there is only one data population repli-

cating the same trait. It is possible that by positioning the beam at the centre of the channel, I had marginally moved the beam away from the streamlines of one bead type. While it is unclear which burst width distribution belongs to which bead type, the sorted data will be used in the later section to trace it. Figure 4.59 (b) show that the integral intensity distributions are distinctly separated in different brightness margins, which centred approximately at 800 counts and 4000 counts. It is clearly evident that the latter distribution closely resembles the Type I beads in Figure 4.22 (b). It was observed in previous sections that Type I beads are significantly brighter than Type II, and so it is relatively straightforward to conjecture that the lower mean distribution is belonged to the Type II beads. The instantaneous count rate statistics in Figure 4.59 (c) show that the two distributions are approximately centred at 2.2 and 4.1 MHz. As expected, the higher mean distribution closely resembles that in Figure 4.22 (c) of Type I beads. However, the lower mean distribution, which is assumed to be belong to the Type II beads, appears to have a higher mean value than the case in Figure 4.45 (c), despite yielding lower integral intensities overall in this data set. It is possible that if the inter-event time is too short, where the Type II beads were detected just before or after the detection of a Type I bead, the instantaneous count rate of the detector would still remain relatively high and not completely reset before the next detection event.

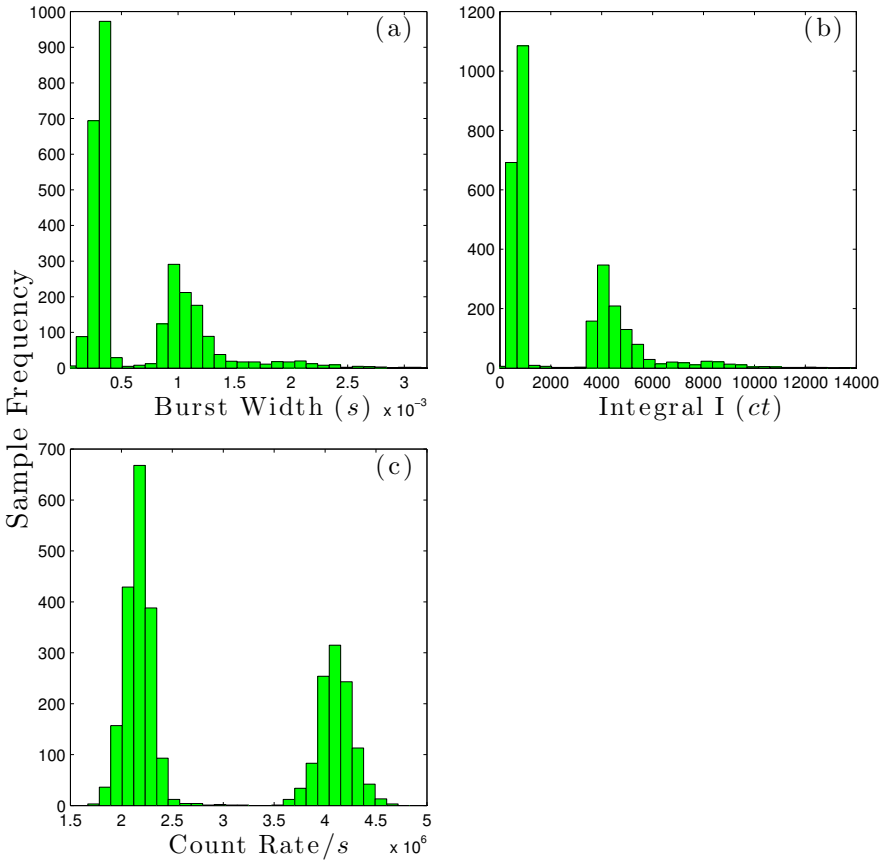

Figure 4.59: Burst characteristics of mixed beads population at 0.16 mW excitation power, where (a), (b), and (c) represents the burst widths, integral intensities, instantaneous count rates during each burst detection, respectively.

4.7.2 Integrated Lifetime Analysis of The Mixed Bead Population at 0.16 mW of Excitation Power

Fitting with NL-MLM Algorithm

The integrated transient profile of the bursts acquired at 0.01 mW excitation power and fitted to a mono-exponential decay by the NL-MLM algorithm is shown in Figure 4.60.

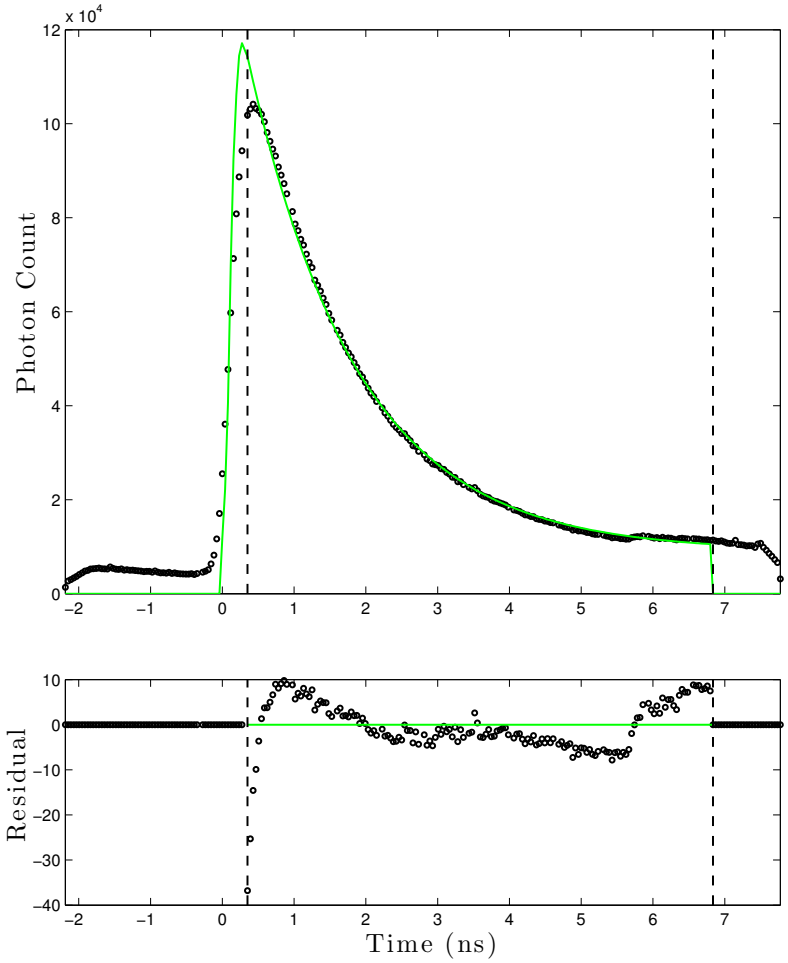

Figure 4.60: Integrated transient profile of mixed bead population. The transient is fitted a mono-exponential model by the NL-MLM.

Z	A	τ	χ^2_R / d.f.
9017	120683	1.52	53

Table 4.61: Summary of the mono-exponential fit by NL-MLM on the integrated transient profile of the mixed beads population (Burst Mode) excited at 0.16 mW, where Z is the baseline level, A is the peak amplitude and τ is the lifetime of the transient in ns. χ^2_R is the goodness of fit parameter.

The lifetime of the integrated transient is calculated to be 1.52 ns by NL-MLM

algorithm. Figure 4.59 shows that the integrated transient profile looks similar to the experimental control data of Type I bead, in Figure 4.23. For an illustrative purpose, the convoluted transient between Type I and II beads will be fitted with a mono-exponential model, despite the presence of the two lifetimes. The sorting mechanism will be used in section 4.10 to explicitly show the integrated transient of each bead type later. The lifetime of this compromised fit is observed to be longer than the reference (1.35 ns) by 170 ps. The long lifetime component of the Type II will definitely play a part in counteracting the reduction of lifetime, but due to the weak contribution from the fluorescence of Type II beads, the effect is minimal.

The secondary excitation from the optical reflection of the system at 6 ns of the processing window, remains sufficiently strong to manifest in transients for Type I beads in this mixed population, as expected.

Fitting with Fourier Transformation of Phasors

Figure 4.61 shows the integrated transient profile of the bursts acquired at 0.16 mW of excitation power where the fit to the data is calculated by the Fourier transformation of the phasors.

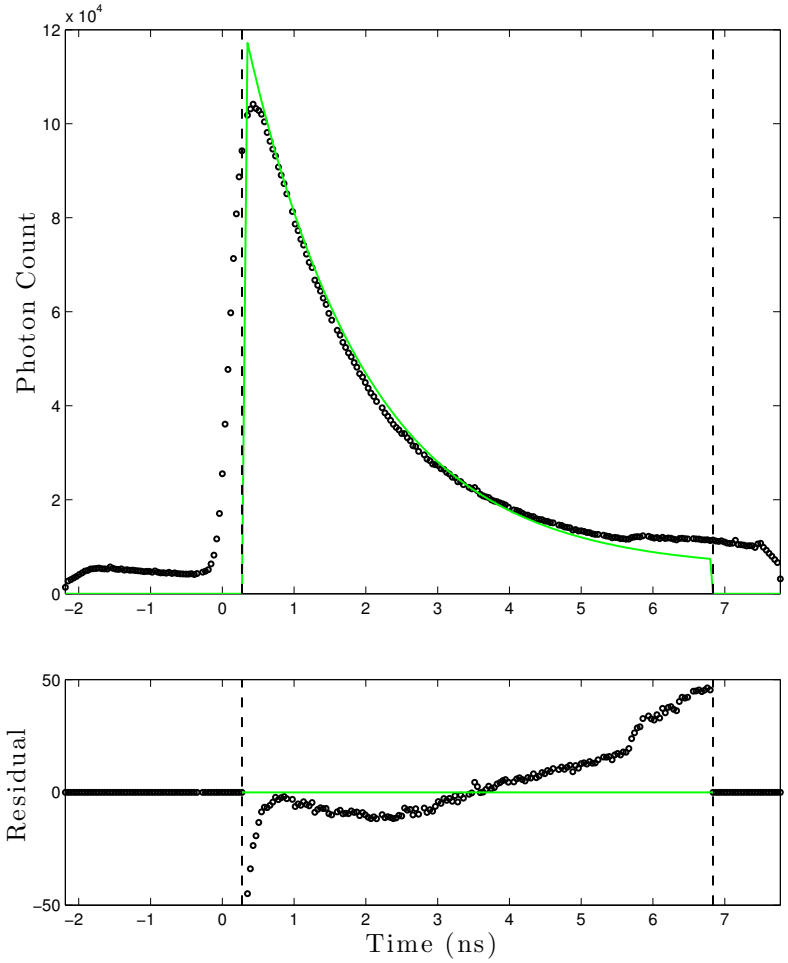

Figure 4.61: Integrated transient profile of the mixed bead types calculated by the Fourier Transformation of the phasors.

u	v	τ_p	τ_m	τ	χ^2_R / d.f.
0.279	0.411	1.53	1.82	1.67	370

Table 4.62: Summary of the lifetime calculation from the integrated transient profile of the mixed beads population by Fourier Transformation of the phasors (Burst Mode) excited at 0.16 mW, where u and v are the centre values of the corresponding axes. τ_p is the lifetime component calculated from the phase delay of the modulated signal waveform from the modulated excitation laser rate in ns, τ_m is the lifetime component calculated from the demodulation between the two modulated waveforms in ns. τ is the average of the two lifetime components in ns and χ^2_R is the goodness of fit (or calculation) parameter of the Fourier transformation of the phasors.

The calculation of the lifetime from the integrate profile in Table 4.62 also shows the average lifetime of the data is longer than the one of the dominant Type I beads (1.48 ns) by 190 ps. The argument on the lengthening of lifetime and the presence of the secondary emission at the tail in section 4.7.2 is also hold true here.

4.8 Flow Experiment: Burst-generated Lifetime Data (Mixed Beads Population)

In this section, the lifetime of mixed sample will be calculated on the individual pixel basis. NL-MLM and phasor analysis will be shown explicitly.

For the NL-MLM fitting method, the corresponding BIFL image with a false colour scale will be used to represent the lifetime of the bursts, alongside the histogram of those lifetimes. The phasor analysis will first introduce a contour plot of the phasors and histograms of the u and v coordinates, before showing the lifetime of the bursts from Fourier transformation of the phasors with the same representation of BIFL image and the corresponding lifetime histogram as the NL-MLM section. The total length of this acquisition is 40 minutes.

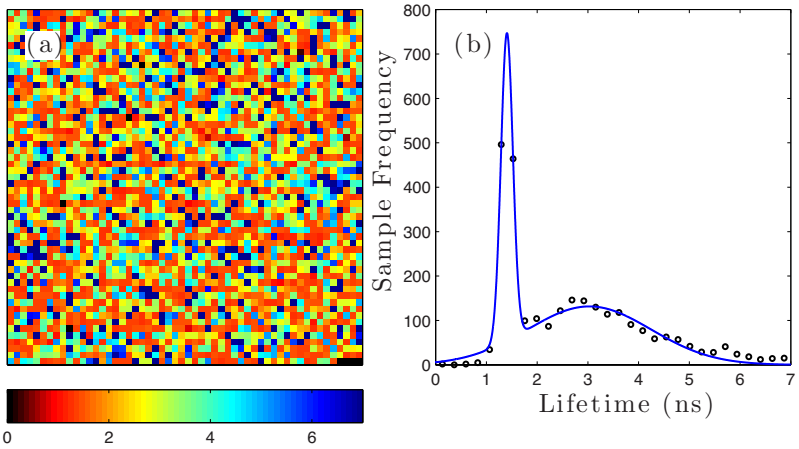

Figure 4.62: A successfully analysed BIFL image (54 by 54 pixels) containing the lifetime of 2912 bursts, by NL-MLM. (b) The corresponding lifetime histogram of the BIFL data.

A_1	τ_1	σ_1	A_2	τ_2	σ_2
132	3.03	1.72	693	1.40	0.17

Table 4.63: Summary of the lifetime fitting parameters of the mixed beads population excited at 0.16 mW by NL-MLM (BIFL) (see Figure 4.62 (b)) . The average lifetime of the control was calculated by a double Gaussian mixture model, where A_1 and A_2 are the fractional contributions from the number of pixel of the image, τ_1 and τ_2 are the mean lifetimes measured in ns, and σ_1 and σ_2 are the standard deviations of each sub-population in ns.

The throughput of the acquisition was calculated to be 728 beads per 10 minute, on average. This is relatively reasonable, as the throughput of Type I and II beads were approximately 776 and 582 beads from the 10 minute acquisitions. The 4-fold expansion of the acquisition time did not affect the flow conditions. If the channel were subject to a full or partial channel clogging, then the number of the detected samples would deteriorate with time.

Figure 4.62 shows that the lifetime of the data is distributed into 2 overlapping populations, one broad and one narrow. The narrow distribution was calculated to have a mean lifetime of 1.40 ± 0.17 ns, while the other was calculated to be

3.03 ± 1.72 ns. The mean value of the narrow distribution closely resembles the Type I bead in subsection 4.4.7 at 1.36 ± 0.13 ns. The broader distribution is similar to the Type II beads in subsection 4.6.5 at 3.70 ± 1.26 ns. However, because of the relatively long timescale of the histogram in Figure 4.62, the inherent skewness of the lifetime distribution of the Type II beads is not obvious in this case.

4.8.1 Phasor Analysis (Type II Beads) at 0.16 mW

Figure 4.63 shows a contour plot of the phasors of the mixed beads population, excited at 0.16 mW and the histograms of each phasor co-ordinate (u and v). The Fourier transformation of the phasors in the BIFL image format along with the corresponding lifetime histogram is given in Figure 4.64.

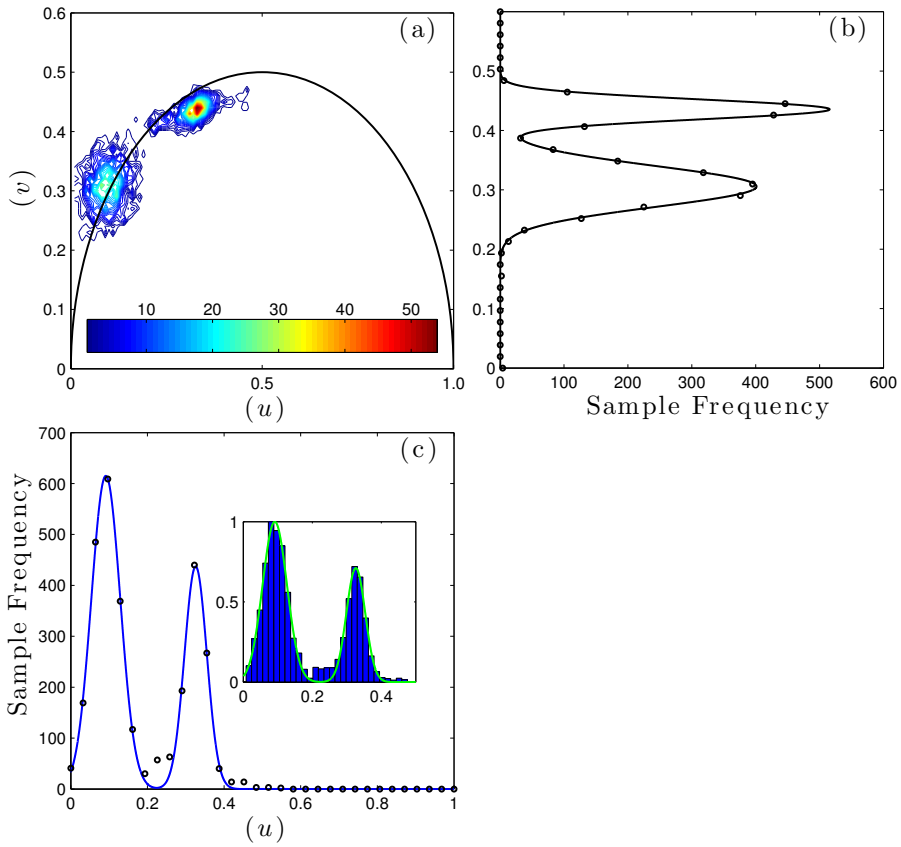

Figure 4.63: (a) Contour plot of phasors from the BIFL image (54 by 54 pixels) containing 2912 bursts. (b) The main panel shows the corresponding v–coordinate distribution of the phasors. (c) The main and inlet shows the corresponding u–coordinate distribution of the phasors.

A_1	u_1	σ_1	A_2	u_2	σ_2
231	0.326	0.039	324	0.091	0.050

Table 4.64: Summary of the Gaussian fit for the u–coordinate of the mixed beads population (BIFL) excited at 0.16 mW (see Figure 4.63 (c)), where A_1 and A_2 are the peak heights, u_1 and u_2 are the centre u-coordinates, and σ_1 and σ_2 are the standard deviation of the centre u-coordinates distributions of each bead population respectively.

A_1	v_1	σ_1	A_2	v_2	σ_2
516	0.436	0.024	401	0.306	0.049

Table 4.65: Summary of the Gaussian fit for the v–coordinate of the mixed beads population (BIFL) excited at 0.16 mW (see Figure 4.63 (b)), where A_1 and A_2 are the peak heights, v_1 and v_2 are the centre v-coordinates, and σ_1 and σ_2 are the standard deviation of the centre v-coordinates distributions of each bead population respectively.

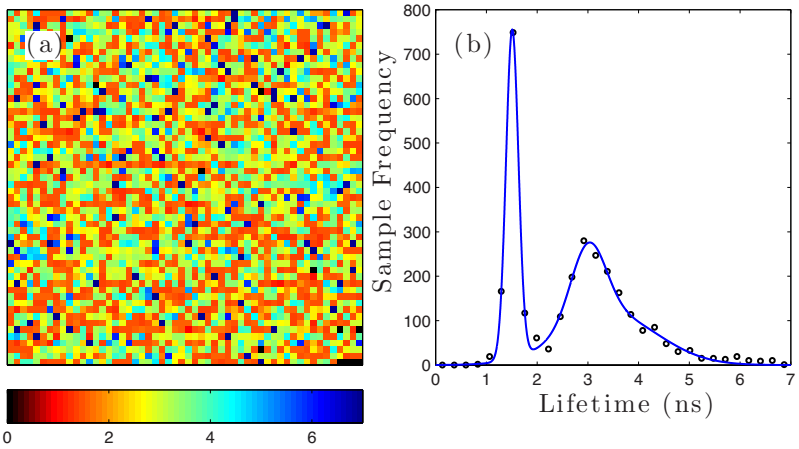

Figure 4.64: (a) A successfully calculated BIFL image by Fourier Transformation of phasors (24 by 24 pixels) containing the lifetime of 575 bursts. (b) The corresponding lifetime histogram of the BIFL data.

A_1	τ_1	σ_1	A_2	τ_2	σ_2
173	3.01	0.49	113	3.43	1.34

A_3	τ_3	σ_3
741	1.51	0.17

Table 4.66: Summary of the lifetime fitting parameters of the mixed beads population excited at 0.16 mW by FT(Phasor) (BIFL) (see Figure 4.64 (b)), where A_1, A_2 and A_3 are the peak heights, τ_1, τ_2 and τ_3 are the lifetime components measured in ns, and σ_1, σ_2 and σ_3 are the standard deviations of each sub-population in ns respectively.

From Figure 4.63, it can be observed that phasors of the two bead populations are clearly separated. One phasor population (population 1) is asymmetrically distributed at (0.326 ± 0.039, 0.436 ± 0.024). While the other (population 2), is approximately evenly distributed at co-ordinates (0.091 ± 0.050, 0.306 ± 0.049) of the contour plot.

The centre coordinate of population 1 closely matches that of Type I beads at (0.342 ± 0.033, 0.437 ± 0.020), while the coordinate of population 2 closely matches to the one of Type II beads at (0.090 ± 0.037, 0.305 ± 0.039).

From Figure 4.64, the Fourier transformation of the phasors shows clearly delineation of lifetime data of each bead type. The distribution was fitted with a 3 Gaussian mixture model. A 2-Mixture was used in outlining the lifetime distribution of Type II bead, while the remaining was responsible for the shape of Type II. It is evident that the higher mean distribution belongs to the Type II beads. The population also exhibits a positive skew, which is an inherent characteristic of the beads. The narrow distribution (population 1/ Type I) has a mean lifetime of 1.50 ± 0.17 ns, while the broader distribution (population 2/ Type II) has a weighted mean lifetime of 3.19 ± 1.03 ns. The distinction of the data is much better when comparing to the NL-MLM case in the previous section.

4.9 Flow Experiment: Sorting Mechanism

As demonstrated in the previous sections, the phasor readout emerged out as the best representation of this multi-population data. The clear-cut differentiation of sub-species in the data on a 2D output format, gives analysts a flexibility in defining the sorting threshold. If fluorescence lifetimes were to be used for the sorting mechanism, then the assessment of the sorting threshold would be limited to only the lifetime axis of the lifetime graph (i.e. locating and using the minimum valley between the populations as the decision point, and accept some small contamination in the tails of the complex histograms). The scatter plot in Figure 4.65 represents the phasors of the mixed population data. It is evident

that the large diagonal gap between each cluster gives us latitude in defining the threshold, with minimal errors, as opposed to the small horizontal margin between the clusters. Additionally, the diagonal threshold would be more robust to any statistical change of data, such as the large and unpredictable extent of lifetime reduction of Type I beads due to changes in the streamline, as shown in the phasor analysis in Figure 4.37. If, for any reason, the lifetimes or phasors of the Type II beads, or in fact, any sample type begins to experience the behaviour, the shift in the valley of the lifetime histogram or phasor cluster could encroach upon the threshold point set along the horizontal axis very easily.

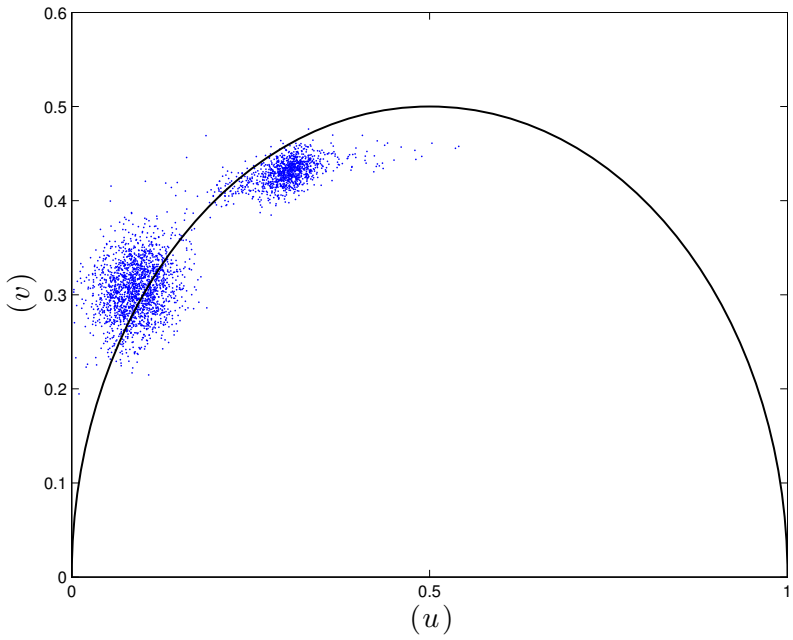

Figure 4.65: Scatter plot of the phasors of the mixed bead population.

This section will show how a simple linear algebra can be used to sort the population quickly and efficiently. The idea of the sorting is to manually draw a straight line (threshold line) across the clusters diagonally from any u-origin until it intercepts with the y-axis, Once accomplished, every data point of the scatter plot, will be treated as their own line series from the same origin as the threshold line and use the linear algebra to calculate each intercept (see Figure 4.66). The func-

tional readout of the mechanism is the y-intercept (i.e. intercepts of data points of population 1 < intercept of the threshold line < intercepts of data points of population 2). Any data point lying on the threshold line will not be classed but should represent a vanishingly small fraction.

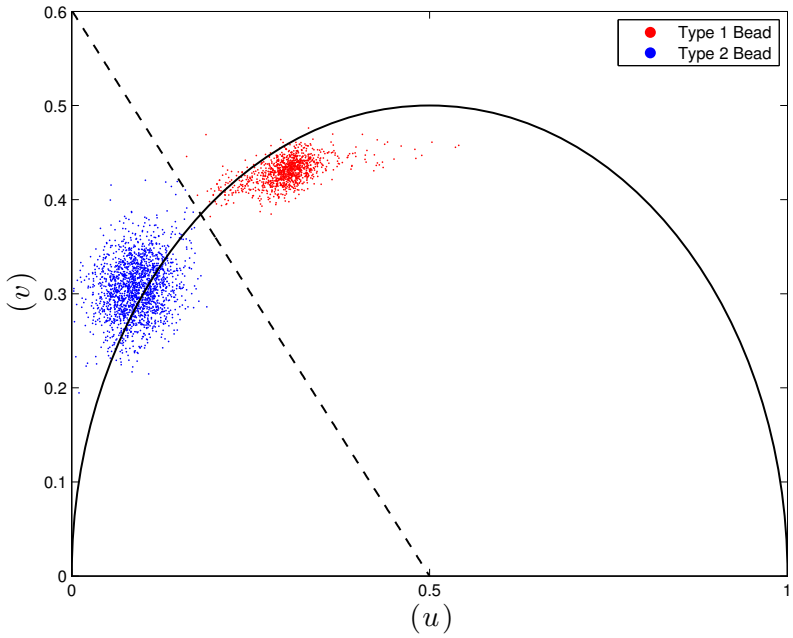

Figure 4.66: Defining a sorting threshold by determining and drawing a line through the two data populations.

Despite the simplicity of the approach, Figure 4.66 shows that this sorting mechanism is in fact effective. There is no anomalous behaviour in the mixture of colour present on the graph. All in all, this is a relatively simple problem for sorting. There are more sophisticated algorithms, such as k-mean clustering [84] and centroiding [85, 86], which iteratively dissecting the data until the optimal solution is found, with minimal analyst intervention. This approach does not involve with any iterative process nor require any assumptions about the data and hence can guarantee a fast computation regardless of the sample type. The only glitch is that it requires an analyst to manually set the threshold. However, once it is done, the corresponding lookup table can be used as the reference for any

experimental repeat. Only when the two clusters are located very close to one and another and it becomes harder for an analyst to manually make a decision would more sophisticated approaches have to be considered.

4.10 Flow Experiment: Sorted Data

4.10.1 Sorted BIFL images of Type I beads

The separation of phasors can be used to trace the BIFL and burst characteristics of the data. Figure 4.67 and Figure 4.68, explicitly show BIFL image of Type I beads from the data, with NL-MLM and FT(Phasor), respectively. Any Type II detection event is masked with zero, which is represented in black colour pixel.

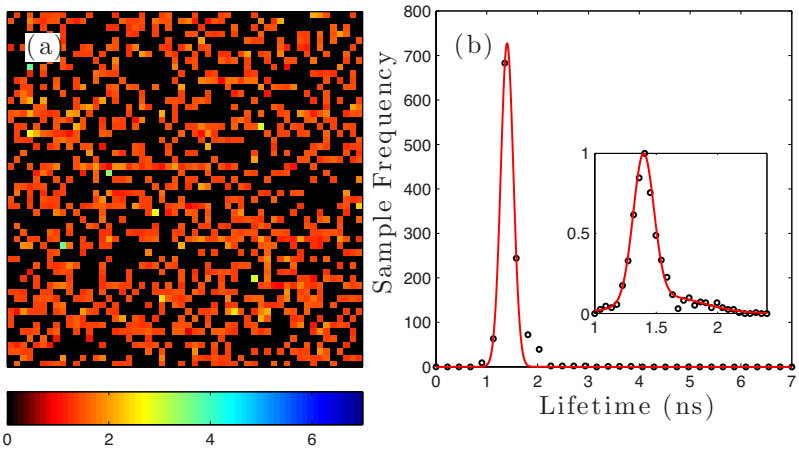

Figure 4.67: BIFL image (54 by 54 pixels) containing the lifetime of 1121 detection events of Type I beads from the mixed population, analysed by NL-MLM. (b) The corresponding lifetime histogram of the BIFL data.

A_1	τ_1	σ_1	A_2	τ_2	σ_2
169	1.40	0.12	19	1.58	0.43

Table 4.67: Summary of the lifetime fitting parameters of the sorted Type I beads excited at 0.16 mW by NL-MLM (BIFL) (see Figure 4.67 (b)). The average lifetime of the control was calculated by a double Gaussian mixture model, where A_1 and A_2 are the fractional contributions from the number of pixel of the image, τ_1 and τ_2 are the mean lifetimes measured in ns, and σ_1 and σ_2 are the standard deviations of each sub-population in ns.

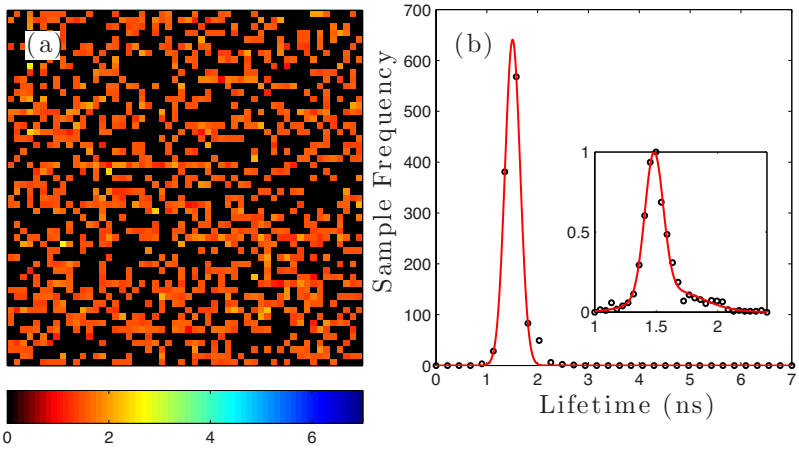

Figure 4.68: BIFL image (54 by 54 pixels) containing the lifetime of 1121 detection events of Type I beads from the mixed population, calculated by Fourier Transformation of phasors. (b) The corresponding lifetime histogram of the BIFL data.

A_1	τ_1	σ_1	A_2	τ_2	σ_2
179	1.48	0.11	27	1.63	0.35

Table 4.68: Summary of the lifetime fitting parameters of the sorted Type I beads excited at 0.16 mW by FT(Phasor) (BIFL) (see Figure 4.68 (b)). The average lifetime of the control was calculated by a double Gaussian mixture model, where A_1 and A_2 are the fractional contributions from the number of pixel of the image, τ_1 and τ_2 are the mean lifetimes measured in ns, and σ_1 and σ_2 are the standard deviations of each sub-population in ns.

From the phasor plot in Figure 4.66, it could be seen that the Type I bead population is aggregated in an elongated or oval shape. This has a direct reflection on the lifetime results on both fitting methods in Figure 4.67 and Figure 4.68. Both Figures show two overlapping lifetime distributions from the data, where the ratio between the populations is approximately 9:1 and 7:1 for the NL-MLM and FT (Phasor) analysis methods, respectively.

The horizontal end of the phasor cluster in Figure 4.66, which lies on the universal semi-circle is observed to have a higher density than the one of the opposite side. It is evident that this is the sub-population of Type I beads, which travels in the streamlines away from the excitation probe and experience smaller quenching of lifetime. The lower density trail on the opposite side shows the rare excessively high lifetime quenching, which likely to come from a small population of the beads travelling very close to the probe. This is credible, remembering the probe is now parked at a compromising position. The lifetime of either population from both analysis methods now have very little importance to us, as the data of bead type is clearly differentiated. The degree of the lifetime quenching is also largely unpredictable at this power setting due to the compromising position of the beam.

4.10.2 Sorted BIFL images of Type II beads

Figure 4.69 and Figure 4.70, show the BIFL image of Type II beads from the mixed population. The detections of Type I beads are similarly masked out by zero values.

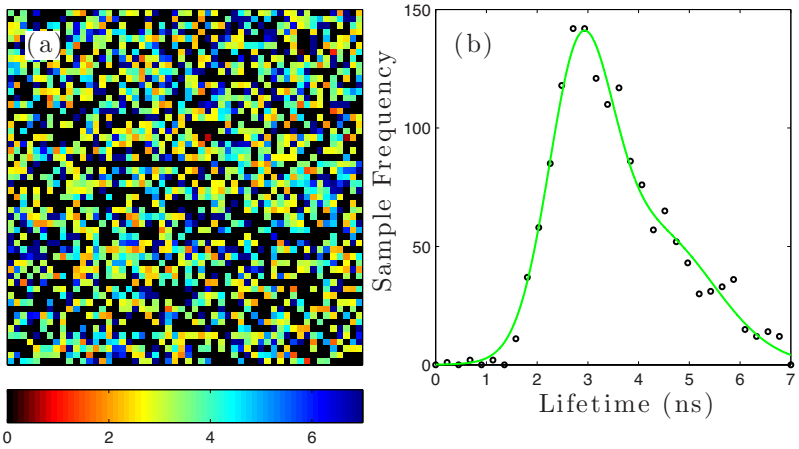

Figure 4.69: BIFL image (54 by 54 pixels) containing the lifetime of 1791 detection events of Type II beads from the mixed population, analysed by NL-MLM. (b) The corresponding lifetime histogram of the BIFL data.

A_1	τ_1	σ_1	A_2	τ_2	σ_2	Ave. τ	Ave. σ
112	2.84	0.88	56	4.26	1.70	3.45	1.28

Table 4.69: Summary of the lifetime fitting for the sorted Type II beads excited at 0.16 mW by NL-MLM (BIFL) (see Figure 4.69 (b)). The average lifetime of the control was calculated by a double Gaussian mixture model, where A_1 and A_2 are the fractional contributions from the number of pixel of the image, τ_1 and τ_2 are the mean lifetimes measured in ns, and σ_1 and σ_2 are the standard deviations of each sub-population in ns. Ave. τ and Ave. σ reprensents the average lifetime and the associated standard deviation in ns respectively.

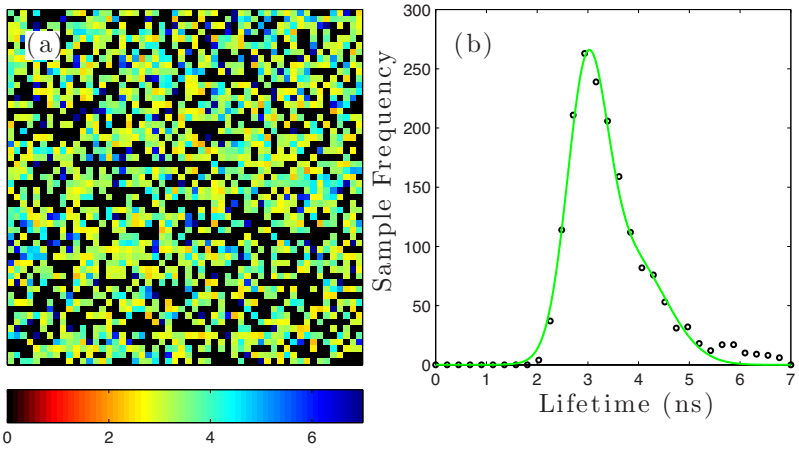

Figure 4.70: BIFL image (54 by 54 pixels) containing the lifetime of 1791 detection events of Type II beads from the mixed population, calculated by Fourier Transformation of phasors. (b) The corresponding lifetime histogram of the BIFL data.

A_1	τ_1	σ_1	A_2	τ_2	σ_2	Ave. τ	Ave. σ
216	2.98	0.55	92	3.81	1.02	3.27	0.76

Table 4.70: Summary of the lifetime fitting for the sorted Type II beads excited at 0.16 mW by FT(Phasor) (BIFL) (see Figure 4.70 (b)). The average lifetime of the control was calculated by a double Gaussian mixture model, where A_1 and A_2 are the fractional contributions from the number of pixel of the image, τ_1 and τ_2 are the mean lifetimes measured in ns, and σ_1 and σ_2 are the standard deviations of each sub-population in ns. Ave. τ and Ave. σ reprensents the average lifetime and the associated standard deviation in ns respectively.

The phasor of Type II beads is evenly distributed on the scatter plot in Figure 4.66. This results in cleaner lifetime distributions in Figure 4.69 and Figure 4.70, which are computed to be naturally and positively skewed by either analysis method. In this case, the Fourier transformation of the phasors is able to give a tighter approximation of lifetime than the NL-MLM, as expected. The average lifetime of the Type II beads is calculated to be 3.45 ± 1.28 ns and 3.26 ± 0.79 ns, by the NL-MLM and FT (Phasor) algorithms, respectively. The values are relatively close to the experimental reference in flow at 3.70 ± 1.26 ns

and 3.33 ± 0.68 ns, respectively, considering the measurement was acquired at approximately 0.03 photon per excitation event.

4.10.3 Sorted Burst Characteristics

Figure 4.71 and Figure 4.72 show the burst characteristics of sorted Type I and II beads, respectively. For the interest of brevity, only the burst width characteristic would be discussed in the context, as conclusions on the bead type from the evidence of the integral burst intensity and instantaneous count rate analysis have already been formed in subsection 4.7.1.

The burst width characteristic in the Figure 4.71 (a) shows the burst width population, which centred around 1 ms in Figure 4.59 (a) in subsection 4.7.1 to belong to the Type I beads. Figure 4.72 (a) shows that burst width distribution of Type II beads is centre around 0.3 ms.

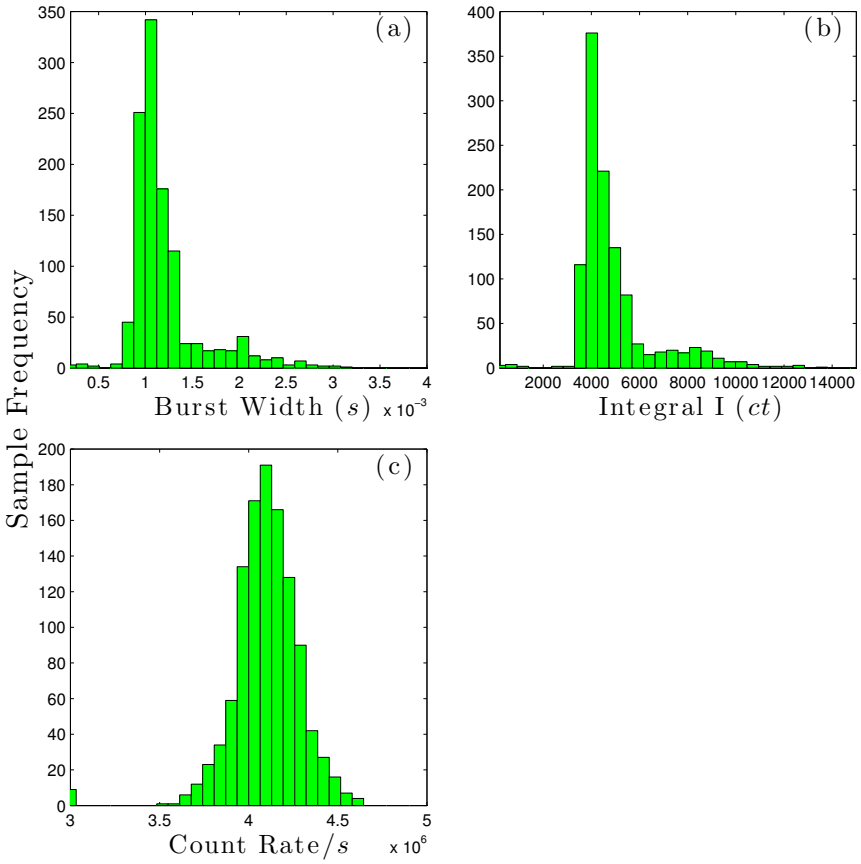

Figure 4.71: Burst characteristics of Type I bead from the mixed beads population at 0.16 mW of excitation power, where (a), (b), and (c) represents the burst widths, integral intensities, instantaneous count rates during each burst detection, respectively.

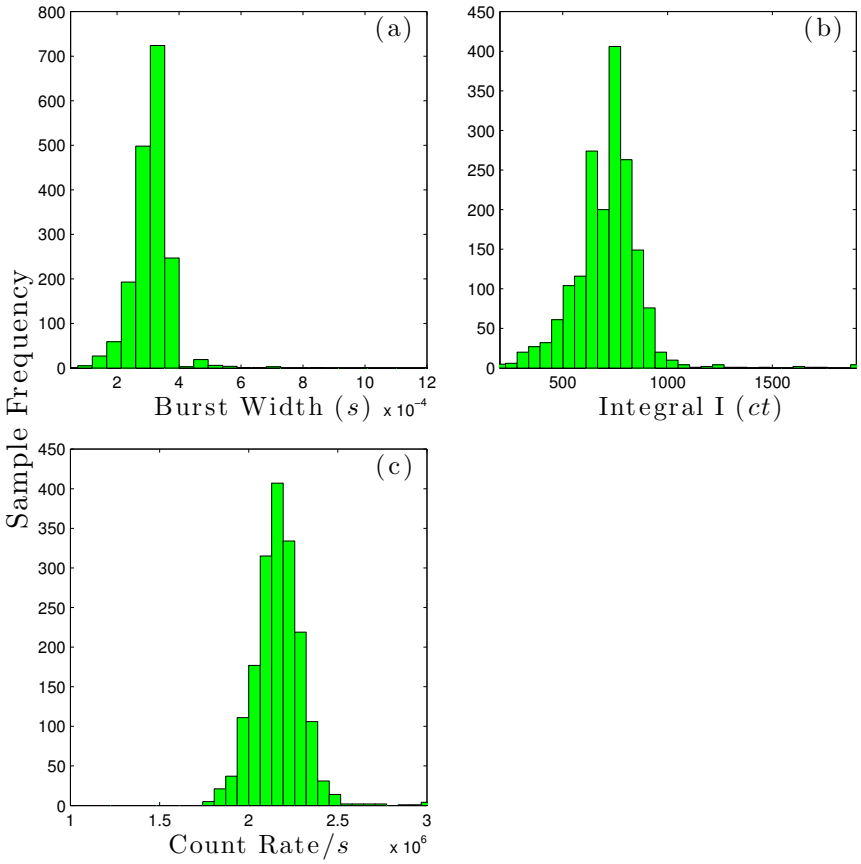

Figure 4.72: Burst characteristics of mixed beads population at 0.16 mW of excitation power, where (a), (b), and (c) represents the burst widths, integral intensities, instantaneous count rates during each burst detection, respectively.

4.10.4 Sorted Integrated Transient of Type I and II beads

It was shown in subsection 4.7.2, that the integrated transient of the mixed population is dominated by the fluorescence of Type I beads, which largely masked out the presence of the Type II. At the present stage of the analysis, the lifetime analysis of each bead type is virtually trivial. However it would still be interesting to observe the integrated shapes of each sorted population to assess the purity of the sorting.

In the interest of brevity, only the data from the Fourier transformation analysis will be presented. Figure 4.73 and Figure 4.74 shows the integrated transient profile of Type I and II beads fitted by the calculation of FT (phasor), respectively. It is evident that integrated shape of the Type II beads is well recovered, which suggests that the sorting of data is very pure. The peak fluorescence of the Type II beads is approximately 12,000 counts, while the average integral intensity of Type I is approximately either 4,000 or 8000 counts. Should one or more Type I bead(s) contaminate the sorted data of Type II, then the shape of the integrated transient in Figure 4.74 would be observably affected. From the Table 4.68 and Table 4.69, the average lifetimes of Type I and II data were calculated to be 1.51 ns and 3.28 ns respectively. The lifetime of the experimental reference in flow by the same method was calculated to be 1.35 ns and 3.29 ns for Type I and II beads respectively. While it is difficult to predict the average lifetime value of Type I beads due to controllable pulse pile-up at this excitation power, the lifetime of Type II between the experimental reference and the sorted data are remarkably close to one and another.

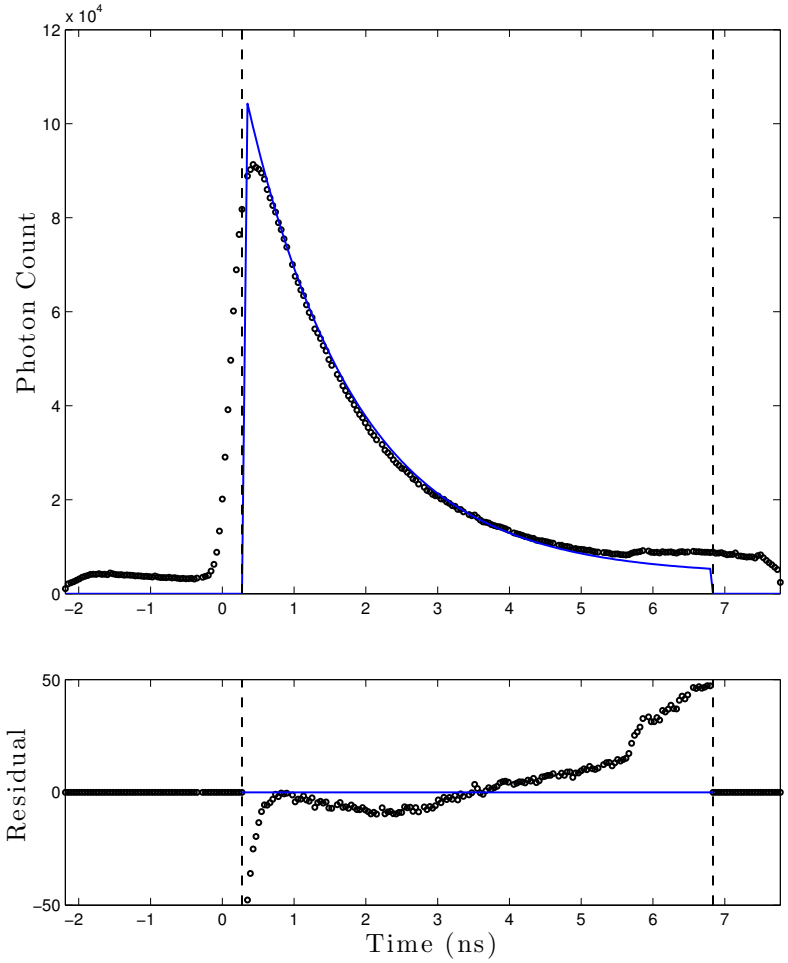

Figure 4.73: Integrated transient profile of the Type I beads from the mixed bead population. The transient is fitted a mono-exponential model by the NL-MLM.

u	v	τ_p	τ_m	τ	χ^2_R / d.f.
0.320	0.434	1.41	1.62	1.51	354

Table 4.71: Summary of the lifetime calculation from the integrated transient profile of sorted Type I beads by Fourier Transformation of the phasors (Burst Mode) excited at 0.16 mW (see Figure 4.73), where u and v are the centre values of the corresponding axes. τ_p is the lifetime component calculated from the phase delay of the modulated signal waveform from the modulated excitation laser rate in ns, τ_m is the lifetime component calculated from the demodulation between the two modulated waveforms in ns. τ is the average of the two lifetime components in ns and χ^2_R is the goodness of fit (or calculation) parameter of the Fourier transformation of the phasors.

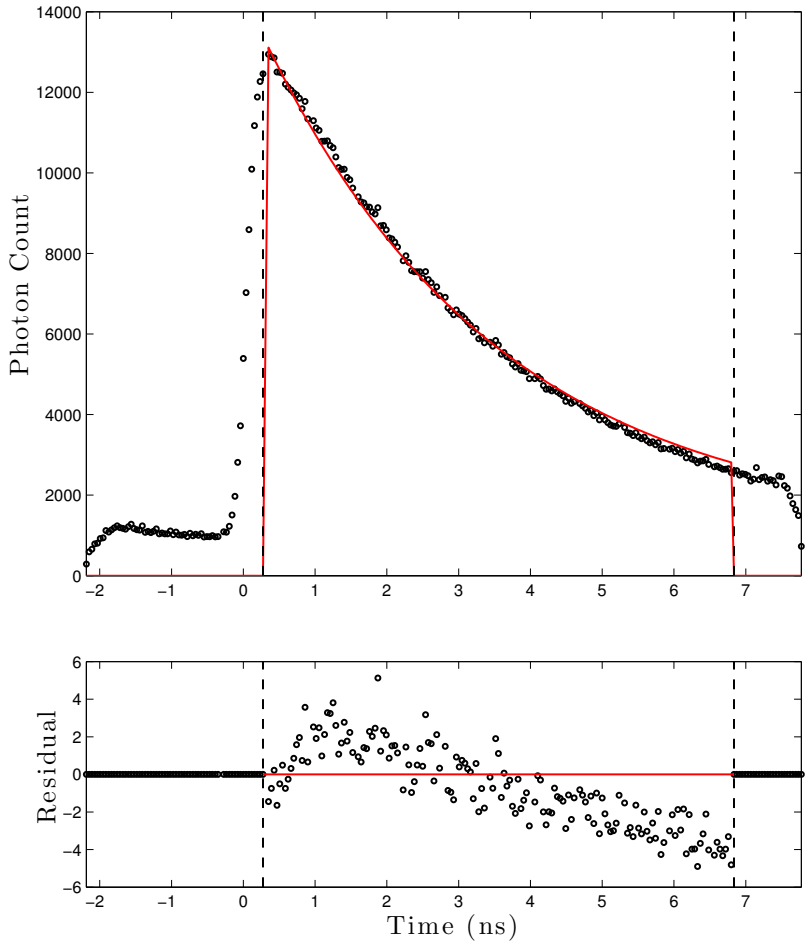

Figure 4.74: Integrated transient profile of the Type II beads from the mixed bead population, calculated by the Fourier Transformation of the phasors.

u	v	τ_p	τ_m	τ	χ^2_R / d.f.
0.092	0.305	3.46	3.09	3.28	6

Table 4.72: Summary of the lifetime calculation from the integrated transient profile of sorted Type II beads by Fourier Transformation of the phasors (Burst Mode) excited at 0.16 mW (see Figure 4.74), where u and v are the centre values of the corresponding axes. τ_p is the lifetime component calculated from the phase delay of the modulated signal waveform from the modulated excitation laser rate in ns, τ_m is the lifetime component calculated from the demodulation between the two modulated waveforms in ns. τ is the average of the two lifetime components in ns and χ^2_R is the goodness of fit (or calculation) parameter of the Fourier transformation of the phasors.

4.11 Conclusion

This chapter have shown that BIFL flow is capable of measuring fluorescence lifetime data in a model system analogous to that of a cell population. Data for two different bead types with different fluorescence lifetimes were shown and their burst characteristic analysed by both iterative re-convolution and phasor methods of data analysis. It has been shown that the phasor readout in the frequency domain provides an alternative mean of differentiating multiple population data, where mixtures of beads can be distinctively differentiated using a virtual sorting in the phase domain. These data show promise for real world application of the BIFL microfluidic cytometer which are further explored in the following chapters.

Chapter 5

System Testing Against Biological Samples

This chapter deals primarily with the ability of the FIFO BiFL method which was developed to identify cell populations with and without acceptors in an engineered FRET construct and the ability of the system to delineate accurately between variations in FRET efficiency. This is a continuation from the previous chapter to a biological context. It was demonstrated in chapter 4 that Phasor analysis is robust to experimental errors such as the secondary excitation from an optical reflection in the system under a high-power illumination (see subsection 4.3.1 in chapter 4). The cell experiments in this chapter will put the system and phasor analysis under sterner tests against potential errors associated with real biological samples, where auto-fluorescence and other spectroscopic contaminations can occur.

A key application of the FIFO BiFL flow system would be to clearly separate positive cells from an experimental control in, for example, a drug-screening assay [21,29,60,87]. Generally, Biological preparations involving immunocytochemistry, are not spectroscopically clean. Investigations of untested or un-optimised FRET assays with standard FLIM systems often report FRET efficiencies of 5% or less in the past. Even after optimisation FRET efficiencys rarely exceed 20% in real world protein-protein interaction studies due to size limitations (distance of

closest approach between fluorophores) and donor/acceptor stoichiometries [18]. Therefore the limits of sensitivity for the FRET measurement which the flow spectrometer can cope with must be known. This is especially relevant in the adverse experimental conditions (imposed by the interference from auto-fluorescence and excitation scattering)

Often FRET assays contain donors both bound and unbound to acceptors are involved with, at least, bi-exponential decay kinetics. This prompts the need for investigations on sensitised acceptor emission to completely validate the strength of FRET interactions. However an additional detector for the acceptor emission was installed to the setup late on during the project, and so the investigation could not be carried out in time. As previously mentioned in theoretical introduction in chapter 4, the NL-MLM algorithm for a bi-exponential decay requires approximately 10,000 photons to resolve bi-exponential decay with an acceptable degree of accuracy and this will still be dependent on good separation of the lifetimes and favourable fractions of the two populations [70]. Whilst the system parameters were optimised to achieve the best possible excitation/emission efficiency with the test samples in chapter 3, the photon yields from biological samples with transfected fluorescent proteins in this system were unknown at the start of the project. The FIFO BiFL flow system can only allow a single irradiation per sample (burst) which will be limited by the flow rate. Contamination from cellular auto-fluorescence will limit the data quality (and also segmentation of bursts if the sample contamination in the solvent is high). Flow speed must be optimised to achieve the required photon and throughput targets, thereby creating a trade-off between burst amplitude and throughput. In the system, the throughput is necessarily modest (it is not intended to maximise the number of cells imaged per minute) but flow rates are reasonable such that if the number density of cells was higher, the burst length would not need to be reduced to accommodate the increase.

5.1 Characterisation of the system dynamic range with Spectroscopic Ruler Standard

FRET standards, similar to those described by Vogel and coworkers [88], but consisting of eGFP linked to mRFP1 (instead of CFP/YFP) by amino acid chains of varying lengths (7, 19, and 32 amino acids) in a 1:1 stoichiometry, will be used for this investigation. The constructs were originally used in the characterisation of acceptor fluorescence anisotropy for a high content screening (HCS) project, which used an automated plate reader [5]. The result from the original work will be used as the experimental reference for this FRET dynamic range characterisation of FIFO BIFL.

Figure 5.1 represents a simplified diagram of the spectroscopic ruler standard. Simply put, the amino acid sequence determines the distance between the fluorescent protein pair, while the lifetime of the donor decreases as a function of distance over the FRET effective range between $R_0/2$ and $3R_0/2$. The R_0 between eGFP and mRFP is approximately 4.6 nm [18]. eGFP-7aa-mRFP is expected to give the strongest FRET interaction, followed by eGFP-19aa-mRFP and eGFP-32aa-mRFP. Since the length of the amino acid sequences (see Appendix A) will limit the strength of FRET interaction for each construct, the ability as a spectroscopic ruler in FRET would be an excellent tool to validate this, provide the lengths of the amino acid chains do not exceed the range between 2.3 to 6.9 nm. (which make them analogous to a spectroscopic ruler). Another main characteristic of the interaction Tis the donor fluorescence intensity of the eGFP-7aa-mRFP construct will beis expected to be strongly quenched in comparison to the opposite number, eGFP-32aa-mRFP (as will be shown by the results of the high content screening in Figure 5.2). According to the direct relationship between FRET interaction and quantum yield of fluorophore in Equation 1.1 in chapter 1, the increase in the strength of the FRET interaction would increase the size of the non-radiative decay pathway, which competes against the radiative pathway.

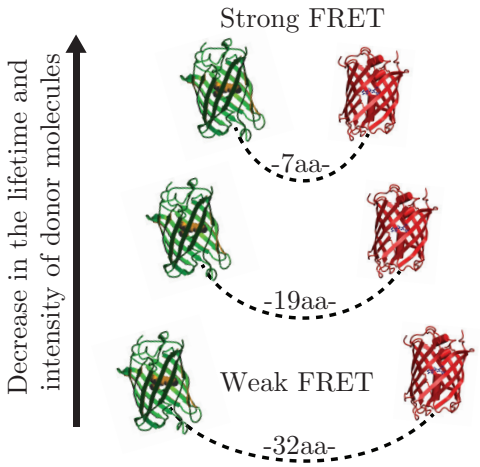

Figure 5.1: Schematic diagram of the spectroscopic ruler interaction (Drawn by candidate)

Typically, for cell experiments, only FRET efficiencies are compared between data sets, since both control and FRET positive cells may change in lifetime due to variation in preparation. Variations of a few hundred picoseconds are normal in biology, however, the samples in this case are all prepared and stored in buffer solution, making them particularly susceptible to dirt and other fluorescent contamination during handlings, the possibility of larger variations is also likely if the samples are stored for an extended period (which allow a larger contamination to be accumulated). FRET efficiency between different experiments should be comparable provided the experimental conditions remain the same, for the screening of each construct.

Figure 5.2 shows sample images of 293T (HEK) cells transiently transfected with the 7AA and 32AA constructs and plated onto a type 1.5 coverglass with Mowoil mounting media (including Dabco antifade reagent) from the high content screening project [5]. The figure includes the wide-field image of the construct (first row), which was used as a fast first-pass screen of the cell intensities, intensity image from the laser scanning (second row) and the corresponding lifetime image (third row).

From Figure 5.2 (a) third row, distinctive decrease in lifetime can be observed

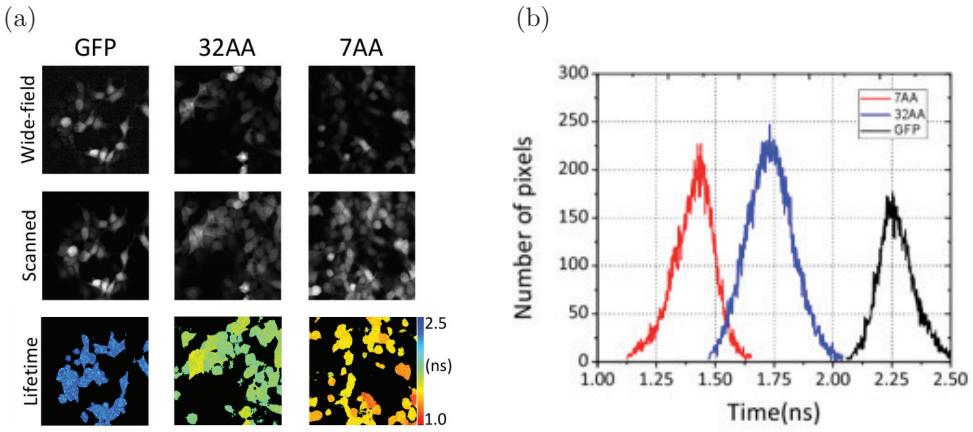

Figure 5.2: Experimental results of the HCS project from the imaging of FRET standard constructs expressed in 293T cells [5], where (a) contains intensity images from wide-field microscopy (first row) and FLIM (second row), as well as the lifetime image obtained from FLIM (third row) for GFP, 32AA and 7AA standards, respectively and (b) shows the corresponding lifetime histogram for each construct.

with a decrease in linker length, through the change of the false colour scale, where Figure 5.2 (b) represents the corresponding histogram of the lifetime data from the images. The lifetime data from Figure 5.2 (b) are translated into FRET efficiency values of 23% and 33% measured for the eGFP-32AA-mRFP and eGFP-7AA-mRFP constructs, respectively. Data for the eGFP-19AA-mRFP construct was omitted from the paper in the interest of clarity, as its FRET efficiency was measured to be 27%, which is only a minor change from the eGFP-32AA-mRFP. The trend in the increment of FRET efficiency follows the one described by Vogel et al [88] closely, even though the cells in that case were transfected with cyan-yellow fluorescent proteins separated by slightly different linker lengths. Cerulean (a blue fluorescent protein variant serving as the donor) was attached to Venus (9) (a yellow variant serving as the acceptor) with either 5, 17, or 32 amino acid linkers in between them, respectively

5.1.1 Method and System Setting

In initial experiments using the FIFO BiFL system with a line focus configuration, noticeable autofluorescence and/or other background fluorescence from unbound probes in solution were observed on the baseline signal during acquisitions. It was observed that reduction in beam power did not significantly improve the discrimination of the fluorescence intensity emission of the cells from the background. Following these investigations, the excitation beam profile was reconfigured to a spot focus (power = 0.25 mW) to reduce the level of the unwanted fluorescence as much as possible. This configuration change increases the discrimination since a much smaller volume of the flow chip is excited and therefore a greater proportion of the excitation is directed at the sample as compared to the solvent. Some of the background signal is almost certainly due to the eGFP or FRET standard constructs (which are expressed as soluble proteins in the cell cytoplasm) lost from the cells during fixing and permeabilisation. As a consequence, a compromise between the single sample resolution and the probability of missed detections by overfilling the channel with under-diluted cell solution (see Figure 5.3) was made. It is normal for transiently transfected cells to express a variety of fluorescence intensities. The experiment was performed at a relatively low flow speed as a precaution to accommodate for longer photon collection times in the expectation of complex transient analysis. Basing on the results of subsection 3.2.1 and subsection 3.2.2 of chapter 3, the reduction in speed would result in a large spatial distribution of streamlines within the channel with a dilute (by volume) sample solution. Aggregations of mammalian cells may also occur and result in different cell shapes and more unpredictable streamlines within the flow. Furthermore, weakly fluorescent cells could potentially be lost or masked by the auto-fluorescence and/or other noise sources. Therefore, a more successful detection rate of the assay would be assured by loading the channel with more cells. The aim for this part of the study is to work out the global lifetime of each cell population, and so simultaneous detection of multiple cells can be tolerated, although this is clearly not ideal.

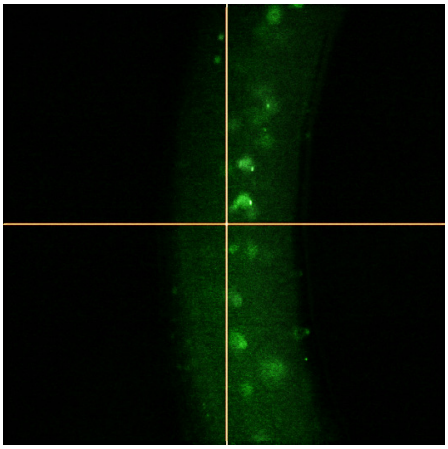

Figure 5.3: An image of an under-diluted sample solution flowing within the channel (at drift velocity) A full video footage can be found on `http://www.youtube.com/watch?v=xUCoahdT28w`. The intensities of the cells in the picture were enhanced by a photo editing software and the crosshair has been superimposed on top of the image to indicate the centre of the field of view.

The FIFO data was collected by a single detector (PMC-100) in the green channel (for the instrument response function, please refer to subsection 2.5.1 in chapter 2. FRET efficiency of each construct will be calculated by the lifetime reduction in relation to the experimental control, as stated in Equation 1.12 [1]. Since the FRET efficiency data from the experimental reference from the HCS project [5], only show a small variation between the data of the eGFP-32aa-mRFP and eGFP-19aa-mRFP, another in-house fitting method [69], which uses Bayes theorem to infer the fit parameters of mono-exponential decays was also adopted (see subsection 5.1.2. This Bayesian fitting is anticipated to give a better resolvability between the constructs, where its performance will be shown in subsection 5.3.3 and subsection 5.3.4. This chapter will describe the burst characteristics and integrated transient profile, before showing the BIFL analysis of the constructs in a similar workflow as chapter 4. The injection of higher sample concentration, the large variability in the cell fluorescence expression, and the adoption of the spot focus, all make the burst characteristics less unique and incomparable to one and another. For the interests of brevity, direct comparison and improvement of the workflow; the burst characteristics, lifetime histograms of individual events,

[1]Equation 1.12: $E = 1 - \frac{\tau_{DA}}{\tau_D}$

and integrated transient data from each construct will be collectively analysed in the respective sections. The BIFL image does not contribute much to the discussion and will be also omitted from the lifetime analysis section to allow the corresponding lifetime histograms to be directly analysed and compared.

5.1.2 Introduction to Bayesian Fitting

When the photon collection per sample is sparse (100 to 200 counts), both standard and modified least square algorithms have been shown to yield poor estimates of fit parameters [70, 89–92]. The nature of this flow experiment makes the regulation of the photon collection time more difficult than imaging, as each sample is subject to a single pass through the excitation beam limited by flow rate (contrary to repetitive scanning). When dyes with low quantum yields or a batch of transiently transfected cells fail to produce high fluorescence expression, or when the flow rate becomes too fast, FIFO BIFL acquisition generally tends to yield bursts with low photon counts (<1000 counts). TRI-2 incorporated a Baysian Inference analysis method [69] to attempt to increase the accuracy of the fitting under such conditions.

In formalising the Bayesian approach to the FLIM analysis, Rowley and coworkers [69] described a decay model that the likelihood of a photon being detected at a particular measured time is purely determined by exponential decay process. The model also accounted for any signicant effect introduced by the data acquisition, such as the influence of a repetitive pulsed excitation on the physical process of photon generation (i.e. the variation in the measured fluorescence decay time in relation to the excitation pulse period) and the effect of instrument response on the measurement which imposes some delays and uncertainties in the time between a generation and the moment of photon detection. The model is then applied in the Bayesian framework, photon-by-photon, to a set of photon arrival times that constitute a decay. Hence the computational time can be relatively long (approximately 2 hours per image analysis in the case for multi-exponential decays) compared to the NL-MLM and phasor methods, for

the benefit of a better accuracy.

5.2 Burst Characterisitics

5.2.1 Control Construct

BIFL data for the construct of the spectroscopic ruler experiment are given in Figure 5.4, Figure 5.5, Figure 5.6 and Figure 5.7 for control, eGFP-32aa-mRFP, eGFP-19aa-mRFP, and eGFP-7aa-mRFP respectively. The total number of detected cells for each case was 3520, 2554, 2097 and 3348 respectively.

The burst width and integral intensity histograms of the constructs all exhibit exponential profiles. This is somewhat expected, as a large variety of protein expression is normal for any transient transfection. More importantly, because the excitation was arranged in the spot configuration and the cell solution was not heavily diluted, the system was likely to be prone to unwanted detection events, ranging from cell aggregations to simultaneous detections from the in and out-of-focal planes. Partial excitation of single cells, were likely to be the most frequently occurred events, due to the lack of control in cell streamlines. All of these factors are the major contribution to the exponential nature of the data. The notable characteristics of the following the figures, are the burst width and instantaneous count rate characteristics of the experimental control. Figure 5.4 (a) shows that the range of burst widths detected in the acquisition closely resembles the range of burst widths detected by Type I beads (comparable diameters), with a similar pumping air pressure. The bead solutions in chapter 3 were properly diluted and behaved well in flow, it is reasonable to assume the acquisition of the control was subject to minimal cell aggregation.

Figure 5.4 (c) shows that the characteristics are more evenly distributed, compared to other constructs (see below). It is centred on the higher mean value than the rest, at approximately 2.5×10^6 counts. The number bodes wells with the theory of the competitive decay pathways of excited fluorescence molecules, since the control contains no additional non-radiative decay route from the ra-

diationless transfer between donor and acceptor. The exponential behaviours of the characteristics make the integral intensities between the constructs incomparable to one and another for the validation, but the increase in the instantaneous count rate is clearly an informative sign. The concern, which the characteristic can impose on the lifetime of the control, is that the value will be subject to pile-up compared to the rest of the constructs due to the high count rate. The instantaneous count rate characteristics of the eGFP-32aa-mRFP, eGFP-19aa-mRFP, and eGFP-7aa-mRFP constructs yielded very similar shape, peak value and count range. It is possible that their lifetimes will be quenched by a similar degree to one and another, but not necessarily guaranteed. One assurance obtained the experiment is that the result from the HCS project [5] shows the difference in lifetime between the control and the longest ruler construct in the 32 amino acid chain, to be approximately 500 to 550 ps. The characterisation of Type I beads at 0.1 mW of excitation power in the previous chapter, showed that the instantaneous count rate in the excess of 2.5 MHz would result in a reduction of lifetime by approximately 200 to 250 ps due to pile-up. Providing the rest of the constructs are also subject to lifetime quenching (which is likely due to the majority of the detected events exceeded the self-imposed safe count rate limit at 0.8 MHz), then the separation between the control and the FRET constructs would remain distinctive. However, it can be almost confidently assumed here, that the FRET efficiency of the FRET construct will yield lesser values compared to the ones of the HCS project [5] if, for example, the lifetimes of the FRET constructs are averagely quenched by approximately 100 ps (i.e. the difference in lifetime between the control and the eGFP-32aa-mRFP construct is approximately 400 to 450 ps).

The majority of the integral burst intensities of the constructs (the peaks and the first half of the exponentially behaved histograms) are less than 5×10^3 counts. Only very small range of the data exceeded 1×10^4 counts. This may have some impact on the lifetime analysis, especially for the NL-MLM. Hence Bayesian analysis is attractive, despite the impractical time scale of the analysis. Bayesian and phasor analysis should provide excellent methodologies to examine the biological data as will be shown in section 5.3 and section 5.4.

Lastly, the observation of the fall in intensity with the longer protein linker cannot be validated by the data set due to the large range of fluorescence expression per construct (see subsection 5.2.2, subsection 5.2.3 and subsection 5.2.4). However the lifetime analysis of the cells would be sufficient in reporting the strength of the interaction with good confidence.

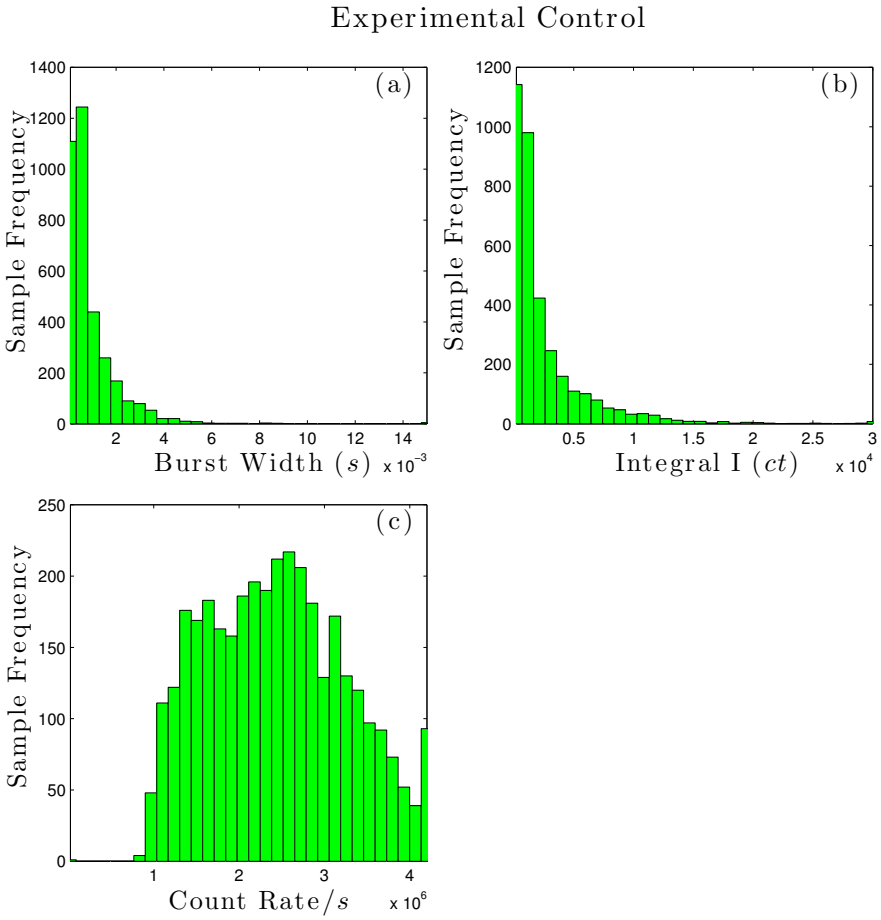

Figure 5.4: Burst characteristics of the control construct, where (a), (b), and (c) represents the histogram of burst widths, integral intensities, and instantaneous count rates of the detected event, respectively.

5.2.2 eGFP-32aa-mRFP Construct

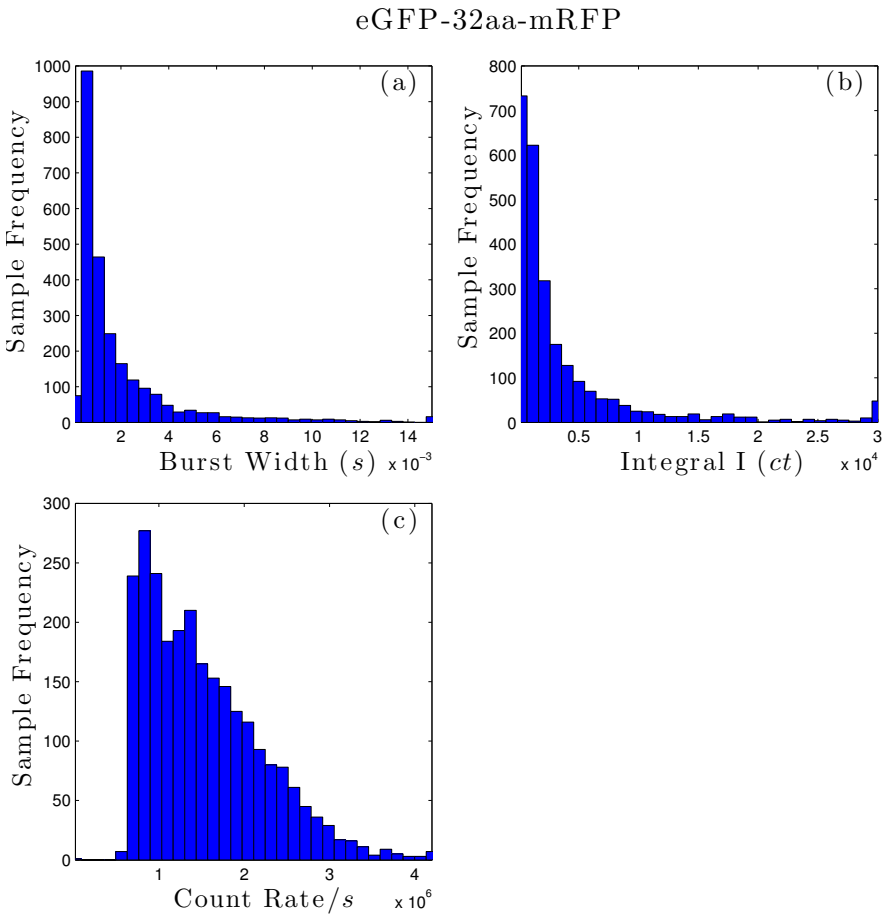

Figure 5.5: Burst characteristics of the eGFP-32aa-mRFP construct, where (a), (b), and (c) represents the histogram of burst widths, integral intensities, and instantaneous count rates of the detected event, respectively.

5.2.3 eGFP-19aa-mRFP Construct

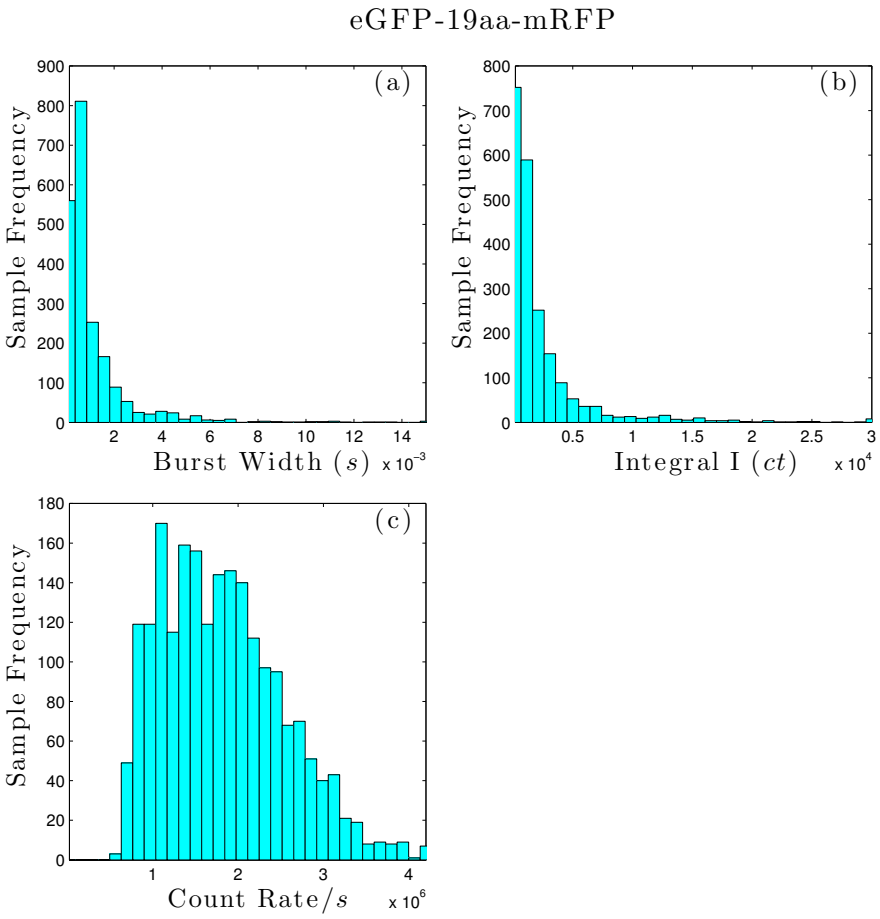

Figure 5.6: Burst characteristics of the eGFP-19aa-mRFP construct, where (a), (b), and (c) represents the histogram of burst widths, integral intensities, and instantaneous count rates of the detected event, respectively.

5.2.4 eGFP-7aa-mRFP Construct

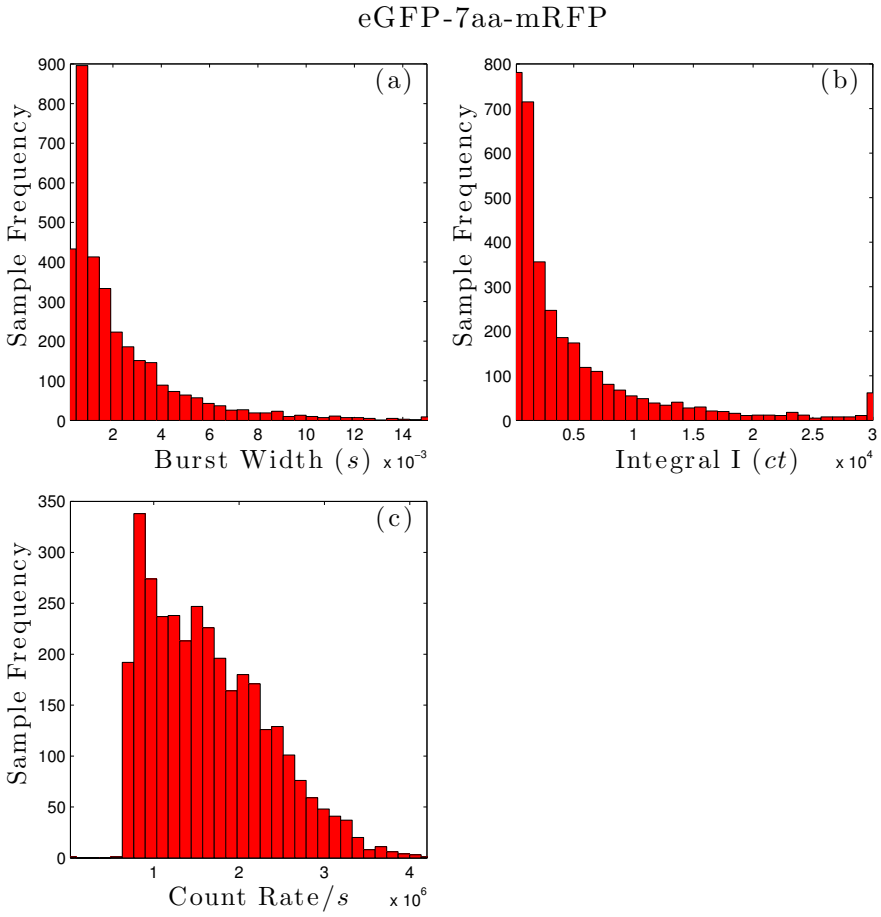

Figure 5.7: Burst characteristics of the eGFP-7aa-mRFP construct, where (a), (b), and (c) represents the histogram of burst widths, integral intensities, and instantaneous count rates of the detected event, respectively.

5.3 BIFL Analysis

As shown in the previous chapter, the calculated lifetimes differ from method to method of analysis. Despite this, FRET efficiencies of the samples (values or the trend in the reduction) are expected to remain largely the same, because they are the physical traits of the involved photo-physics. In this section, the FRET analysis will be performed separately per analysis method.

As mentioned in the previous chapter in subsection 4.3.10 and subsection 4.5.7, NL-MLM analysis did not work well for data which is consisted of bursts with low photon numbers (< 1000 counts). For any pixel or burst with a small number of photons (< 500 counts), which subsequently results in noisy decay profile (Poissonian problem), the NL-MLM algorithm of TRI-2 tended to fit it with anomalously long decay profile (regardless of the samples type). As a consequence, this positively skews the lifetime histograms into asymmetric shapes.

In the double Gaussian mixture analysis, the averaging of the two lifetime components is probably going to be the most robust method for determining a lifetime and FRET efficiency from the data (see Equation 5.1).

$$AverageParameter = \frac{A_1P_1^2 + A_2P_2^2}{A_1P_1 + A_2P_2} = f_1P_1 + f_2P_2 \tag{5.1}$$

Here A is the sample frequency, P is the parameter under calculation (lifetime or FRET effciency) and f is the fractional contribution of each parameter. The number in the subscript represents the affiliation of each parameter to a specific Gaussian population.

However, if the weighted mean lifetimes of the constructs were used in the analysis, then the quadratic terms of the averaging expression will treat any negative FRET efficiency value of the long lifetime components, as extra positive FRET components and shift the average value of the FRET efficiency in the analysis (as will be shown in this section). This would spuriously appear as systematic error, especially when the mean of the control is not centred at zero along the x-axis of the FRET histogram. In this case, the FRET efficiency will be determined solely from the larger fractional contribution of the lifetime distribution to avoid the problem (provided the data makes sense in the photo-physical term).

5.3.1 NL-MLM analysis of BIFL Data

The analysed burst event data, using NL-MLM is summarised in Figure 5.8. Please note differences in histogram scale for the cell frequency.

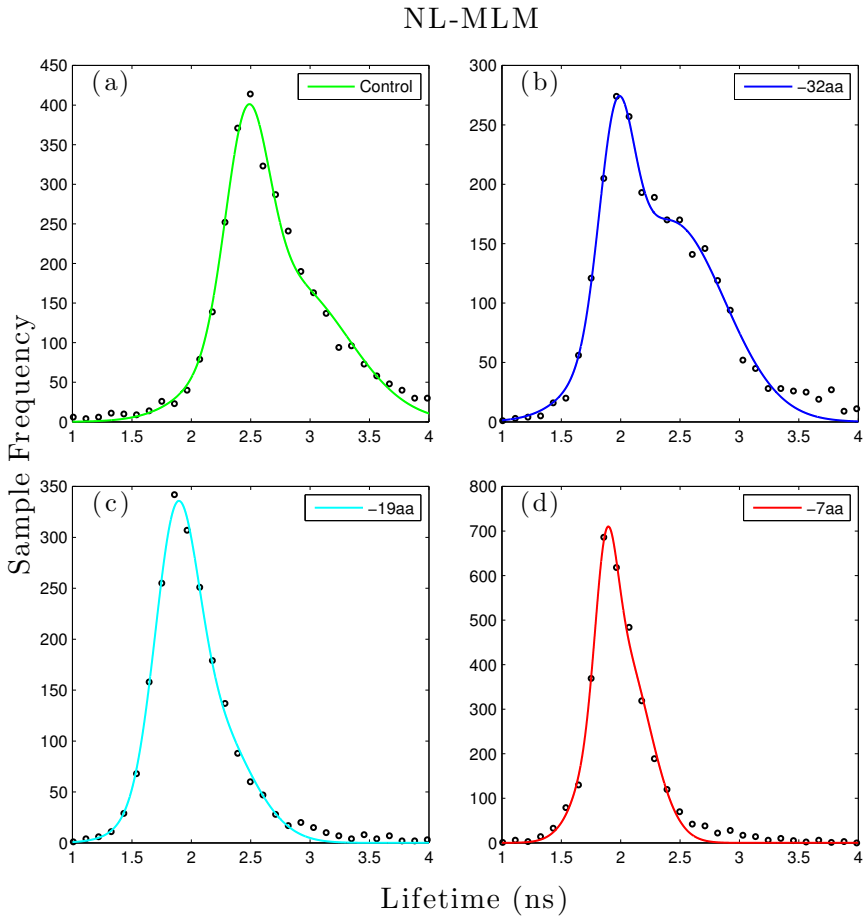

Figure 5.8: Lifetime determination by BIFL with NL-MLM, where a, b, c and d represent the lifetime histogram of the BIFL images of experimental control, eGFP-32aa-mRFP, eGFP-19aa-mRFP, and eGFP-7aa-mRFP, respectively.

	A_1	A_2	τ_1	τ_2	σ_1	σ_2	Ave. τ	Ave. σ
Control	261	176	2.47	2.81	0.25	0.72	2.62	0.55
32aa	169	169	1.96	2.42	0.21	0.65	2.21	0.54
19aa	234	127	1.87	2.11	0.25	0.49	1.96	0.39
7aa	327	434	1.88	2.00	0.13	0.34	1.95	0.29

Table 5.1: The table of summary for the lifetime fitting (NL-MLM). The average lifetime of the was calculated by a double Gaussian mixture model, where, A_1 and A_2 are the fractional contributions, τ_1 and τ_2 are the mean lifetimes in ns, and σ_1 and σ_2 are the standard deviations of each sub-population in ns, respectively. Ave. τ is the average lifetime in ns and Ave. σ is the average standard deviation of each construct in ns, respectively. Here, control, 32aa, 19aa and 7aa represent the control (eGFP alone), eGFP-32aa-mRFP, eGFP-19aa-mRFP and eGFP-7aa-mRFP constructs respectively.

From Figure 5.8 (a), the lifetime characteristic of the control shows a shoulder in the positive direction. Whilst the positive skew tends to be a natural characteristic of the NL-MLM approach, this actually looks excessive. As previously mentioned in the burst characteristics analysis in section 5.2, the average instantaneous count rate of the detector from the acquisition was higher for the control compared to the rest of the cases. It is very likely that the pulse pile-up effect and any low photo bursts which were fit poorly (where $\chi^2 \ll 1$) would have moderately contributed would have contributed in the skew. From Figure 5.8 (b), the eGFP-32aa-mRFP construct also shows a well-pronounced shoulder in the positive direction on the graph. The centre lifetime of the shoulder at 2.42 ns bears a similar value to the dominant population of the control, at 2.47 ns. It will be shown in the Bayesian and Phasor analysis in subsection 5.3.3 and subsection 5.3.5 that the shoulder is, in fact, the result of contamination between the control and the eGFP-32aa-mRFP construct. From Table 5.1, a progressive reduction in the lifetime between the control and the FRET constructs could be clearly observed with shorter linker lengths. The average lifetime between the eGFP-19aa-mRFP and eGFP-7aa-mRFP are very close to one another. The data of the 19aa linker was omitted in the data summary, since its average lifetime is very similar to the ones of the 7aa linker. The omission would also allow a di-

rect comparison with the results available from the HCS project [5] in this section.

As previously mentioned at the start of the section, the data in Figure 5.9 was fit to a double Gaussian model with the long lifetime component removed to give the result in Figure 5.10, as the shoulders in the positive directions are likely to be artefacts of the data/fitting rather than the characteristics of the fluorescence.

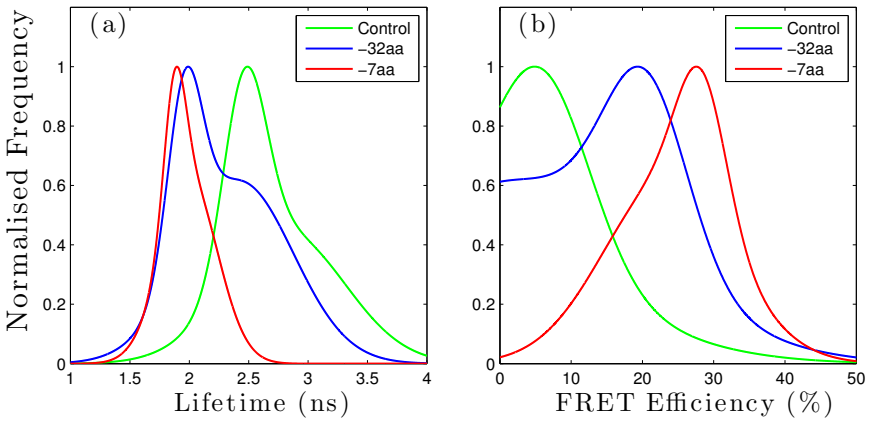

Figure 5.9: A summary of lifetime (a) and FRET efficiency (b) histograms from each construct.

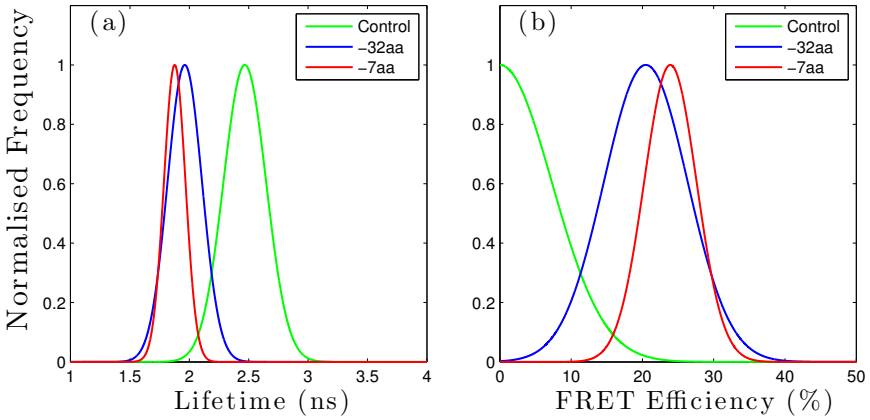

Figure 5.10: A revised summary of lifetime (a) and FRET efficiency (b) histograms from each construct. The histograms ignore the fractional contribution from the anomalously long lifetime components.

	τ	σ	FRET efficiency	σ_F
Control	2.47	0.25		
32aa	1.96	0.21	20.47	8.31
19aa	1.87	0.25	24.16	10.14
7aa	1.88	0.13	23.92	5.20

Table 5.2: The table of summary for the revised lifetime fitting (NL-MLM) (ignoring the sub-population with anomalously long lifetime), where τ is the mean lifetimes in ns, and σ is the standard deviations of each construct in ns, respectively. The FRET efficiency is expressed in % and σ_F is the standard deviation of the corresponding FRET efficiency in %. Here, control, 32aa, 19aa and 7aa represent the control (eGFP alone), eGFP-32aa-mRFP, eGFP-19aa-mRFP and eGFP-7aa-mRFP constructs respectively.

From Table 5.2, it could be seen that by ignoring the anomalous skews on the lifetime histograms, the FRET efficiency of the spectroscopic ruler data set was calculated to be 20.47%, 24.16% and 23.92% for the eGFP-32aa-mRFP, eGFP-19aa-mRFP, and eGFP-7aa-mRFP constructs, respectively. The values are reasonable, apart from the 7aa linker case. It raises a question whether the eGFP-

19aa-mRFP, eGFP-7aa-mRFP constructs are actually the same type or not, as the interaction of the eGFP-7aa-mRFP construct is expected to be as strong as 33% but did vary in previous experiments due to cell type and fixing conditions. According to Equation 1.10 in chapter 1, the linker spacing in -32aa, -19aa and -7aa were calculated (using FRET efficiency as a decimal number instead of the percentage value) to be 5.77, 5.56 and 5.57 nm, respectively. According to the data of the HCS project[2] [5], the linker spaces of the FRET constructs, -32aa, -19aa and -7aa, were calculated to be 5.62, 5.42 and 5.17 nm, respectively. The effective range of FRET interaction for eGFP-and-mRFP is between 2.3 and 6.9 nm, and so there are rooms for further shortening of the linker spacing of the -19aa and -7aa for even stronger FRET interactions. This will be further analysed by the integrated transient analysis with NL-MLM as well as other fitting methods (both pixel-by-pixel and integrated transient data).

As predicted in the instantaneous count rate analysis, the FRET efficiency of the eGFP-32aa-mRFP and eGFP-19aa-mRFP constructs both fell short by approximately 3%, but remains within the experimental error from the results obtained from the HCS project [5] (which were also analysed by the NL-MLM). The instantaneous count rate characteristics of the two constructs closely resembled one another and so their lifetimes were possibly quenched by approximately the same amount. On the other hand, the lifetime of the control must have been more strongly quenched compared to the two constructs, and so the lifetime difference in the control versus eGFP-32aa-mRFP and control versus eGFP-19aa-mRFP were reduced, which contributed to the small experimental uncertainty of 3%.

5.3.2 NL-MLM Analysis of Integrated Fluorescence Profile

The integrated analysis of the lifetime with NL-MLM is shown in Figure 5.11, while the fit data is summarised in Table 5.3. The graphs in Figure 5.11 are

[2]The FRET Efficiencies of the eGFP-32aa-mRFP, eGFP-19aa-mRFP, and eGFP-7aa-mRFP constructs of the HCS project were calculated to be 23%, 27% and 33% respectively

then re-plotted on a log scale in Figure 5.12. The data in Table 5.3 shows that average lifetime of eGFP-19aa-mRFP construct is almost identical to the one of eGFP-7aa-mRFP. The similarity is also re-confirmed by the overlay between the two data in Figure 5.12. From Table 5.3, the FRET efficiency of eGFP-32aa-mRFP is in fact incorrect, due to the contamination with the control. The FRET efficiencies of the eGFP-19aa-mRFP construct (or eGFP-7aa-mRFP, given that they are the same type) is also smaller than the one calculated in the HCS project [5], but this could be the result of the accumulated fluorescence impurities in the background.

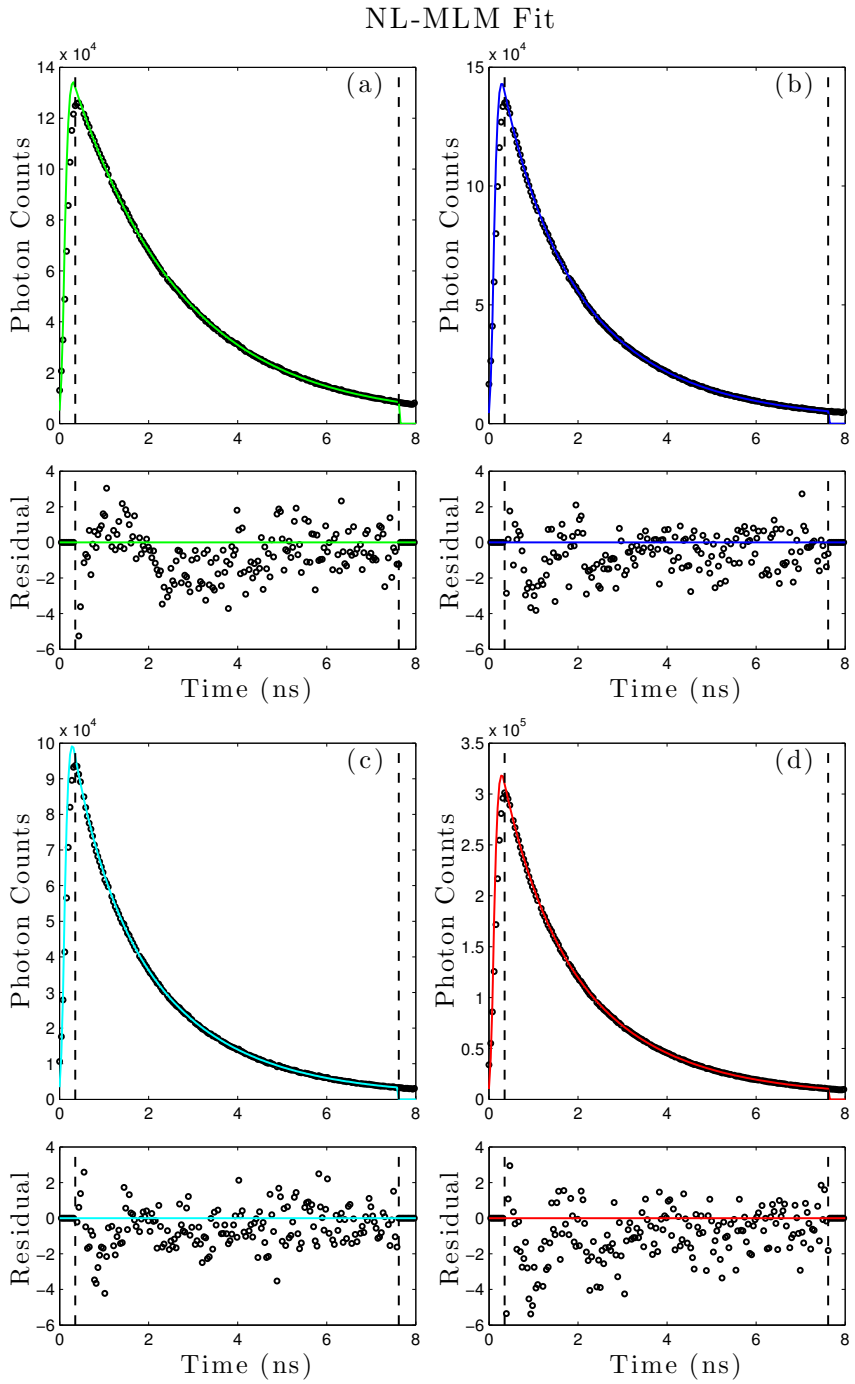

Figure 5.11: Summary of integrated transients from all the pixels of each BIFL image (analysed by NL-MLM), where (a), (b), (c) and (d) represents the transient of the control, eGFP-32aa-mRFP, eGFP-19aa-mRFP, and eGFP-7aa-mRFP constructs, respectively.

	Z	A_1	A_2	τ_1	τ_2	Ave. τ	χ^2_R	F.Eff
Control	1938	108665	33155	2.43	2.43	2.43	16	
32aa	447	110091	84711	2.71	1.25	2.33	15	4.22
19aa	904	77558	32923	2.15	0.74	1.97	8	18.8
7aa	2164	229515	122920	2.25	0.93	2.01	24	17.18

Table 5.3: The table of summary for the lifetime fitting on the integrated transients by NL-MLM, where A_1 and A_2 are the fractional contributions, τ_1 and τ_2 are the mean lifetimes in ns, and σ_1 and σ_2 are the standard deviations of each sub-population, respectively. Ave. τ is the average lifetime in ns, χ^2_R is the goodness of fit parameter and F. Eff is the FRET efficiency in %. Here, control, 32aa, 19aa and 7aa represent the control (eGFP alone), eGFP-32aa-mRFP, eGFP-19aa-mRFP and eGFP-7aa-mRFP constructs respectively.

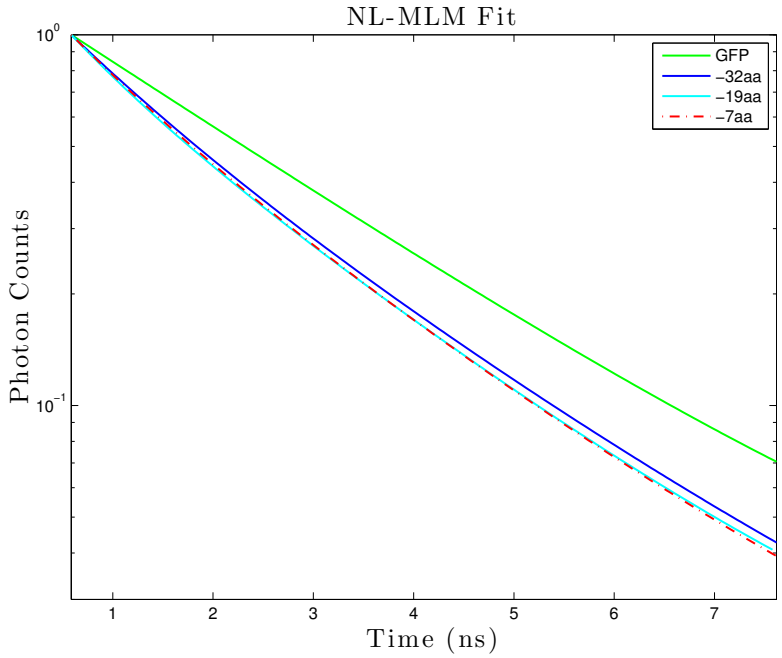

Figure 5.12: The collation of every transient in Figure 5.11, expressed in log scale.

5.3.3 Bayesian Analysis of BIFL Data

The analysed burst event data, using Bayesian analysis is summarised in Figure 5.13. Note that the histogram scale is variable for cell frequency in (a) to (d).

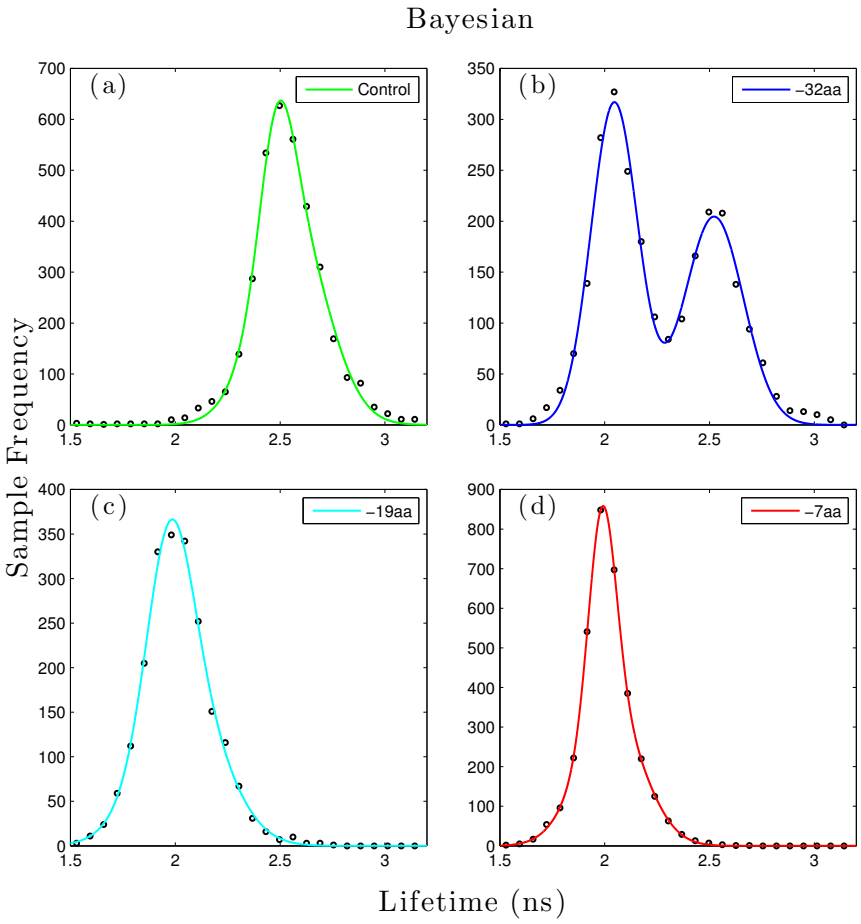

Figure 5.13: Lifetime determination by BIFL with NL-MLM, where a, b, c and d represent the lifetime histogram of the BIFL images of experimental control, eGFP-32aa-mRFP, eGFP 19aa-mRFP, and eGFP-7aa-mRFP, respectively.

	A_1	A_2	τ_1	τ_2	σ_1	σ_2	Ave. τ	Ave. σ
Control	274	388	2.49	2.56	0.12	0.24	2.53	0.21
32aa	316	205	2.05	2.52	0.16	0.20	2.26	0.18
19aa	205	170	1.97	2.04	0.15	0.27	2.00	0.22
7aa	540	329	1.99	2.03	0.09	0.22	2.00	0.17

Table 5.4: The table of summary for the lifetime fitting (Bayesian). The average lifetime of the was calculated by a double Gaussian mixture model, where, A_1 and A_2 are the fractional contributions, τ_1 and τ_2 are the mean lifetimes in ns, and σ_1 and σ_2 are the standard deviations of each sub-population in ns, respectively. Ave. τ is the average lifetime in ns and Ave. σ is the average standard deviation of each construct in ns, respectively. Here, control, 32aa, 19aa and 7aa represent the control (eGFP alone), eGFP-32aa-mRFP, eGFP-19aa-mRFP and eGFP-7aa-mRFP constructs respectively.

Each BIFL data set in Figure 5.13 took approximately 2 hours to fit. However such lengthy time consumption is paid off by a reduction in standard deviation and better-behaved lifetime distribution in all the constructs in Figure 5.13. Interestingly, since the lifetime distributions are now narrower and better defined, what was observed to be the shoulder on the lifetime distribution of the eGFP-32aa-mRFP construct during the NL-MLM analysis in Figure 5.8 (b), is now, closely resembled to the lifetime distribution of the control in Figure 5.13 (a). This can be observed by the additional peak, centring approximately near the 2.5 ns mark along the x-axis of the graph in Figure 5.13 (b). Table 5.4 shows the average lifetime of the control was calculated to be 2.53 ns, whilst the centre lifetime value of the secondary peak in the eGFP 32aa-mRFP data is 2.52 ns. The lifetime of the eGFP-19aa-mRFP and eGFP 7aa mRFP constructs were also calculated to be the same, which further suggested that both data sets were from the eGFP-19aa-mRFP construct.

Applying the same methodology to analyse the histograms as in the imaging data, the data in Figure 5.14 was fit to a double Gaussian model with the long lifetime component removed to give the result in Figure 5.15. From Table 5.5, the FRET efficiency values are observed to be lower than the NL-MLM case, but the trend

in the reduction remains very similar, 3% increase in the FRET efficiency from the eGFP-32aa-mRFP to the eGFP-19aa-mRFP constructs.

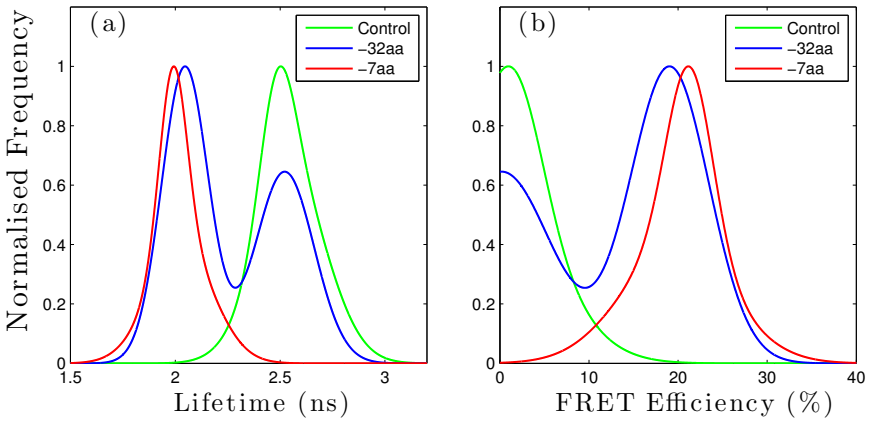

Figure 5.14: A summary of lifetime (a) and FRET efficiency (b) histograms from each construct.

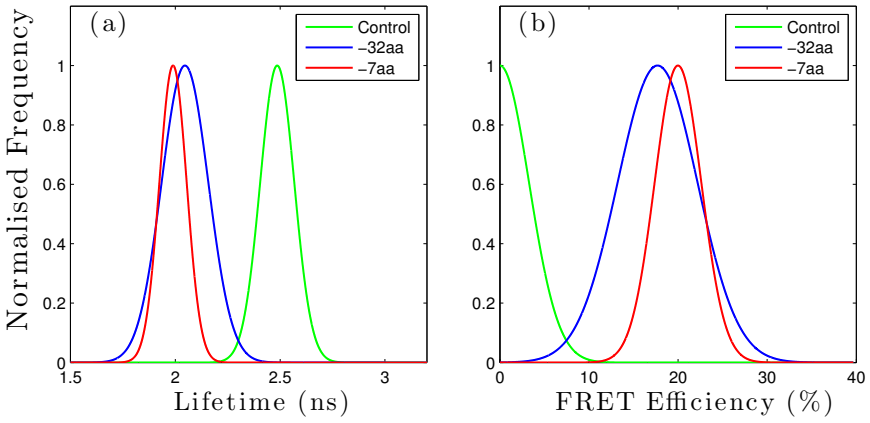

Figure 5.15: A revised summary of lifetime (a) and FRET efficiency (b) histograms from each construct. The histograms ignore the fractional contribution from the anomalously long lifetime components.

	τ	σ	FRET efficiency	σ_F
Control	2.49	0.12		
32aa	2.05	0.16	17.7	6.95
19aa	1.97	0.15	20.64	8.69
7aa	1.99	0.09	19.99	6.53

Table 5.5: The table of summary for the revised lifetime fitting (Bayesian) (ignoring the sub-population with anomalously long lifetime), where τ is the mean lifetimes in ns, and σ is the standard deviations of each construct in ns, respectively. The FRET efficiency is expressed in % and σ_F is the standard deviation of the corresponding FRET efficiency in %. Here, control, 32aa, 19aa and 7aa represent the control (eGFP alone), eGFP-32aa-mRFP, eGFP-19aa-mRFP and eGFP-7aa-mRFP constructs respectively.

5.3.4 Bayesian Analysis of Integrated Fluorescence Profile

The integrated analysis of the lifetime with Bayesian in Figure 5.16 seems to be behave well overall. There seems to be higher order multi-exponential decay in all cases, but the characteristic for these heavily contaminated data is now familiarised. Table 5.6 again shows that the average lifetime of the eGFP-19aa-mRFP and eGFP-7aa-mRFP are comparable to one and another. The calculated FRET efficiencies of the construct are remarkably close to those calculated on a pixel-by-pixel basis.

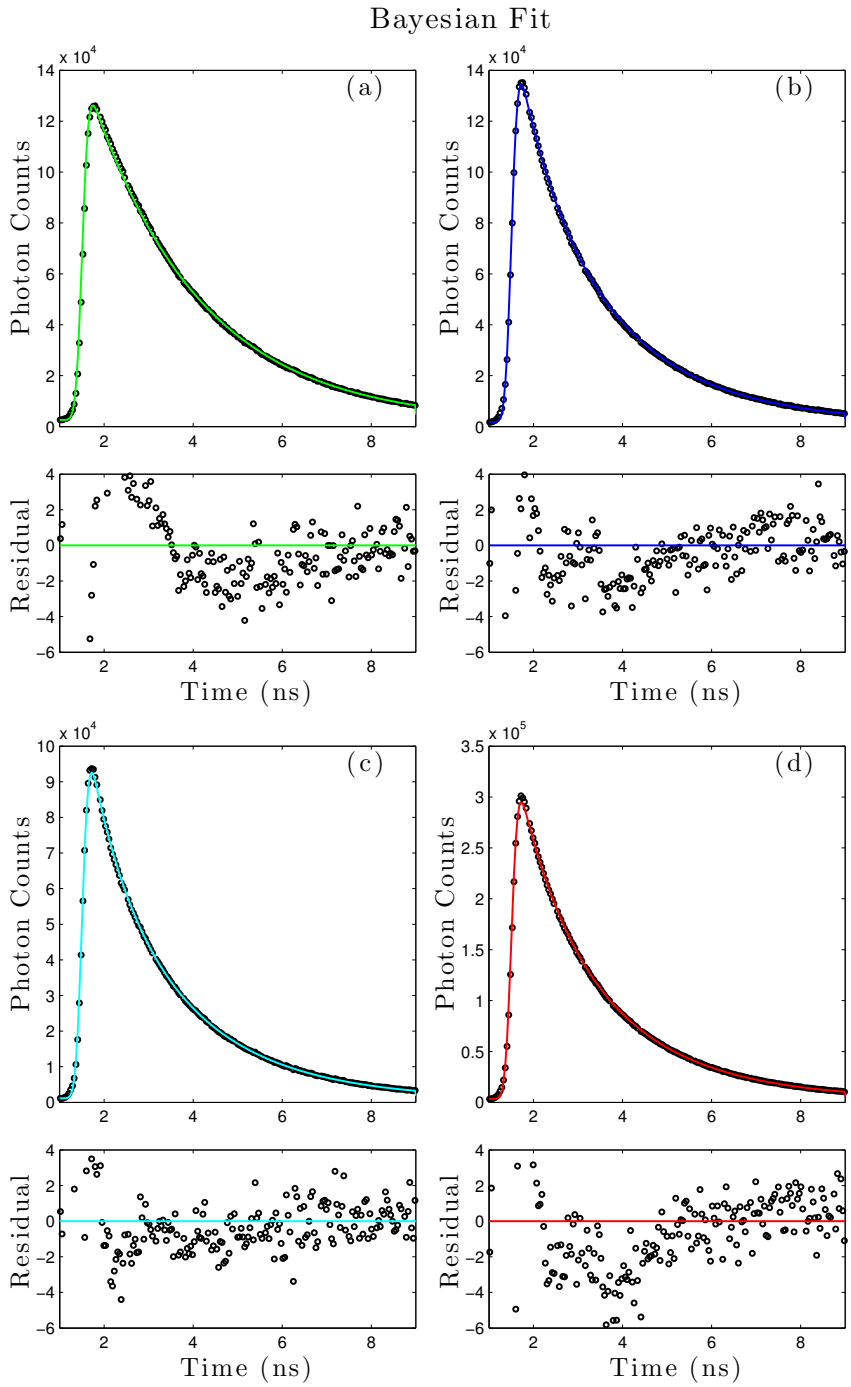

Figure 5.16: Summary of integrated transients from all the pixels of each BIFL image (analysed by Bayesian), where (a), (b), (c) and (d) represents the transient of the control, eGFP-32aa-mRFP, eGFP-19aa-mRFP, and eGFP-7aa-mRFP constructs, respectively.

	Z	A_1	A_2	τ_1	τ_2	Ave. τ	χ^2_R	F.Eff
Control	1526	138675	27.33	2.48	2.37	2.48	18.31	
32aa	1242	113800	41721	2.22	0.89	2.05	12.02	17.54
19aa	839	77093	31931	2.16	0.76	1.98	7.73	20.02
7aa	2428	235927	106196	2.20	0.98	2.00	29.04	19.35

Table 5.6: The table of summary for the lifetime fitting on the integrated transients by Bayesian, where A_1 and A_2 are the fractional contributions, τ_1 and τ_2 are the mean lifetimes in ns, and σ_1 and σ_2 are the standard deviations of each sub-population, respectively. Ave. τ is the average lifetime in ns, χ^2_R is the goodness of fit parameter and F. Eff is the FRET efficiency in %. Here, control, 32aa, 19aa and 7aa represent the control (eGFP alone), eGFP-32aa-mRFP, eGFP-19aa-mRFP and eGFP-7aa-mRFP constructs respectively.

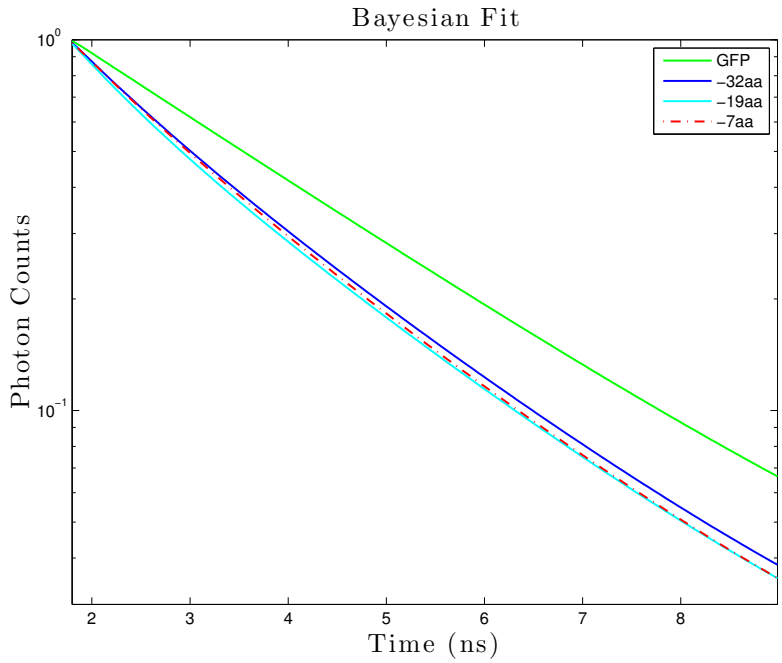

Figure 5.17: The collation of every transient in Figure 5.16, expressed in log scale.

5.3.5 Lifetime Analysis of BIFL Data by Phasor Method

In this section, the BIFL results are now analysed by the Fourier transformation of the phasors. The Fourier transformations of the phasors are chosen to be introduced prior to the phasor analysis in the phase domain to preserve the continuity of the lifetime context from one analysis method to the next. The analysed burst event data, using the Fourier transformation of the Phasors, is summarised in Figure 5.18. Note that the histogram scale is variable in cell frequency for (a) to (d).

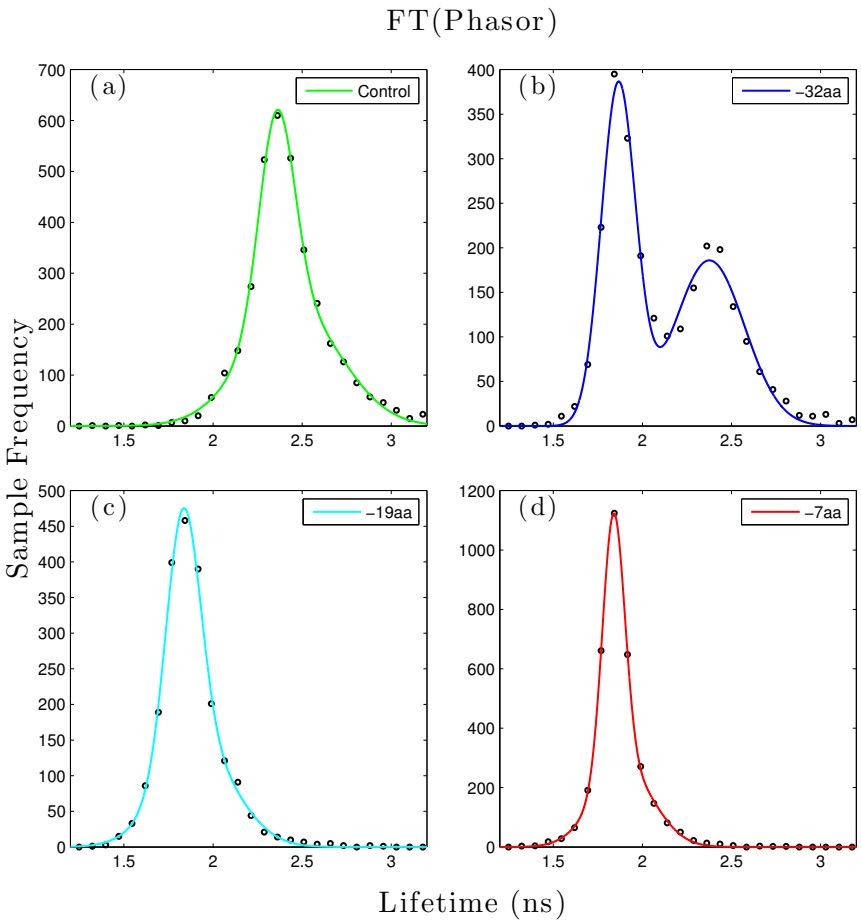

Figure 5.18: Lifetime determination by BIFL with FT(Phasors), where a, b, c and d represent the lifetime histogram of the BIFL images of experimental control, eGFP-32aa-mRFP, eGFP 19aa-mRFP, and eGFP-7aa-mRFP, respectively.

	A_1	A_2	τ_1	τ_2	σ_1	σ_2	Ave. τ	Ave. σ
Control	405	227	2.36	2.45	0.14	0.38	2.39	0.28
32aa	380	186	1.87	2.38	0.14	0.28	2.06	0.21
19aa	351	133	1.83	1.91	0.14	0.3	1.86	0.21
7aa	877	259	1.84	1.89	0.09	0.24	1.86	0.15

Table 5.7: The table of summary for the lifetime fitting FT(Phasors). The average lifetime of the was calculated by a double Gaussian mixture model, where, A_1 and A_2 are the fractional contributions, τ_1 and τ_2 are the mean lifetimes in ns, and σ_1 and σ_2 are the standard deviations of each sub-population in ns, respectively. Ave. τ is the average lifetime in ns and Ave. σ is the average standard deviation of each construct in ns, respectively. Here, control, 32aa, 19aa and 7aa represent the control (eGFP alone), eGFP-32aa-mRFP, eGFP-19aa-mRFP and eGFP-7aa-mRFP constructs respectively.

By and large, the standard deviations of the average lifetimes of each construct in Table 5.7 are marginally larger than the ones calculated by the Bayesian method (see Table 5.4). Consider the analysis was completed within seconds, this holds an attractive advantage over the Bayesian analysis. The evidence in Figure 5.18 (b) delineates the presence of the control in the eGFP-32aa-mRFP construct to good effect. The average lifetime of the eGFP-19aa-mRFP and eGFP-7aa-mRFP constructs are also calculated to be approximately the same in this method. The eGFP-7aa-mRFP and eGFP-19aa-mRFP continue to appear similar.

Applying the same methodology to analyse the histograms as in the imaging data, the data in Figure 5.19 was fit to a double Gaussian model with the long lifetime component removed to give the result in Figure 5.20. From Table 5.8, the FRET efficiency values are observed to be comparable to the Bayesian case, where there is approximately 1.5% increase in the FRET efficiency from the eGFP-32aa-mRFP to the eGFP-19aa-mRFP constructs.

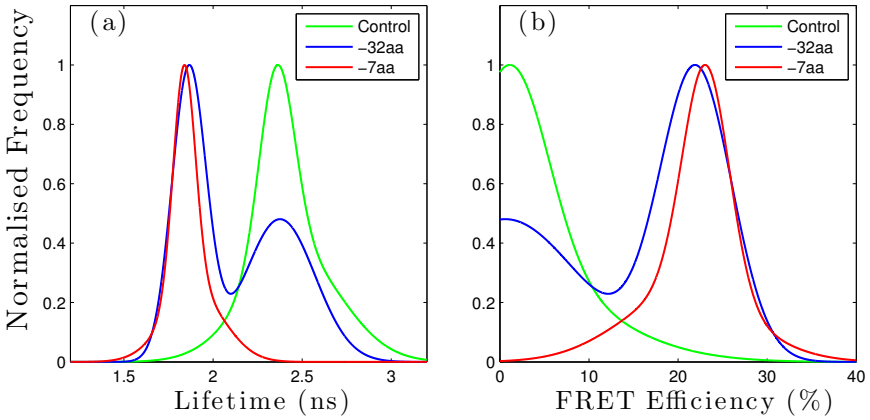

Figure 5.19: A summary of lifetime (a) and FRET efficiency (b) histograms from each construct.

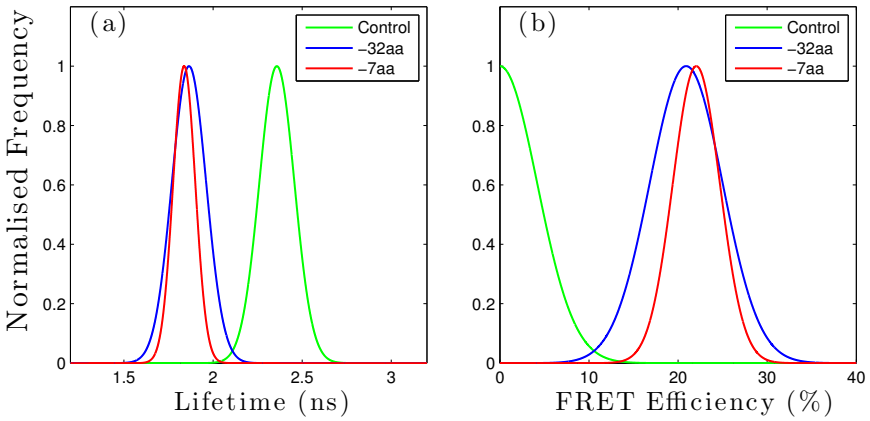

Figure 5.20: A revised summary of lifetime (a) and FRET efficiency (b) histograms from each construct. The histograms ignore the fractional contribution from the anomalously long lifetime components.

	τ	σ	FRET efficiency	σ_F
Control	2.34	0.14		
32aa	1.87	0.14	20.91	5.79
19aa	1.83	0.14	22.31	5.74
7aa	1.84	0.09	22.05	3.73

Table 5.8: The table of summary for the revised lifetime fitting FT(Phasors) (ignoring the sub-population with anomalously long lifetime), where τ is the mean lifetimes in ns, and σ is the standard deviations of each construct in ns, respectively. The FRET efficiency is expressed in % and σ_F is the standard deviation of the corresponding FRET efficiency in %. Here, control, 32aa, 19aa and 7aa represent the control (eGFP alone), eGFP-32aa-mRFP, eGFP-19aa-mRFP and eGFP-7aa-mRFP constructs respectively.

5.3.6 Integrated Fluorescence Profile: Phasor Analysis

The integrated analysis of the lifetime with FT(Phasors) in Figure 5.21 all yielded terrible fits. The large Reduced χ^2 are likely caused by the results of autofluorescence or other fluorescence impurity in the experiment. Once these unwanted characteristics are accumulated over the available photons in the data set, the effect becomes prominent and significantly impairs the correct phase delays of the functional fluorescence.

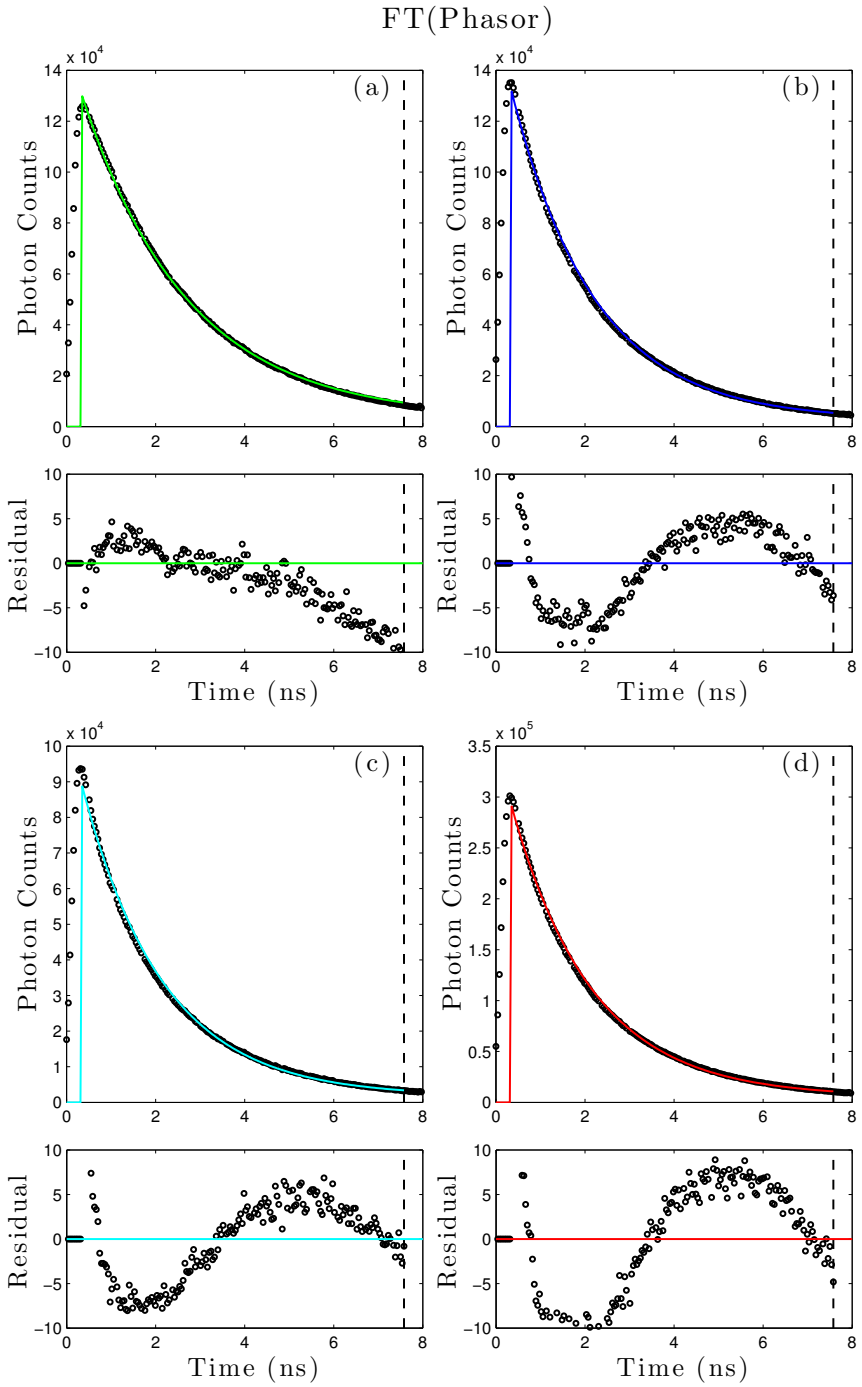

Figure 5.21: Summary of integrated transients from all the pixels of each BIFL image (analysed by FT (Phasors)), where (a), (b), (c) and (d) represents the transient of the control, eGFP-32aa-mRFP, eGFP-19aa-mRFP, and eGFP-7aa-mRFP constructs, respectively.

	Ave. τ	χ^2_R	F.Eff
Control	2.36	28.21	
32aa	2.01	32.92	14.64
19aa	1.81	30.08	23.14
7aa	1.82	73.25	23.00

Table 5.9: The table of summary for the lifetime fitting on the accummulated transients by the Fourier Transformation of the phasors, where Ave. τ is the mean lifetimes in ns, χ^2_R is the goodness of fit parameter of each construct and F. Eff is the FRET effienciency in %. Here, control, 32aa, 19aa and 7aa represent the control (eGFP alone), eGFP-32aa-mRFP, eGFP-19aa-mRFP and eGFP-7aa-mRFP constructs respectively.

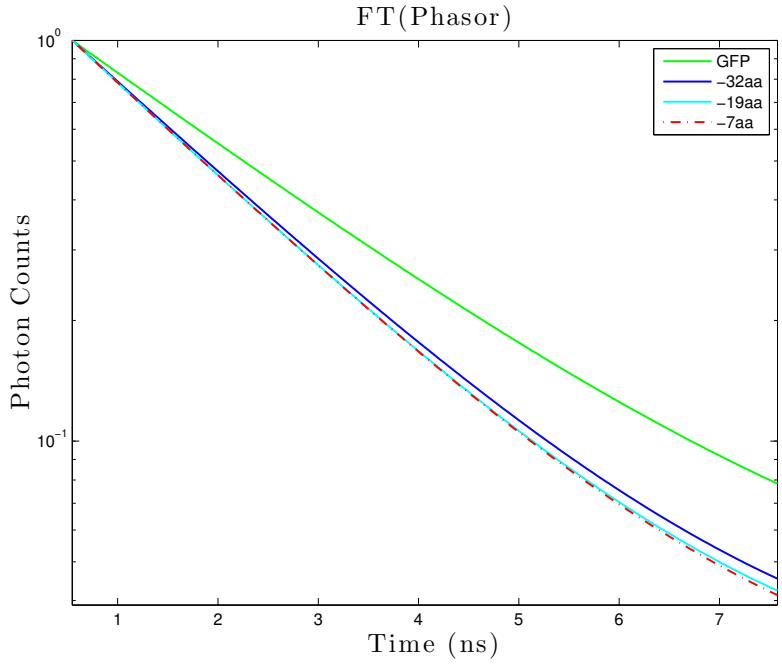

Figure 5.22: The collation of every transient in Figure 5.21, expressed in log scale.

5.3.7 Phasor Analysis of BIFL data

The contour plot of the phasors in Figure 5.23, gives the clearest evidence on the contamination with the control in the eGFP-32aa-mRFP construct. All the

phasors in each acquisition (a to d) appear to be evenly distributed, even from the sub phasor groups in Figure 5.23 (b). The centre co-ordinates of the control population in Figure 5.23 (a) lies on the semi-circle, whilst the rest from the FRET constructs (b to d) are all distributed inside the margin. The centre value of the u coordinates is directly proportional to the lifetime value, where any value towards $u = 0.5$ (right) will correspond to shorter lifetimes than those situated towards $u = 0$ (left). The dotted line drawn across the panel (b) and (d) on Figure 5.23 highlighted the right shift of the centre u values from the eGFP-32aa-mRFP to eGFP-7aa-mRFP constructs (or eGFP-7aa19aa-mRFP, assuming they are the same). The shifts in the centre u values are properly shown in Figure 5.24 and Figure 5.25.

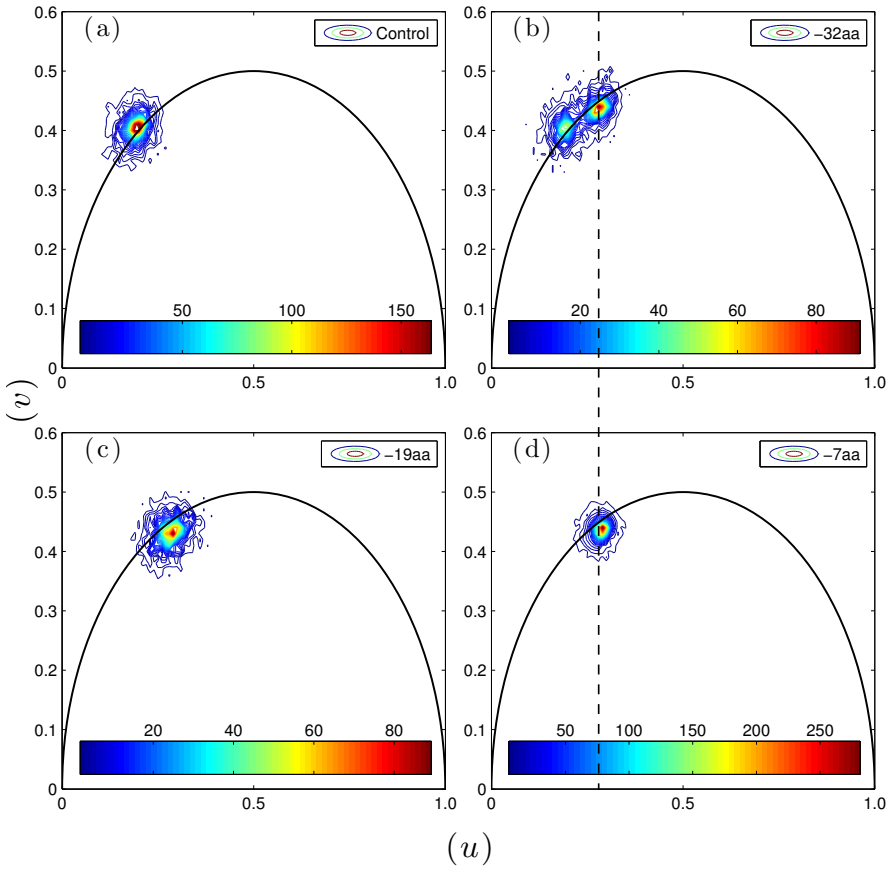

Figure 5.23: Contour plots of Phasors, where (a), (b), and (c) represent the phasor image of the control, the auto-phosphorylation state (without EGF) and the induced phosphorylation with EGF respectively.

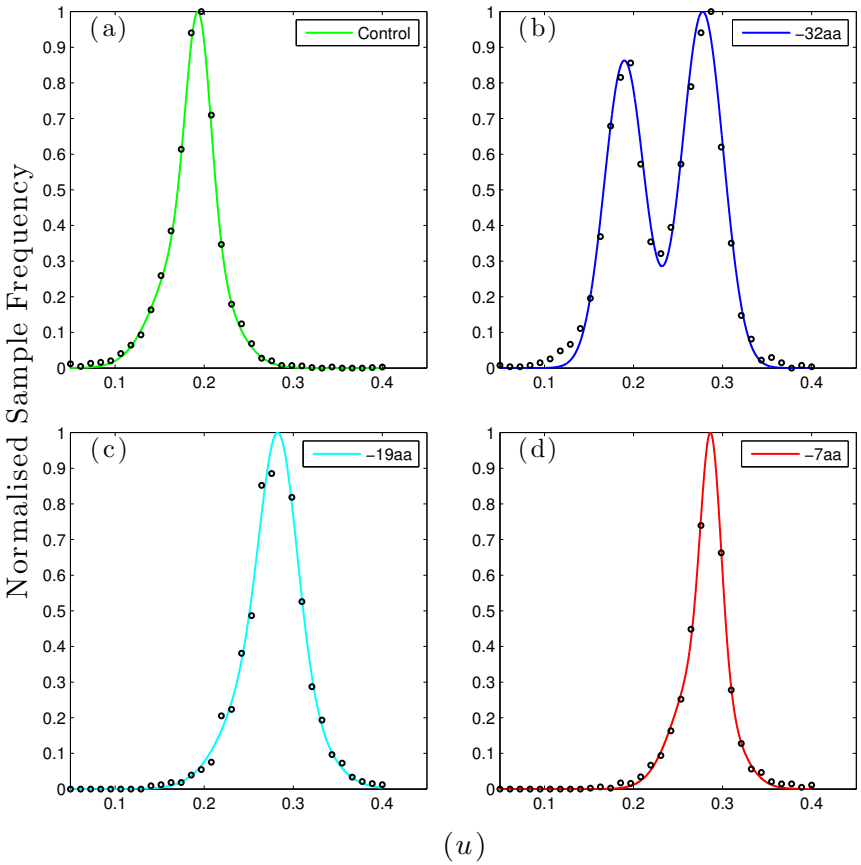

Figure 5.24: Comparison of u coordinates between the construct from Figure 5.23, where (a), (b), (c) and (d) represents the phasor image of the control, the auto-phosphorylation state (without EGF) and the induced phosphorylation with EGF respectively.

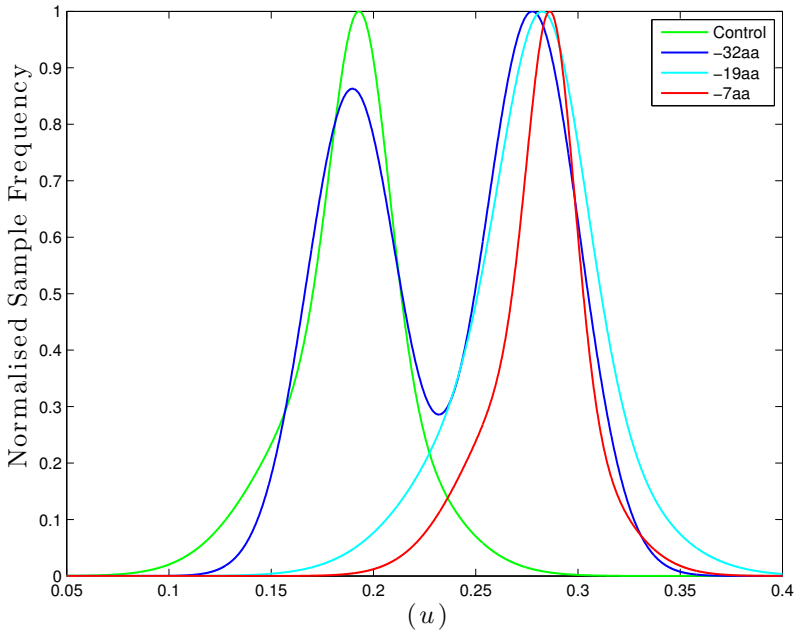

Figure 5.25: Summary of the u-coordinates in Figure 5.24 of the spectroscopic ruler data.

5.4 Recovery of the eGFP-32aa-mRFP

A recap of the histograms of the control and eGFP-32aa-mRFP constructs from the NL-MLM, Baysian and Phasors in the time domain are shown in Figure 5.26 and Figure 5.27, respectively. The first and second row of each figure represents the lifetime distributions of the control, and the contaminated eGFP-32aa-mRFP construct respectively. It can be seen that the control population has a broad distribution in all cases. Whilst the removal of the control population gave us the ability to calculate the relative shifts in FRET efficiencies from each construct to good effect in section 5.3, the ability to map the burst indices to respective construct in the contaminated data is still considerably restricted due to the large degree of overlapping and the standard deviation of each population.

The phasor analysis in the phase domain not only pictorially shows the contamination problem very clearly, it also give us an ability to sort the population to a

lower contamination rate than from the lifetime domain, as previously shown in chapter 4.

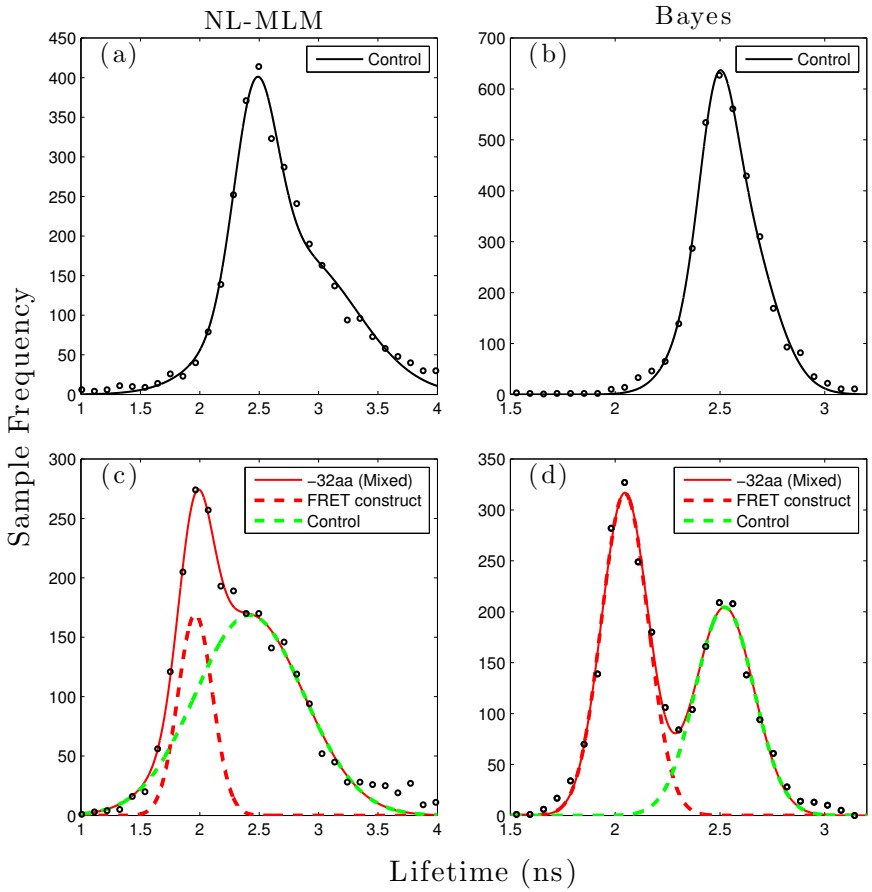

Figure 5.26: Histogram of individual lifetime of each burst for the control and -32aa construct, where the first and second column represents the data from the NL-MLM and Bayesian respectively. The first and second row represents the data from the control and eGFP-32aa-mRFP, respectively.

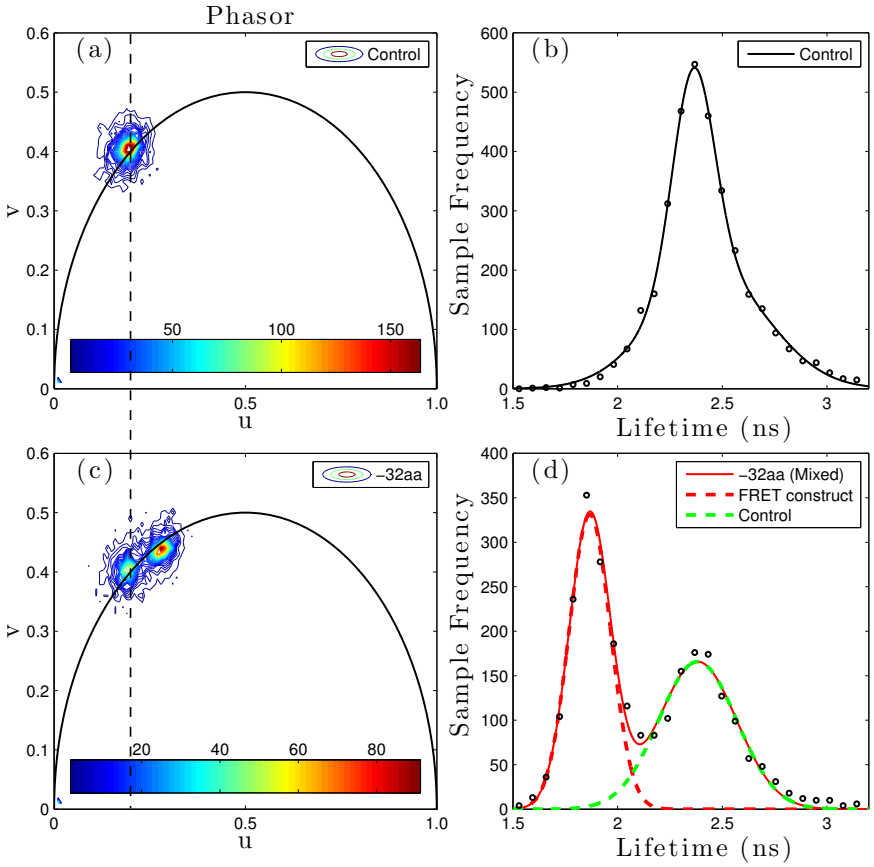

Figure 5.27: Histogram of individual lifetime of each burst for the control and -32aa construct, where the first and second column represents the data from the Phasors in the phase domain and Fourier transformation of the phasor in the time domain, respectively. The first and second row represents the data from the control and eGFP-32aa-mRFP, respectively.

Scatter plots of the phasors are shown in Figure 5.27, where the sorting line was drawn from the bottom right corner of the plot, co-ordinate (1,1) (see Figure 5.27 (b)). Figure 5.28 shows the separation of the data by using the sorting trigger in the phase domain. The plot in the figure, only shows the outlines of the histogram of each population, where green and red represents the populations from the control and FRET construct, respectively. The first, second and third row of the figure shows the lifetime histograms from NL-MLM, Baysian, and FT(Phasors)

in the respective order. From the figure, normal distributions from each construct can now be observed. From the first row, the small degree of positive skew in the FRET construct (plot in red) could even be observed, which was pointed out to be the anecdotal characteristic of the NL-MLM of low photon data. The lifetime and FRET efficiency of the sorted FRET construct are all comparable to the ones shown in the section 5.3 from each analysis method. In the interest of brevity, the functional analysis of the sorted data will not be repeated.

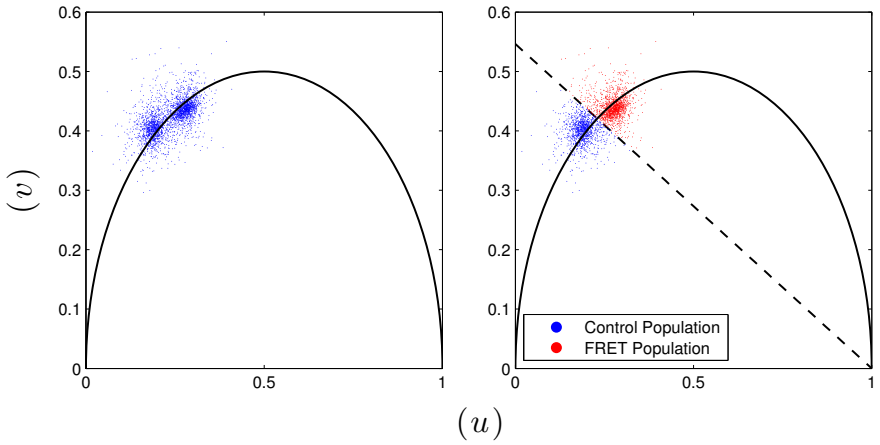

Figure 5.28: Sorting the contaminated EGFP-32aa-mRFP construct in the phase domain. (a) and (b) represents scatter plots of the unsorted and sorted phasors, respectively.

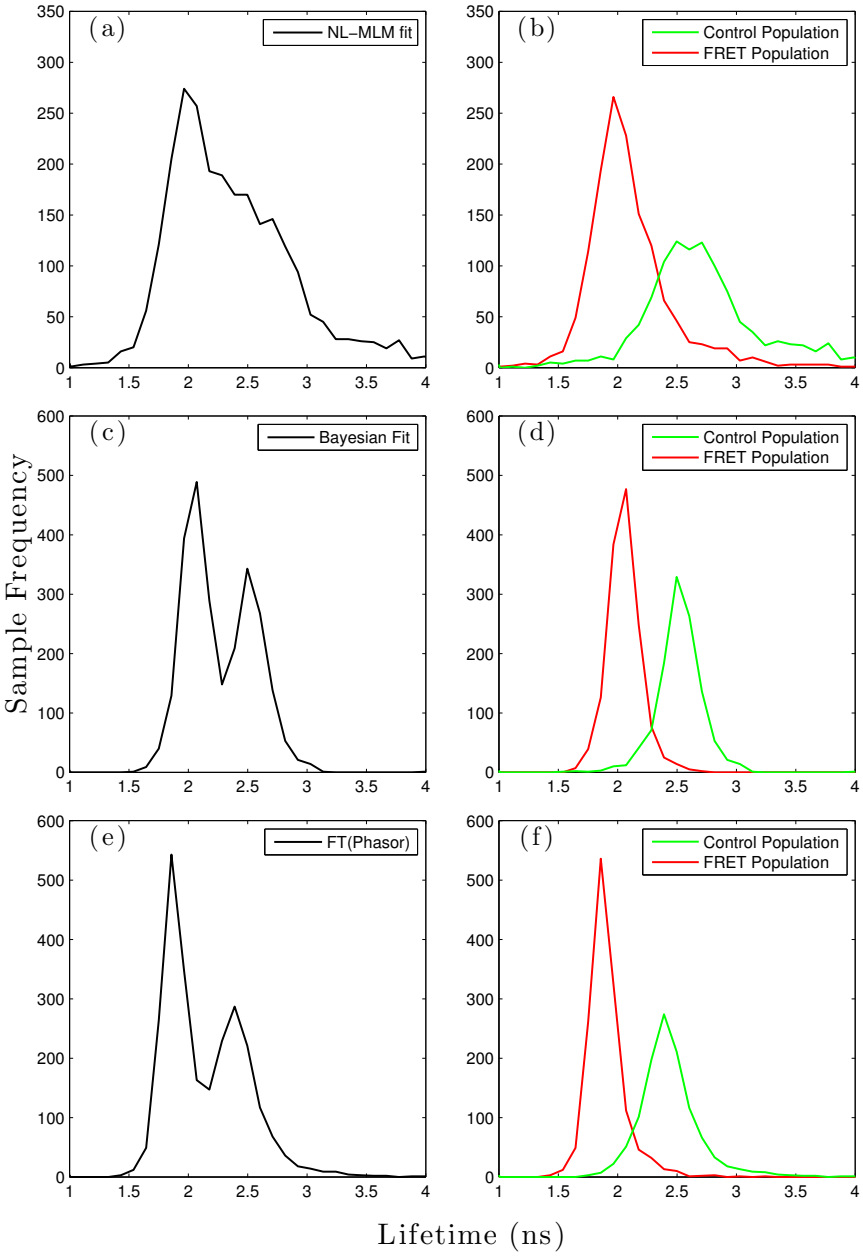

Figure 5.29: Sorted lifetime data of the eGFP-32aa-mRFP constuct, where the first and second column represents the unsorted and sorted histogram of the data respectively. The first, second, and third row, respresents the lifetime histogram analysed by NL-MLM, Bayesian, and FT(Phasors), respectively.

5.5 Summary of Chapter 5

The work on the spectroscopic ruler construct provided an invaluable insight on the dynamic range of the system. Whilst the trade-off on the use of high laser power which mostly exceeded the self-imposed safe count limit at 800 kHz to ensure good excitation on the samples was accepted, it is still difficult to systematically control the instantaneous count rate from construct to construct to be comparable to one another. Until a solution is found on a better cell delivery and safer counting operation (hydro-dynamic focussing facility or on-chip detector), the instantaneous count rate of the system must be regulated for experiments which investigate several constructs at once. This is to ensure the lifetimes of every construct are ubiquitously shifted similarly due to pulse pile-up. Figure 5.29 and Figure 5.30 compares the effect the instantaneous count rate has on lifetime of the control (eGFP) and eGFP-7aa-mRFP constructs. It can be observed that the lifetime of the control was quenched with higher instantaneous count rate (depicted by the negative skew of the data cluster), while the lifetime of the FRET construct remained almost unchanged. The exponential profile from the instantaneous count rate characteristics of the FRET construct shows the burst with low photon yields (the majority of the data) was relatively safe from the lifetime quenching, even though the range of the count rate of the entire BIFL sequence, spanned over from approximately 1 MHz to 3.5 MHz (note the peak value or approximately one fourth of the exponential profile is approximately below 1.5 MHz).

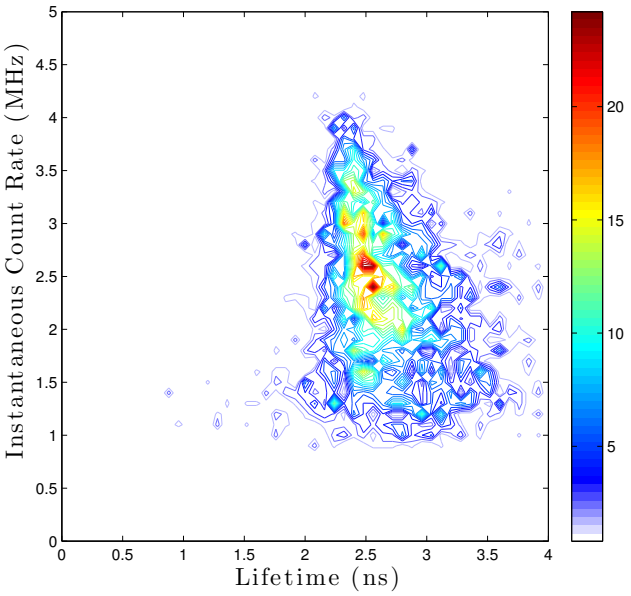

Figure 5.30: The control lifetime of the spectroscopic ruler as a function of instantaneous rate.

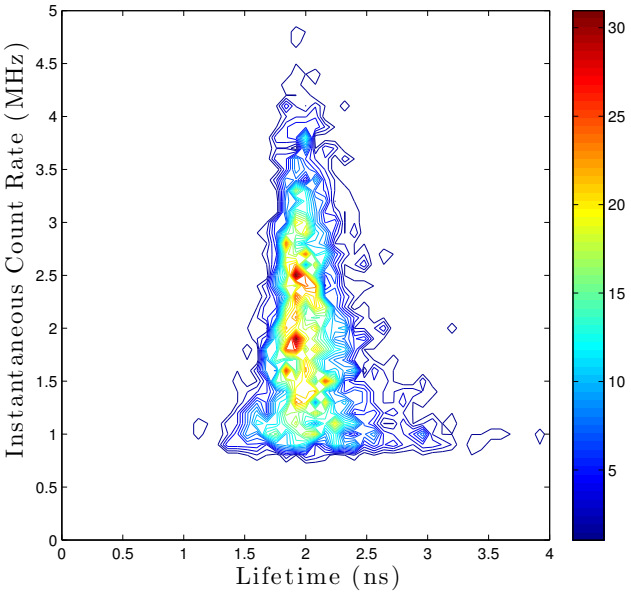

Figure 5.31: The lifetime of eGFP-32aa-mRFP as a function of instantaneous rate.

The monitoring of lifetime quenching per construct is very important for the clinically relevant assay, as the shift in lifetimes from the immunocytochemistry can be small and the shifts would need to be systematic and reliable. At the moment, this is difficult to avoid, due to the compromise from the overloaded cell delivery. Variations of laser power and flow speed from construct-to-construct will add a degree of complexity in the experimental operation.

This investigation would have been better regulated if the spectroscopic ruler constructs were stably transfected, as this would give us an additional ability to compare the burst width as well as the integral intensities between the constructs from the FRET interactions. Nonetheless, there are several positives, which can be taken from the experiment. The calculated FRET efficiency of the eGFP-32aa-mRFP and eGFP-19aa-mRFP constructs were found to be comparable to the ones from the from the HCS project, which were analysed by the NL-MLM method. The results from this experiment contained a systematic offset of approximately 3% from the HCS project. The shift in the FRET efficiency between the eGFP-32aa-mRFP and eGFP-19aa-mRFP constructs, of approximately 4% (27% to 23% (HCS [5]) and 24.16% to 20.47% (FIFO BIFL)), is considered to be small, the fact that this could be observed, is a remarkable outcome. The experiment would have been more complete, if a correct construct was used for the eGFP-7aa-mRFP. All in all, the sample identification should have been studied at the outset with FLIM prior to any BIFL screenings, but due to the lack of experience at the time of investigation, this procedure was regrettably neglected. Although this was later realised in the subsequent experimental repeats, the success rates of those experiments were actually poor, due to some mix up of biological samples in the transfection protocol and BIFL experiments. In the interest of time remaining in the project, this was not pursued any further, to allow other biological experiments to be examined (see chapter 6).

Another positive, which should not go unmentioned, is that the 20% shift in the FRET efficiency observed from the control to eGFP-32aa-mRFP constructs in this study, was sufficient for the data of the contaminated construct to be sorted in the analysis very clearly. The evidence, which have accrued in this

chapter possibly suggests that the use of phasor in the phase domain might be able to sort the mixed solution between the control and FRET population, which contained only 10% FRET efficiency, to good effect.

Chapter 6

BIFL Screening Performance Against Clinically Relevant Assay

This chapter presents work on a clinically related assay, which looks at the catalytic effect of epidermal growth factor (EGF) on the phosphorylation of tyrosine sites along the c-terminus . It was shown in the previous chapter that the phasor method was able to give a tighter lifetime approximation from the available data from a cell-based assay than the NL-MLM method. In this chapter, Bayesian analysis method will be omitted, as the process is time-consuming and yielded very poor fits in these particular cases. The automatic data inference of the Bayesian method gives very little freedom on the data initialisation, as the accuracy of the computation is predominantly influenced by the prompt signal. The BIFL analysis software also selected the bursts, which contained more than 200 photons, and hence makes its merit on the low photon data relatively trivial and simply adds to the computational overhead.

6.1 Introduction on Clinical Study on Stimulation of phosphotyrosine on Human Epidermal Growth Receptor (EGFR) with Epidermal Growth Factor EGF

A tyrosine kinase is an enzyme that can transfer a phosphate (or phosphenol) group from donor molecules such as ATP to acceptor tyrosine residues in proteins (where the process is known as phosphorylation). The phosphorylation of tyrosine residues (phosphotyrosine), in turn, causes a change in the functional state of the protein (which can be thought of as an activation state of sub-hierarchical functions) [14, 93–97]. Phosphorylation plays a pivotal role in regulating many enzymatic activities, subcellular localisation, and myriad of signalling cascades from interactions between molecules [14, 93–97]. Many signal transduction cascades from extracellular signals are transmitted through the cell membrane to the cytoplasm and often to the nucleus, where gene expression may be modified [93–97]. Mutations can cause some tyrosine kinases to become constitutively active a nonstop functional state that may contribute to initiation or proliferation of cancer [14, 93–97]. Therefore early detection of phosphorylation activities during a specific state of a signalling pathway is a valuable tool for many cancer studies [93–95].

In this case study, a well-characterised stimulation routine of phosphotyrosine activities from the Epidermal Growth Factor antigens, to a specific structurally related variant of Human Epidermal Growth Receptor (HER) HER-1 (or EGFR) will be investigated.

The HER (or sometimes known as ErbB) protein-tyrosine kinases, which include the epidermal growth factor receptor, consist of a growth-factor-binding ectodomain, a single trans-membrane segment, an intracellular protein-tyrosine kinase catalytic domain, and a tyrosine-containing cytoplasmic tail [98]. The genes for the four members of this family, ErbB1 - ErbB4, are found on dierent human chromosomes. ErbB1 and ErbB2 are overexpressed in a wide variety of tumours

including breast, colorectal, ovarian, and non-small cell lung cancers [96–98].

Once EGF is bound to EGFRs, then the receptors become available for dimerisation with other HER receptors on the ecto-domain [98]. The activation then stimulates the phosphorylation activities from the basal state, on the intracellular protein-tyrosine kinase catalytic domain, which allows other interactions of signalling molecules to trigger other signalling pathways [96–98]. In this assay, the phosphorylation of the tyrosine site of EGFR with- and without EGF treatment in the MCF-7 cell line will be investigated from the level of FRET interactions. The EGFR was tagged with eGFP, while the basal/stimulated phosphotyrosine site was targeted by the specific antibody against mono phosphortyrosines (PY72) labelled with (up to 3) Cy-3 molecules. The transfection protocol and experimental procedure can be found in Appendix B.

6.2 Initial Transfection Validation with Widefield Imaging

The success rate of the cell labelling was crudely assessed with widefield imaging ratiometrically and is shown in Figure 6.1. No FRET measurements will be taken. The samples were directly transferred into a 3 by 2 chamber well, which has the same base thickness as the standard coverslip (Nunc Lab-Tek II Chambered coverglass slide system). The sample volume in use per cell type was approximately 2 μl. Once the sample droplets were loaded into the wells, they were left standing and unfixed for approximately 5 minutes to allow the cells to settle in an equilibrium z-position on the bottom of the slide and avoid any blurring during the imaging. Hence it is normal for the images in the Figure 6.1 to show several cells in different focal planes within the field of view[1].

[1]Please note that the system inherently has a slight z-offset between the green and red channels (used for observing donor and acceptor fluorescent molecules respectively). This could not be corrected at the time of the investigation, due to the piezo mount attached to the objective broke down and could not be repaired in time for any subsequent repeats.

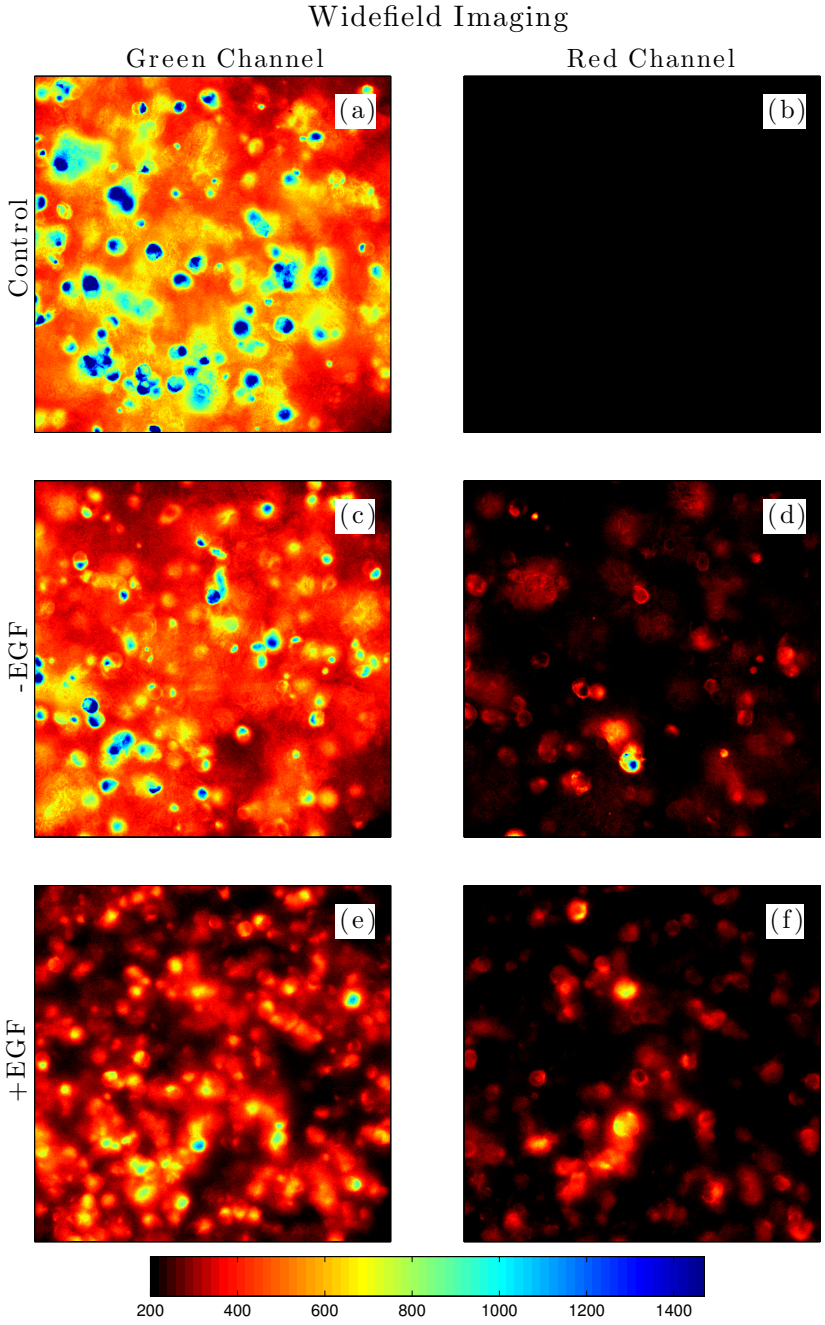

Figure 6.1: The first-point check on the fluorescence expression between the control and acceptor with widefield imaging, where the first and second column represent the data from the green and red channel respectively. The first, second and third row represent the control, the auto-phosphorylation state (without EGF) and the induced phosphorylation state with EGF respectively.

From the images in Figure 6.1, it could be observed that the stoichiometry between the donor and acceptor is incorrect. The level of eGFP on the donors in relation to the Cy-3 on the acceptors is far exceeding the required 1:1 ratio for a proper FRET examination in panels (c and d) and (e and f). Please note that it is generally safer to mildly saturate the number of acceptor fluorescent molecules to ensure a strong interaction during FRET interaction between proteins, but at the same time, there is always a danger in an excessive saturation of the acceptor fluorescent molecules, which could mislead users to false detections of FRET [18]. The assay would require some optimising of the ratio to ensure that the maximum dynamic range was found for the assay. However, the expensive cost of PY72 anti-bodies only permitted the examination of the assay in a limited number of trials. Additionally, another problem was encountered whereby cells were permanently adhered to the walls of the containers during some of the trails, which further hindered the progress of the investigation. The results presented here represent the best outcome of the investigation to date. From Figure 6.1, it could be observed that the level of green signal in the donor channel is becoming progressively less from the control in (a) to the auto-phosphorylation state in (c) and to the stimulated case in (e). Although the change between (c) and (e) is somewhat subtle, some lifetime changes between the cases could still be expected, judging from the global change in intensities between the two images.

6.3 Lifetime Investigation with FLIM

The lifetime of each cell type was analysed with FLIM. The cell handling and system setting were identical to the ones in the previous investigation in chapter 5, where the laser power was adjusted until a single scanning across the field of view yielded an instantaneous count rate of a few thousand counts per second. The region of interest of each cell type in this section was identical to those of the wide-field images in Figure 6.1.

Provided the extra laser power used in the later BIFL experiments does not cause too much pulse pile up, then the lifetime observed in this section should be iden-

tical to those of the later BIFL experiment. Otherwise, if the global change of the lifetime data from the pulse pile up effect were to be observed, then the trend in the lifetime reduction is expected to be comparable to the following results, as the cells are contained and handled in a similar condition for both cases.

6.3.1 NL-MLM Analysis

Analysis of the FLIM data with NL-MLM is shown in Figure 6.2. The fit parameter of lifetime distributions and FRET efficiency calculations are summarised in Table 6.1 and Table 6.2, respectively. The difference in average lifetime between Control (EGFR transfected with eGFP) and EGFR-eGFP + PY72-Cy3 with EGF treatment is observed to be very small. It is likely that the lifetimes calculated from the individual pixels (with no spatial binning [reference]) resulted in a large distribution of data, which curtail the resolvability between the average lifetimes of the two data sets. Typically, FRET data such as this would be spatially binned to increase signal to noise, but this was avoided to keep the photon counts of individual pixels (containing fluorescent samples) comparable to the ones of a typical BIFL image (containing individual cells).

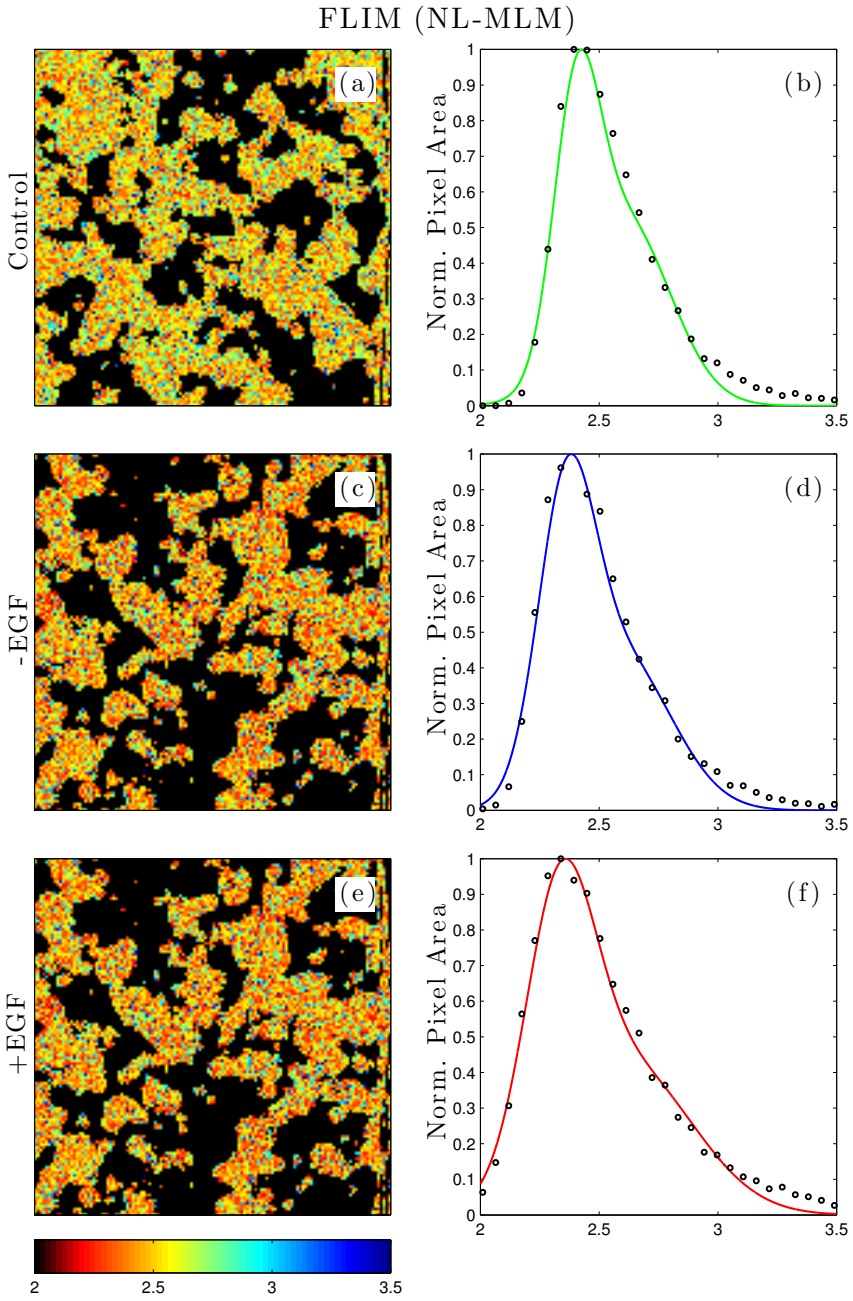

Figure 6.2: Initial lifetime determination by FLIM with the NL-MLM, where the first and second column represent the lifetime image and the corresponding lifetime histogram in the green channel respectively. The first, second and third row represent the control, the auto-phosphorylation state (without EGF) and the induced phosphorylation with EGF respectively.

The biggest problem encountered, especially with the NL-MLM analysis, is that for any pixel or burst with either small number of photons (<1000 counts) or noisy transient outlines, TRI-2 tended to fit them with anomalously long lifetime profiles regardless of the samples types. It is also possible that auto-fluorescence will have some contributions in this behaviour as well. As a consequence, this positively skews the lifetime histograms into asymmetric shapes, which erroneously shift the FRET efficiency to higher values, both pictorially and numerically as can be seen in Figure 6.3 (b).

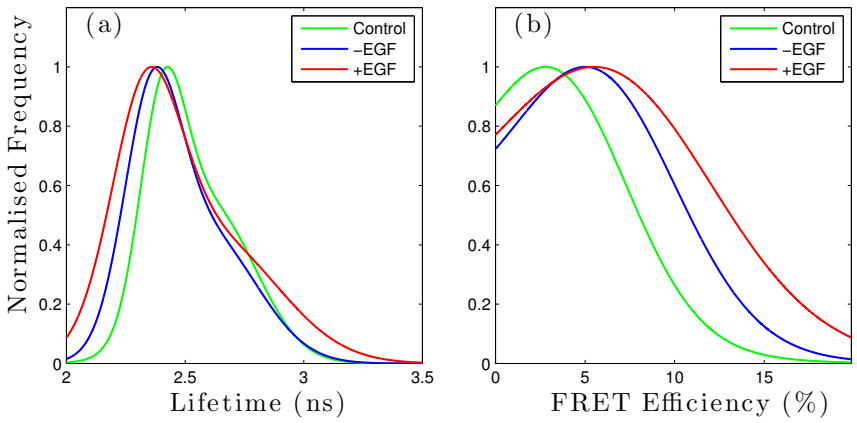

Figure 6.3: A summary of lifetime (a) and FRET efficiency (b) histograms from each construct.

As previous shown in the previous chapter of the NL-MLM section if the data are left untreated as in Figure 6.3, then the quadratic terms of the averaging expression (see section 5.3 in chapter 5) will treat any negative centring FRET efficiency value of the long lifetime component, as an extra positive FRET component and shift up the average value of the FRET efficiency in the analysis. For the purpose of lifetime screening, the FRET efficiency will be determined solely from the main fractional contribution of the lifetime distribution to avoid the problem as shown in Figure 6.4.

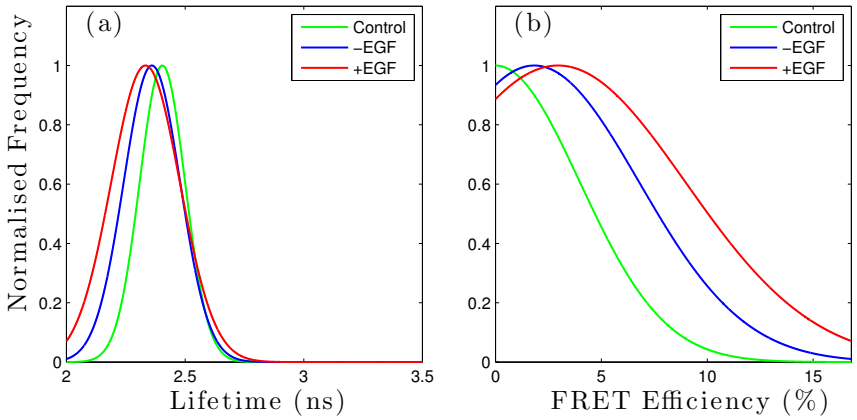

Figure 6.4: A revised summary of lifetime (a) and FRET efficiency (b) histograms from each construct. The histograms ignore the fractional contribution from the anomalously long lifetime components.

	A_1	A_2	τ_1	τ_2	σ_1	σ_2	Ave. τ	Ave. σ
Control	918	686	2.4	2.61	0.14	0.27	2.5	0.22
-EGF	807	440	2.36	2.6	0.17	0.3	2.45	0.23
+EGF	680	378	2.33	2.62	0.2	0.39	2.44	0.3

Table 6.1: The table of summary for the lifetime fitting (NL-MLM). The average lifetime of the was calculated by a double Gaussian mixture model, where, A_1 and A_2 are the fractional contributions, τ_1 and τ_2 are the mean lifetimes in ns, and σ_1 and σ_2 are the standard deviations of each sub-population in ns, respectively. Ave. τ is the average lifetime in ns and Ave. σ is the average standard deviation of each construct in ns, respectively.

	τ	σ	FRET efficiency	σ_F
Control	2.4	0.14		
-EGF	2.36	0.17	1.83	7
+EGF	2.33	0.2	2.95	8.51

Table 6.2: The table of summary for the revised lifetime fitting (NL-MLM) (ignoring the sub-population with anomalously long lifetime), where τ is the mean lifetimes in ns, and σ is the standard deviations of each construct in ns, respectively. The FRET efficiency is expressed in % and σ_F is the standard deviation of the corresponding FRET efficiency in %.

As mentioned earlier, that the stoichiometry of the donor/acceptor pair has not been optimised for this assay. This is reflected in the very low FRET efficiency values in both basal and stimulated cases. From both the original and revised data, it was observed that the treatment of EGF had broadened the lifetime distribution by more than any other case. This is probably a real characteristic, as there would be a portion of an unphosphorylated EGFR, even for the Basal level and cells will be activated to a great or lesser extent depending on exposure to EGF. Some cells simply will not respond. In this case the relative proportion of probed molecules is small (perhaps the antibody tags the most available EGFR at low concentrations which are also those molecules most available for phosphylation). For the purposes of the project, a small increase in FRET efficiency for the acceptor positive cases would hold a stern test for the BIFL screening. This cell type may also not be the best example for this study since MCF7 cells are normally deficient in EGFR [99] and may respond anomalously when transfected with EGFR-eGFP. Autophosphorylation is very likely with over-expressed EGFR since dimers are very likely to form without stimulation [99]. It is likely that this is the main reason why there is no significant difference between stimulated and unstimulated samples.

6.3.2 Phasor Analysis (Lifetime)

Analysis of the FLIM data by Fourier transform of phasors is given in Figure 6.5. The fit parameter of lifetime distributions and FRET efficiency calculations are summarised in Table 6.3 and Table 6.4, respectively. The phasor analysis was able to give a tighter approximation than the untreated data of NL-MLM, which resulted in a clearer shift in the FRET efficiency seen both pictorially in the Table 6.4 and for the histograms. This reflects the robustness of the phasor analysis to low photon counts. The difference in FRET efficiency between the basal and stimulated cases is now observed to be 2.63% (see Table 6.4), but is still much comparable to the number of the more error-prone NL-MLM method.

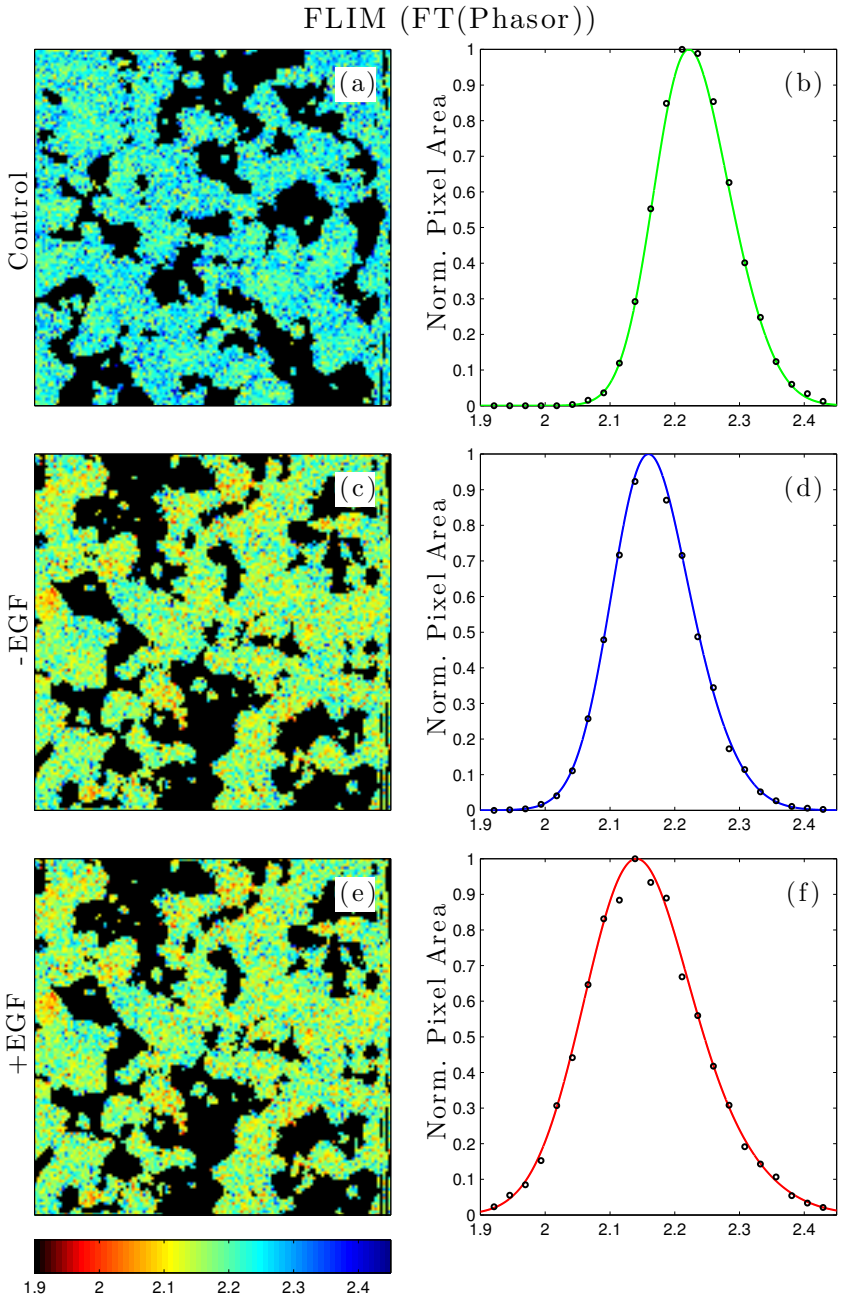

Figure 6.5: Initial lifetime determination by FLIM with Fourier Transformation of Phasors, where the first and second column represent the lifetime image and the corresponding lifetime histogram in the green channel respectively. The first, second and third row represent the control, the auto-phosphorylation state (without EGF) and the induced phosphorylation with EGF respectively.

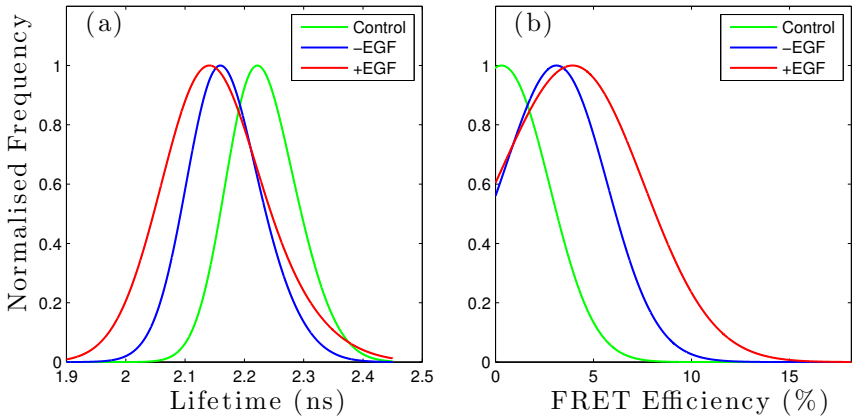

Figure 6.6: A summary of lifetime (a) and FRET efficiency (b) histograms from each construct.

	A_1	A_2	τ_1	τ_2	σ_1	σ_2	Ave. τ	Ave. σ
Control	1053	1024	2.21	2.25	0.07	0.08	2.23	0.08
-EGF	935	845	2.15	2.19	0.07	0.10	2.17	0.09
+EGF	845	264	2.13	2.22	0.11	0.13	2.15	0.11

Table 6.3: The table of summary for the lifetime fitting by Fourier Transformation of Phasors, where A_1 and A_2 are the fractional contributions, τ_1 and τ_2 are the mean lifetimes in ns, and σ_1 and σ_2 are the standard deviations of each sub-population in ns, respectively. Ave. τ is the average lifetime in ns and Ave. σ is the average standard deviation of each construct in ns, respectively.

	τ	σ	FRET efficiency	σ_F
Control	2.23	0.08		
32aa	2.17	0.09	3.11	3.84
19aa	2.15	0.11	4.27	5.15

Table 6.4: The table of summary for the FRET efficiency calculated by Fourier Transformation of Phasors, where τ is the mean lifetimes in ns, and σ is the standard deviations of each construct in ns, respectively. The FRET efficiency is expressed in % and σ_F is the standard deviation of the corresponding FRET efficiency in %.

The shifts of lifetime due to FRET yielded symmetric distributions in both cases. The effect of EGF treatment also resulted in the broadening of the lifetime distribution, as seen the NL-MLM analysis section, which gives further evidence on the nature of this feature.

6.3.3 Phasor Plot Analysis

As expected, the distributions of u coordinates of the construct are the mirror image of the lifetime distribution in Figure 6.6 (a). The evidence from the contour plots of phasors in Figure 6.7 seems to suggest that all the transients are mono exponential, with a slight possibility of (c) having a small additional lifetime component. However when the transients were fitted with the mono-exponential model with NL-MLM method, a misfit and the erratic behaviour was observed. Therefore the constructs were fitted with the bi-exponential with the NL-MLM instead, despite the conflicted evidence from the phasor plots.

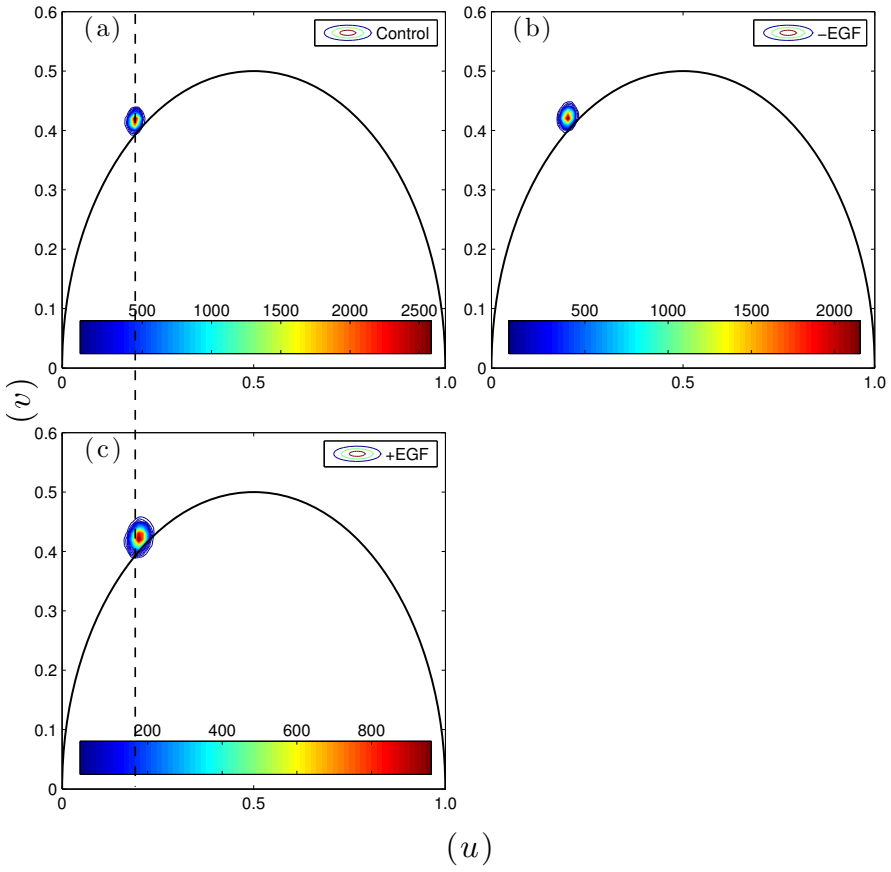

Figure 6.7: Contour plots of Phasors, where (a), (b), and (c) represent the phasor image of the control, the auto-phosphorylation state (without EGF) and the induced phosphorylation with EGF respectively.

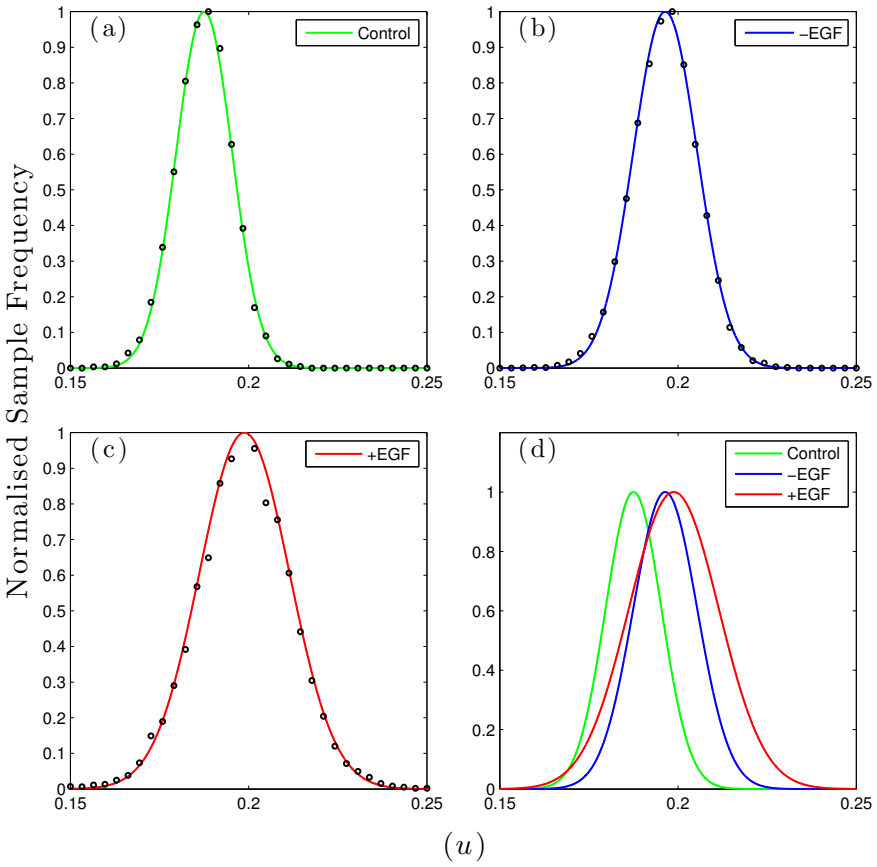

Figure 6.8: Comparison of u coordinates between the construct from Figure 6.7, where (a), (b), and (c) represent the phasor image of the control, the auto-phosphorylation state (without EGF) and the induced phosphorylation with EGF respectively.

	u	σ
Control	0.188	0.011
-EGF	0.196	0.013
+EGF	0.199	0.018

Table 6.5: The table of summary for the u coordinate distributions of each construct, where u is centring coordinate and σ is the associated standard deviation in each case.

6.3.4 Integrated Lifetime Analysis of FLIM Data

The NL-MLM analysis of lifetime from the spatially integrated FLIM data is shown in Figure 6.9. It could be observed in the residual plots at the bottom of (a), (b) and (c) in the figure that there were some oscillations on the data series of every transient. The reasons behind this are unknown, but both the trend of the transient behaviours and the lifetime estimations are very reasonable. Overall, the collation of transients in Figure 6.9 (d), show that there were observable changes in the decay rates in the FRET experiments in relation to the control, while the shift of the rate between the FRET experiments themselves is only marginal.

In contrast to the results in Figure 6.9, the phasor estimation yielded very poor fits as shown in Figure 6.10. This is somewhat normal, as the Fourier Transformation of the phasor is not a fitting method at all but an estimator. The method cannot determine the peak of the fluorescence, as the lifetime of each data point was computed from the phase delay of the modulated transient data in relation to the modulated laser repetition interval. Please note that the extent of this obvious systematic error does not manifest when the decay rate of each individual FLIM pixel is estimated.

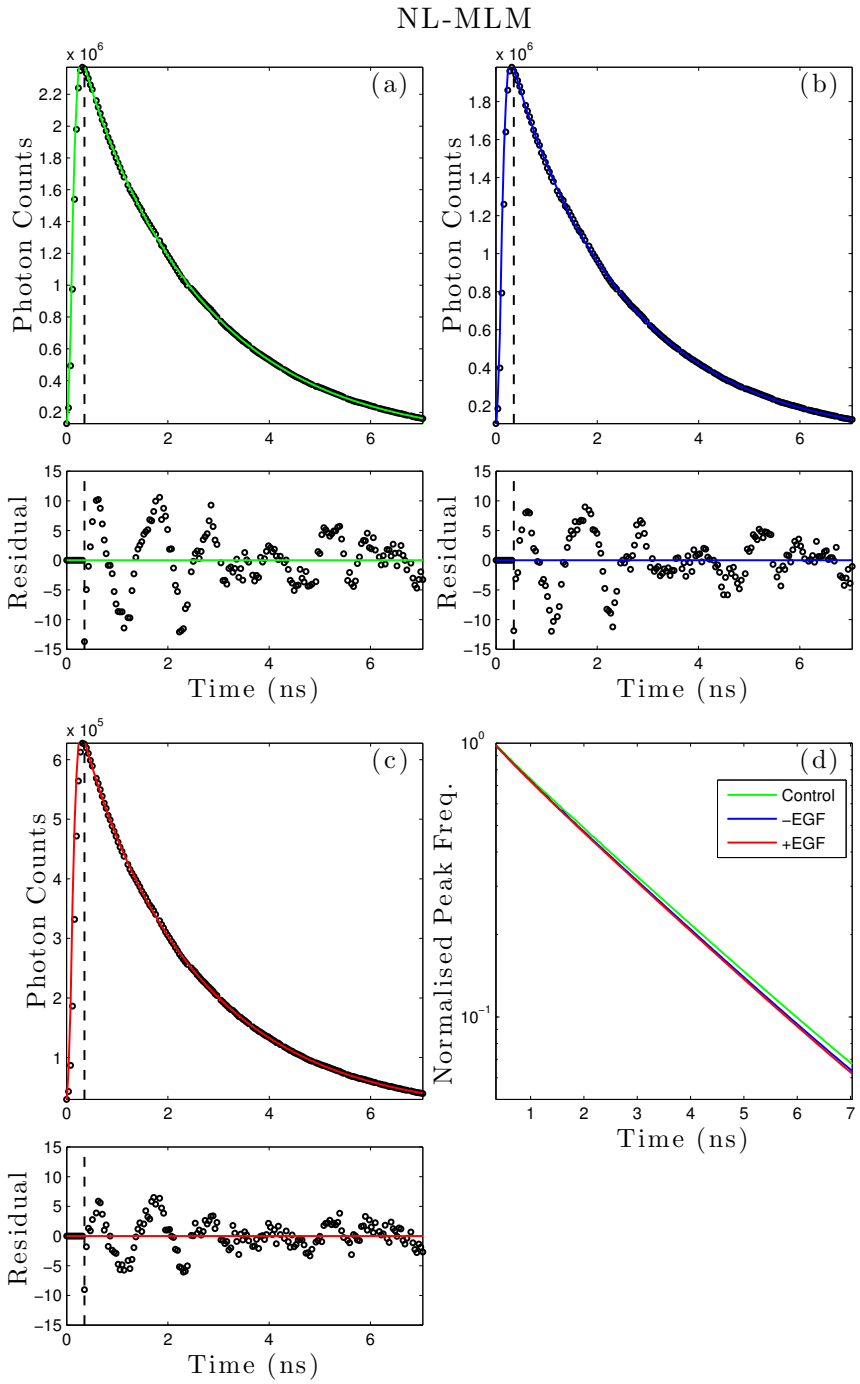

Figure 6.9: Summary of accumulated transients from all the pixels in each FLIM image (NL-MLM), where (a), (b) and (c) represents the transient the control, the auto-phosphorylation state (without EGF) and the induced phosphorylation with EGF respectively. (d) is the collation of all the transient shown in log scale.

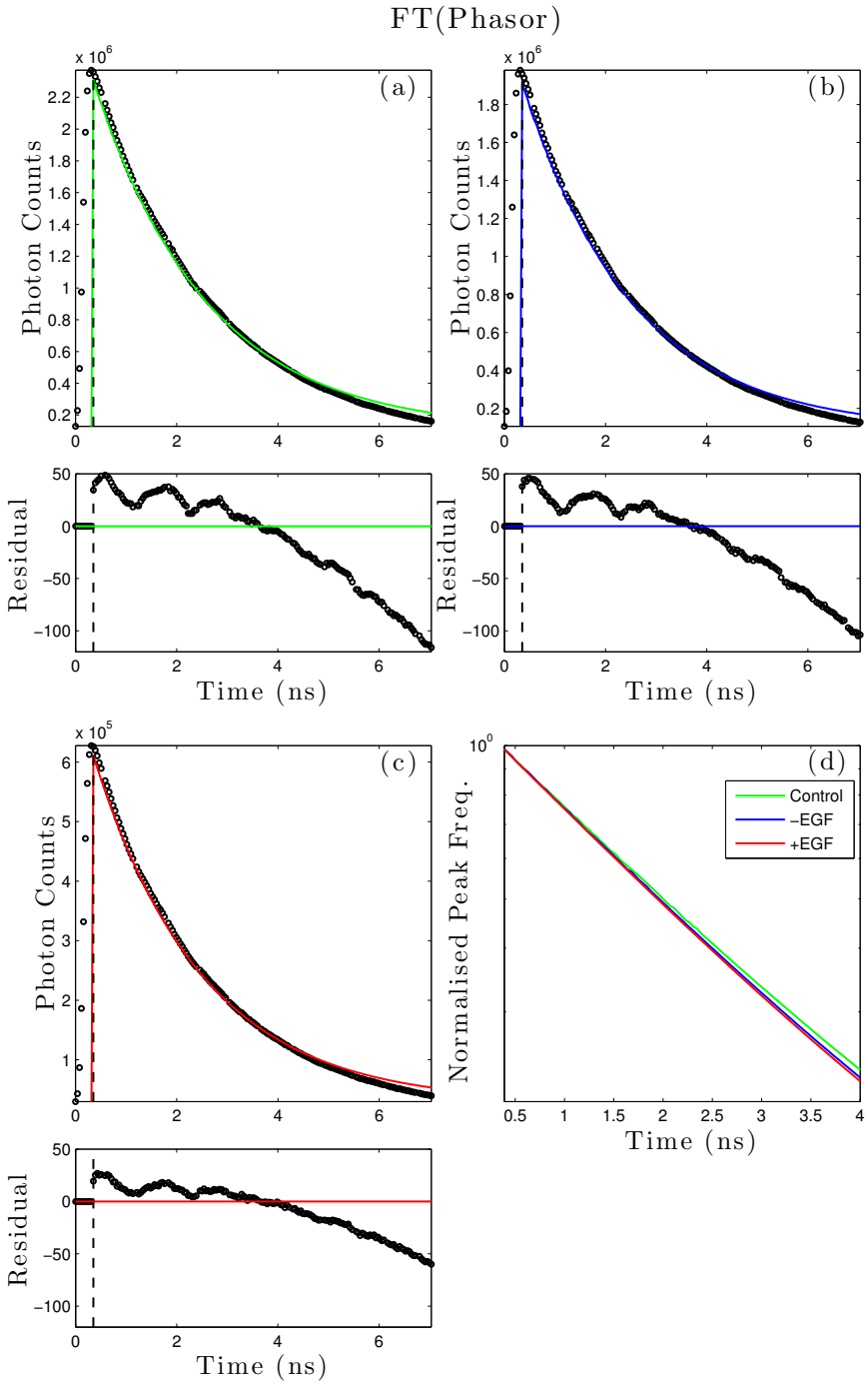

Figure 6.10: Summary of accumulated transients from all the pixels in each FLIM image (FT(Phasor)), where (a), (b) and (c) represents the transient the control, the auto-phosphorylation state (without EGF) and the induced phosphorylation with EGF respectively. (d) is the collation of all the transient shown in log scale.

	A_1	A_2	τ_1	τ_2	Ave. τ	χ^2_R	F.Eff
Control	2500630	107307	2.43	0.48	2.42	18.09	
-EGF	2052010	132293	2.39	0.50	2.37	23.41	2.13
+EGF	651474	47739	2.38	0.54	2.35	7.23	2.73

Table 6.6: The table of summary for the lifetime fitting on the integrated transients by NL-MLM, where A_1 and A_2 are the fractional contributions, τ_1 and τ_2 are the mean lifetimes in ns, and σ_1 and σ_2 are the standard deviations of each sub-population, respectively. Ave. τ is the average lifetime in ns, χ^2_R is the goodness of fit parameter and F. Eff is the FRET efficiency in %.

	τ	χ^2_R	F. Eff
Control	2.23	2366	
-EGF	2.17	1904	2.76
+EGF	2.15	588	3.66

Table 6.7: The table of summary for the lifetime fitting on the accummulated transients by the Fourier Transformation of the phasors, where τ is the mean lifetimes in ns, χ^2_R is the goodness of fit parameter of each construct and F. Eff is the FRET effienciency in %.

From the residual plots, the misfit become very large after 4ns, and hence only the transient information during the first 4ns were only demonstrated in Figure 6.10 (d). The behaviour of the dacay rate is very similar to the NL-MLM case in Figure 6.9 (d).

6.4 Lifetime Investigation with BIFL (Flow Experiment)

The cell solutions were pumped at 500 mbar for 10 minutes, with the exception of the EGF case, where the solution had to be pumped at 200 mbar instead. For an unknown reason, the level of staining has become dimmer than it was initially inspected with wildfield imaging in Figure 6.1. The pump rate was reduced to

allow more photons to be collected.

The fluorescence excitation employs the spot profile. In this section, the burst characteristics, lifetime and the corresponding FRET efficiency histogram of the data (NL-MLM and Phasors), and the integrated transient from the data are presented.

6.4.1 Burst Characteristics

BIFL data for the three conditions of the EGFR phosphorylation experiment are given in Figure 6.11, Figure 6.12 and Figure 6.13 for control, -EGF/+Acceptor and +EGF/+Acceptor respectively. When comparing the burst widths and instantaneous count rate of the EGF and +EGF cases in Figure 6.12 (a and c) and Figure 6.13 (a and c), the burst width of the detected cells of the EGF population is observed to be distributed over less time range than the +EGF population. However, the instantaneous count rate of the EGF case is evenly distributed and centred around 2.5×10^6 counts on the x-axis. This centring value is higher than the peak count rate at 1.0×10^6 counts of the more exponential looking profile in the +EGF case, which contains a larger fraction of bursts with longer residence time at the excitation volume. It is possible the EGF case suffered from the donor dyes became unbounded and leaked into the solution, and so several bursts were blinded by the high background count (depicted by the large instantaneous count rate), which resulted in the less number of burst detection and shorter burst widths. The lifetime of the construct is hence expected is strongly quenched, compared to the rest of the constructs.

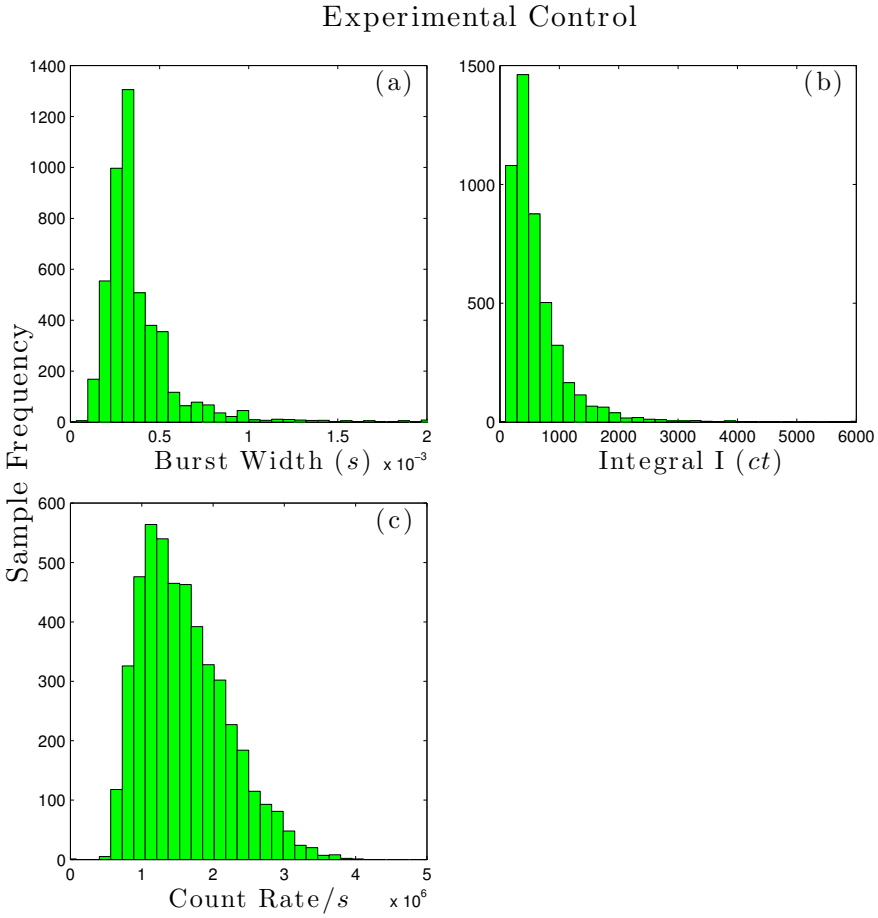

Figure 6.11: Burst characteristics of the control population, where (a), (b) and (c) represents the burst widths, integral intensities, and instantaneous count rates during each detection event, respectively.

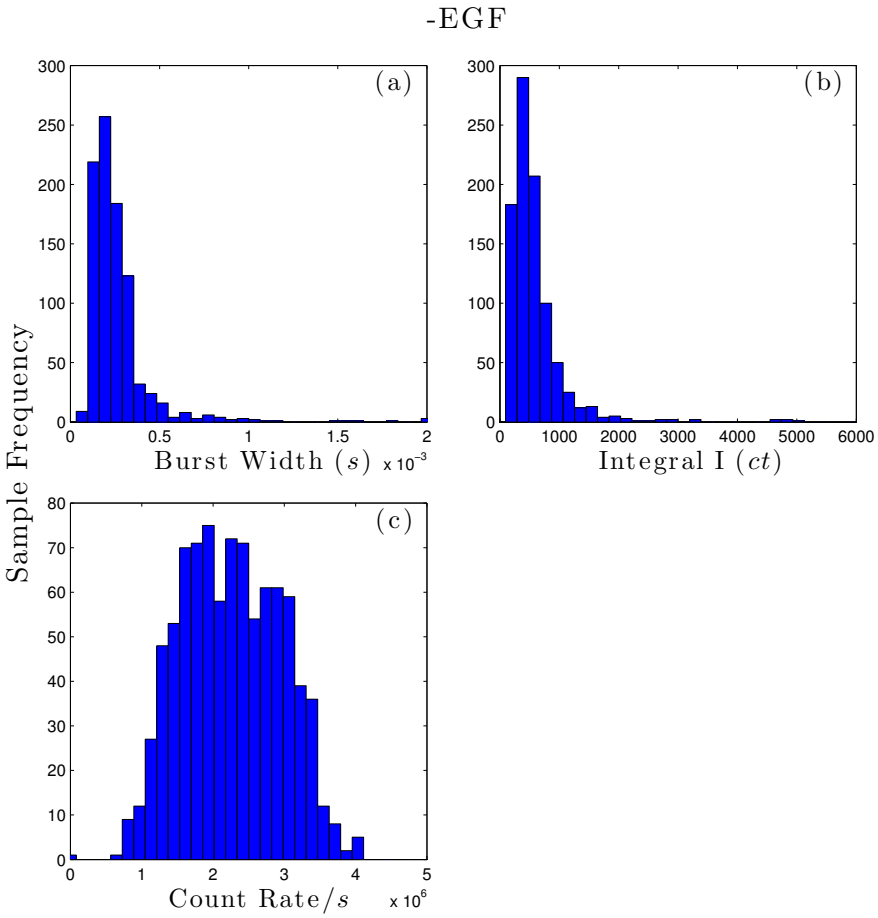

Figure 6.12: Burst characteristics of the unstimulated cells (-EGF), where (a), (b) and (c) represents the burst widths, integral intensities, and instantaneous count rates during each detection event, respectively.

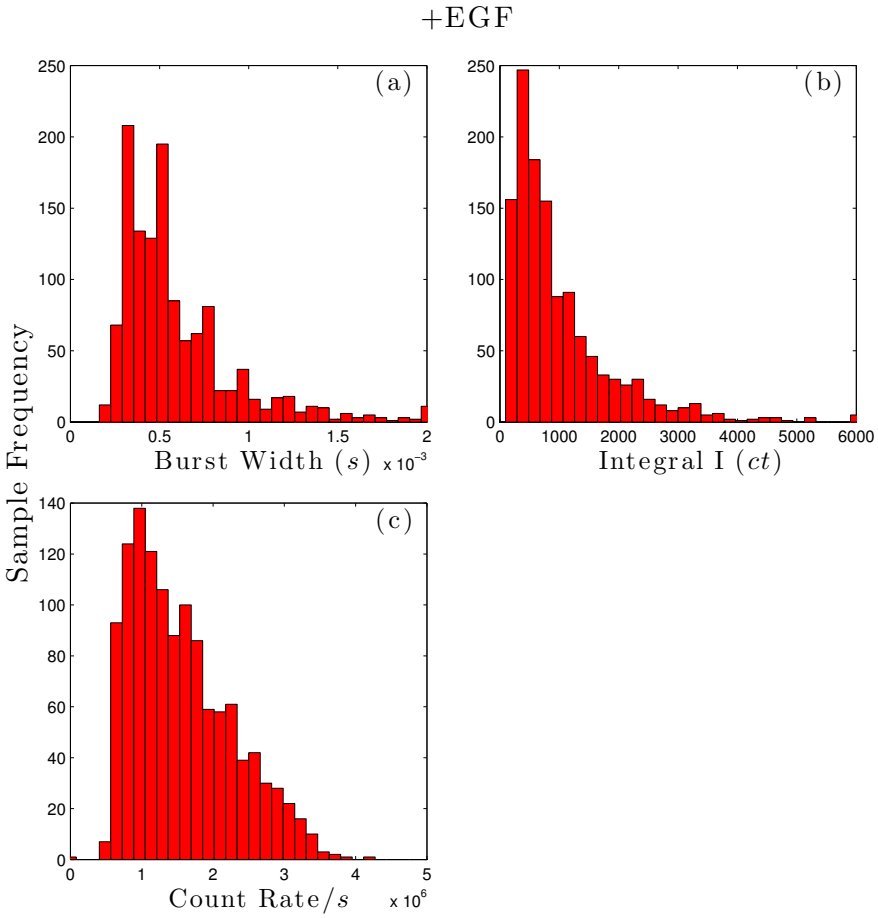

Figure 6.13: Burst characteristics of the stimulated cells (+EGF), where (a), (b) and (c) represents the burst widths, integral intensities, and instantaneous count rates during each detection event, respectively.

6.4.2 Number of detected Events

	Number of detected events (10 minutes)
Control	4790
-EGF	905
+EGF	1236

Table 6.8: The table of summary for the number of detected events, where the control and +EGF cases where pumped at 500 mbar, while the -EGF case was pumped at 200 mbar.

6.4.3 NL-MLM Analysis (BIFL)

The analysed burst event data using NL-MLM is summarised in Figure 6.14.

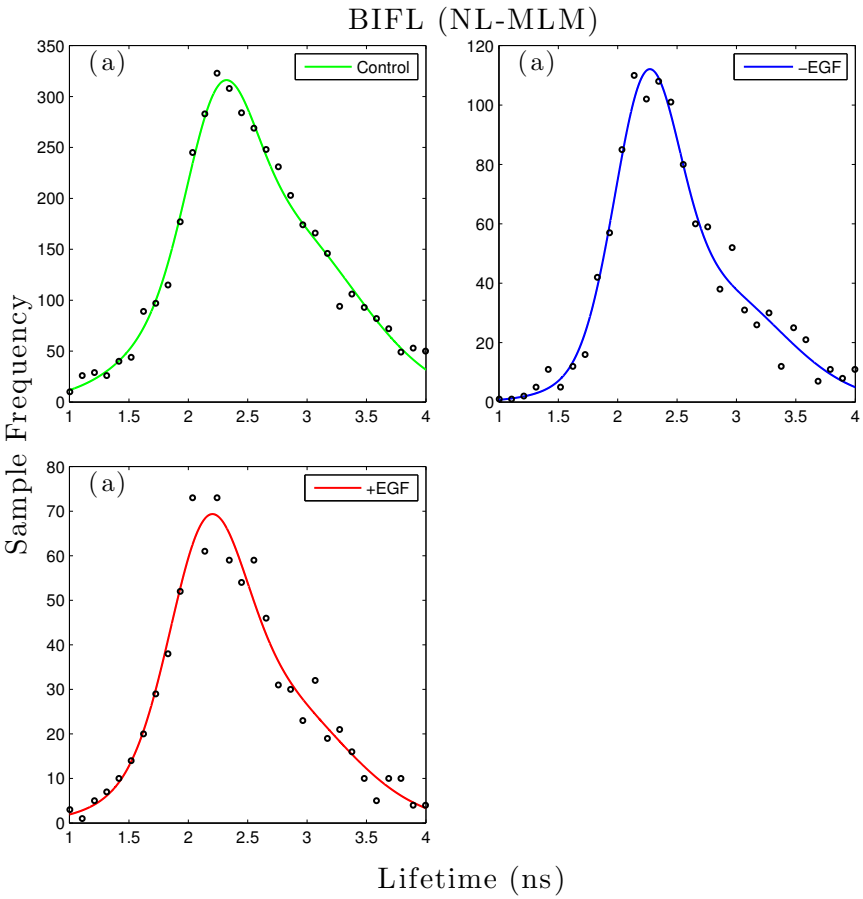

Figure 6.14: Lifetime determination by BIFL with NL-MLM, where the first and second column represent the lifetime image and the corresponding lifetime histogram in the green channel respectively. The first, second and third row represent the control, the auto-phosphorylation state (without EGF) and the induced phosphorylation with EGF respectively.

Applying the same methodology to analyse the histograms as in the imaging data, the data in Figure 6.15 was fit to a double Gaussian model with the long lifetime component removed to give the result in Figure 6.16. When comparing the results from Figure 6.16 (b) with Figure 6.4 (b) of the FLIM section, the only real difference between the results, is the behaviour of the EGF case. In this BIFL section, there is only a marginal difference between the FRET efficiency of the control and -EGF population which, almost certainly reflects the poor sample

yield for this construct.

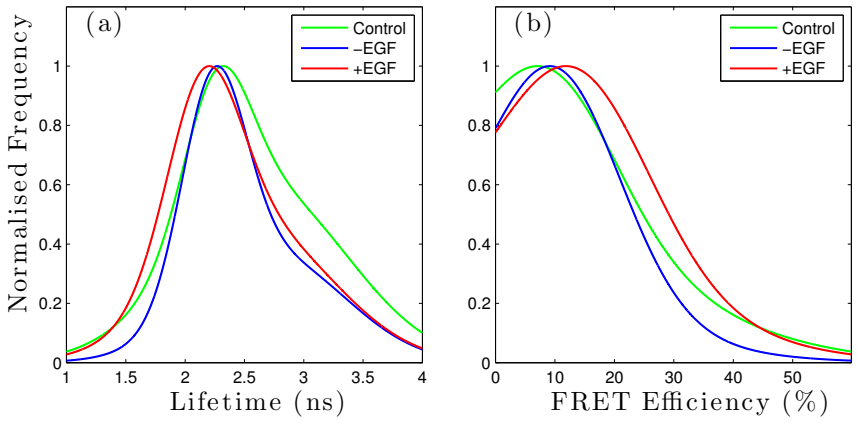

Figure 6.15: A summary of lifetime (a) and FRET efficiency (b) histograms from each construct.

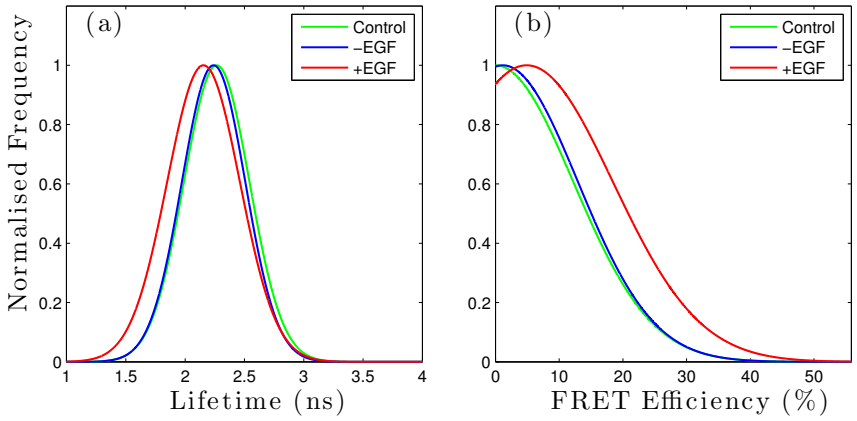

Figure 6.16: A revised summary of lifetime (a) and FRET efficiency (b) histograms from each construct. The histograms ignore the fractional contribution from the anomalously long lifetime components.

	A_1	A_2	τ_1	τ_2	σ_1	σ_2	Ave. τ	Ave. σ
Control	156	184	2.27	2.67	0.39	1.00	2.50	0.85
-EGF	83	40	2.24	2.74	0.38	0.87	2.43	0.64
+EGF	44	31	2.16	2.59	0.43	0.95	2.35	0.75

Table 6.9: The table of summary for the lifetime fitting (NL-MLM). The average lifetime of the was calculated by a double Gaussian mixture model, where, A_1 and A_2 are the fractional contributions, τ_1 and τ_2 are the mean lifetimes in ns, and σ_1 and σ_2 are the standard deviations of each sub-population in ns, respectively. Ave. τ is the average lifetime in ns and Ave. σ is the average standard deviation of each construct in ns, respectively.

	τ	σ	FRET efficiency	σ_F
Control	2.27	0.39		
-EGF	2.24	0.38	1.15	16.69
+EGF	2.16	0.43	4.9	19.14

Table 6.10: The table of summary for the revised lifetime fitting (NL-MLM) (ignoring the sub-population with anomalously long lifetime), where τ is the mean lifetimes in ns, and σ is the standard deviations of each construct in ns, respectively. The FRET efficiency is expressed in % and σ_F is the standard deviation of the corresponding FRET efficiency in %.

With the average photon count being around 1000 – 2000 counts, the NL-MLM is perhaps unable to differentiate the lifetime of the two constructs faithfully. This problem is made worse by the previous suggestion, where the stoichiometry of the two dyes is sub-optimal and a fraction of donor dyes in the -EGF population could have become unbounded. This might be a reflection in the age of the samples which were analysed over the course of a few days and stored in the fridge when not used.

When comparing the lifetime of the constucts in this BIFL section with the FLIM case (see Table 6.2), there seem to be a collective shift down in the lifetimes.

However, the FRET efficiencies of the constructs in both cases are comparable to one and another, which suggests that the strength of the interaction is relatively consistent, despite any possible change in the local environments between the chamber well and microfluidics.

6.4.4 Integrated transient analysis of BIFL data (NL-MLM)

The integrated analysis of the lifetime in Figure 6.17 clearly reinforces the argument on the inefficiency of NL-MLM in resolving the lifetimes of each construct from the available photon number present in the BIFL experiment. The changes in the integrated transient profiles of all the construct are now more reminiscent of those measured by accumulated transient measured with FLIM in Figure 6.9 (d). The lifetimes of the control, -EGF and +EGF populations measured by FLIM were calculated to be 2.42 ns, 2.37 ns and 2.35 ns, respectively (see Table 6.6). These values are very close to the those listed in Table 6.11, with the exception of the +EGF population. The χ^2_R of the accummulated transients are also better behaved than the FLIM case with no interference from the oscillations along the transients, which possibly gave a better differentiation between the EGF and +EGF population in this section.

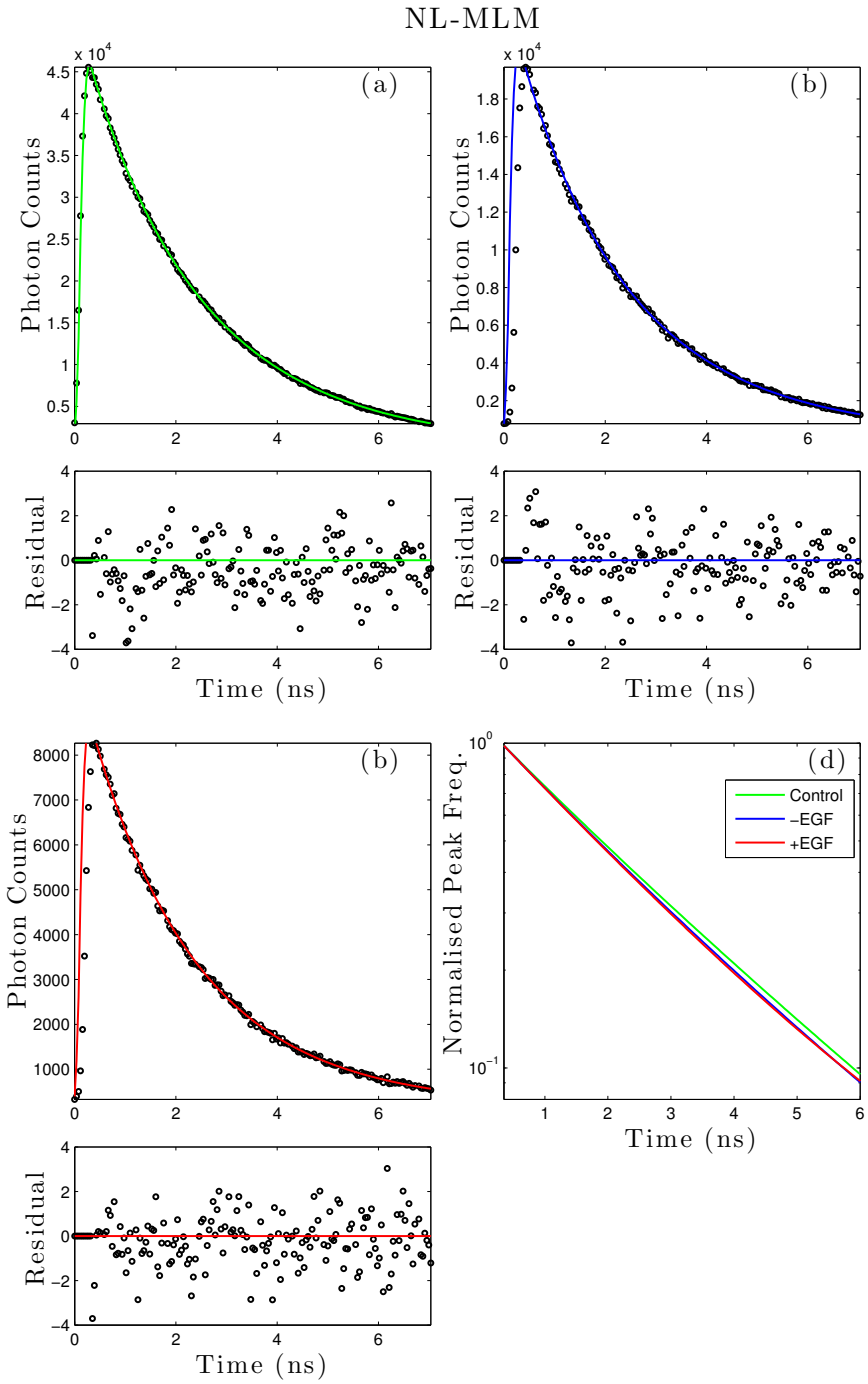

Figure 6.17: Summary of accumulated transients from all the pixels in each BIFL image (NL-MLM), where (a), (b) and (c) represents the transient the control, the auto-phosphorylation state (without EGF) and the induced phosphorylation with EGF respectively. (d) is the collation of all the transient shown in log scale.

	A_1	A_2	τ_1	τ_2	Ave. τ	χ^2_R	F. eff
Control	39596	9731	2.57	1.37	2.43	4.82	
-EGF	16607	5709	2.53	1.41	2.35	4.28	3.36
+EGF	7844	1445	2.28	1.39	2.19	2.05	9.88

Table 6.11: The table of summary for the lifetime fitting on the accummulated transients by NL-MLM, where A_1 and A_2 are the fractional contributions, τ_1 and τ_2 are the mean lifetimes in ns, and σ_1 and σ_2 are the standard deviations of each sub-population, respectively. Ave. τ is the average lifetime in ns, χ^2_R is the goodness of fit parameter and F. EFF is the FRET efficiency in %.

6.4.5 Phasor Analysis (Lifetime)

In this section, the BIFL results are now analysed by the Fourier transformation of the phasors. From previous investigations in the FRET ruler experiment (chapter 5) and fluorescent beads (chapter 4), the phasor analysis, usually gave tight and symmetric lifetime distributions without compromising data accuracy made on the analysis. In this case, however, some degrees of positive skewnesses were observed on the distributions in all the samples (Figure 6.18 (a, b and c)). Therefore when analysing the FRET efficiency of the data, the major fractional distribution of the data was exclusively used for the calculation as in the NL-MLM case.

The lifetimes of the control, -EGF and +EGF populations measured by FLIM were calculated to be 2.23 ns, 2.17 ns and 2.15 ns, respectively (see Table 6.3). The values give a similar trend in the lifetime as in NL-MLM. However the FRET efficiencies in this case, are significantly different from the ones measured by FLIM (see Table 6.4), where the FRET efficiency of -EGF and +EGF populations are increased by approximately two-fold with similar increase in the standard deviations.

	A_1	A_2	τ_1	τ_2	σ_1	σ_2	Ave. τ	Ave. σ
Control	254	167	2.17	2.39	0.26	0.45	2.26	0.36
-EGF	80	62	2.04	2.15	0.16	0.4	2.09	0.31
+EGF	70	18	1.98	2.33	0.27	0.46	2.06	0.33

Table 6.12: The table of summary for the lifetime fitting by Fourier Transformation of Phasors, , where A_1 and A_2 are the fractional contributions, τ_1 and τ_2 are the mean lifetimes in ns, and σ_1 and σ_2 are the standard deviations of each sub-population in ns, respectively. Ave. τ is the average lifetime in ns and Ave. σ is the average standard deviation of each construct in ns, respectively.

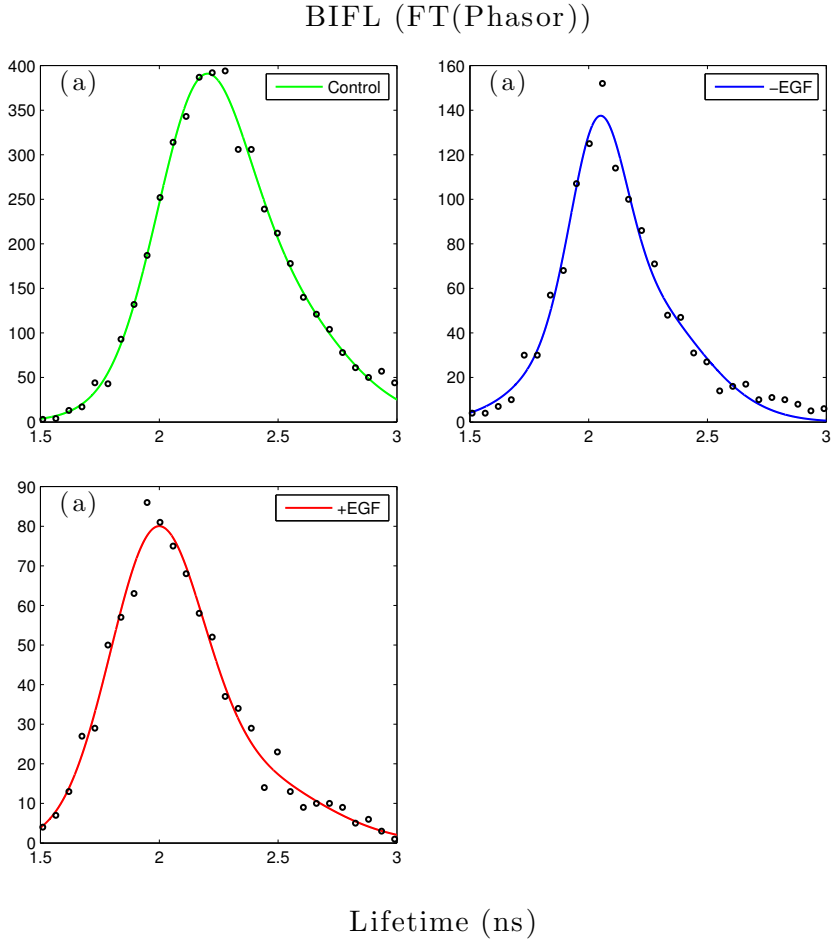

Figure 6.18: Lifetime determination by BIFL with Fourier Transformation of Phasors, where the first and second column represent the lifetime image and the corresponding lifetime histogram in the green channel respectively. The first, second and third row represent the control, the auto-phosphorylation state (without EGF) and the induced phosphorylation with EGF respectively.

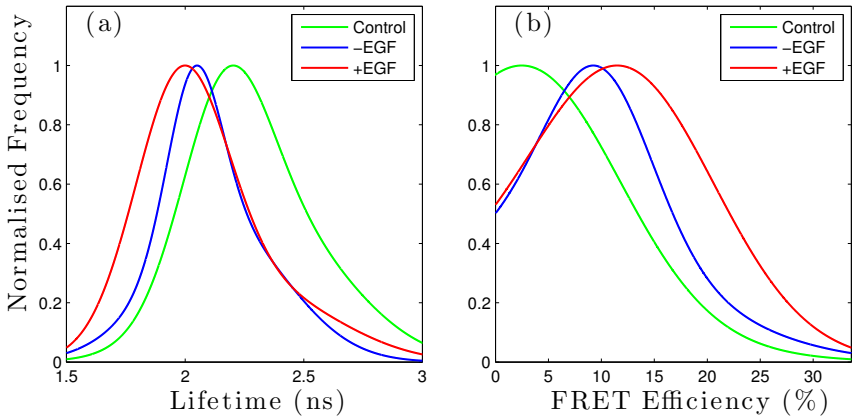

Figure 6.19: A summary of lifetime (a) and FRET efficiency (b) histograms.

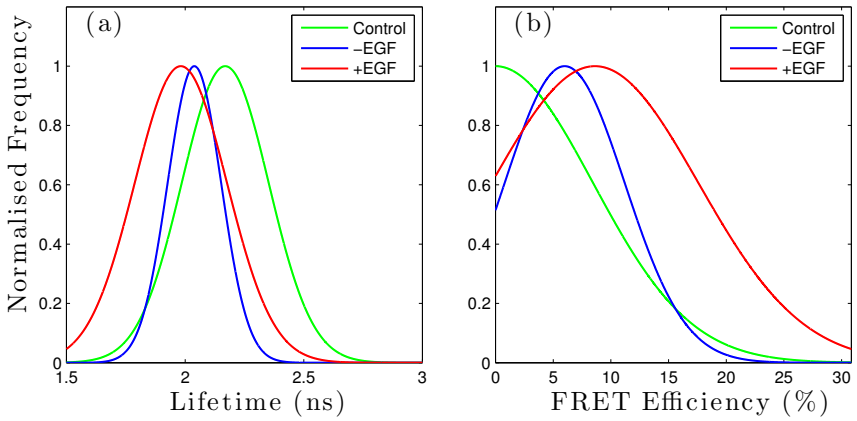

Figure 6.20: A revised summary of lifetime (a) and FRET efficiency (b) histograms from each construct. The histograms ignore the fractional contribution from the anomalously long lifetime components.

	τ	σ	FRET efficiency	σ_F
Control	2.17	0.26		
-EGF	2.04	0.16	5.99	7.35
+EGF	1.98	0.27	8.62	12.67

Table 6.13: The table of summary for the revised lifetime fitting with Fourier Transformation of Phasors (ignoring the sub-population with anomalously long lifetime), where τ is the mean lifetimes in ns, and σ is the standard deviations of each construct in ns, respectively. The FRET efficiency is expressed in % and σ_F is the standard deviation of the corresponding FRET efficiency in %.

6.4.6 Integrated Lifetime analysis of BIFL data (FT (Phasor)

The approximation of the fit by FT(Phasor) yield better and cleaner results, compare to the FLIM case in subsection 6.3.2, with some minor offsets along the tail of the transients after 4ns. The strength of the FRET interactions of the -EGF and +EGF populations in the BIFL experiment Table 6.14 is much stronger than the FLIM case (Table 6.7) . However the increase in the FRET efficiencies between the -EGF and +EGF populations is still somewhat comparable by both techniques, where the BIFL saw an increase in the FRET efficiency by approximately 2%, while FLIM calculated the increase by approximately 1%.

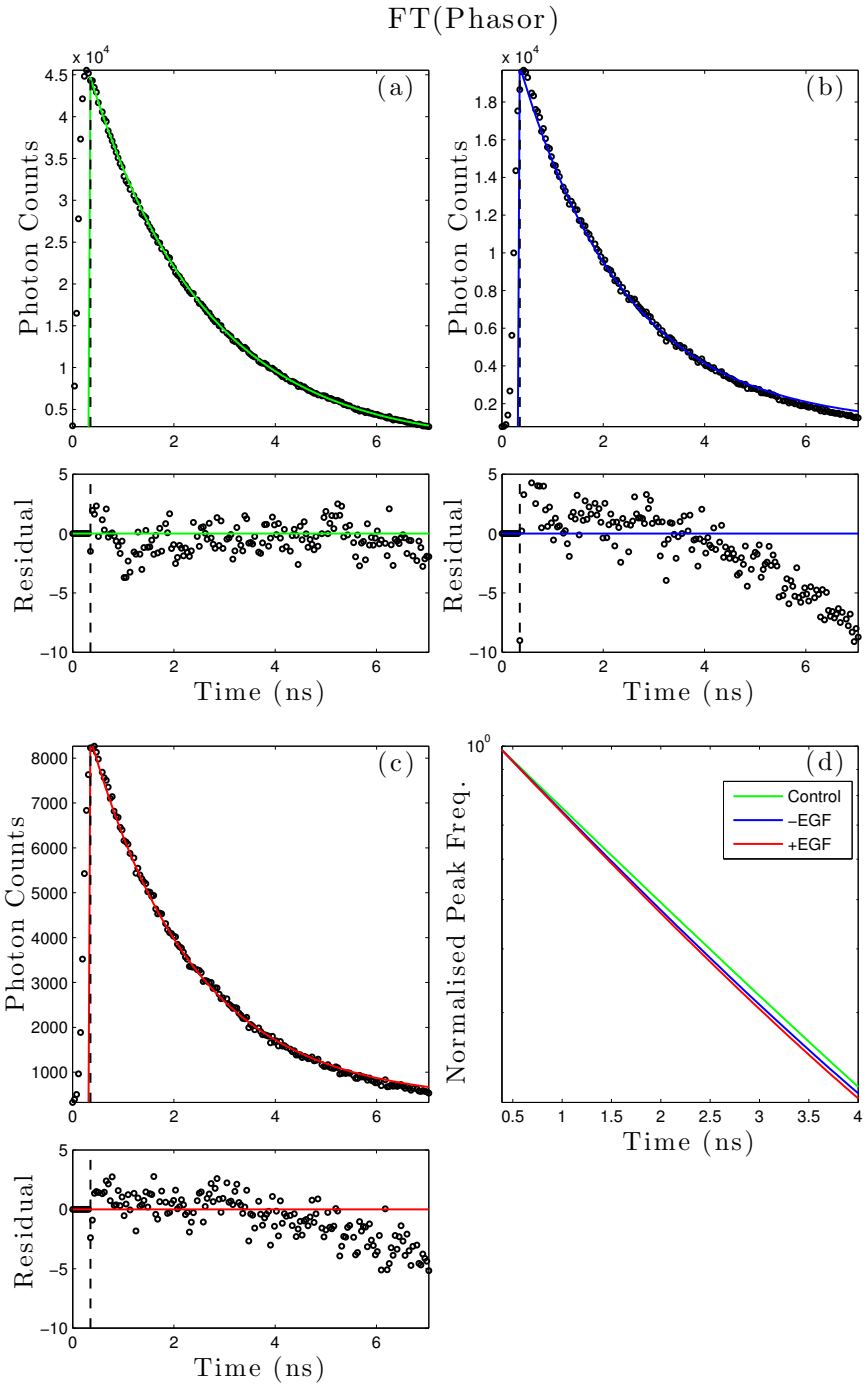

Figure 6.21: Summary of accumulated transients from all the pixels in each FLIM image (FT (Phasor)), where (a), (b) and (c) represents the transient the control, the auto-phosphorylation state (without EGF) and the induced phosphorylation with EGF respectively. (d) is the collation of all the transient shown in log scale.

	τ	χ^2_R	F. Eff
Control	2.28	5.11	
-EGF	2.09	14.75	8.29
+EGF	2.04	4.87	10.31

Table 6.14: The table of summary for the lifetime fitting on the accummulated transients by the Fourier Transformation of the phasors, where τ is the mean lifetimes in ns, χ^2_R is the goodness of fit parameter of each construct and F. Eff is the FRET effienciency in %.

6.4.7 Phasor Plot Analysis

The contour plot of the phasors saw a larger increase in similar changes in the u separations between each contruct to the FLIM experiment in subsection 6.3.3 (see Table 6.5), but gained a visibly larger spread in the standard deviations, as expected. The lifetime results of the +EGF in both FLIM and BIFL experiments, and large spread in the standard deviation of the u coordinates of the same construct show consistent support on the lifetime broadening effect upon the treatment of EGF.

The phasor plot in Figure 6.22, also shows signs of mono-exponential as to the FLIM case, where the centring u coordinates of each construct all lay along the universal semi-circle.

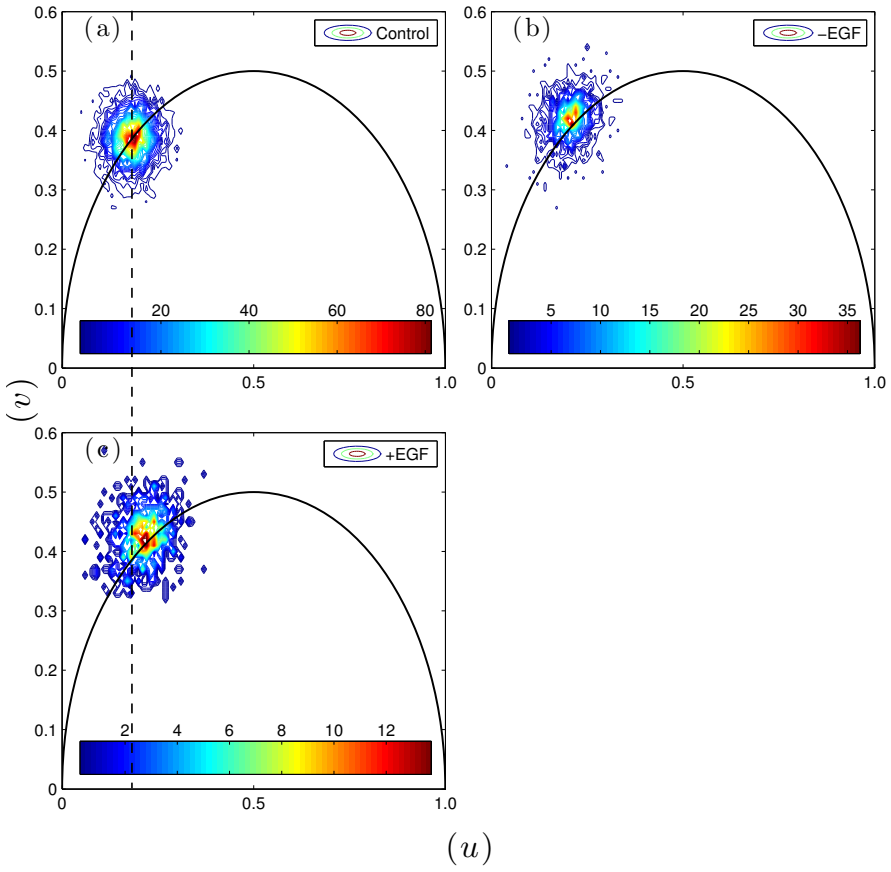

Figure 6.22: Contour plots of Phasors, where (a), (b), and (c) represent the phasor image of the control, the auto-phosphorylation state (without EGF) and the induced phosphorylation with EGF respectively.

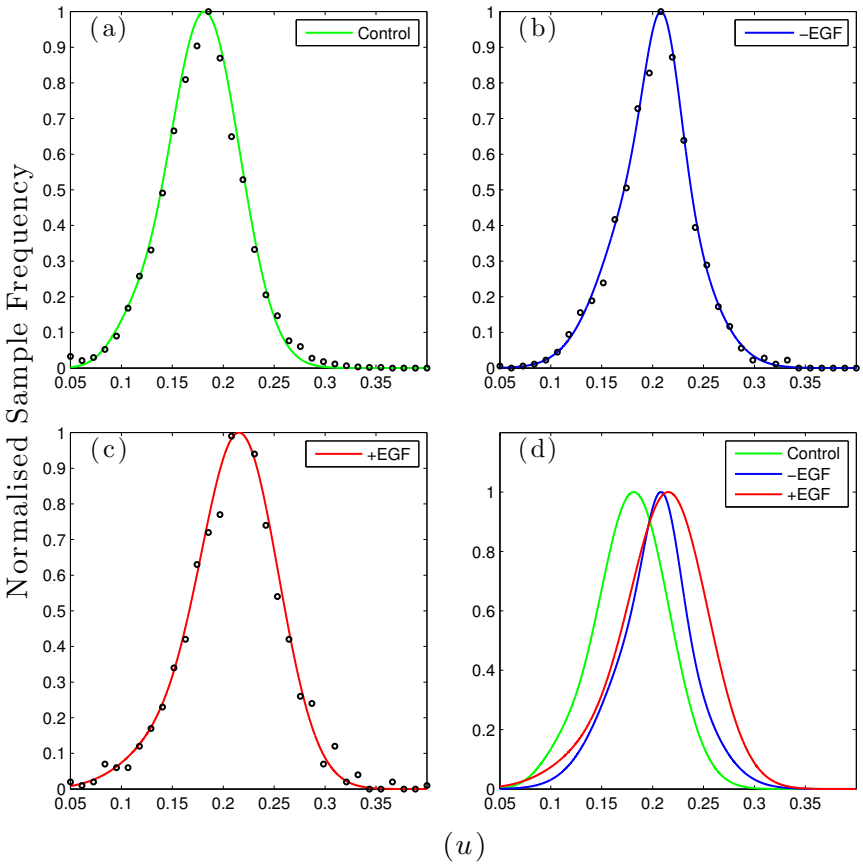

Figure 6.23: Comparison of u coordinates between the construct from Figure 6.7, where (a), (b), and (c) represent the phasor image of the control, the auto-phosphorylation state (without EGF) and the induced phosphorylation with EGF respectively.

	A_1	A_2	u_1	u_2	σ_1	σ_2	Ave. u	Ave. σ
Control	580	44	0.182	0.108	0.049	0.029	0.178	0.048
-EGF	74	103	0.210	0.200	0.024	0.059	0.205	0.051
+EGF	94	11	0.217	0.143	0.054	0.057	0.212	0.054

Table 6.15: The table of summary for the lifetime fitting by Fourier Transformation of Phasors, where τ is the mean lifetimes in ns, and σ is the standard deviations of each construct in ns, respectively.

6.5 Summary of Clinical Study

By and large, the shift in the decay rate of the integrated transients from the BIFL data bahaved in the similar fashion to the FLIM case for both by the NL-MLM and FT (Phasor) methods. In the NL-MLM analysis, the result from the FLIM and BIFL experiments, showed some degree of correlations in terms of the lifetime reduction and the FRET efficiencies data. However, in the phasor case, it is still remains inconclusive as to why the the FRET efficiencies of individual data are approximately doubled from those calculated by FLIM. Nonetheless, the change in the FRET efficiency from the -EGF to +EGF populations are also approximately doubled. The instantaneous count rates of all data are above the safe count rate of 0.8×10^6 counts per second. It is very likely that the pulse pile-up effect would play a role in the changes observed.

In conclusion, the trend in the lifetime reduction from all the decribed analysis methods in this chapter consistently show some evidence on the increase in phosphorylation of the phosphotyrosine residue P72 of EGFR receptor. Undoubtedly, the results would become more pronounced, with optimisation of the labelling stoichimetry. However, due to the time available for the project, the biological parameters could not optimised any further. This experiment is a step forward in the capabilities of the system in clinically relevant applications.

Chapter 7

Conclusion and Future Work

The novel use of the FIFO BIFL in flow has shown great credential in providing useful functional readout in the high throughput arena. The proof-of-concept of the system was extensively described in chapter 4 with 2 types of fluorescent beads, which provided a better understanding on the caveats from the unusually high power set-up in the photon counting operation. It has been shown in parts of chapter 5 on the investigation of the spectroscopic ruler construct that the dynamic range of the lifetime modality is preserved to a good extent, despite the use of the high laser power and possible interference from auto-fluorescence. The partial success on the clinically relevant assay on the well-characterised stimulation of phosphorylation by the EGF agonists in chapter 6 was limited by the in the incorrect stoichiometry of the transfection, but could be improved with further biochemical optimisation and experimental repeats.

All in all, the system can serve many in-house biological applications within the Dimbleby department. Should the users are interested in fast, first-pass, high throughput screenings of FRET constructs, where the control population is screened against a FRET construct with at least 10% efficiency, then the system would be able to cater the need to good effect (provided the difference between the constructs are the only concern). This way the use of the high laser power does not need to be strictly regulated.

However the need for such application is minimal. Most of the work being done

here are clinically relevant and the count rate problem need to be addressed. Individual cells variably react to a drug treatment, and hence the need for a high volume screening is very important in obtaining a robust statistic on the reaction. The compromises on the high power to ensure the cells travelling in the streamlines near to the probe are receiving sufficient excitation power, is always likely to put the system beyond the self-imposed safe count limit at 800 kHz. At the pulse pile-up regime, it is impossible to ensure that every fluorescence lifetime are ubiquitous quenched by the same amount, due to the cell variability and uncertainties in the immunocytochemisty.

As previously mentioned in the various parts of the thesis, a hydro-dynamic focusing facility would be advantage, as a spot probe is preferred to the line type in biological investigations, to reduce the background noise and any unexpected auto-fluorescence. Once a pinpoint location of the streamline can be located to ensure a clean, uniform and efficient excitation, a more moderate excitation power can be afforded to possibly contain the count rate to the safe limit.

The type of microfluidic chip is common nowadays. It is simply the question of the ease on the fluidic handling and their compatibilities to the pressure pump in-hand. Each cell type would need to be diluted differently and optimised. With unsecured inter-fluidic connection on any new chip, the cell concentration optimisation process can cause the fluidic network to become to be leaky and inefficient. The pumping method in the project is good at maintaining the sample in suspension with the magnetic stirrer, and does not need to swiftly inject the sample into the interrogation fluidic. This is significantly beneficial to the interrogation time needed for TCSPC.

Additionally, high instantaneous count rate can also be the result of strong auto-fluorescence detection, which is proportionally increased with higher excitation power. It has been reported that the use of long fluorescence lifetime probes such as Lanthanide Chelate [100–102] and a time-gated measurement can alleviate the auto-fluorescence problem. The methodology samples a fraction of fluorescence decays away from the origin of auto-fluorescence near the peak of the transient,

to give a cleaner functional data. However modifications to the ACD and microchannel analyser would be required to physically blind the histogram bins near the peak of fluorescence to truly reduce the count rate of the TCSPC to the safe limit [49, 61]. It is also unknown how the dyes are going to bind to the antibodies in-hands. The methodology is hence unfavourable for the project. However, the use of green excitation (around 520 nm) is also sufficient in removing the auto-fluorescence problem, which is inherently induced by the blue excitation [25, 100, 101]. This does not require any modification to the TCSPC, and allow us to exploit all the available photons from the entire fluorescence decay in the analysis. This will be very useful for the clinical assays in the future, which contain malignant cells from paraffin section of archival formaldehyde-fixed samples (biopsy). The paraffin is used to preserve the cells, but is well known in expressing high level of auto-fluorescence with the blue excitation.

The workflow of clinical assay would be to first observe a functional state of malignant cells in their endogenous state, and observe the catalytic or attenuation effect of a drug on the function (as shown by the example in chapter 6, which still needs further experimental repeats), and then prepare the system for the cell detection contained in paraffin which does not necessary require any drug treatment. This step of the workflow would require the system to be switched over to the green excitation to excite the dyes such as Alexa-546 anyway. Hence the next of step of the FIFO BIFL development would be to ensure that the cell detection in paraffin is confidently achieved with the set-up, before moving on the final step in analysing patient samples contained in paraffin, with-and-without the effect of drug treatments.

It was shown in chapter 5 that the use of phasors in the phase domain can be used to sort the FRET construct with 20% FRET efficiency to good effect, in the post-acquisition analysis. The identified burst indices of the two sub-populations were consistent and applicable to the data selection in every lifetime fitting method (as shown in Figure 5.28).

However more work on FRET interaction are still need to assess the requirement

of photon population for complex spectra analysis, to yield tightly more distributed phasors for FRET interaction with less than 20% efficiency. The sorting trigger in the phase domain is attractive platform in enabling the live sorting capability, as the methodology is non-computationally intensive, and can give an extremely rapid mean of sorting different sub-population in real-time through an on-board programming hardware such as FPGA.

Referring to the example in chapter 5, where the histogram of u and v co ordinates of the control and the eGFP-32aa-mRFP and eGFP-7aa-mRFP constructs are re-summarised in Figure 7.1.

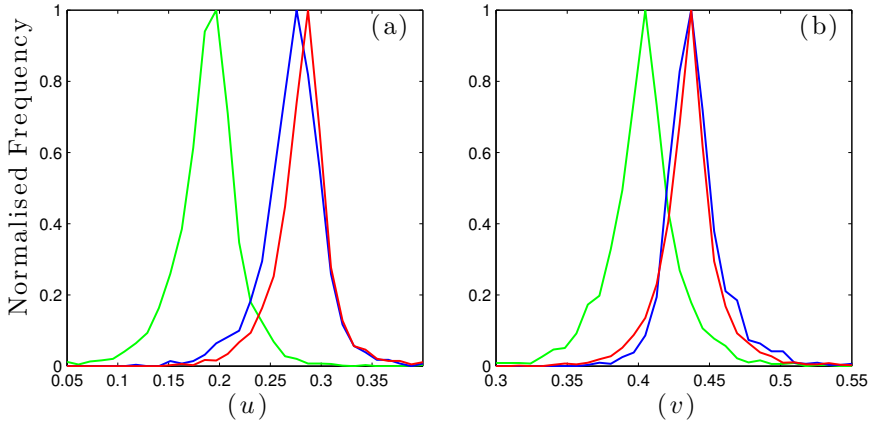

Figure 7.1: (a) Summary of the u co-ordinate histogram (b) Summary of the v co-ordinate histogram of the phasors of the control (green), eGFP-32aa-mRFP (blue) and eGFP-7aa-mRFP (red) constructs, respectively.

It can observed from the figure that the u information is already sufficient in resolving samples with differences in lifetime by approximately 330 ps (control versus eGFP-32aa-mRFP analysed by FT(Phasors)) with small contaminations. The sole computation the u co ordinates will take a few steps away from the already rapid phasor computation. The sorting trigger in the u co-ordinates can be confidently implemented to the lifetime screening application, where the samples in-question exhibit largely separated lifetimes ($\geq$ 0.8 ns) from one and another,

as shown by the 2 fluorescent beads example in chapter 4.

There are many sorting hardware available in the market, such as the acoustic, and charge-induced electrostatic sorting, but these are not easily implementable to the microscopical platform. Optical sorting [59] is clearly an attractive platform. With the use of the long wavelength infra-red laser, it is straightforward to include a short-pass dichroic filter along the path between the rotating mirror and the object holder, see the re-introduction of the system layout in Figure 7.2.

Provided the interrogation point is positioned close to the outlets (within the FOV of the objective) and there is enough to room to steer the IR beam onto the entrance of one of the outlets, through the same objective, the computations of the phasors and the triggering of IR laser need to be ensured to be completed in-time within the space between the two probes. However, the system has a stronger likelihood to be redeveloped into a standalone unit to accommodate longer processing time in the meander of the micro-mixing part, and deploy a separate objective for the sorting laser.

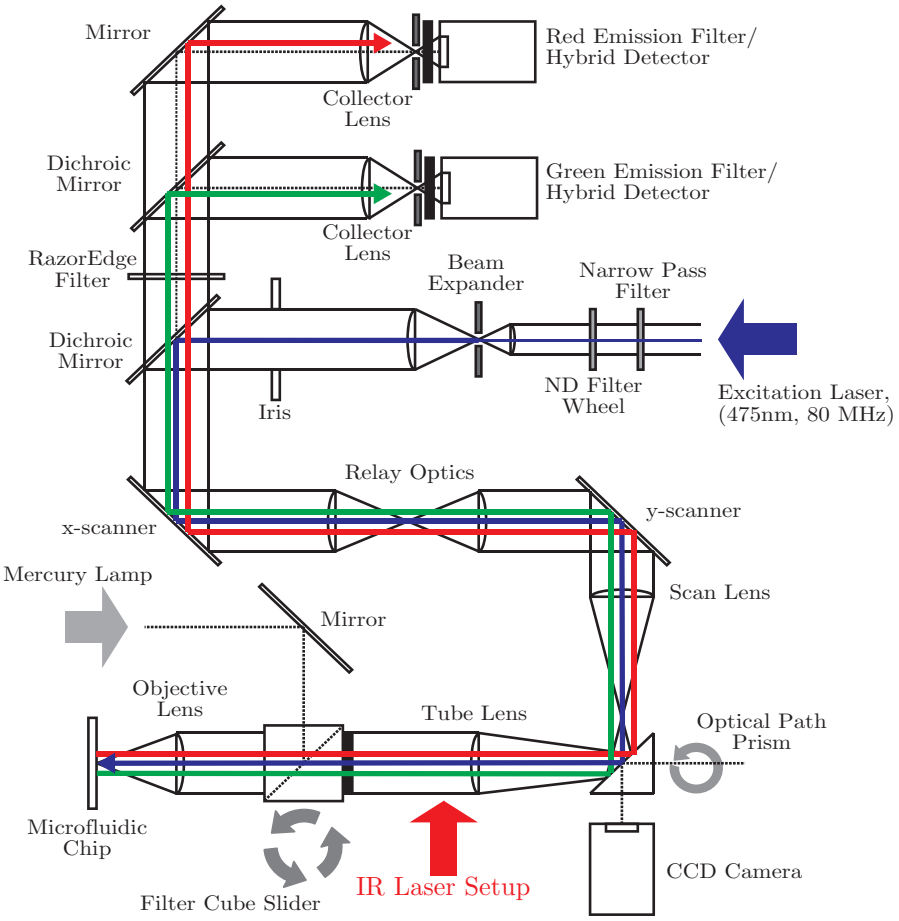

Figure 7.2: A schematic layout of the development system with a possible location of the optical sorting laser setup (see red arrow).

Appendix A

Cell Preparation Protocol (Chapter 5)

Plasmid

mRFP-eGFP FRET standards were constructed by the ligation of mRFP1 into the pEGFP-N1 vector used in the manufacture of the Raichu biosensor constructs, generating random amino acid linkers. The linker for the 7AA sequence is RDPPVAT, for the 19AA sequence is KLRILQSTVPRARDPPVAT, and for the 32AA sequence is KLRILDITSGLETRDASGQSTVPRARDPPVAT. These constructs were expressed transiently in human embryonic kidney (HEK)-293T cells [59] obtained from the American Type Culture Collection (ATCC).

Transfection Protocol

- Day 1: Count 293T cells on the CASY and plate 1.7×10^6 cells in 10 cm dishes.
- Day 2: Transfect each dish with 6 μg DNA (set up 600 μl Optimem with 6 μg DNA and 18 μl Fugene6, incubate at room temp for 30 to 45 minutes, then add to cells). Allowing 48 hours for the proteins to fold.
- Day 4: Trypsinise cells and re-suspend in 4% paraformaldehyde to fix. Wash

fixed cells 3 times with PBS and re-suspend in small volume PBS (200 μl). Wash 3 times with PBS and treat cells with NaBH4 (1 mg/mL) for 5 minutes at room temperature. Rinse 3 times with PBS

Appendix B

Cell Preparation Protocol (Chapter 6)

Transfection Protocol

Biological Constructs:

1. EGFR-EGFP (control)
2. EGFR-EGFP + PY72-Cy3 basal
3. EGFR-EGFP + PY72-Cy3 with EGF treatment (10 min)

Dr. Elena Zapater-Otiz (Division of Cancer Studies, Kings College London), kindly prepared samples for this experiment.

- Day 1: Treat plates with polylysine following normal protocol. Plate 1×10^6 MCF-7 cells in four 10 cm dishes.
- Day 2: Transfect each dish with 6 μg of DNA (EGFR-EGFP). The DNA solution is prepared by mixing 600 μl of OPTIMEM with the DNA for 5 minutes, before adding 18 μl of Fugene6 (at room temperature) to petri dishes. Mix the solutions well and incubate the dishes at room temperature for 30 minutes, before adding to cells.
- Day 3 - late evening: Starve cells with 5 ml of DMEM without FBS.

- Day 4 - morning: Stimulate 2 plates with EGF (1:1000 stock) for 10 minutes. Rinse 2x with PBS and fix with PFA 4% for 12 minutes. Wash 3 times with PBS and treat cells with $NaBH_4$ (1 mg/mL) for 5 minutes, RT. Rinse 3x with PBS. Permeabilize: with TX-100 0.2% in PBS for 10 minutes. Rinse 4x with PBS. Blocking solution: 2% BSA in PBS, pH 7.4, filter through 0.2 μm filter. Incubate for 1 hour at room temperature.

- Ab: Incubate with PY72-Cy3 labelled ab (15 mg/mL) for 4 hours at room temperature.

- tubes. Centrifuge 1000 rpm, 5 min. Re-suspend the pellet in approximately 500 μl of PBS.

Bibliography

[1] R. A. Colyer, O. H. W. Siegmund, A. S. Tremsin, J. V. Vallerga, S. Weiss, and X. Michalet, "Phasor imaging with a widefield photon-counting detector," *J Biomed Opt*, vol. 17, p. 016008, Jan 2012.

[2] O. Reynolds, "An experimental investigation of the circumstances which determine whether the motion of water shall be direct or sinuous, and of the law of resistance in parallel channels," *Philosophical Transactions of the Royal Society of London*, vol. 174, pp. pp. 935–982, 1883.

[3] T. M. Squires and S. R. Quake, "Microfluidics: Fluid physics at the nanoliter scale," *Rev. Mod. Phys.*, vol. 77, pp. 977–1026, Oct 2005.

[4] C. Lin, *The theory of hydrodynamic stability*. Cambridge University Press, 1955.

[5] D. R. Matthews, G. O. Fruhwirth, G. Weitsman, L. M. Carlin, E. Ofo, M. Keppler, P. R. Barber, I. D. C. Tullis, B. Vojnovic, T. Ng, and S. M. Ameer-Beg, "A multi-functional imaging approach to high-content protein interaction screening," *PLoS One*, vol. 7, no. 4, p. e33231, 2012.

[6] F. S. Wouters, P. J. Verveer, and P. I. Bastiaens, "Imaging biochemistry inside cells.," *Trends Cell Biol*, vol. 11, pp. 203–211, May 2001.

[7] J. W. Legg, C. A. Lewis, M. Parsons, T. Ng, and C. M. Isacke, "A novel PKC-regulated mechanism controls CD44 ezrin association and directional cell motility," *Nat Cell Biol*, vol. 4, pp. 399–407, Jun 2002.

[8] T. Ng, M. Parsons, W. E. Hughes, J. Monypenny, D. Zicha, A. Gautreau, M. Arpin, S. Gschmeissner, P. J. Verveer, P. I. Bastiaens, and P. J. Parker,

"Ezrin is a downstream effector of trafficking PKC-integrin complexes involved in the control of cell motility," *EMBO J*, vol. 20, pp. 2723–41, Jun 2001.

[9] T. Meyer and M. N. Teruel, "Fluorescence imaging of signaling networks," *Trends in cell biology*, vol. 13, no. 2, pp. 101–106, 2003.

[10] C. Berney and G. Danuser, "FRET or no FRET: a quantitative comparison.," *Biophys J*, vol. 84, pp. 3992–4010, Jun 2003.

[11] T. Ng, A. Squire, G. Hansra, F. Bornancin, C. Prevostel, A. Hanby, W. Harris, D. Barnes, S. Schmidt, H. Mellor, P. I. Bastiaens, and P. J. Parker, "Imaging protein kinase Calpha activation in cells," *Science*, vol. 283, pp. 2085–9, Mar 1999.

[12] N. Anilkumar, M. Parsons, R. Monk, T. Ng, and J. C. Adams, "Interaction of fascin and protein kinase Calpha: a novel intersection in cell adhesion and motility," *EMBO J*, vol. 22, pp. 5390–402, Oct 2003.

[13] J. Herreros, T. Ng, and G. Schiavo, "Lipid rafts act as specialized domains for tetanus toxin binding and internalization into neurons," *Mol Biol Cell*, vol. 12, pp. 2947–60, Oct 2001.

[14] T. W. Gadella, Jr and T. M. Jovin, "Oligomerization of epidermal growth factor receptors on A431 cells studied by time-resolved fluorescence imaging microscopy. a stereochemical model for tyrosine kinase receptor activation," *J Cell Biol*, vol. 129, pp. 1543–58, Jun 1995.

[15] T. Ng, D. Shima, A. Squire, P. I. Bastiaens, S. Gschmeissner, M. J. Humphries, and P. J. Parker, "PKCalpha regulates beta1 integrin-dependent cell motility through association and control of integrin traffic," *EMBO J*, vol. 18, pp. 3909–23, Jul 1999.

[16] M. Parsons, M. D. Keppler, A. Kline, A. Messent, M. J. Humphries, R. Gilchrist, I. R. Hart, C. Quittau-Prevostel, W. E. Hughes, P. J. Parker,

and T. Ng, "Site-directed perturbation of protein kinase C- integrin interaction blocks carcinoma cell chemotaxis.," *Mol Cell Biol*, vol. 22, pp. 5897–5911, Aug 2002.

[17] E. A. Jares-Erijman and T. M. Jovin, "FRET imaging," *Nat Biotechnol*, vol. 21, pp. 1387–1395, Nov 2003.

[18] P. Barber, S. Ameer-Beg, J. Gilbey, L. Carlin, M. Keppler, T. Ng, and B. Vojnovic, "Multiphoton time-domain fluorescence lifetime imaging microscopy: practical application to protein–protein interactions using global analysis," *Journal of The Royal Society Interface*, vol. 6, no. Suppl 1, pp. S93–S105, 2009.

[19] Lakowicz, I. Gryczynski, and Z. Gryczynski, "High throughput screening with multiphoton excitation," *J Biomol Screen*, vol. 4, no. 6, pp. 355–362, 1999.

[20] D. R. Matthews, L. M. Carlin, E. Ofo, P. R. Barber, B. Vojnovic, M. Irving, T. Ng, and S. M. Ameer-Beg, "Time-lapse FRET microscopy using fluorescence anisotropy," *J Microsc*, vol. 237, pp. 51–62, Jan 2010.

[21] A. Esposito, C. P. Dohm, M. Bähr, and F. S. Wouters, "Unsupervised fluorescence lifetime imaging microscopy for high content and high throughput screening," *Mol Cell Proteomics*, vol. 6, pp. 1446–54, Aug 2007.

[22] K. Suhling, P. M. W. French, and D. Phillips, "Time-resolved fluorescence microscopy.," *Photochem Photobiol Sci*, vol. 4, pp. 13–22, Jan 2005.

[23] L. He, D. P. Olson, X. Wu, T. S. Karpova, J. G. McNally, and P. E. Lipsky, "A flow cytometric method to detect protein-protein interaction in living cells by directly visualizing donor fluorophore quenching during CFP–¿YFP fluorescence resonance energy transfer (FRET)," *Cytometry A*, vol. 55, pp. 71–85, Oct 2003.

[24] C. Banning, J. Votteler, D. Hoffmann, H. Koppensteiner, M. Warmer, R. Reimer, F. Kirchhoff, U. Schubert, J. Hauber, and M. Schindler, "A

flow cytometry-based FRET assay to identify and analyse protein-protein interactions in living cells," *PLoS One*, vol. 5, no. 2, p. e9344, 2010.

[25] J. F. Keij and J. A. Steinkamp, "Flow cytometric characterization and classification of multiple dual-color fluorescent microspheres using fluorescence lifetime," *Cytometry*, vol. 33, pp. 318–23, Nov 1998.

[26] L. He, T. D. Bradrick, T. S. Karpova, X. Wu, M. H. Fox, R. Fischer, J. G. McNally, J. R. Knutson, A. C. Grammer, and P. E. Lipsky, "Flow cytometric measurement of fluorescence (förster) resonance energy transfer from cyan fluorescent protein to yellow fluorescent protein using single-laser excitation at 458 nm," *Cytometry A*, vol. 53, pp. 39–54, May 2003.

[27] F. K. Chan, R. M. Siegel, D. Zacharias, R. Swofford, K. L. Holmes, R. Y. Tsien, and M. J. Lenardo, "Fluorescence resonance energy transfer analysis of cell surface receptor interactions and signaling using spectral variants of the green fluorescent protein," *Cytometry*, vol. 44, pp. 361–8, Aug 2001.

[28] Z. Sebestyén, P. Nagy, G. Horváth, G. Vámosi, R. Debets, J. W. Gratama, D. R. Alexander, and J. Szöllosi, "Long wavelength fluorophores and cell-by-cell correction for autofluorescence significantly improves the accuracy of flow cytometric energy transfer measurements on a dual-laser benchtop flow cytometer," *Cytometry*, vol. 48, pp. 124–35, Jul 2002.

[29] M. Foquet, J. Korlach, W. R. Zipfel, W. W. Webb, and H. G. Craighead, "Focal volume confinement by submicrometer-sized fluidic channels," *Anal Chem*, vol. 76, pp. 1618–26, Mar 2004.

[30] J. B. Edel and A. J. de Mello, "Single particle confocal fluorescence spectroscopy in microchannels: dependence of burst width and burst area distributions on particle size and flow rate," *Anal Sci*, vol. 19, pp. 1065–9, Jul 2003.

[31] P. Schwille, F. J. Meyer-Almes, and R. Rigler, "Dual-color fluorescence cross-correlation spectroscopy for multicomponent diffusional analysis in solution," *Biophys J*, vol. 72, pp. 1878–86, Apr 1997.

[32] M. Böhmer, M. Wahl, H.-J. Rahn, R. Erdmann, and J. Enderlein, "Time-resolved fluorescence correlation spectroscopy," *Chemical Physics Letters*, vol. 353, no. 5–6, pp. 439 – 445, 2002.

[33] K. M. Berland, P. T. So, and E. Gratton, "Two-photon fluorescence correlation spectroscopy: method and application to the intracellular environment," *Biophys J*, vol. 68, pp. 694–701, Feb 1995.

[34] K. Palo, L. Brand, C. Eggeling, S. Jäger, P. Kask, and K. Gall, "Fluorescence intensity and lifetime distribution analysis: toward higher accuracy in fluorescence fluctuation spectroscopy," *Biophys J*, vol. 83, pp. 605–18, Aug 2002.

[35] P. Kask, K. Palo, D. Ullmann, and K. Gall, "Fluorescence-intensity distribution analysis and its application in biomolecular detection technology," *Proc Natl Acad Sci U S A*, vol. 96, pp. 13756–61, Nov 1999.

[36] Y. Chen, J. D. Muller, P. T. So, and E. Gratton, "The photon counting histogram in fluorescence fluctuation spectroscopy.," *Biophys J*, vol. 77, pp. 553–567, Jul 1999.

[37] L. N. Hillesheim and J. D. Müller, "The photon counting histogram in fluorescence fluctuation spectroscopy with non-ideal photodetectors," *Biophys J*, vol. 85, pp. 1948–58, Sep 2003.

[38] P. Kask, K. Palo, N. Fay, L. Brand, U. Mets, D. Ullmann, J. Jungmann, J. Pschorr, and K. Gall, "Two-dimensional fluorescence intensity distribution analysis: theory and applications.," *Biophys J*, vol. 78, pp. 1703–1713, Apr 2000.

[39] P. R. Barber, S. M. Ameer-Beg, S. Pathmananthan, M. Rowley, and A. C. C. Coolen, "A bayesian method for single molecule, fluorescence burst analysis," *Biomed Opt Express*, vol. 1, no. 4, pp. 1148–1158, 2010.

[40] C. Eggeling, S. Berger, L. Brand, J. R. Fries, J. Schaffer, A. Volkmer, and C. A. Seidel, "Data registration and selective single-molecule analysis using

multi-parameter fluorescence detection," *J Biotechnol*, vol. 86, pp. 163–80, Apr 2001.

[41] M. Prummer, B. Sick, A. Renn, and U. P. Wild, "Multiparameter microscopy and spectroscopy for single-molecule analytics," *Anal Chem*, vol. 76, pp. 1633–40, Mar 2004.

[42] R. K. P. Benninger, O. Hofmann, B. Onfelt, I. Munro, C. Dunsby, D. M. Davis, M. A. A. Neil, P. M. W. French, and A. J. de Mello, "Fluorescence-lifetime imaging of DNA-dye interactions within continuous-flow microfluidic systems," *Angew Chem Int Ed Engl*, vol. 46, no. 13, pp. 2228–31, 2007.

[43] B. Valeur and M. Berberan-Santos, *Molecular fluorescence: principles and applications*. Wiley, 2013.

[44] G. G. Stokes, "On the change of refrangibility of light," *Royal Society of London Philosophical Transactions Series I*, vol. 142, pp. 463–562, 1852.

[45] S. W. Hell, "Far-field optical nanoscopy," *Science*, vol. 316, pp. 1153–8, May 2007.

[46] J. R. Lakowicz, *Principles of fluorescence spectroscopy*. Kluwer Academic/Plenum Publishers, second ed., 1999.

[47] E. Abbe, "Beiträge zur theorie des mikroskops und der mikroskopischen wahrnehmung," *Archiv für mikroskopische Anatomie*, vol. 9, no. 1, pp. 413–418, 1873.

[48] A. V. Agronskaia, L. Tertoolen, and H. C. Gerritsen, "Fast fluorescence lifetime imaging of calcium in living cells.," *J Biomed Opt*, vol. 9, pp. 1230–1237, Nov-Dec 2004.

[49] W. Becker, *Advanced time-correlated single photon counting techniques*. Springer Series in Chemical Physics, Springer, 2010.

[50] J. Szöllosi, P. Nagy, Z. Sebestyén, S. Damjanovicha, J. W. Park, and L. Mátyus, "Applications of fluorescence resonance energy transfer for mapping biological membranes," *J Biotechnol*, vol. 82, pp. 251–66, Jan 2002.

[51] W. Beisker, F. Dolbeare, and J. W. Gray, "An improved immunocytochemical procedure for high-sensitivity detection of incorporated bromodeoxyuridine," *Cytometry*, vol. 8, pp. 235–9, Mar 1987.

[52] O. Bilsel, C. Kayatekin, L. A. Wallace, and C. R. Matthews, "A microchannel solution mixer for studying microsecond protein folding reactions," *Review of Scientific Instruments*, vol. 76, no. 1, p. 014302, 2005.

[53] O. Bilsel, Y. Wu, C. Kayatekin, and C. R. Matthews, "Merging microsecond mixing and time-correlated single-photon counting: using time-resolved FRET and time-resolved anisotropy to probe early events in protein folding," 2007.

[54] Y. Wu, E. Kondrashkina, C. Kayatekin, C. R. Matthews, and O. Bilsel, "Microsecond acquisition of heterogeneous structure in the folding of a TIM barrel protein.," *Proc Natl Acad Sci U S A*, vol. 105, pp. 13367–13372, Sep 2008.

[55] A. Van Orden, N. P. Machara, P. M. Goodwin, and R. A. Keller, "Single-molecule identification in flowing sample streams by fluorescence burst size and intraburst fluorescence decay rate," *Anal Chem*, vol. 70, pp. 1444–51, Apr 1998.

[56] E. Schonbrun, P. E. Steinvurzel, and K. B. Crozier, "A microfluidic fluorescence measurement system using an astigmatic diffractive microlens array," *Opt Express*, vol. 19, pp. 1385–94, Jan 2011.

[57] B. K. McKenna, J. G. Evans, M. C. Cheung, and D. J. Ehrlich, "A parallel microfluidic flow cytometer for high-content screening," *Nat Methods*, vol. 8, pp. 401–3, May 2011.

[58] L. M. Davis, J. L. Lubbeck, K. M. Dean, A. E. Palmer, and R. Jimenez, "Microfluidic cell sorter for use in developing red fluorescent proteins with improved photostability," *Lab Chip*, vol. 13, pp. 2320–7, Jun 2013.

[59] M. M. Wang, E. Tu, D. E. Raymond, J. M. Yang, H. Zhang, N. Hagen, B. Dees, E. M. Mercer, A. H. Forster, I. Kariv, P. J. Marchand, and W. F.

Butler, "Microfluidic sorting of mammalian cells by optical force switching," *Nat Biotechnol*, vol. 23, pp. 83–7, Jan 2005.

[60] D. J. Ehrlich, B. K. McKenna, J. G. Evans, A. C. Belkina, G. V. Denis, D. H. Sherr, and M. C. Cheung, "Parallel imaging microfluidic cytometer," *Methods Cell Biol*, vol. 102, pp. 49–75, 2011.

[61] J. Pawley, *Handbook of biological confocal microscopy*. Cognition and Language, Springer Dordrecht, 1995.

[62] K. Levenberg, "A method for the solution of certain non-linear problems in least squares," *Quarterly Journal of Applied Mathmatics*, vol. II, no. 2, pp. 164–168, 1944.

[63] K. K. Sharman, A. Periasamy, H. Ashworth, and J. N. Demas, "Error analysis of the rapid lifetime determination method for double-exponential decays and new windowing schemes," *Anal Chem*, vol. 71, pp. 947–52, Mar 1999.

[64] R. J. Woods, S. Scypinski, L. J. Love, and H. A. Ashworth, "Transient digitizer for the determination of microsecond luminescence lifetimes," *Anal Chem*, vol. 56, pp. 1395–400, Jul 1984.

[65] P. J. Verveer and P. I. H. Bastiaens, "Evaluation of global analysis algorithms for single frequency fluorescence lifetime imaging microscopy data," *J Microsc*, vol. 209, pp. 1–7, Jan 2003.

[66] A. H. A. Clayton, Q. S. Hanley, and P. J. Verveer, "Graphical representation and multicomponent analysis of single-frequency fluorescence lifetime imaging microscopy data," *J Microsc*, vol. 213, pp. 1–5, Jan 2004.

[67] H. E. Grecco, P. Roda-Navarro, and P. J. Verveer, "Global analysis of time correlated single photon counting FRET-FLIM data," *Opt Express*, vol. 17, pp. 6493–508, Apr 2009.

[68] M. A. Digman, V. R. Caiolfa, M. Zamai, and E. Gratton, "The phasor approach to fluorescence lifetime imaging analysis," *Biophys J*, vol. 94, pp. L14–6, Jan 2008.

[69] M. I. Rowley, P. R. Barber, A. C. C. Coolen, and B. Vojnovic, "Bayesian analysis of fluorescence lifetime imaging data," in *Society of Photo-Optical Instrumentation Engineers (SPIE) Conference Series*, vol. 7903 of *Society of Photo-Optical Instrumentation Engineers (SPIE) Conference Series*, Feb. 2011.

[70] P. R. Barber, S. M. Ameer-Beg, J. D. Gilbey, R. J. Edens, I. Ezike, and B. Vojnovic, "Global and pixel kinetic data analysis for FRET detection by multi-photon time-domain FLIM," *Proc. SPIE*, vol. 5700, pp. 171–181, 2005.

[71] C.-G. Yang, Z.-R. Xu, A. P. Lee, and J.-H. Wang, "A microfluidic concentration-gradient droplet array generator for the production of multi-color nanoparticles," *Lab Chip*, vol. 13, pp. 2815–20, Jul 2013.

[72] F. Pereira, X. Niu, and A. J. deMello, "A nano lc-maldi mass spectrometry droplet interface for the analysis of complex protein samples," *PLoS One*, vol. 8, no. 5, p. e63087, 2013.

[73] F. Chen, Y. Zhang, Y. Nakagawa, H. Zeng, C. Luo, H. Nakajima, K. Uchiyama, and J.-M. Lin, "A piezoelectric drop-on-demand generator for accurate samples in capillary electrophoresis," *Talanta*, vol. 107, pp. 111–7, Mar 2013.

[74] X. Leng and C. J. Yang, "Agarose droplet microfluidics for highly parallel and efficient single molecule emulsion pcr," *Methods Mol Biol*, vol. 949, pp. 413–22, 2013.

[75] T. Glawdel and C. L. Ren, "Droplet formation in microfluidic t-junction generators operating in the transitional regime. iii. dynamic surfactant effects," *Phys Rev E Stat Nonlin Soft Matter Phys*, vol. 86, p. 026308, Aug 2012.

[76] A. S. Basu, "Droplet morphometry and velocimetry (DMV): a video processing software for time-resolved, label-free tracking of droplet parameters," *Lab Chip*, vol. 13, pp. 1892–901, May 2013.

[77] E. W. M. Kemna, L. I. Segerink, F. Wolbers, I. Vermes, and A. van den Berg, "Label-free, high-throughput, electrical detection of cells in droplets," *Analyst*, vol. 138, pp. 4585–92, Aug 2013.

[78] S. Gschwind, H. Hagendorfer, D. A. Frick, and D. Günther, "Mass quantification of nanoparticles by single droplet calibration using inductively coupled plasma mass spectrometry," *Anal Chem*, vol. 85, pp. 5875–83, Jun 2013.

[79] D. J. Han, J. H. Jung, J. S. Choi, Y. T. Kim, and T. S. Seo, "Synthesis of a 3d graphite microball using a microfluidic droplet generator and its polymer composite with core-shell structure," *Lab Chip*, Aug 2013.

[80] J. V. Watson, "The early fluidic and optical physics of cytometry," *Cytometry*, vol. 38, pp. 2–14; discussion 1, Feb 1999.

[81] G. Batchelor, *An introduction to fluid dynamics*. Cambridge Mathematical Library, Cambridge University Press, 2000.

[82] D. Acheson, *Elementary fluid dynamics*. Oxford Applied Mathematics and Computing Science Series, Clarendon Press, 1990.

[83] J. M. Borwein and P. B. Borwein, *Pi and the AGM: A Study in Analytic Number Theory and Computational Complexity*. Wiley, 1987.

[84] C. M. Bishop, *Neural Networks for Pattern Recognition*. New York, NY, USA: Oxford University Press, Inc., 1995.

[85] C. R. Company, *CRC standard mathematical tables and formulae*. CRC Press, 1991.

[86] R. Honsberger and M. A. of America, *Episodes in Nineteenth and Twentieth Century Euclidean Geometry*. No. v. 37 in ANNELI LAX NEW MATHEMATICAL LIBRARY, Mathematical Association of America, 1995.

[87] C. Buehler, J. Dreessen, K. Mueller, P. T. C. So, A. Schilb, U. Hassiepen, K. A. Stoeckli, and M. Auer, "Multi-photon excitation of intrinsic protein

fluorescence and its application to pharmaceutical drug screening," *Assay Drug Dev Technol*, vol. 3, pp. 155–67, Apr 2005.

[88] S. V. Koushik, H. Chen, C. Thaler, H. L. Puhl, 3rd, and S. S. Vogel, "Cerulean, venus, and venusY67C fret reference standards," *Biophys J*, vol. 91, pp. L99–L101, Dec 2006.

[89] G. Nishimura and M. Tamura, "Artefacts in the analysis of temporal response functions measured by photon counting," *Phys Med Biol*, vol. 50, pp. 1327–42, Mar 2005.

[90] P. Hall and B. Selinger, "Better estimates of exponential decay parameters," *The Journal of Physical Chemistry*, vol. 85, no. 20, pp. 2941–2946, 1981.

[91] J. Tellinghuisen and C. W. Wilkerson, "Bias and precision in the estimation of exponential decay parameters from sparse data," *Analytical Chemistry*, vol. 65, no. 9, pp. 1240–1246, 1993.

[92] Ž. Bajzer, T. Therneau, J. Sharp, and F. Prendergast, "Maximum likelihood method for the analysis of time-resolved fluorescence decay curves," *European Biophysics Journal*, vol. 20, no. 5, pp. 247–262, 1991.

[93] S. Menard, E. Tagliabue, M. Campiglio, and S. M. Pupa, "Role of HER2 gene overexpression in breast carcinoma.," *J Cell Physiol*, vol. 182, pp. 150–162, Feb 2000.

[94] E. Tagliabue, R. Agresti, M. L. Carcangiu, C. Ghirelli, D. Morelli, M. Campiglio, M. Martel, R. Giovanazzi, M. Greco, A. Balsari, and S. Ménard, "Role of HER2 in wound-induced breast carcinoma proliferation," *Lancet*, vol. 362, pp. 527–33, Aug 2003.

[95] S. Ménard, P. Casalini, M. Campiglio, S. M. Pupa, and E. Tagliabue, "Role of HER2/neu in tumor progression and therapy," *Cell Mol Life Sci*, vol. 61, pp. 2965–78, Dec 2004.

[96] M. H. Kirschbaum and Y. Yarden, "The ErbB/HER family of receptor tyrosine kinases: A potential target for chemoprevention of epithelial neoplasms," *J Cell Biochem Suppl*, vol. 34, pp. 52–60, 2000.

[97] R. A. Walker, "The ErbB/HER type 1 tyrosine kinase receptor family," *J Pathol*, vol. 185, pp. 234–5, Jul 1998.

[98] R. Roskoski, Jr, "The ErbB/HER receptor protein-tyrosine kinases and cancer," *Biochem Biophys Res Commun*, vol. 319, pp. 1–11, Jun 2004.

[99] M. Peter and S. M. Ameer-Beg, "Imaging molecular interactions by multiphoton FLIM," *Biology of the Cell*, vol. 96, no. 3, pp. 231 – 236, 2004.

[100] M. A. Condrau, R. A. Schwendener, P. Niederer, and M. Anliker, "Time-resolved flow cytometry for the measurement of lanthanide chelate fluorescence: I. concept and theoretical evaluation," *Cytometry*, vol. 16, pp. 187–94, Jul 1994.

[101] M. A. Condrau, R. A. Schwendener, M. Zimmermann, M. H. Muser, U. Graf, P. Niederer, and M. Anliker, "Time-resolved flow cytometry for the measurement of lanthanide chelate fluorescence: II. instrument design and experimental results," *Cytometry*, vol. 16, pp. 195–205, Jul 1994.

[102] L. Seveus, M. Väisälä, S. Syrjänen, M. Sandberg, A. Kuusisto, R. Harju, J. Salo, I. Hemmilä, H. Kojola, and E. Soini, "Time-resolved fluorescence imaging of europium chelate label in immunohistochemistry and in situ hybridization," *Cytometry*, vol. 13, no. 4, pp. 329–38, 1992.